



A University of Sussex DPhil thesis

Available online via Sussex Research Online:

<http://sro.sussex.ac.uk/>

This thesis is protected by copyright which belongs to the author.

This thesis cannot be reproduced or quoted extensively from without first obtaining permission in writing from the Author

The content must not be changed in any way or sold commercially in any format or medium without the formal permission of the Author

When referring to this work, full bibliographic details including the author, title, awarding institution and date of the thesis must be given

Please visit Sussex Research Online for more information and further details



**Investigation into Nonlinear Dynamics of
Rotor-Floating Ring Bearing Systems in
Automotive Turbochargers**

Liang Tian

Submitted for the degree of Doctor of Philosophy

University of Sussex

October 2012

Declaration

I hereby declare that this thesis has not been and will not be submitted in whole or in part to another University for the award of any other degree.

Signature:

Liang Tian

UNIVERSITY OF SUSSEX

LIANG TIAN, DOCTOR OF PHILOSOPHY

INVESTIGATION INTO NONLINEAR DYNAMICS OF ROTOR-FLOATING RING
BEARING SYSTEMS IN AUTOMOTIVE TURBOCHARGERS

SUMMARY

As a high speed rotating device, a modern turbocharger rotor is commonly supported by floating ring bearings (FRBs), owing to their cost effectiveness for mass production and good damping performance. Thanks to the rapid growth of the power of the modern computer, rotordynamic analysis of turbocharger rotor-bearing systems becomes feasible, and it is closely related to the healthy operation and noise generation of turbochargers. The work in this thesis is concerned with the nonlinear rotordynamic modelling, simulation and analysis in the rotor-FRB system of turbochargers. The conventional linear eigenvalue analysis is shown first in a gradually deepening manner to provide a deeper insight into the results from nonlinear simulations and reported experimental results. It is subsequently found the onset of first two nonlinear jumps can be effectively predicted by the linearized FRB model, although the rotordynamic characteristics at higher rotor speeds can hardly be linearly predicted. The desired oil-film forces for nonlinear simulations are calculated from a newly proposed analytical method, which is extended from the Capone's journal bearing model. Stationary simulations under the perfectly balanced condition show two major subsynchronous components throughout the considered speed range, while the inclusion of in-phase unbalance places a considerable effect on the rotor response at relatively low speed and delays the occurrence of oil-film instability. However, at higher rotor speeds, the

lower subsynchronous component can still establish the dominance. The engine induced vibrations are also considered, and it is seen the rotor response over the lower end of the speed range will be considerably affected, whereas, at higher rotor speeds, the engine induced vibrations can be suppressed by the dominant lower subsynchronous vibrations. Through carrying out many run-up and run-down simulations, the FRB outer clearance is found to be a critical parameter of the rotordynamic performance of the investigated TC rotor-FRB system, since distinct frequency maps are obtained with varying FRB outer clearances. The nonlinear effects of unbalance are also investigated, and it is observed the rotor response can be considerably affected by the amount and distribution of the imposed unbalance.

Acknowledgements

First of all, I would like to express my sincere gratitude to Dr. William Wang for him to offer me the opportunity to pursue my research under his invaluable guidance. He introduced me to the interesting field of rotordynamics and supported my work in a number of ways.

Moreover, special thanks are due to Dr. Jun Peng for his co-supervision, constant support and constructive advice throughout my PhD studies. He provided me with the precious opportunity of joining the SCODECE project, which I deeply appreciated.

I acknowledge and appreciate the financial support from the Graduate Teaching Assistant Fund of the University of Sussex and the European Regional Development Fund through INTERREG IVA (SCODECE).

I would like to thank all my colleagues in the Automotive Dynamics and Control Group, Siska, Thana and Luis, who bring me the help as and when required.

I am also immensely grateful to Dr. Feng Pan of the Northeastern University of China, for his practical suggestions and information to improve my MATLAB programming skills during his visit.

The completion of the thesis would not be possible without a mention of the whole-hearted support given by my beloved wife, Chao. I would like to thank you all most sincerely, for your continuous encouragement and for always being there for me.

Dedication

This thesis is dedicated to my dear father and mother, and to my dear lovely wife, Chao.

Contents

List of Tables	x
List of Figures	xix
Nomenclature	xx
1 Introduction	1
1.1 Background	1
1.2 Turbocharger Rotordynamics	2
1.3 Literature Review	6
1.3.1 FRB analytical and experimental analysis in the early stage	6
1.3.2 Thermal analysis of FRBs	10
1.3.3 Detailed analysis of FRBs	11
1.3.4 Linear stability analysis	12
1.3.5 Nonlinear stability analysis	13
1.3.6 Rotordynamic analysis of rotor-FRB systems	15
1.3.7 Rotordynamic analysis of rotor-SFRB systems	25
1.3.8 Journal bearings in low-speed TCs	26
1.3.9 Ball bearing investigation	26
1.3.10 Bearing system comparisons and other bearing systems	27
1.4 Research Objectives	30
1.5 Thesis Outline	30
2 Turbocharger Linear Rotordynamics	32
2.1 Finite Element Modelling	32
2.2 Isotropic Spring Supports	35
2.3 Anisotropic Spring Supports	36
2.4 Linearized Journal Bearings	37

2.5	Isotropic Spring Supports with Ring Masses	39
2.6	Linearized FRBs	41
2.6.1	Linearization without ring mass	41
2.6.2	Linearization with ring mass	42
2.7	Synchronous Response	47
3	Stationary Nonlinear Analysis	50
3.1	Nonlinear FRB Model	50
3.2	Equations of Motion for the Floating Rings	56
3.3	Model Validation	57
3.3.1	Non-dimensional analysis	57
3.3.2	Perfectly balanced TC rotor	58
3.4	Unbalanced TC Rotor	62
4	Effects of Engine Excitation	69
4.1	Engine Vibration Modelling	69
4.2	Stationary Simulation Results	70
5	Nonlinear Effects of Bearing Outer Clearance	78
5.1	Nonstationary Simulation Method	78
5.2	Simulation Results	79
5.2.1	Simulation 1 ($C_2 = 30 \mu\text{m}$)	80
5.2.2	Simulation 2 ($C_2 = 35 \mu\text{m}$)	85
5.2.3	Simulation 3 ($C_2 = 40 \mu\text{m}$)	92
5.2.4	Simulation 4 ($C_2 = 44 \mu\text{m}$)	98
5.2.5	Discussions	104
6	Nonlinear Effects of Unbalance	106
6.1	Simulation 1 ($C_2 = 35 \mu\text{m}$)	107
6.1.1	Perfectly balanced rotor: $e = 0$	107
6.1.2	Out-of-phase unbalance: $\delta_c = 0, \delta_t = \pi$	110
6.1.3	In-phase unbalance: $\delta_c = \delta_t = 0$	114
6.2	Simulation 2 ($C_2 = 40 \mu\text{m}$)	117
6.2.1	Perfectly balanced rotor: $e = 0$	117
6.2.2	Out of phase unbalance: $\delta_c = 0, \delta_t = \pi$	120
6.2.3	In-phase unbalance: $\delta_c = \delta_t = 0$	124

CONTENTS

6.3	Simulation 3 ($C_2 = 50 \mu\text{m}$)	129
6.3.1	Perfectly balanced rotor: $e = 0$	129
6.3.2	Out of phase unbalance: $\delta_c = 0, \delta_t = \pi$	132
6.3.3	In phase unbalance: $\delta_c = \delta_t = 0$	137
6.4	Discussions of the Simulation Results	143
7	Conclusions, Novel Contributions and Outlook	146
7.1	Summary of Results	146
7.2	Novel Contributions	148
7.3	Future Work	150
	References	151
A	Research Publications	161

List of Tables

2.1	TC rotor-FRB system details	34
3.1	Symmetric rigid rotor-FRB system parameters	57
4.1	Selected simulation parameters	73
5.1	Parameters for run-up and run-down simulations	79
5.2	Parameters for MATLAB spectrogram [®] function	79
6.1	Parameters for run-up and run-down simulations	107

List of Figures

1.1	Cross section of a Bosch Mahle [®] TC rotor assembly (courtesy of Bosch Mahle Turbo Systems)	2
1.2	A TC rotor supported on SFRB [100]	3
1.3	Schematic view of FRB, SFRB and a ball bearing with squeeze film damper [60]	3
1.4	Sketches of various types of waterfall diagrams commonly observed in TC rotor-FRB systems. [86]	5
2.1	TC finite element model. The dash rectangles at the rotor ends represent the compressor disk attached to Node 1 and the turbine disk attached to Node 4.	33
2.2	TC rotor with constant stiffness bearing supports: (a) the front view, (b) the side view at Node 2.	35
2.3	Campbell diagram (isotropic spring with stiffness of 1×10^6 N/m), the dash line is the synchronous line; mode shape plots are obtained at 1000 Hz.	35
2.4	Campbell diagram (isotropic spring with stiffness of 1×10^8 N/m), the dash line is the synchronous line; mode shape plots are obtained at 1000 Hz.	36
2.5	Campbell diagram (anisotropic spring supports with stiffness of 1×10^6 N/m in the X direction and 2×10^6 N/m in the Y direction), the dash line is the synchronous line; mode shape plots are obtained at 1000 Hz.	37
2.6	TC rotor supported by linearized journal bearings	37
2.7	Campbell diagram with linearized journal bearings, the dash line is the synchronous line; mode shape plots are obtained at 1000 Hz.	38
2.8	Stability analysis with journal bearings: (a) Campbell diagram with unstable modes, (b) stability map and (c) damping factor plot.	39
2.9	TC rotor with constant stiffness bearing supports including floating ring masses; $K_{xi} = K_{xo} = K_{yi} = K_{yo} = 1 \times 10^6$ N/m.	40

LIST OF FIGURES

2.10	Campbell diagram with linearized journal bearings, the dash line is the synchronous line; mode shape plots are obtained at 1000 Hz.	40
2.11	Mode shapes of forward whirls when the ring masses are considered and connected by constant stiffness supports; ring orbits are represented by the red dotted circles; the rotor speed is set to be 1000 Hz.	40
2.12	TC rotor supported by linearized FRBs including floating ring masses . . .	41
2.13	Stability analysis with linearized FRBs without ring masses: (a) Campbell diagram with unstable modes, (b) stability map. Both ring speed ratios are assumed to be 0.2.	42
2.14	Campbell diagrams (two oil films in series) with the identically varying FRB outer clearances: (a) 30 μm , (b) 35 μm , (c) 40 μm , (d) 44 μm , (e) 60 μm and (f) 74 μm . Forward whirl is diamond; backward whirl is square; mixed whirl is triangle. Both ring speed ratios are assumed to be 0.2.	43
2.15	Mode shapes of the unstable modes at four different speeds when both FRB clearances are 44 μm : (a) 200 Hz, (b) 500 Hz, (c) 1000 Hz and (d) 2000 Hz. The floating ring orbits are represented by the dotted circles, while the dashed lines in mode shapes indicate the positions of the four nodes at a certain moment. Both ring speed ratios are assumed to be 0.2.	44
2.16	Stability maps with the identically varying FRB outer clearances: (a) 30 μm , (b) 35 μm , (c) 40 μm , (d) 44 μm , (e) 60 μm and (f) 74 μm	45
2.17	Predicted synchronous response of the compressor centre in the X and the Y directions	48
2.18	Campbell digram of linearized FRBs when the ring masses are included and the bearing outer clearance is 74 μm ; the dashed line is the synchronous line.	48
3.1	FRB middle plane and reference frame	51
3.2	Orbit maps of dimensionless analysis results: (a) $\nu = 4.0$, (b) $\nu = 4.5$ and (c) $\nu = 5.0$	58
3.3	Orbits and ring speed ratios of FRBs without unbalance (FRB1 first row, FRB2 second row), where the outer dashed circles indicate the border of motion. (a) 24,000 rpm, (b) 36,000 rpm, (c) 60,000 rpm, (d) 90,000 rpm, (e) 148,000 rpm and (f) 180,000 rpm.	59
3.3	(continued)	60
3.4	Waterfall plots under the perfectly balanced condition: (a) x_2/C_1 and (b) x_3/C_1	61

LIST OF FIGURES

3.5	Displacement plot of the two ends of the rotor in the X direction: (a) 60,000 rpm and (b) 90,000 rpm. The dashed line indicates x_1/C_1 ; the solid line indicates x_4/C_1	62
3.6	Orbits and ring speed ratios of FRBs subject to unbalance (FRB1 is at first row; FRB2 is at second row), where the outer dashed circles indicate the border of motion. (a) 24,000 rpm, (b) 12,000 rpm, (c) 18,000 rpm, (d) 24,000 rpm, (e) 36,000 rpm, (f) 60,000 rpm, (g) 90,000 rpm, (h) 148,000 rpm and (i) 180,000 rpm.	63
3.6	(continued)	64
3.6	(continued)	65
3.7	Waterfall plots at FRB 1 and FRB 2 in the X direction with unbalance: (a) waterfall plot at FRB 1 for x_2/C_1 and (b) waterfall plot at FRB 2 for x_3/C_1	66
4.1	Orbits and ring speed ratios of FRBs subject to unbalance and engine excitation (FRB1 first row, FRB2 second row), where the outer dashed circles indicate the border of motion. x_e, y_e denote the TC housing motions in the X direction and the Y direction, respectively. (a) 6,000 rpm, (b) 12,000 rpm, (c) 18,000 rpm, (d) 24,000 rpm, (e) 36,000 rpm, (f) 60,000 rpm and (g) 90,000 rpm.	71
4.1	(continued)	72
4.1	(continued)	73
4.2	Frequency spectrum of the journal at FRB1 at 24,000 rpm: (a) upper FFT for x_2/C_1 , lower for y_2/C_1 ; with unbalance only, (b) upper FFT for $(x_2 - x_e)/C_1$, lower for $(y_2 - x_e)/C_1$; with unbalance and engine excitation.	74
4.3	Waterfall plot at FRB 1 and FRB 2 in the X direction with unbalance and engine excitation: (a) at FRB 1 for $(x_2 - x_e)/C_1$, (b) at FRB 2 for $(x_3 - x_e)/C_1$	75
4.4	Zoomed waterfall plot at low speed range at FRB1 in the X direction: (a) waterfall for x_2/C_1 ; with unbalance only, (b) waterfall for $(x_2 - x_e)/C_1$; with unbalance and engine excitation.	76

LIST OF FIGURES

5.1	Run-up simulation when the TC rotor is perfectly balanced and $C_2 = 30\ \mu\text{m}$: (a), (b) waterfall plots of the compressor end y_1/C_1 and turbine end y_4/C_1 in Y axis direction, respectively, (c), (d) top-views of the waterfall diagrams given in (a) and (b), corresponding to y_1/C_1 and y_4/C_1 , respectively, (e) and (f) displacement plots of y_1/C_1 and y_4/C_1 , (g), (h) eccentricity plots of the inner and outer oil films at FRB 1 and FRB 2, respectively, (i) ring speed ratios of FRB 1 and FRB 2.	81
5.1	(continued)	82
5.2	Filtered mode shapes and orbits for Sub 1 when the outer clearances are $30\ \mu\text{m}$ at selected rotor speeds: (a) 507 Hz and (b) 2504 Hz.	83
5.3	Run-down simulation when the TC rotor is perfectly balanced and $C_2 = 30\ \mu\text{m}$: (a) waterfall plot of the turbine end y_4/C_1 in Y axis direction, (b) displacement plot of y_4/C_1 , (c), (d) eccentricity plot of the inner and outer oil films at FRB 1 and FRB 2, respectively.	83
5.4	Run-up simulation when the TC rotor is perfectly balanced and $C_2 = 35\ \mu\text{m}$: (a), (b) waterfall plots of the compressor end y_1/C_1 and turbine end y_4/C_1 in Y axis direction, respectively, (c), (d) top-views of the waterfall diagrams given in (a) and (b), corresponding to y_1/C_1 and y_4/C_1 , respectively, (e) and (f) displacement plots of y_1/C_1 and y_4/C_1 , (g), (h) eccentricity plots of the inner and outer oil films at FRB 1 and FRB 2, respectively, (i) ring speed ratios of FRB 1 and FRB 2.	86
5.4	(continued)	87
5.5	Filtered mode shapes and orbits for Sub 1 and Sub 2 when the outer clearances are $35\ \mu\text{m}$ at selected rotor speeds: (a) 307 Hz for Sub 1, (b) 707 Hz for Sub 2, (c) 2012 Hz for Sub 1 and (d) 2504 Hz for Sub 1.	88
5.6	Top-views for the waterfall diagrams of run-down simulation: $C_2 = 35\ \mu\text{m}$. (a) for y_1/C_1 and (b) for y_4/C_1	88
5.7	Top-views of the waterfall diagrams of the run-up and run-down simulation results when the outer clearances of both bearings are $34\ \mu\text{m}$: (a) run-up simulation results for y_1/C_1 , (b) run-down simulation results for y_1/C_1 . . .	89
5.8	Comparisons of the top-views of waterfall diagrams for y_1/C_1 from run-up simulations: (a) $C_2 = 36\ \mu\text{m}$, (b) $C_2 = 37\ \mu\text{m}$, (c) $C_2 = 38\ \mu\text{m}$ and (d) $C_2 = 39\ \mu\text{m}$	90

LIST OF FIGURES

5.9	Run-up simulation when the TC rotor is perfectly balanced and $C_2 = 40\ \mu\text{m}$: (a), (b) waterfall plots of the compressor end y_1/C_1 and turbine end y_4/C_1 in Y axis direction, respectively, (c), (d) top-views of the waterfall diagrams given in (a) and (b), corresponding to y_1/C_1 and y_4/C_1 , respectively, (e) and (f) displacement plots of y_1/C_1 and y_4/C_1 , (g), (h) eccentricity plots of the inner and outer oil films at FRB 1 and FRB 2, respectively, (i) ring speed ratios of FRB 1 and FRB 2.	93
5.9	(continued)	94
5.10	Filtered mode shapes and orbits for Sub 1, Sub 2 and Sub 3 when the outer clearances are $40\ \mu\text{m}$ at selected rotor speeds: (a) 169 Hz for Sub 1, (b) 507 Hz for Sub 2, (c) 998 Hz for Sub 1 and (d) 2012 Hz for Sub 3.	95
5.11	Top-views for the waterfall diagrams of run-down simulation when $C_2 = 40\ \mu\text{m}$: (a) for y_1/C_1 and (b) for y_4/C_1	95
5.12	Comparisons of the top-views of waterfall diagrams for y_1/C_1 from run-up simulations: (a) $C_2 = 42\ \mu\text{m}$, (b) $C_2 = 43\ \mu\text{m}$	95
5.13	Run-up simulation when the TC rotor is perfectly balanced and $C_2 = 44\ \mu\text{m}$: (a), (b) waterfall plots of the compressor end y_1/C_1 and turbine end y_4/C_1 in Y axis direction, respectively, (c), (d) top-views of the waterfall diagrams given in (a) and (b), corresponding to y_1/C_1 and y_4/C_1 , respectively, (e) and (f) displacement plots of y_1/C_1 and y_4/C_1 , (g), (h) eccentricity plots of the inner and outer oil films at FRB 1 and FRB 2, respectively, (i) ring speed ratios of FRB 1 and FRB 2.	99
5.13	(continued)	100
5.14	Filtered mode shapes and orbits for Sub 1, Sub 2 and Sub 3 when the outer clearances are $44\ \mu\text{m}$ at selected rotor speeds: (a) 108 Hz for Sub 1, (b) 399 Hz for Sub 2, (c) 1505 Hz for Sub 3 and (d) 2611 Hz for Sub 3.	101
5.15	Top-views for the waterfall diagrams of run-down simulation: $C_2 = 44\ \mu\text{m}$. (a) for y_1/C_1 and (b) for y_4/C_1	101
5.16	Comparisons of the top-views of waterfall diagrams for y_1/C_1 from run-up simulations: (a) $C_2 = 45\ \mu\text{m}$, (b) $C_2 = 46\ \mu\text{m}$, (c) $C_2 = 47\ \mu\text{m}$, (d) $C_2 = 48\ \mu\text{m}$, (e) $C_2 = 49\ \mu\text{m}$ and (f) $C_2 = 50\ \mu\text{m}$	102

6.1	Run-up simulation when the TC-FRB system is in a perfectly balanced condition ($e = 0$) and $C_2 = 35 \mu\text{m}$: (a), (b) non-dimensional waterfall plots for the displacements of the compressor end and turbine end in Y axis direction, i.e., y_1/C_1 and y_4/C_1 , respectively, (c) top-view of (a), (d) displacement plot of y_4/C_1 , (e) eccentricity plot of the inner and outer oil films at FRB 1, (f) ring speed ratio plot of FRB 1 and FRB 2.	108
6.2	Run-down simulation when the TC-FRB system is in a perfectly balanced condition ($e = 0$) and $C_2 = 35 \mu\text{m}$: (a) top-view of the waterfall diagram of y_1/C_1 , (b) eccentricity plot of the inner and outer oil films at FRB 1.	109
6.3	Filtered mode shapes and orbits for Sub 1 and Sub 2 of run-up simulation when the outer clearances are $35 \mu\text{m}$ and the rotor is perfectly balanced at selected rotor speeds: (a) 409 Hz, (b) 896 Hz, (c) 1997 Hz and (d) 2995 Hz.	109
6.4	Top-views of the waterfall plots of y_1/C_1 in run-up simulations when the out-of-phase unbalance is imposed ($\delta_c = 0, \delta_t = \pi$) and $C_2 = 35 \mu\text{m}$: (a) $e = 5 \mu\text{m}$, (b) $e = 10 \mu\text{m}$, (c) $e = 15 \mu\text{m}$, (d) $e = 20 \mu\text{m}$, (e) $e = 25 \mu\text{m}$ and (f) $e = 30 \mu\text{m}$	111
6.5	Run-up simulation results when $C_2 = 35 \mu\text{m}$ and the $30 \mu\text{m}$ out-of-phase unbalance offset is imposed: (a) eccentricity plot of the inner and outer oil films at FRB 1, (b) eccentricity plot of the inner and outer oil films at FRB 2, (c) displacement plot of y_4/C_1 and (d) ring speed ratio plot of FRB 1 and FRB 2.	112
6.6	Top-views of the waterfall plots of y_1/C_1 in run-down simulations when the out-of-phase unbalance is imposed ($\delta_c = 0, \delta_t = \pi$) and $C_2 = 35 \mu\text{m}$: (a) $e = 5 \mu\text{m}$, (b) $e = 10 \mu\text{m}$, (c) $e = 15 \mu\text{m}$, (d) $e = 20 \mu\text{m}$, (e) $e = 25 \mu\text{m}$ and (f) $e = 30 \mu\text{m}$	113
6.7	Top-views of the waterfall plots of y_1/C_1 in run-up simulations when the in-phase unbalance is imposed ($\delta_c = 0, \delta_t = 0$) and $C_2 = 35 \mu\text{m}$: (a) $e = 5 \mu\text{m}$, (b) $e = 10 \mu\text{m}$, (c) $e = 15 \mu\text{m}$, (d) $e = 20 \mu\text{m}$, the red as well as green lines in (c) and (d) correspond to the ring speeds at FRB 1 as well as FRB 2, respectively.	115
6.8	Eccentricities of FRB 1 in run-up simulations when the in-phase unbalance is imposed ($\delta_c = 0, \delta_t = 0$) and $C_2 = 35 \mu\text{m}$: (a) $e = 5 \mu\text{m}$, (b) $e = 10 \mu\text{m}$. . .	116

6.9	Top-views of the waterfall plots of y_1/C_1 in run-down simulations when the in-phase unbalance is imposed ($\delta_c = 0, \delta_t = 0$) and $C_2 = 35 \mu\text{m}$: (a) $e = 5 \mu\text{m}$, (b) $e = 10 \mu\text{m}$, (c) $e = 15 \mu\text{m}$, (d) $e = 20 \mu\text{m}$	116
6.10	Run-up simulation when the TC-FRB system is in a perfectly balanced condition ($e = 0$) and $C_2 = 40 \mu\text{m}$: (a), (b) non-dimensional waterfall plots for the displacements of the compressor end and turbine end in Y axis direction, i.e., y_1/C_1 and y_4/C_1 , respectively, (c), (d) top-views of (a) and (b), respectively, (e), (f) eccentricity plot of the inner and outer oil films at FRB 1 and FRB 2, (g) displacement plot of y_4/C_1 , (h) ring speed ratio plot of FRB 1 and FRB 2.	118
6.10	<i>(continued)</i>	119
6.11	Filtered mode shapes and orbits for Sub 1, Sub 2 and Sub 3 of run-up simulation when the outer clearances are $40 \mu\text{m}$ and the rotor is perfectly balanced at selected rotor speeds: (a) 128 Hz, (b) 589 Hz, (c) 1178 Hz and (d) 2458 Hz.	119
6.12	Run-down simulation when the TC-FRB system is in a perfectly balanced condition ($e = 0$) and $C_2 = 40 \mu\text{m}$: (a), (b) top-view of the waterfall diagram of y_1/C_1 and y_4/C_1 , respectively.	120
6.13	Top-views of the waterfall plots of y_1/C_1 in run-up simulations when the out-of-phase unbalance is imposed ($\delta_c = 0, \delta_t = \pi$) and $C_2 = 40 \mu\text{m}$: (a) $e = 5 \mu\text{m}$, (b) $e = 10 \mu\text{m}$, (c) $e = 15 \mu\text{m}$, (d) $e = 20 \mu\text{m}$, (e) $e = 25 \mu\text{m}$ and (f) $e = 30 \mu\text{m}$	121
6.14	Eccentricities of the inner and outer films at FRB 1 during run-up simulation when $C_2 = 40 \mu\text{m}$ and out-of-phase unbalance is imposed: (a) $e = 20 \mu\text{m}$, (b) $e = 25 \mu\text{m}$	122
6.15	Top-views of the waterfall plots of y_1/C_1 in run-down simulations when the out-of-phase unbalance is imposed ($\delta_c = 0, \delta_t = \pi$) and $C_2 = 40 \mu\text{m}$: (a) $e = 5 \mu\text{m}$, (b) $e = 10 \mu\text{m}$, (c) $e = 15 \mu\text{m}$, (d) $e = 20 \mu\text{m}$, (e) $e = 25 \mu\text{m}$ and (f) $e = 30 \mu\text{m}$	123
6.16	Top-views of the waterfall plots of y_1/C_1 in run-up simulations when the in-phase unbalance is imposed ($\delta_c = 0, \delta_t = 0$) and $C_2 = 40 \mu\text{m}$: (a) $e = 5 \mu\text{m}$, (b) $e = 10 \mu\text{m}$, (c) $e = 15 \mu\text{m}$, (d) $e = 20 \mu\text{m}$, (e) $e = 25 \mu\text{m}$ and (f) $e = 30 \mu\text{m}$, the red as well as green lines in (d), (e) and (f) correspond to the ring speeds at FRB 1 as well as FRB 2, respectively.	125

6.17 Run-up simulation results when $C_2 = 40\ \mu\text{m}$ and $5\ \mu\text{m}$ in-phase unbalance is imposed: (a), (b) inner and outer films eccentricities of FRB 1 and FRB 2, respectively, (c) displacement plot of y_4/C_1 and (d) ring speed ratio plot.	126
6.18 Eccentricities at FRB 1 when $C_2 = 40\ \mu\text{m}$ and in-phase unbalance is imposed: (a) $e = 10\ \mu\text{m}$, (b) $e = 15\ \mu\text{m}$, (c) $e = 20\ \mu\text{m}$ and (d) $e = 25\ \mu\text{m}$. . .	127
6.19 Top-views of the waterfall plots of y_1/C_1 in run-down simulations when the in-phase unbalance is imposed ($\delta_c = 0$, $\delta_t = 0$) and $C_2 = 40\ \mu\text{m}$: (a) $e = 5\ \mu\text{m}$, (b) $e = 10\ \mu\text{m}$, (c) $e = 15\ \mu\text{m}$, (d) $e = 20\ \mu\text{m}$	128
6.20 Run-up simulation when the TC-FRB system is in a perfectly balanced condition ($e = 0$) and $C_2 = 50\ \mu\text{m}$: (a), (b) non-dimensional waterfall plots for the displacements of the compressor end and turbine end in Y axis direction, i.e., y_1/C_1 and y_4/C_1 , respectively, (c), (d) top-views of (a) and (b), respectively, (e), (f) eccentricity plot of the inner and outer oil films at FRB 1 and FRB 2, (g) displacement plot of y_4/C_1 , (h) ring speed ratio plot of FRB 1 and FRB 2.	130
6.20 (<i>continued</i>)	131
6.21 Filtered mode shapes and orbits for Sub 1, Sub 2 and Sub 3 of run-up simulation when the outer clearances are $50\ \mu\text{m}$ and the rotor is perfectly balanced at selected rotor speeds: (a) 102 Hz, (b) 512 Hz, (c) 1510 Hz and (d) 2509 Hz.	131
6.22 Run-down simulation when the TC-FRB system is in a perfectly balanced condition ($e = 0$) and $C_2 = 50\ \mu\text{m}$: (a), (b) top-view of the waterfall diagram of y_1/C_1 and y_4/C_1 , respectively.	132
6.23 Top-views of the waterfall plots of y_1/C_1 in run-up simulations when the out-of-phase unbalance is imposed ($\delta_c = 0$, $\delta_t = \pi$) and $C_2 = 50\ \mu\text{m}$: (a) $e = 5\ \mu\text{m}$, (b) $e = 10\ \mu\text{m}$, (c) $e = 15\ \mu\text{m}$, (d) $e = 20\ \mu\text{m}$, (e) $e = 25\ \mu\text{m}$ and (f) $e = 30\ \mu\text{m}$	133
6.24 FRB eccentricities in run-up simulations when $C_2 = 50\ \mu\text{m}$ and out-of-phase unbalance is imposed: (a), (c) and (e) bearing eccentricities at FRB 1 when $e = 10\ \mu\text{m}$, $e = 20\ \mu\text{m}$ and $e = 30\ \mu\text{m}$, respectively, (b), (d) and (f) bearing eccentricities at FRB 2 when $e = 10\ \mu\text{m}$, $e = 20\ \mu\text{m}$ and $e = 30\ \mu\text{m}$ respectively.	134

LIST OF FIGURES

6.25 Top-views of the waterfall plots of y_1/C_1 in run-down simulations when the out-of-phase unbalance is imposed ($\delta_c = 0, \delta_t = \pi$) and $C_2 = 50 \mu\text{m}$: (a) $e = 5 \mu\text{m}$, (b) $e = 10 \mu\text{m}$, (c) $e = 15 \mu\text{m}$, (d) $e = 20 \mu\text{m}$, (e) $e = 25 \mu\text{m}$ and (f) $e = 30 \mu\text{m}$ 135

6.26 FRB eccentricities in run-down simulations when $C_2 = 50 \mu\text{m}$ and out-of-phase unbalance is imposed: (a), (c) bearing eccentricities at FRB 1 when $e = 25 \mu\text{m}$ and $e = 30 \mu\text{m}$, respectively, (b), (d) bearing eccentricities at FRB 2 when $e = 25 \mu\text{m}$ and $e = 30 \mu\text{m}$, respectively. 136

6.27 Top-views of the waterfall plots of y_1/C_1 in run-up simulations when the in-phase unbalance is imposed ($\delta_c = 0, \delta_t = 0$) and $C_2 = 50 \mu\text{m}$: (a) $e = 5 \mu\text{m}$, (b) $e = 10 \mu\text{m}$, (c) $e = 15 \mu\text{m}$, (d) $e = 20 \mu\text{m}$, (e) $e = 25 \mu\text{m}$ and (f) $e = 30 \mu\text{m}$. 138

6.28 FRB eccentricities in run-up simulations when $C_2 = 50 \mu\text{m}$ and in-phase unbalance is imposed: (a), (c), (e) and (g) bearing eccentricities at FRB 1 when $e = 5 \mu\text{m}$, $e = 10 \mu\text{m}$, $e = 15 \mu\text{m}$ and $e = 20 \mu\text{m}$, respectively, (b), (d), (f) and (h) bearing eccentricities at FRB 2 when $e = 5 \mu\text{m}$, $e = 10 \mu\text{m}$, $e = 15 \mu\text{m}$ and $e = 20 \mu\text{m}$, respectively. 139

6.28 (continued) 140

6.29 Filtered mode shapes and orbits for subsynchronous components in run-up simulation when the outer clearances are $50 \mu\text{m}$ and $5 \mu\text{m}$ in-phase imbalance offset is imposed: (a) 1510 Hz and (b) 2508 Hz. 140

6.30 Top-views of the waterfall plots of y_1/C_1 in run-down simulations when the in-phase unbalance is imposed ($\delta_c = 0, \delta_t = 0$) and $C_2 = 50 \mu\text{m}$: (a) $e = 5 \mu\text{m}$, (b) $e = 10 \mu\text{m}$, (c) $e = 15 \mu\text{m}$, (d) $e = 20 \mu\text{m}$, (e) $e = 25 \mu\text{m}$ and (f) $e = 30 \mu\text{m}$ 141

Nomenclature

Roman Symbols

\mathbf{C}	system external damping matrix
C_1	inner clearance
c_{in}	inner clearance in non-dimensional analysis
C_2	outer clearance
c_{ou}	outer clearance in non-dimensional analysis
D_j	journal diameter
D_{ro}	ring outer diameter
e	unbalance offset displacement
\mathbf{F}_i	inner oil film force vector
F_{i_x}, F_{i_y}	real oil film forces of inner film
f_{i_x}, f_{i_y}	non-dimensional oil film forces of inner film
F_{o_x}, F_{o_y}	real oil film forces of outer film
f_{o_x}, f_{o_y}	non-dimensional oil film forces of outer film
\mathbf{F}_s	static gravitational force vector
\mathbf{F}_{ub}	unbalance force vector
\mathbf{F}_{ubc}	unbalance force vector at compressor disk
\mathbf{F}_{ubt}	unbalance force vector at turbine disk
\mathbf{G}	skew-symmetric gyroscopic matrix

NOMENCLATURE

g	acceleration of gravity
G	oil film force function
h	oil film thickness
I_r	polar moment of inertia of floating ring
K	system stiffness matrix
K_x	stiffness coefficient of flexible supports in X direction
K_y	stiffness coefficient of flexible supports in Y direction
L_i	bearing inner length
L_{in}	floating ring inner length in non-dimensional analysis
\bar{x}_j, \bar{y}_j	non-dimensional coordinates of x_j, y_j
L_o	bearing outer length
L_{ou}	floating ring outer length in non-dimensional analysis
M	distributed symmetric mass matrix
m_c	mass of the compressor disk
m_r	floating ring mass
m_{ring}	floating ring mass in non-dimensional analysis
m_{rotor}	rotor mass in non-dimensional analysis
m_t	mass of the turbine disk
O_b	bearing origin
O_j	journal centre
O_r	ring centre
p	oil film pressure
\bar{p}	non-dimensional oil-film pressure p
q	system displacement vector

R_{in}	floating ring inner radius in non-dimensional analysis
R_j	journal radius
R_{ou}	floating ring outer radius in non-dimensional analysis
R_{ri}	floating ring inner radius
R_{ro}	floating ring outer radius
S	oil film force function
T	oil film friction torque
V	oil film force function
W_{rotor}	rotor weight in non-dimensional analysis
XYZ	reference frame
\bar{x}'_j, \bar{y}'_j	non-dimensional velocities of \dot{x}_j, \dot{y}_j
\dot{x}_j, \dot{y}_j	velocities of O_j relative to O_r
\dot{X}_j, \dot{Y}_j	absolute velocities of O_j
X_j, Y_j	journal centre displacements in the fixed reference frame
x_j, y_j	journal centre displacements relative to ring centre O_r
x_n	lateral displacements in X direction of the n th node
\bar{x}_r, \bar{y}_r	non-dimensional coordinates of X_r, Y_r
\dot{X}_r, \dot{Y}_r	absolute velocities of O_r
X_r, Y_r	ring centre displacements in the fixed reference frame
y_n	lateral displacements in Y direction of the n th node
\bar{z}_i, \bar{z}_o	non-dimensional coordinates of Z_i, Z_o

Acronyms

CLC	critical limit cycle
FRB	full floating ring bearing

IC internal combustion engine

SFRB semi floating ring bearing

Sub subsynchronous

TC turbocharger

Greek Symbols

α oil-film locator

β ramp rate of rotor linear acceleration or deceleration

δ_c phase of unbalance offset at compressor disk

δ_t phase of unbalance offset at turbine disk

λ non-dimensional parameter in non-dimensional analysis

μ oil viscosity

ν non-dimensional parameter in non-dimensional analysis

Ω angular velocity

Ω_{rotor} rotor speed in non-dimensional analysis

$\ddot{\phi}$ rotor acceleration or deceleration

$\dot{\phi}$ rotor speed, equivalent to Ω_j

ϕ rotor rotational angle

Θ angular coordinate for oil-films

θ_{xn} rotational displacements about X axis of the n th node

θ_{yn} rotational displacements about Y axis of the n th node

ε eccentricity ratio

Subscripts

c FRB 1 close to the compressor end

i inner oil film

NOMENCLATURE

<i>in</i>	inner film in non-dimensional analysis
<i>j</i>	journal
<i>n</i>	node number ($n = 1, \dots, 4$)
<i>o</i>	outer oil film
<i>ou</i>	outer film in non-dimensional analysis
<i>r</i>	floating ring
<i>ri</i>	floating ring inner
<i>ring</i>	floating ring in non-dimensional analysis
<i>ro</i>	floating ring outer
<i>rotor</i>	rotor in non-dimensional analysis
<i>t</i>	FRB 2 close to the turbine end

Chapter 1

Introduction

The work of the author begins with the background introduced in Section 1.1, which is followed by a brief introduction in the field of turbocharger rotordynamics shown in Section 1.2. An extensive literature survey is detailed in Section 1.3. The research objectives of the work are given in Section 1.4. Subsequently, the thesis outline is presented in Section 1.5.

1.1 Background

A turbocharger (TC) is a compressor driven by a turbine [10], which is spun by the exhaust gas from the engine cylinders passing through the turbine blades. Normally, the turbine is connected to the compressor by a single overhung rotor (see Fig. 1.1). The more exhaust gas passing through the blades, the faster the rotor spins. The compressor, a type of centrifugal pump, pressurizes the air going into the engine cylinders. It functions through drawing air in at the centre of its blades and flinging it outward as it spins.

Automotive TCs are mainly employed to achieve a higher power density of reciprocating piston internal combustion engines (ICs) through increasing the pressure ratio of induction air [36]. The increase of the air density is accompanied by the rise of the oxygen intake, which means more fuel can be burnt in a fixed volume cylinder during one working cycle. Accordingly, the power output of the ICs will considerably benefit from the increase of the air intake without enlarging the engine size. The TCs are driven by the expansion of the hot exhaust gas, of which the energy would otherwise be totally lost during the exhaust stroke. Thus, apart from increasing the power, the adoption of a TC will hardly affect the engine efficiency. Nowadays, to comply with the more stringent emission regulations, ICs are following a downsizing trend. However, the reduction of engine power

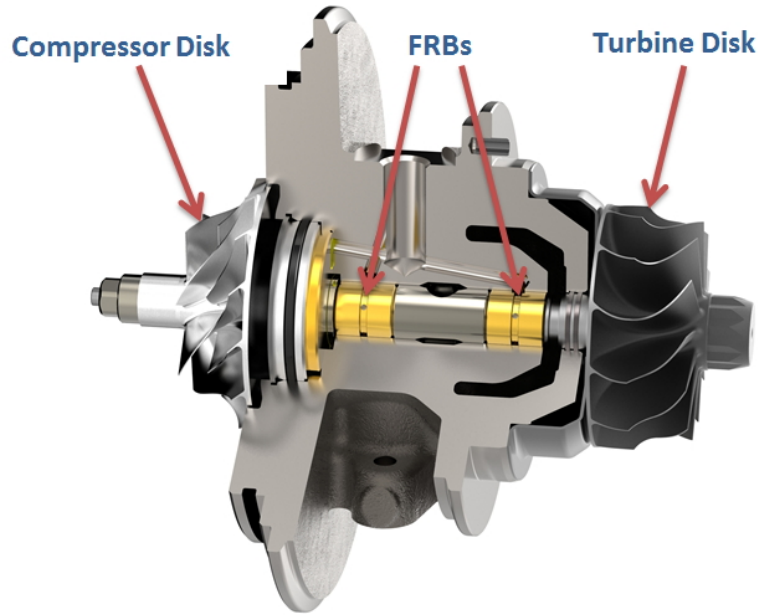


Fig. 1.1. Cross section of a Bosch Mahle[®] TC rotor assembly (courtesy of Bosch Mahle Turbo Systems)

brought about by the decrease of engine size can be counterweighed by the utilization of TCs, which, therefore, leads to the wide application in automotive engines currently.

Facing the increasingly cut-throat competition in the automotive market, TCs are normally under mass production and must be inexpensive, although the reliability should be ensured at the same time. The compressor impellers are exclusively made of aluminium cast alloys [36]. By contrast, due to the high temperature imposed by the exhaust gas on the turbine side, the materials must be carefully selected to withstand the extremely hot environment and to provide sufficient strength to bear the considerable stresses given by the high circumferential speeds as required for the compression process. Today, two materials are mainly used to build the turbine disk for mass production, i.e., GMR 235 for turbocharged diesel engines as well as Inconel (73% Ni, 13% Cr) for higher temperature in gasoline engine applications [36]. The compressor disk is usually attached to one end of the rotor by a loose or very light interference fit, while the turbine disk is commonly connected to the other end by friction welding or electron-beam welding [50].

1.2 Turbocharger Rotordynamics

Driven by the continuous desire for higher engine power, the speed of a TC rotor, which can go to over 200,000 rpm for a passenger car, firmly places it among the high-speed rotating applications. Meanwhile, the durability of the mass-produced TCs must be en-

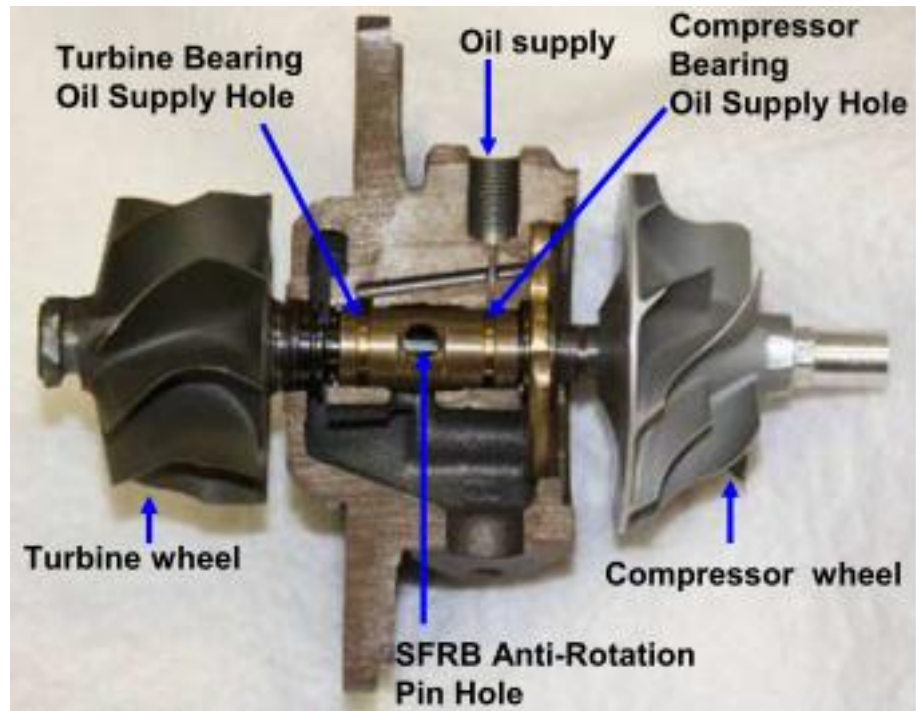


Fig. 1.2. A TC rotor supported on SFRB [100]

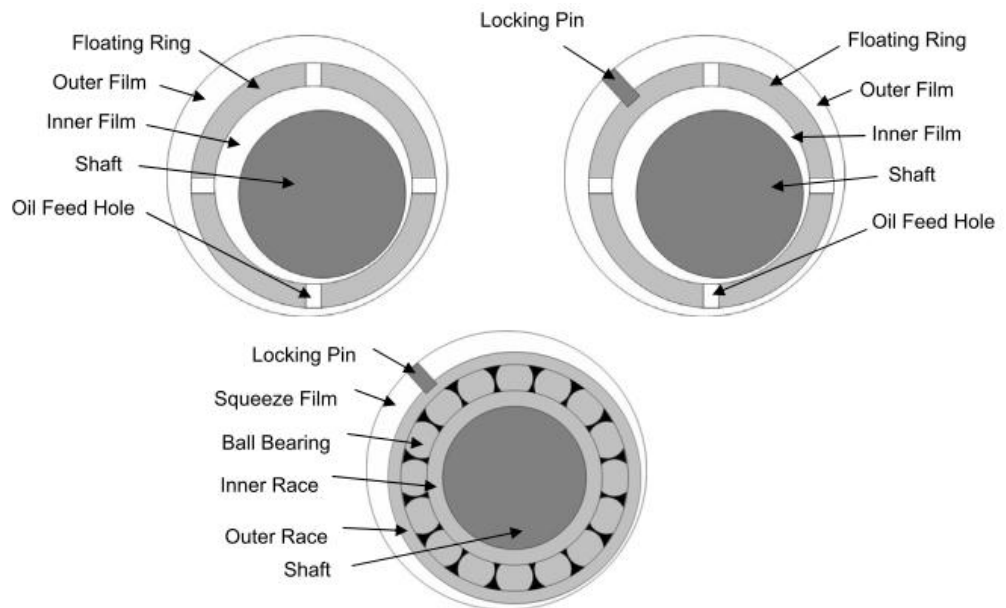


Fig. 1.3. Schematic view of FRB, SFRB and a ball bearing with squeeze film damper [60]

sured. For example, the service lifetime of a TC in truck applications can be up to one million kilometres [36]. Only specially developed floating ring bearing systems, including full floating ring bearings (FRBs) and semi-floating ring bearings (SFRBs), can reliably meet those tough requirements and achieve an inexpensive cost. In the FRB design, two cylindrical floating rings are freely placed between the TC rotor shaft and the compressor- as well as turbine-side bearing housing. Therefore, two oil films are formed in series, and, in operation, the bushes can freely rotate due to the friction torque of the inner film. The speeds of the rings are normally smaller than half of the TC rotor speed. As a result, FRBs can considerably reduce the bearing friction losses than the plain journal bearing design. Furthermore, it can offer a better damping effect. By contrast, SFRB usually includes a single bush only, but it has been prevented from rotating by a locking pin on the outer face. Therefore, two oil films are also formed in the SFRB design, although the outer film will be utilized as a squeeze film damper, which means its outer clearance can be specially optimized to achieve a better damping effect than FRBs. However, the FRB puts in a better performance in the oil contaminated and insufficient lubrication environment as compared to SFRBs. In contrast with FRBs and SFRBs, ball bearings are relatively expensive, and their lifespan is shorter, but they can give even less friction loss to reach higher TC efficiency and, therefore, a rapid acceleration. Thus, ball bearings are one of the future TC bearing candidates, though they have not been widely used by TC manufacturers. Today, in the automotive industry, owing to the low-cost and satisfactory durability, FRBs and SFRBs dominate the bearing candidates in TC applications. However, as typical fluid lubricated bearings, the well-known oil film instability phenomena of plain journal bearings, i.e. oil whirl and oil whip, which have been thoroughly investigated and reported in many publications [2–4, 23, 44, 65, 66], can also be observed in rotor-FRB/SFRB systems [38, 50, 51, 53, 78, 80–82, 85–88].

The instability in rotor-FRB systems, which is closely related to TC noise generation as well as healthy operation, is normally presented by single or multiple subsynchronous components found in the waterfall diagrams (see Fig. 1.4). Based upon classical linear eigenvalue analysis and indicated by the positive real part of the obtained complex eigenvalues, the high shaft speed can frequently lead to the instability of both inner and outer films, because the effective journal speed for the inner film of FRB is higher than the plain journal bearings due to the rotation of floating ring. Surprisingly, resulting from the high non-linearity of the inner and outer oil films, it has been further observed that the loss of stability will usually induce the onset of stable limit cycles with subsynchronous

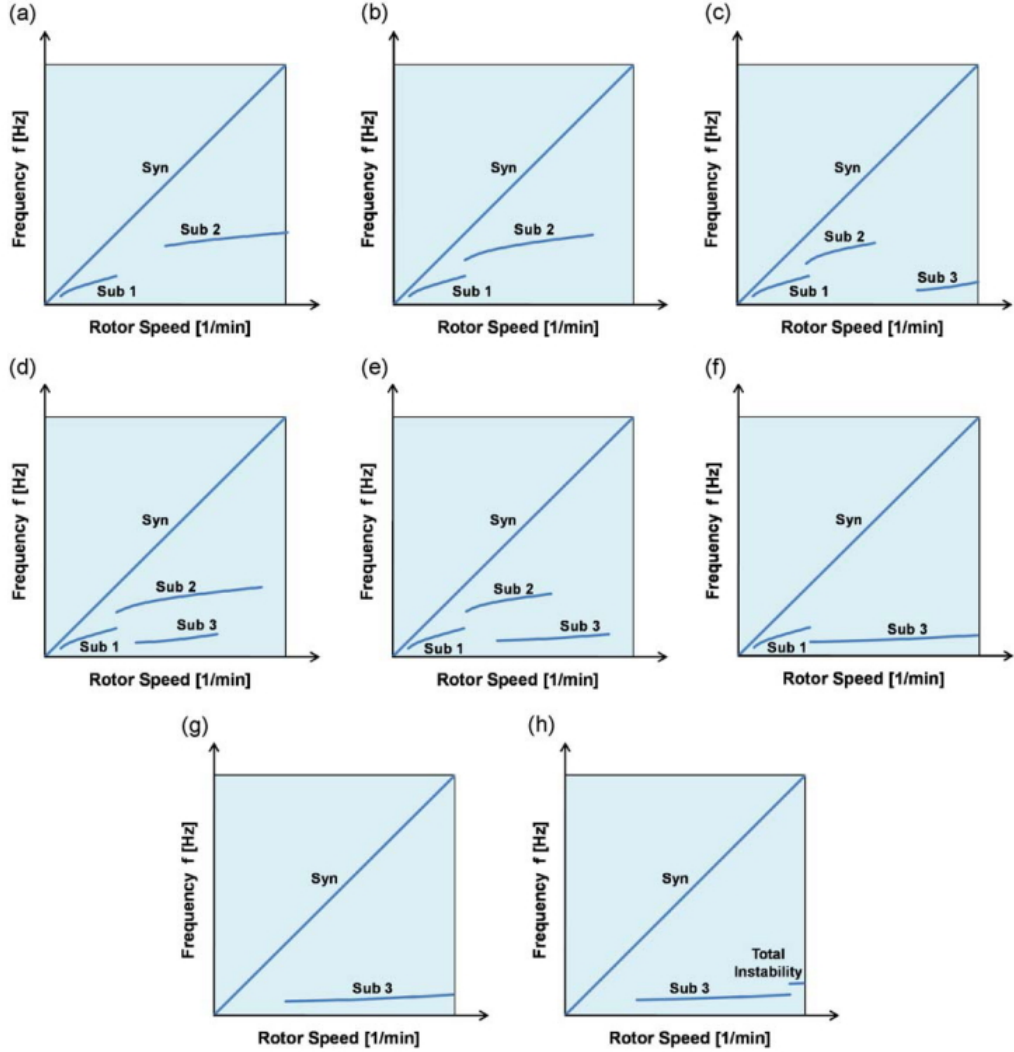


Fig. 1.4. Sketches of various types of waterfall diagrams commonly observed in TC rotor-FRB systems. [86]

frequency by Hopf bifurcation [8, 15, 16], which can always ensure the safe operation of the TC [87]. With increasing rotor speed, the obtained stable limit cycle is likely to become unstable and to bifurcate into another limit cycle [86, 87]. In the meantime, the ascending rotor speed may also lead to the collapse of limit cycles and the disappearance of the corresponding subsynchronous component on the frequency map, which means the system becomes stable again [87]. When the rotor speed is high enough, the most dangerous state named *Total Instability* or *Critical Limit Cycle Oscillation (CLC Oscillation)* is possible to occur, because of the synchronization of the inner and outer film limit cycles, which excites the rotor natural frequency. This phenomenon, which can cause the total failure of the TC, is only investigated and reported by Schweizer and Boyaci in Ref. [15, 16, 85, 86]. Interestingly, according to the published simulation and experimental results [85–88, 100], it has been proved that the final occurrence of the above-mentioned possibilities is highly

sensitive to the rotor-FRB system physical parameters, i.e. bearing structural parameters, oil feeding conditions and unbalance levels. The deep sensitivity clearly implies the possibility to optimize the TC rotor dynamic response and reduce the vibration level through adjusting the physical parameters. Nevertheless, accomplishing this objective through experimental prototype testing will be enormously costly and quite time-consuming, which makes the development of reliable computational tools more desirable than ever.

1.3 Literature Review

The research on turbocharger rotordynamics is closely related to the utilized bearing type. Different bearings exhibit qualitatively different rotordynamic characteristics.

1.3.1 FRB analytical and experimental analysis in the early stage

On the assumption that the FRB has an infinite length, Shaw and Nussdorfer [89] analytically showed the ring speed ratio can be determined by the ratio of bearing inner and outer clearances as well as by the ratio of the inner and outer radii of the floating ring. In addition, the heat generation in the two oil films of the FRB is proved to be less than in an equivalent single oil-film journal bearing. The “equivalent” means the normal journal bearing has the same shaft diameter and clearance as the inner clearance of the FRB. Thus, due to the rotation of the floating ring, FRB puts in a better performance on the friction loss than the normal journal bearing.

Kettleborough [49] presented the results of friction experiments on lightly-loaded FRBs, which further confirm that the friction loss of the FRB are lower than conventional journal bearings. Furthermore, the increase of bearing outer clearance leads to the significant decrease of the ring speed ratio. However, it is observed that the experimental ring speed ratios are considerably smaller than the values obtained from the theoretical analysis. In addition, when the oil temperature is above 50 degrees, the floating ring is reluctant to start to rotate, since the frictional moment given by the inner film is insufficient to drive the ring. Therefore, wear is possible to occur as a result of the metal-to-metal contact in the outer film, but this problem might be solved by high pressure oil feeding.

Including the consideration of pressurized lubricant feeding, Orcutt and Ng [69] analytically and experimentally showed the steady-state and dynamic properties of a rotor-FRB system when the rotor operating speed is less than 10,000 rpm. The analytical analysis is carried out by linearizing the oil film forces around the bearing steady-state position to obtain the bearing stiffness and damping coefficients. With regard to the steady-state

properties, good agreement between the analytical and experimental results is observed, although the measured ring speeds are always from 10 to 20 percent smaller than the calculated ones. In the dynamic property study, satisfactory agreement is also found between the analytical and experimental results, and a critical speed is identified. However, sub-synchronous whirl is obtained in all the tests, which show that the whirl amplitude can be effectively controlled by reducing the lower lubricant feeding pressure, increasing the bearing outer clearance and using higher viscosity lubricant. Furthermore, the authors point out that the criterion of oil whirl control cannot be obtained by carrying out the conventional linear stability analysis.

Tatara [94] experimentally conducted a study on the stabilising effect of FRBs, in which the rotor spins up to 70,000 rpm. When the rotor speed is higher than the onset speed of oil whirl, it is shown that a stable range can be identified in many tests with different bearing clearance values. In addition, the whirl amplitude cannot further increase as the rotor speed goes up. The deflections of the journal and disk in the tests with FRBs are much smaller than those with plain journal bearings, due to the additional damping given by the outer film. Moreover, at a particular rotor speed, the inner clearance plays a determinant role on the ring speed ratio rather than the ratio of outer clearance to inner clearance. By contrast, the conclusion regarding the effect of rotor speed on the ring speed ratio cannot be drawn easily, since the relationship between them can hardly be identified. This kind of behaviour cannot be explained by the conventional analytical analysis presented by Shaw and Nussdorfer [89] nor by Orcutt and Ng [69]. Furthermore, it is shown that heavier floating ring can leave a larger stabilizing effect, and the temperature rise in FRB is better controlled as compared to plain journal bearing, although great reduction of friction losses cannot be realized because the ring speed is fairly low.

Based upon the short bearing approximation, Tanaka and Hori [93] investigated the stability characteristics of FRBs theoretically. Experimental results are given for comparison with the analytical results, and good agreement is exhibited. In addition, the experimental results show that relatively high inner bearing mean pressure can efficiently retard the occurrence of oil whirl instability to a considerably high rotor speed, and relatively low inner bearing mean pressure can reliably control the vibration amplitude caused by the oil whirl appearing at a very early stage. Furthermore, in the analytical analysis, the following methods are found to be helpful for the stability improvement: (a) stiffening the rotor shaft, (b) increasing the ratio of the ring inner and outer radii, (c) increasing the bearing clearance ratio, (d) reducing the bearing modulus and (e) reducing the oil feeding

pressure.

Nakagawa and Aoki [67] carried out the unbalance vibration analysis of an overhung rotor-FRB system by linearizing the oil film force around the static equilibrium. The analytically calculated ring speeds coincide with the computer simulated results given by Orcutt and Ng [69], but significant difference is seen in comparison with the experimental results. Higher oil feeding pressure can reduce the inner and outer bearing eccentricities. Moreover, at the critical speed, the vibration amplitude becomes lower, provided that a higher bearing clearance ratio and a smaller ratio of journal radius to inner clearance are given. The following bearing structural data are suggested by the authors for an optimal design: the bearing length to journal diameter ratio should be nearly 2; the ratio of bearing outer to inner clearance is better to be in the range from 1.5 to 2.0, and the ratio of journal radius to the inner clearance should be approximately 250.

Considering the effect of lubricant viscosity variations, Nikolajsen [68] gave the computational results from the stability analysis of plain journal bearings and FRBs. With regard to the plain journal bearings, it is shown that the decrease of oil viscosity can lead to the reduction of the threshold whirl frequency, minimum film thickness and friction power loss, especially at high Sommerfeld numbers. In comparison with the bearing clearance ratio and radius ratio, the oil viscosity gradient plays a less influential role on FRBs. Better stability characteristics are exhibited on the stability map, provided that the bearing clearance ratio has magnitude of about from 1.2 to 2.0. In addition, it is seen that, if designed properly, the adoption of FRB design can considerably improve the bearing stability and significantly reduce the friction losses as compared to plain journal bearings.

Rohde and Ezzat [74] investigated the frictional performance of FRBs under dynamic loads to evaluate the feasibility of using FRBs to replace conventional journal bearings in automotive applications. In contrast with the plain journal bearings, the results indicate increasing inner and outer clearances result in the decrease of frictional power losses, although this advantage will be penalised by the higher oil flow requirements as well as noise generation. Furthermore, it is shown that the criteria of minimum oil film thickness for successful engine bearing operation can be satisfied by careful selection of the bearing inner and outer clearance values.

With the bearing forces calculated from the impedance method given by Childs et al. [21], Li and Rohde [59] performed the analysis of the steady-state performance characteristics of FRBs used in turbocharger applications, based upon the traditional linear stability

analysis. The results show the influence of bearing clearance ratio on the eccentricity ratio of inner film is smaller than on the eccentricity ratio of outer film. At relatively high Sommerfeld numbers, bigger bearing clearance ratio results in a higher eccentricity ratio of the outer film and higher floating ring speeds. Moreover, as presented by Nikolajsen [68], the obtained stability charts show the bearing clearance ratio can heavily affect the bearing stability characteristics. Providing that the bearing clearance ratio is small enough, the bearing overall stability will be only determined by the outer film. By contrast, instability of the inner film will be introduced by increasing the bearing clearance ratio. The stability of outer film again becomes dominant if the bearing clearance ratio is further increased to a high value. The transient analysis, in which the short bearing approximation is adopted, is also carried out to study the dynamic characteristics of FRBs by real-time integration. Surprisingly, instead of exponentially increasing, the journal displacement amplitude finally reaches stable limit cycles with the bearing parameters selected from the linearly unstable region. The unique nonlinear phenomenon can properly explain the superior stability characteristics of the TC rotor-FRB system, which is always incorrectly predicted to be unstable from a linear viewpoint.

Based upon the infinitely long bearing approximation, Mokhtar [63] analytically presented the design data and the performance characteristics of FRBs. The obtained results show that bearing dimension can considerably affect the final bearing behaviour. The introduced ring leads to a smaller eccentricity ratio of the inner clearance, compared to the eccentricity ratio of the outer clearance. However, the value of the latter can be reduced by the adoption of thicker rings and higher bearing clearance ratios. It is further shown that higher bearing clearance ratio can produce a bigger ring speed. With reference to the same eccentricity, reducing the ring thickness will also result in the increase of ring speed. In comparison with the plain journal bearings, as mentioned by Shaw and Nussdorfer [89], Kettleborough [49] and Rohde and Ezzat [74], because of the smaller relative speed between journal and ring, FRB shows lower friction loss, although this will be accompanied by the reduction of load capacity.

Trippett [99] performed experiments to verify the ability of FRB to lower the friction loss at rotor speeds up to 15,000 rpm. The experimental results do not show the rotation of floating ring can significantly reduce the bearing friction loss, compared with the single-film journal bearing formed when the ring is prevented from rotating. In the meantime, it is seen that the occurrence of ring rotation is not predictable under different load conditions. Under a variety of load and rotor speed conditions, the ring speeds and bearing friction

losses predicted by the isothermal model match well with the measured data, although greater discrepancy has been observed in the highest speed and load conditions.

Dong and Zhao [25] experimentally proved that FRBs can be applied to engines where the load is nonstationary. The experimental results indicate during acceleration the floating ring does not rotate unless the crank shaft speed reaches 740 rpm. By contrast, in the engine decelerating process, the rotation of the ring can still be identified until the engine speed drops to 200 rpm. In conclusion, the existence of highly nonstationary load of the engine is an advantage to make the floating ring lift off much easier than other heavy load applications.

1.3.2 Thermal analysis of FRBs

Trippett and Li [98] undertook an experimental programme and analytically perform a thermal analysis to explain the ring speed discrepancy between measurements and predictions shown previously by Kettleborough [49], Orcutt and Ng [69] and Nakagawa and Aoki [67]. The results show the ring speed obtained from the thermal analysis agree well with the measured data, which confirms the decrease of oil viscosity caused by the temperature rise can considerably reduce the ring speed. Moreover, it is observed that reducing the bearing inner clearance and increasing the bearing outer clearance will lead to the increase of ring speed. At relatively high TC rotor speeds, i.e. above 75,000 rpm, lower oil supply pressure can effect a significant decrease of the ring speed, as a result of the reduction of the oil film thickness in the outer clearance given by the insufficient oil supply. The results further show either changing the number of oil feeding holes or grooving the inner or outer surface of the ring can reduce the ring speed, compared to the original ungrooved design with six oil feeding holes.

In order to evaluate the feasibility of employing the FRB in a power generating environment, Clarke et al. [22] presented a steady-state FRB model including the thermal effects. Under the given load condition, the obtained results suggest neither the bearing eccentricities nor the maximum oil temperature is excessive. In comparison with the isothermal analysis, the newly proposed model shows the inclusion of thermal effects leads to higher eccentricities with respect to the descending Sommerfeld number. Moreover, the calculated differences between the inner and outer eccentricities in the thermal analysis are bigger than in the isothermal analysis at relatively high Sommerfeld numbers. Under relatively high loads, the thermal analysis brings about considerably lower friction losses than in the isothermal analysis.

1.3.3 Detailed analysis of FRBs

Dowson et al. [26] developed a close-loop numerical method to determine the position of the reformation boundary in a circumferentially grooved FRB for TC applications. In comparison with the analysis in which the cavitation region is located by setting the negative pressures to zero, the results given by the analysis with the more accurate reformation boundary do not show significant differences. However, the axial lubricant flow rate produced by the simple boundary condition clearly exhibits the lack of continuity. Additionally, it is seen that the oil supply pressure at the groove can considerably affect the bearing performance.

Cheong and Kim [20] performed static and dynamic analysis of the circumferentially grooved FRBs with the consideration of cavitation region variation. It is observed that the increasing oil supply pressure leaves descending inner and outer eccentricities, especially at relatively high Sommerfeld numbers. With small oil supply pressure and high journal speed, starvation of the lubricant can even be found within the converging wedge, which can bring about the dramatical decrease of bearing load capacity. In addition, the effect of oil supply pressure on the ring speed as well as the friction factor is relatively small. The dynamic analysis shows the inclusion of bearing supply pressure can significantly change the linearized bearing coefficients. Furthermore, it is seen the supply pressure drop given by the centrifugal force due to the rotation of the floating ring can lower the load capacity of the inner film. Thus, sufficient oil feeding pressure should be ensured to counterweigh the pressure drop caused by the ring rotation.

Considering the centrifugal force acting on the oil films, Hatakenaka et al. [34] presented a theoretical analysis with a modified Reynolds equation to explain the discrepancies between the conventional linear analysis given by Tanaka and Hori [93] and the experimental results presented by Tatara [94], and Trippett and Li [98]. The obtained results show that, with the consideration of centrifugal force, the calculated ring speed ratio steadily declines as the rotor speed goes up, and so does the friction torque of the inner film on the floating ring. In comparison with the results shown in Ref. [92], the results from the stability analysis obtained by the newly proposed model indicate a considerable extension of the stable region at high bearing modulus values, due to the decrease of cross-coupling bearing stiffness of the inner film caused by the axial oil film rupture. Hence, if the bearing is designed with appropriately selected bearing modulus, the rotor supported by FRBs can stably run until its maximum rated speed is reached. In addition, it is seen the reduction of oil supply pressure can extend the stable region on the stability

map, whereas the further decrease of the supply pressure can shrink the stable region, as a result of its effect on the lower border. It is further shown, with respect to a bearing modulus, when the rotor speed is below the lower stability border, the outer film plays a stabilising role while the inner film destabilise the rotor-FRB system. By contrast, both inner and outer films have a destabilising effect, provided that the rotor speed is above the upper stability border.

Shi and Deng [90] carried out a comprehensive analysis of FRBs in TC applications. It is observed that the increases of inner and outer bearing clearances result in the reduction of Couette power loss and the rise of Poiseuille power loss. In comparison with SFRBs, FRBs put in a better performance in reducing both Couette and Poiseuille power losses, despite a smaller minimum film thickness under a given dynamic loading condition. Moreover, it is found that the ring speed ratio increases with increasing outer clearance, but decreases with increasing inner clearance. In addition, the increase of the radii ratio can reduce the speed of floating ring, which leads to the decrease of cavitation effect in the outer film. By contrast, it can hardly affect the cavitation in the inner film. Furthermore, the ring speed ratio clearly follows a descending trend with increasing rotor speed.

Zhang et al. [103] studied the pressure profiles of the inner and outer films in FRBs considering the influenced of oil feeding pressure, oil viscosity and bearing clearance. It is found that the effect of oil supply pressure on the pressure profile shape is insignificant, although the oil inlet pressure close to ambient pressure leads to a much smaller pressure distribution in the circumferential direction. Moreover, it is seen that the higher viscosity results in higher inner and outer film pressure, especially the inner film pressure. Further observations show the bearing clearance mainly affects the outer film pressure distribution in the axial direction.

1.3.4 Linear stability analysis

Assuming the Sommerfeld boundary condition for the inner film and the half Sommerfeld boundary condition for the outer film are satisfied, Tanaka [92] performed another linear stability analysis to explain the peculiar stability behaviour observed by Tatara [94] in rotor-FRB systems. It is shown that, with the newly proposed boundary condition for the inner film, significant differences are obtained, compared with the results previously shown in Ref. [93]. Moreover, the stabilising effect of FRBs at high journal speeds shown by Tatara [94] can possibly be explained by the new results. It is found that the bearing is unstable when the journal speed is low enough, although, with increasing journal speed,

a stable region appears, and it can be extended to considerably high speeds if the FRB structural parameters are selected properly.

Holmes [37] presented a simple stability analysis to explain the subsynchronous vibrations commonly observed in the TC rotor-FRB system. With the outer film of FRB modelled as an externally damped bearing, the linear eigenvalue analysis shows the subsynchronous component follows a slope of approximately 0.08 order, which is a close resemblance to the experimental results. It is also shown that the rotation of floating ring is not a determinant of external damping, since a ring prevented from rotation can still give the similar results. However, no attempt has been made to provide remedial measures to eliminate the subsynchronous vibrations.

Using the same simple stability analysis method as previously described in Ref. [37], Holmes et al. [38] performed the stability analysis for a real TC to closely examine the subsynchronous vibrations generated. Two unstable roots are obtained from the analysis, and the relative magnitudes of the real parts of them vary at some points over the considered speed range. Accordingly, a sudden change of the frequency of the dominant subsynchronous component is likely to occur. Moreover, the predicted results are in qualitative agreement with the experimental results supplied from different TC manufactures, which confirms the effectiveness of the linear theory employed to investigate the characteristics of the TC rotor-FRB system.

1.3.5 Nonlinear stability analysis

Boyaci et al. [14] carried out the bifurcation analysis of a perfectly balanced rotor-FRB system. It is shown that the system undergoes a Hopf bifurcation at the linear stability limit. Further investigations, conducted by applying the central manifold theory, indicate the Hopf bifurcation occurring at the stability limit is either subcritical or supercritical subject to the FRB design parameters.

Boyaci et al. [13] analytically performed the bifurcation analysis of a perfectly balanced symmetric rotor-FRB system. The linear stability analysis indicates that the system stability border depends on the real part of the first conjugate pairs of the eigenvalues within the lower end of the non-dimensionalised load parameter, while the stability at relatively high load parameter values is determined by the second conjugate pair of the eigenvalues. Further investigations are performed to determine the type of Hopf bifurcation at the stability borders using the central manifold theory. It is found that lower load parameters lead to the occurrence of supercritical bifurcations, but higher load parameters

will give rise to subcritical bifurcation, which is undesirable in a practical sense. Thus, the load parameter should be carefully chosen as low as possible in the bearing design. It should be pointed out that, in most cases, the change of bifurcation type coincides with the change of the critical pair of eigenvalues. In the meantime, the borders between supercritical and subcritical regimes are considerably affected by the bearing clearance ratio. Bigger clearance ratio leads to a longer supercritical regime. Nevertheless, the increase of bearing clearance ratio can cause the reduction of the instability onset speed. Once the desired load parameter and clearance ratio are set, increasing the ratio of the bearing outer diameter to the inner diameter can result in the increase of instability onset speed. However, it can hardly affect the border between super- and sub-critical bifurcations. Regarding the limit cycle amplitude, it is found that the expansion of bearing clearance can lead to lower displacements with respect to the entire radial clearance. Furthermore, it is observed that the lower load parameters lead to smaller amplitude limit cycles.

In order to study the mode interaction or nonlinear jump phenomenon occurring at rotor speeds higher above the linear threshold speed of instability, Boyaci et al. [15] performed a stability analysis of a symmetric rotor-FRB bearing system using numerical continuation method. The linear stability analysis shows that the inner-film instability occurs first for relatively low loads, while the outer film becomes unstable earlier than the inner film under heavier loads. There are two unstable modes, i.e., conical and cylindrical modes, corresponding to the instability of each film. The orbit plot of the conical mode of the outer film exhibits quasi-periodic motions rather than the single-frequency limit cycles given by the other three unstable modes. The nonlinear stability analysis demonstrates the emergence of *Critical Limit Cycle* oscillations, characterised by extremely high bearing eccentricities and excessively growing amplitudes of rotor displacement. Normally, the onset of *Critical Limit Cycle* oscillation indicates a Neimark-Sacker bifurcation in the run-up as well as a saddle-node bifurcation in the run-down. Moreover, a transition from a more rigid mode to a correspondingly bending mode or a degenerated mode can always be appreciated at the onset of *Critical Limit Cycle* oscillations, owing to the extremely stiff bearings. The case with a more lightly loaded rotor shows the existence of mode interactions. Furthermore, the onset speed of the critical limit cycle becomes higher with increasing load parameter, which means that, in practice, the bifurcation into critical limit cycles is not highly likely to occur in lightly loaded rotor-FRB systems.

Boyaci et al. [16] carried out the bifurcation analysis of a perfectly balanced TC

rotor-FRB system over the entire operating speed range using the numerical continuation method. The term nonlinear critical speed is defined as the onset speed of the so-called *Critical Limit Cycle Oscillation* or *Total Instability* phenomenon, which has been shown in Boyaci et al. [15], Schweizer [85, 86]. Additionally, there is an absolute limit speed indicating the end of the noncritical oscillations. The elasticity of the shaft can hardly influence the nonlinear critical speed, but it can considerably affect the rotor response over the higher rotor speed range, especially the speed range in which the critical and noncritical solutions coexist. Furthermore, it is seen that a transition from a rigidly conical mode to a bending or degenerated mode, which can produce extremely high amplitude vibrations when the *Critical Limit Cycle Oscillation* occurs.

Amamou and Chouchane [8] performed the nonlinear stability analysis of a perfectly balanced symmetric rotor-FRB system. The results correlate well with the findings given by Boyaci et al. [13]. It is seen that the existence of supercritical and subcritical Hopf bifurcations, of which the border is mainly controlled by the bearing clearance ratio. In addition, it is observed increasing the bearing modulus within the supercritical region leads to the decrease of the amplitudes of stable limit cycles. By contrast, within the subcritical region, higher bearing modulus corresponds to lower amplitudes of unstable limit cycles. Moreover, the numerical simulation results confirm the analytically determined stability characteristics of limit cycles.

1.3.6 Rotordynamic analysis of rotor-FRB systems

Considering the rotor gyroscopic moments and shaft flexibility, Li [58] presented a lumped parameter model to, numerically, investigate the self-excited response of a high speed TC rotor-FRB system. With the operating parameters picked from the unstable region in the stability map, the results show a limit cycle is always achieved, which brings the journal and floating ring centres to whirl well within the bearing inner and outer clearances, respectively. Moreover, it is found that the displacements of the two ends of the rotor are, in fact, out of phase by 180 degrees, which indicates the rotor undergoes a conical whirl. Further to this, it is shown the unbalance phase angle can hardly affect the rotor whirl. However, it should be pointed out that the conclusion is drawn based upon insufficient parameter simulations, and the effect of imbalance phase angle will be thoroughly investigated by the author later in this thesis. In addition, the inner clearance size is proved to be critical to the whirl amplitude, and the developed limit cycle can satisfactorily control the rotor motion even under compact loads.

In order to improve the stability performance of a redesigned TC rotor-FRB system, Born [12], following the thermal analysis presented by Trippett and Li [98], undertook a parameter study through conventional linear stability analysis. In comparison with the measured data, it is shown that the linear eigenvalue analysis can well predict the threshold speed of instability of the TC rotor-FRB system under investigation. The parameter study reveals that increasing the bearing inner clearance results in a bigger threshold speed of instability of the outer film, despite decreasing the onset speed of the inner film instability. Moreover, it can also be observed that the reduction of bearing outer clearance can considerably improve the bearing stability, albeit this advantage is at the expense of the reduced damping for the inner film. According to the linear parameter analysis, the tests with the structurally modified FRBs indicate the stability threshold is well above the measured speed range, which is as high as 65,000 rpm. Furthermore, experiments with different types of bearing design are also given. The one with SFRBs, i.e. squeeze film backed cylindrical bore bearings, shows better stability performance at high rotor speeds than FRBs, despite the strong subsynchronous vibrations found at the lower end of the speed range. The other one with squeeze film supported three-lobe bearings exhibits the best stability performance within the whole speed range, since the rotor merely undergoes synchronous motions due to the unbalance.

Based upon the short bearing approximation and bearing force linearisation, Gjika and LaRue [29] proposed a model to predict the synchronous dynamic behaviours of a rotor-SFRB system and presented a method to, accurately, measure the rotor inertia properties for turbochargers. The predicted frequency of the maximum amplitude is in good agreement with the measurements, despite slightly bigger differences found at the relatively high rotor speed.

Using the finite difference method to obtain the bearing stiffness and damping coefficients, Hemmi and Inoue [35] investigated the effects of FRB characteristics on the stability of TC rotor-FRB systems. Two types of floating ring are considered in the analysis, i.e. the cut type and outer groove type. It is shown that the predictions from the linear eigenvalue analysis agree well with the experimental results. Moreover, it is observed that there are four rigid modes, which can be unstable. Furthermore, the stiffness characteristics of the outer film can exert a powerful effect on the stability of the first two modes. However, its damping characteristics can influence the stability of all the four modes. Therefore, the dominant mode appearing in the waterfall diagram is likely to be selected through tuning the characteristics of the outer film.

Holt et al. [39, 41] carried out experiments to examine the effects of oil feeding pressure and temperature on the rotordynamic performance of a FRB supported TC rotor. Two subsynchronous components are identified from the obtained data measured on the TC housing. One of them appears at a lower rotor speed and ranges from 15 to 20 krpm, while the other abruptly starts at around 40 krpm with higher amplitudes until approximately 90 krpm. The obtained results show that the increase of oil feeding pressure leads to a bigger onset speed of instability, although it can also bring about higher synchronous vibration displacements. By contrast, the influence of oil feeding temperature on the onset and ending speeds of instability is negligible, whereas feeding colder oil can produce lower amplitudes of synchronous and subsynchronous motions. Surprisingly, when the rotor speed is higher above 90 krpm, the observed sun-synchronous instability disappears until the maximum rotor speed, i.e., 115 krpm. Additionally, the oil whip phenomenon widely observed in conventional journal bearings has not been found during the experiments and the slope of the whirl-frequency ratio data versus speed seems to be independent of the oil feeding conditions.

In order to compare with the experimental results described in Ref. [39], Holt et al. [40] performed linear and nonlinear rotordynamic analysis with a comprehensively developed FRB model. The predicted results show the ring speed ratio follows a descending trend with increasing rotor speed. Moreover, it is seen that the linear model can correctly predict the onset speed of instability, i.e., 20 krpm, but it cannot predict the stable range from 45 krpm to 60 krpm and the re-stabilisation of the system at above 82 krpm. The nonlinear simulations are carried out at constant rotor speeds with an increment of 10 krpm for the perfectly balanced rotor and the unbalanced rotor, respectively. The simulation with the perfectly balanced rotor exhibits subsynchronous instabilities over the entire speed range. By contrast, the unbalanced simulation shows that the subsynchronous components disappear above 70 krpm. Moreover, in the unbalanced simulation, the amplitude of the subsynchronous components in the lower speed range is smaller than the case without unbalance.

Soh et al. [91] presented the TC noise reduction methods for diesel engines. To reduce the howling noise introduced by subsynchronous instability, six bearing clearance tolerance combinations are tested. The experimental results show that the combination of minimum inner clearance, and maximum outer clearance gives the least whirl vibration, while the combination of maximum inner clearance and minimum outer clearance brings about the worst whirl vibration.

San Andrés and Kerth [78] detailed a lumped parameter thermal FRB model to investigate the thermal effects on the performance of a TC rotor-FRB system. The predictions show that the ring speed ratio clearly follows a descending trend with increasing TC rotor speed, which complies with the experimental findings given by Tatara [94], Trippett and Li [98]. It is also observed that the inner film temperature and power dissipation are considerably higher than those of the outer film, which causes the inner film viscosity to drop more than that of the outer film. In addition, the change of the inner clearance is found to be negligible as compared to the drop of the outer clearance. In spite of the fact that the measurements under different oil feeding conditions show a more dramatic decrease than the predicted results, the predictions provide a reasonable approximation of the experimentally obtained speed ratio. It should be noted that the effect of oil feeding conditions, i.e., oil supply temperature and pressure, on the ring speed ratio is insignificant according to the tests. Additionally, the subsynchronous components can be identified from the experimental results. The one with the smaller frequency is at around 50 percent of the ring speed, starting to appear at a rotor speed of 30 krpm until the top end of the considered speed range. The other with higher frequency occurs at half the ring plus rotor speeds and appears from the start of the running, which indicates the early instability of the inner oil film. The results of stationary simulation show smaller amplitudes of synchronous vibration, and the persistence of two main subsynchronous components over the entire speed range, due to unknown unbalance distribution. Nonetheless, predicted unstable whirl frequencies agree well with the experimental results.

Gunter and Chen [32] analytically investigated the linear and nonlinear behaviours of a TC rotor-FRB system. It should be mentioned that there is an inducer stage in front of the compressor impeller, which produces a longer overhang at the compressor section than that of the commonly utilised automotive TCs. With the nominal bearing stiffness values obtained from the nonlinear simulations, the undamped natural frequency calculations show that three critical speeds are encountered over the TC operating speed range, of which the third critical speed is unique to the TC rotor design. With the consideration of Alford aerodynamic forces acting at the impeller and turbine, the damped eigenvalue analysis indicates the first forward whirling mode is conical in shape with bigger amplitudes at the turbine end. By contrast, the in-phase mode with higher frequency is marginally stable and gives higher displacement on the compressor side. Experimental data shows either one or both of these modes may appear simultaneously. The nonlinear synchronous response exhibits the highest displacement at 123 krpm, which is slightly higher than the

third critical speed of the linear analysis. Additionally, as a result of the highly nonlinear FRBs, the time transient analysis evidences the existence of controlled limit cycles, which can ensure the safe operation of the TC in most cases. Most importantly, the results also show that enlarging inner and outer clearances can lead to the switch of the whirling mode from an in-phase mode to a conical mode. This implies that the change of FRB clearance can significantly affect the TC rotordynamic behaviour, although detailed investigation concerning this phenomenon was not given.

Alsaeed [6], Kirk et al. [50] investigated the stability characteristics of a FRB supported high speed TC. The time transient analysis at constant speed steps exhibits a dominant subsynchronous component over the range from 20 krpm to 150 krpm, which corresponds to a conical forward mode. The second in-phase whirling mode is identified at speeds between 80 krpm and 100 krpm. It is also shown that the traditional linear stability analysis can be used to interpret the whirling modes of the nonlinear simulation results. Although the TC rotor-FRB is always linearly unstable, the high nonlinearity of FRBs can control the vibration amplitude of the TC rotor within an acceptable range. Additionally, using a damped support is proved to be an effective method to stabilise the TC rotor at relatively high operating speeds.

Through changing the bearing inner and outer clearances, Kuma et al. [57] presented a reduction method of the subsynchronous noise in a TC rotor-FRB system for diesel engines. It is found that the bearing clearance plays a crucial role in reducing the whirl noise. In the “same clearance” case, the reduction of inner clearances and the extension of outer clearances for both FRBs can lead to the decrease of whirl vibration. It is thought that the outer clearance affects the conical mode, and the inner clearance is related to the parallel mode. In addition, analysis with “different-clearance” specification applied to the compressor side and turbine side shows the reduced inner clearance on the compressor side can further reduce the whirl amplitude by restricting the development of the parallel mode. The numerical simulations qualitatively agree with the measurements, albeit the calculated frequency of the parallel mode is slightly higher than in the experiment.

McLuckie and Barrett [61] presented a promising FRB model which can be employed to save the development time of TC bearing systems. The TC rotor is assumed to be rigid in the dynamic transient analysis, and the ring speed ratio is fixed at 0.25. It is worth pointing out the suppressing effect of the imposed unbalance on oil whirl. The amount of unbalance can greatly affect the system response and sometimes restabilise the system at relatively high rotor speeds.

Using the computational programme given in Ref. [78], Rivadeneira [72], San Andrés et al. [81, 82] showed further progress on the validation against measurements of linear and nonlinear rotordynamic models to predict shaft motions in the rotor-FRB system of automotive TCs. The measured data show a subsynchronous component corresponding to the outer film instability occurs over the low-speed range, while another subsynchronous component representing the inner film instability emerges when the rotor speed is above 55 krpm. Generally, the amplitudes of the subsynchronous motions follow a descending trend with increasing rotor speed, yet a sudden large-amplitude subsynchronous component appears at the maximum rotor speed (65 krpm) at approximately fifty percent of the shaft speed. Measurements at higher rotor speeds cannot be completed as floating ring locking occurs owing to oil contamination, which can cause severe damage to the TC under investigation. The predicted ring speed ratios only correlate well with the experimental results within the midrange of the rotor speed, although the calculated oil exit temperatures are in good agreement with the measurements. Through treating the FRBs as normal journal bearings at higher rotor speeds, the nonlinear transient simulation correctly reproduces the large-amplitude subsynchronous component at fifty percent rotor speed. Even better results are obtained by using the measured ring speeds.

Corresponding to the analytical stability analysis shown in Ref. [50], Kirk et al. [51] presented the experimental test results of a TC rotor-FRB system for diesel engines. The tests are conducted under the engine unloaded and loaded conditions, respectively. When the engine is unloaded, the highest possible speed of the TC rotor is 97,200 rpm, and two main subsynchronous components are shown on the waterfall diagram, as predicted by the nonlinear simulations given in Ref. [50]. The TC rotor reaches a higher maximum speed of 135,810 rpm in the loaded condition than the idle running. The identified subsynchronous components under the unloaded condition can still be observed.

Kozhenkov and Deitch [56] detailed a three-dimensional finite element model of a TC rotor-SFRB system, of which the operating speed is between 15,000 rpm and 40,200 rpm. The equations of motion for the rotating body are derived from the model of a rotating elastic medium, and the rotor system is discretized by the three-dimensional contact finite element method. The oil film forces are obtained by solving the Reynolds equations using the finite difference method. Numerical calculations show two self-excited modes (subsynchronous components). The one at lower frequency exists in the whole speed range and is conical in shape, while the other one with higher frequency appears later at 23,760 rpm, and its shape is initially cylindrical. The increase of the rotor speed can

eventually lead to the increase of the curvature of both modes at top rotor speeds. The simulated amplitudes of the self-excited modes correlate well with those results obtained from experiments.

Rübel [75], Schilder et al. [84] presented an efficient method to calculate the quasi-periodic oscillations in the high speed TC rotor-journal bearing system. It is shown that the proposed method, i.e., formulating the model in co-rotating coordinates, can significantly save the computation time, and the gravitational force can be neglected at relatively high rotational speeds. The method can also be applied to other lightly loaded systems with high rotating speeds.

Bonello [11] carried out the transient analysis of a perfectly balanced TC rotor FRB/SFRB system. Nonlinear oil film forces are obtained from a short-bearing approximated model. The results with FRBs show that there are three distinct subsynchronous trains on the waterfall diagrams. The experiment results demonstrate a range of speeds for which the subsynchronous frequencies are quite weak, which is probably caused by the assumed perfectly balanced condition, since the TC rotor is inherently unbalanced and the existence of unbalance can significantly alter the rotor response. The simulation results with SFRBs provide better stability characteristics than FRBs when the rotor speed is relatively high. In addition, the sensitivity of the obtained results to the choice of cavitation pressure is also examined. It is seen that the cavitation pressure exerts insignificant influence on the frequency spectra of the vibration for both FRBs and SFRBs. The effect of cavitation pressure on the ring speed behaviour is also negligible, regardless of the fact that it can affect the orbit-size and shape towards the lower end of the speed range.

Kirk et al. [53] presented experimental vibration results of a turbocharger mounted on an engine. Under the unloaded condition, the engine can drive the TC rotor rotating at the maximum speed of 97,200 rpm. Two main subsynchronous components are shown and nonlinear jumps between them are identified during acceleration and deceleration. At 80,000 rpm, the subsynchronous component with lower frequency at 18,000 cpm drops out and the other one at a frequency of 33,900 cpm sets in. When the engine is loaded by the dynamometer, the onset speed of the nonlinear jump becomes 54,000 rpm, which is much lower than that under the unloaded condition. Moreover, the test results show a side load force causes the eccentric position of the shaft when the engine is at full speed.

Schweizer and Sievert [88] carried out the run-up measurements of a TC rotor-FRB system with varying operating and system parameters, including oil supply pressure, oil supply temperature and rotor imbalance. Despite the constant bearing stiffness over the

entire speed range, it is seen that the linearly predicted natural modes can be qualitatively correlated with the observed subsynchronous components from the experiments. In addition, it is shown that decreasing the oil supply pressure will bring out the third subsynchronous component, which indicates the outer-film instability. In the meantime, the jump from the first subsynchronous component (inner-film instability) to the second subsynchronous component (inner-film instability) becomes earlier. Moreover, the third subsynchronous component becomes more apparent with a higher oil supply temperature. Furthermore, the smaller artificial unbalance applied to the compressor disk can hardly affect the rotor response, but the utilisation of higher unbalance leads to an intermittently stabilised speed range from 44 krpm to 58 krpm and a locking effect appearing from 58 krpm to 84 krpm.

Using run-up simulation method, Schweizer [86] investigated the stability of a medium-sized TC rotor-FRB system. The first two run-ups with relatively small bearing inner and outer clearances do not exhibit *Total Instability*, whereas the last three run-ups with increased inner and outer clearances show the bifurcation from third subsynchronous component into the so-called *Total Instability* over the higher end of the considered speed range. The observed *Total Instability* phenomenon can produce extremely high inner and outer eccentricities of both FRBs, and significantly high displacements of the compressor and turbine centres. Accordingly, *Total Instability* is extremely harmful to the safe operation of TCs and restricts the speed increase. It possibly can be explained as the synchronization between the inner-film instability and the outer film instability, as a result of the loss of the mutual damping, which is caused by the steadily increasing bearing eccentricities prior to the bifurcation. Further simulations show the onset speed of *Total Instability* can be reduced by reducing unbalance, outer clearance, and inner bearing width or by decreasing outer bearing width and oil supply pressure.

Schweizer [85] also examined the *Total Instability* phenomenon in a laval rotor-FRB system. The simulated results show the inner-film instability usually brings about a limit-cycle oscillation with a perfectly circular orbit, provided that the rotor weight and unbalance are neglected. However, the outer-film instability leads to a more complex state, in which the rotor orbit is a coupling of circumferential and radial motion, even if the rotor weight and unbalance are not included. Therefore, the outer-film instability can be interpreted as symmetry breaking. *Total Instability* occurs when inner film and outer film become unstable simultaneously and the two limit cycles synchronize, i.e., both excite the natural frequency of the laval rotor.

Considering the foundation excitation effect, Ying et al. [102] investigated the nonlinear dynamic behaviour of an automotive TC. For simplification, FRBs are replaced by two plain journal bearings. It is shown that the engine induced vibration can markedly affect the rotor response in a nonlinear manner. In the meantime, the rotor orbits become more complex than that without foundation effect, and a chaotic state can appear at relatively low rotor speeds.

Knoll et al. [55] performed the run-up simulations of two TC rotor-FRB systems. The oil-forces are obtained from the impedance method presented by Childs et al. [21], and the thermal effects are also considered. The heavier TC rotor exhibits the so-called *Absolute Instability* phenomenon (same as the *Total Instability* given by Schweizer [86]) over the higher end of the considered speed range. However, the lighter rotor does not show the existence of *Absolute Instability*. This is in accordance with the findings given by Boyaci et al. [15], which demonstrates the onset speed of *Critical Limit Cycle* Oscillation can be increased through reducing the rotor weight.

Schweizer [87] investigated the dynamics and stability characteristics of a lightly loaded automotive TC rotor-FRB system through run-up simulations with varying physical parameters, such as the width of the outer film. It is shown that the second subsynchronous component cannot be passed through if the outer-film width is increased by 1.3 mm. By contrast, reducing the outer-film width by 0.7 mm introduces the third subsynchronous component over the higher end of the considered speed range. The results prove the high sensitivity of the rotor-FRB system to the bearing parameters.

Tomm et al. [97] carried out the rotordynamic analysis of a TC rotor-FRB system using the run-up simulation method and the analytical bifurcation analysis. It is shown that the results obtained from the two methods are in very good agreement. In addition, the bifurcation analysis can provide a deeper insight into the nonlinear rotordynamic characteristics of TCs.

Inagaki et al. [43] carried out a coupling analysis of rotordynamics and oil-film lubrication in a rotor-FRB system. The oil-film forces are calculated from short bearing approximation, and the thermal effects are also considered. The thermal analysis shows a temperature rise of 20 degrees in the inner film, which is higher than the outer film, as a result of the heat generated by friction. In addition, it is seen that reducing the inner clearance leads to the decrease of the ring speed ratio. The rotordynamic analysis demonstrates two subsynchronous components, which are represented by a conical mode and a parallel mode, respectively. The conical mode can be restricted by lowering the in-

ner clearance, while the parallel mode can be suppressed by reducing the outer clearance. Furthermore, it is observed that the utilisation of higher unbalance offsets results in the reduction of subsynchronous vibrations over the speed range from 200 Hz to 600 Hz.

Alsaeed [7], Kirk and Alsaeed [52] investigated the feasibility of using induced unbalance to improve the dynamic stability of TC rotor-FRB systems. It is found that the induced unbalance is effective to suppress the lowest subsynchronous component. However, further increase the unbalance offset at the compressor disk leads to the increase of the vibration amplitude of the higher subsynchronous component, although the frequency map is dominated by the synchronous component. By contrast, the higher subsynchronous component can be reduced by increasing the unbalance offset at the turbine centre.

Kirk et al. [54] presented the nonlinear jump phenomena observed in the tests of a diesel engine TC with various bearing combinations. The measurements show that the load capacity of FRBs is better than that of axial groove bearings. Moreover, the gravity load is not the only load, which should be considered in the TC bearing design. Furthermore, a nonlinear jump is possible to occur under both loaded and unloaded conditions.

Considering engine induced vibrations, Tian et al. [95] analytically investigated the dynamic behaviours of a TC rotor-FRB system. The bearing force model is developed from the model given in Ref. [18]. It is seen that the introduced unbalance can significantly influence the rotor response at relatively low rotor speeds as compared to the simulation results under the perfectly balanced condition. At higher rotor speeds, the rotor response is dominated by the subsynchronous vibrations induced by the oil film instability. The engine induced vibration can significantly affect the rotor response at lower speeds as well, while the dominant subsynchronous components can suppress the engine induced vibration at higher rotor speeds.

Kamesh [45], Kamesh et al. [46] investigated the stabilising effect of gyroscopic moments in an automotive TC. It is shown that the gyroscopic coefficient, i.e., the ratio of the polar to the transverse inertia of the rotor, can significantly affect the stability characteristics of the conical whirl. It is stable on condition that the gyroscopic coefficient is bigger than 0.5.

The highly nonlinear FRBs, widely used in modern TC rotor-bearing system designs, lead to rotor motion instabilities in rather wide ranges of operating conditions. The high sensitivity of the rotordynamic behaviour to the rotor-FRB system parameters emphasizes the importance of parameter study in the TC rotordynamic optimisation. This thesis aims to develop a reliable, efficient rotor-FRB model to obtain a deep insight into the

complex characteristics possessed by the rotor-FRB system. The investigation into the effects of the important physical parameters is described in detail. The lately obtained results systematically reveal a lot of intriguing phenomena, which will be helpful for the TC research and development.

1.3.7 Rotordynamic analysis of rotor-SFRB systems

San Andrés et al. [80] developed a complete nonlinear SFRB bearing model to investigate the rotordynamic performance of a TC rotor-SFRB system. It is shown that the predicted nonlinear results exhibit two subsynchronous frequencies over the entire rotor speed range, which is in satisfactory agreement with the measured data. It should be mentioned that a third subsynchronous with a higher frequency can also be observed from the nonlinear predictions, but it does not appear on the waterfall diagram of the measured data. What can also be seen is the rise of rotor speed brings about the steady decrease of the whirl frequency ratio of both subsynchronous components. Furthermore, both linear and nonlinear models reproduce the measured synchronous response very well, despite the fact that the linear model produces higher amplitudes at the critical speed. As a result, considerable savings in product development and prototype testing can be achieved by applying the developed predictive tool.

Gjika et al. [30] investigated the nonlinear dynamic behaviour of a TC rotor-SFRB system using the comprehensively modelled bearing forces. The corresponding tests are also carried out, and it is seen that the results from simulations are in good agreement with those from the experiments. Four bearing inner and outer clearance combinations are used both in the simulations and experiments. It is observed that the highest rotor vibration amplitudes occur over the lower end of the speed range, i.e., less than 1 kHz. The configuration of the smallest outer clearance and the biggest inner clearance results in the largest rotor vibrations. Moreover, two typical subsynchronous components are identified. The one with higher frequency is related to a cylindrical mode of the rotor, while the other with smaller frequency corresponds to a conical mode.

Maruyama [60], San Andrés et al. [79] investigated the nonlinear response of a TC rotor-SFRB system considering the engine induced vibrations. The measured data show the rigid housing assumption of TCs is not adequate, since the vibration amplitudes of the compressor housing are much smaller than the centre housing. Another finding is that $2\times$, $4\times$ and $6\times$ engine speed order frequencies greatly contribute to the total compressor housing motion, which can probably be attributed to the engine firing frequency. The

nonlinear simulations with the engine induced vibrations show a broad, low frequency response, which can also be appreciated from the test data. However, the predicted results disregarding housing movement deviate significantly from those including engine induced vibrations. In addition, the predictions show that the TC shaft motions are mainly attributed to the engine speed orders lower than $6\times$, although measurements exhibit considerable amplitudes at higher-order frequencies. Furthermore, the analysis also reveals the damped natural frequencies of the investigated TC can be excited by the super-harmonics of the engine speed.

Using the run-up as well as run-down simulation method, San Andrés and Vistamehr [83], Vistamehr [100] presented a parameter study on the nonlinear jump phenomena in a TC rotor-SFRB system. It is seen reducing the oil supply pressure leads to the earlier occurrence of the jump to the second whirl frequency, which can also be realised by increasing the oil inlet temperature. However, a faster rotor acceleration can delay the onset speeds of nonlinear jumps as compared to the corresponding run-up with smaller acceleration, and so does faster deceleration. The run-up under the condition of turbine back-plane out-of-phase imbalance exhibits a smaller onset speed of the nonlinear jump to the second whirl frequency, and, shortly, it disappears at relatively high rotor speeds, which let the rotor undergo a pure synchronous motion. Further simulation with twice as large mass imbalances produces an even wider speed range without the subsynchronous components, and the frequency jump cannot be identified.

1.3.8 Journal bearings in low-speed TCs

Pantelelis et al. [70] combined a simple finite element model with neural networks to establish the fault diagnosis of a practical naval TC rotor-journal bearing system. The engine induced vibrations are considered as four sinusoidal forces, and the bearing housing is modelled as a large concentrated mass. It should be noted that the two journal bearings are outboard mounted rather than the inboard mounted in automotive applications. Additionally, the operating speed of the investigated TC, i.e., 12,000 rpm, is much lower than that of automotive TCs. With the linearised bearing forces, the proposed method can offer more detailed diagnosis.

1.3.9 Ball bearing investigation

Miyashita et al. [62] presented a development of high efficiency ball bearing supported TCs, whose speed can climb up to 250,000 rpm. It is shown the mechanical efficiency of

the TC with ball bearings is higher than that with FRBs. It is seen a 20% increase of efficiency at the low gas flow range and a 5% increase at the high gas flow range. Moreover, the adoption of ball bearing can significantly improve the TC lag during acceleration as well. However, additional damping method is needed to reduce the vibration level when the rotor climbs over the critical speed, and excessive endurance test is required before it enters the market.

Aida et al. [5] replaced the FRBs in an automotive TC with ball bearings to improve the TC acceleration response. In contrast to the TC with FRBs, the one with ball bearings shows a considerable decrease of friction loss in the low speed range of less than 60,000 rpm. As presented by Miyashita et al. [62], the newly designed rotor-ball bearing system can give a faster response during the acceleration. The structural parameters of the squeeze film damper, which is positioned between the ball bearings and bearing housing, should be carefully selected with respect to the calculated first three critical speeds.

To reduce the mechanical loss of the TC for heavy-duty diesel truck engines, Griffith et al. [31] substituted ball bearing rings for conventional hydrodynamic radial and thrust bearings. The experimental results evidence a dramatical decrease of the bearing friction loss as compared to the journal bearings, which, in turn, produce higher turbine efficiency, especially at relatively low expansion ratios. In addition, it is seen that the ball bearings can offer an improvement in the transient response with higher idle speeds. Further experimental investigation shows that the adoption of ball bearings can significantly increase the contaminated lube resistance of the system in contrast to the conventional journal bearing system.

Ashtekar and Sadeghi [9] experimentally and analytically investigated the rotordynamic performance of a high-speed TC rotor-ball bearing system. It is seen that the experimental results correlate well with the predictions obtained from the coupled model including a discrete element ball bearing model. Further observations show that preloading and imbalance can significantly affect the rotordynamic characteristics of the investigated TC rotor-ball bearing system.

1.3.10 Bearing system comparisons and other bearing systems

Sahay [76] presented the TC rotor-bearing system optimisation process with the analytically and experimentally obtained results. The experimental results show the difference in friction loss between FRBs and SFRBs is quite small. Moreover, the power loss reduction can be realised by reducing the journal diameter and bearing length. It is also

found the adoption of SFRB or ball bearing can easily meet the design requirements, compared to FRBs of which the successful utilisation can only be ensured by excessive bearing parameter tests. The author further concludes that the time and cost needed for TC rotor-bearing system optimisation work can be considerably reduced, provided that more accurate bearing models become available.

Keller et al. [47] showed an improved TC hybrid bearing design, consisting of a single ball bearing close to the compressor end and a single FRB close to the turbine end, to resolve the wear failure of the thrust bearing under competitive conditions in motorsports. In comparison with the original FRB design, the linear stability analysis with the new bearing system shows a considerable increase of the critical speed due to the first bending mode. This advantage can significantly enlarge the critical speed margin and, thus, reduces the possibility of thrust bearing failure, on condition that sufficient damping is given to run through the first critical speed.

Sahay and LaRue [77] showed SFRB is a cost effective solution to reduce the oil whirl amplitude by up to 35% compared to FRBs, and the design of ball bearings supported by a squeeze film damper can lead to the absence of the subsynchronous vibrations, although the cost of a ball bearing system restricts its use. Additionally, it is observed that the TC shaft motion on an engine is 20 to 30% percentage points higher than that on a gas test stand, as a result of the engine vibrations being transmitted to the TC bearing supports and the aerodynamic pulsation load on the turbine blade imposed by the exhaust gas. Furthermore, as mentioned in Ref. [76], the authors again state that the urgent needs for a reliable computational tool to help reduce the heavy dependence on experimental tests.

Howard [42] analytically presented a preliminary design process of air foil bearings for diesel truck TCs to replace FRBs. Two possible design solutions, i.e. short rotor and long rotor, are analysed, and both of them exhibit satisfactory performance to be employed in the truck TC applications. However, it is further seen the long rotor design can bear more shock loads with tolerable shaft stresses, although more damping is needed to ensure the stable operation of the system at the maximum rotor speed.

De Choudhury [24], Pettinato and DeChoudhury [71] analytically and experimentally demonstrated that the redesign of a high speed locomotive TC bearing system to improve the rotordynamic characteristics and the mechanical performance. The original design is a pair of journal and thrust combination bearings located close to the rotor ends, which is changed to a pair of three lobe journal bearings with a double acting thrust bearing at the centre of the unit. It is theoretically proved that the new design exhibits superior thermal

and stability characteristics in contrast with the original design with three-axial-groove journal bearings. Conducted tests confirm the predicted results, and the redesigned rotor-bearing system shows subsynchronous vibrations with much smaller amplitudes than the original case. It should also be pointed out that the assumed maximum operating speed of the investigated TC is 20 krpm.

Rodríguez et al. [73] optimised the rotordynamic characteristics of a TC rotor-bearing system for a locomotive turbocharger. The original three-lobed symmetric rigid pad bearing is changed to three-lobe canted rigid pad bearing with a profile, and the stability analysis of the new bearing configuration with the optimised clearance ratio indicates the system can be dynamically stable over the entire operating speed range of the investigated TC. The experimental results confirm the predictions. It is seen that the tightest bearing clearance leads to the best stability performance, whereas the bearing temperature is about 17 degrees higher than the bearing configuration with the largest bearing clearance. As a result of the trade-off in journal metal temperature, a value between the large and small clearances is selected as the optimised bearing clearance for production.

Through simulation and corresponding experiments, Kelly [48] compared the rotordynamic performance of three turbocharger bearing systems: FRB, SFRB and ball bearing. It is shown the configuration of ball bearings supported by a squeezing film damper can eliminate the subsynchronous vibration caused by the oil-whirl instability. However, at relatively high rotor speeds, transmitted forces of ball bearing are predicted to be higher than those of FRB and SFRB due to the bending mode is approached.

Chen [19] presented the rotordynamic characteristics of various bearing designs in relatively large TCs for locomotive and marine applications. It is shown that the taper land bearing is suitable for applications with high speed and low bearing load, while the preloaded 3-lobe and 3-lobe bearing with damper can be adopted to reduce the bearing and oil temperature. In addition, tilting pad bearing is also a good choice, albeit the cost is much higher, which greatly restrict its use.

Mokhtar et al. [64] analytically drew a comparison between the frictional performance of the conventional journal bearings and FRBs under transient load conditions. The results show that a considerable decrease of friction power loss can be obtained with the utilisation of FRBs in automotive engines. Moreover, the inner minimum film thickness is found to be sensitive to both inner and outer clearances, while the outer minimum film thickness is only sensitive to the outer clearance.

Tomek et al. [96] theoretically and experimentally made a comparison of TC rotor

stability with rotating and non-rotating floating rings. It is found that the self-excited vibrations induced by the outer film instability persist over the entire speed range. By contrast, the utilisation of stalled bushings and bidirectional three-lobbed inner geometry can effectively suppress the outer-film instability, which is confirmed by the experiment. In addition, the calculated results show that the unidirectional bearings perform even better than the bidirectional bearings.

1.4 Research Objectives

The current work aims to understand the inherent complex phenomena in the rotor-FRB system of modern turbochargers, which is modelled by building the FEM model of a practical TC rotor-FRB system and performing the linear and nonlinear simulations with the rotordynamic toolbox according to Ref. [27] based upon the numerical computation platform MATLAB[®]. The objectives of the thesis are to:

- (a) carry out the linear stability analysis with different types of linearized bearing models and compare the outputs of those models with the nonlinear simulated results to, linearly, interpret the nonlinear results and to find out the applicability of those linear models;
- (b) propose an efficient and reliable nonlinear oil-film force model for nonlinear rotordynamic calculations, and perform the stationary nonlinear simulations to preliminarily study the nonlinear dynamics of the rotor-FRB system;
- (c) investigate the effects of engine induced excitations on the rotordynamic performance of the rotor-FRB system;
- (d) clarify the nonlinear effects of the FRB outer clearance on the rotordynamic characteristics of the rotor-FRB system by nonlinear run-up and run-down simulations;
- (e) examine the influence of unbalance in the rotor-FRB system by run-up and run-down simulations, considering both the variations of unbalance amount and distribution.

1.5 Thesis Outline

Chapter 1 introduces the background, motivations, literature survey and the objectives. Chapter 2 presents the linear rotordynamic characteristics of the rotor-FRB system under investigation. Chapter 3 shows the newly developed analytical model of oil-film forces and

the nonlinear simulations with the constant speed assumption. Chapter 4 investigates the engine excitation effect on the rotordynamic performance of the TC rotor-FRB system. Chapter 5 studies the effect of the bearing outer clearance on the rotor response by carrying out a series of run-up and run-down simulations. Using the same simulation method as in Chapter 5, Chapter 6 presents the nonlinear effects of unbalance applied to the compressor and turbine disks. Subsequently, the conclusions and future work are shown in Chapter 7.

Chapter 2

Turbocharger Linear Rotordynamics

Although the TC rotor-FRB system behaves in a highly nonlinear manner, recent studies [6, 35, 50–52, 95] show that the linear stability analysis can offer a deeper insight into the nonlinear results obtained from nonlinear simulations or experiments. Chapter 2 presents the results of the linear stability analysis of a realistic TC rotor-FRB system in a gradually deepening manner. The finite element model of the investigated TC rotor is given in Section 2.1, in which FRB parameters are also detailed. The simplest isotropic constant stiffness support is introduced in Section 2.2, which is followed by the anisotropic constant stiffness supports shown in Section 2.3. The linearized journal bearing supports are presented first in Section 2.4 to illustrate the complexity introduced by the linearization of fluid film lubricated bearings. The ring masses connected by isotropic constant stiffness springs are considered in Section 2.5. Subsequently, two methods of FRB linearization are shown in Section 2.6.

2.1 Finite Element Modelling

The structural parameters of a real TC rotor-FRB system are listed in Table 2.1. They have been previously shown in Ref. [11]. Since the partial differential equations given by modelling of the rotor shaft in a continuous system are difficult to be tackled, discretizing the continuum to a discretized system by the finite element method in the form of a set of ordinary differential equations is the only feasible method. As shown in Fig. 2.1, the TC rotor is simplified to four nodes connected by three uniformly circular beam sections. With the help of MATLAB[®] toolbox Rotor Software V1 according to Ref. [27], the continuous

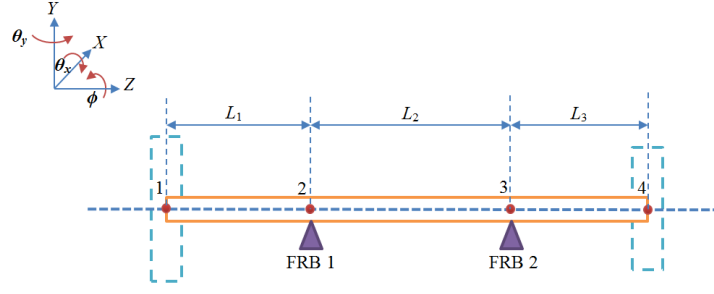


Fig. 2.1. TC finite element model. The dash rectangles at the rotor ends represent the compressor disk attached to Node 1 and the turbine disk attached to Node 4.

beam can be discretized by employing the Timoshenko circular beam theory, and the shear effect has also been considered. The model is an upgrade version of the lumped parameter model described in Ref. [95]. The masses and the moments of inertia of the two overhung disks have been concentrated to the corresponding nodes at the two ends of the rotor, respectively. Following the procedures given in Ref. [27], the general governing equations of motion for the investigated TC rotor-FRB system can be derived as follows.

$$\mathbf{M}\ddot{\mathbf{q}} + \mathbf{C}\dot{\mathbf{q}} + \dot{\phi}\mathbf{G}\dot{\mathbf{q}} + \mathbf{K}\mathbf{q} = \mathbf{F}_i + \mathbf{F}_{ub} + \mathbf{F}_s \quad (2.1)$$

where $\mathbf{q} = \{x_1 \ y_1 \ \theta_{x1} \ \theta_{y1} \ x_2 \ y_2 \ \theta_{x2} \ \theta_{y2} \ x_3 \ y_3 \ \theta_{x3} \ \theta_{y3} \ x_4 \ y_4 \ \theta_{x4} \ \theta_{y4}\}^T$ is the system displacement vector related to the fixed reference frame described in Fig. 2.1; (x_n, y_n) and $(\theta_{xn}, \theta_{yn})$ represent the lateral and rotational displacements of the n th node ($n = 1, \dots, 4$), corresponding to the horizontal direction X and the vertical direction Y , respectively; \mathbf{M} is the distributed symmetric mass matrix; \mathbf{C} is the system external damping matrix, while \mathbf{G} is the skew-symmetric gyroscopic matrix; \mathbf{K} denotes the system stiffness matrix. The following three external force terms are on the right-hand side of Eq. (2.1): \mathbf{F}_i denotes the inner oil film force vector supporting the journal at Node 2 and Node 3 (see Fig. 2.1). In linear rotordynamics, for simplicity, the inherently nonlinear oil-film forces are normally replaced by springs with constant stiffness and damping properties (see Section 2.5 and Section 2.3) [86, 87]. Alternatively, according to fluid lubrication theory [17], they can also be linearized to bearing stiffness and damping coefficients around its equilibrium (see Section 2.4 and Section 2.6). In this case, the bearing stiffness and damping coefficients vary with the rotor speed. Both linearization can lead to a combination with the stiffness matrix \mathbf{K} and the damping matrix \mathbf{C} , which means the linearized oil-film force elements can be moved to the left-hand side of the system governing equations. As shown in Eqs.

Physical properties	Compressor disk	Turbine disk
Mass (kg)	$m_c = 0.118$	$m_t = 0.326$
Polar MoI (10^{-6} kg m ²)	$I_{P_c} = 44.0$	$I_{P_t} = 81.0$
Transverse MoI (10^{-6} kg m ²)	$I_{T_c} = 32.7$	$I_{T_t} = 77.0$

(a) Compressor and turbine disks details

Shaft parameters	Values
Density (kg m ⁻³)	7860
Young's modulus (GPa)	200
Diameter (mm)	$d = 2R_j = 11$
Length (mm)	$L_1 = 33; L_2 = 39; L_3 = 33$

(b) Shaft details

FRB parameters	FRB 1		FRB 2	
	Inner film	Outer film	Inner film	Outer film
Viscosity (10^{-3} Pa s)	$\mu_i = 6.4$	$\mu_o = 6.4$	$\mu_i = 4.9$	$\mu_o = 4.9$
Radial clearance (μm)	$C_1 = 34$	$C_2 = 74$	$C_1 = 34$	$C_2 = 74$
Bore radius (mm)	$R_{ri} = 5.534$	$R_{ro} = 8.000$	$R_{ri} = 5.534$	$R_{ro} = 8.000$
Length (mm)	$L_i = 6.5$	$L_o = 9.0$	$L_i = 6.5$	$L_o = 9.0$
Ring mass (kg)	$m_{rc} = 7.2\text{E} - 3$		$m_{rt} = 7.2\text{E} - 3$	
Ring's polar MoI (10^{-6} kg m ²)	$I_{rc} = 33.641$		$I_{rt} = 33.641$	

(c) FRB details

Table 2.1. TC rotor-FRB system details

(2.2a) and (2.2b), \mathbf{F}_{ub} , consisting of \mathbf{F}_{ub_c} and \mathbf{F}_{ub_t} , is the unbalance force vector, which only exists at compressor and turbine disks. m_c , m_t denote the mass of the compressor and turbine disks, respectively. e is the unbalance offset displacement, which is assumed to be the same value for both disks. ϕ is the rotor rotational angle around the Z axis, and, therefore, $\dot{\phi}$, $\ddot{\phi}$ represent the rotor speed and rotor acceleration, respectively. In stationary simulations (see Chapter 3), $\dot{\phi}$ is a given constant rotor speed for each calculation, and the terms with $\ddot{\phi}$ are equal to zero. In the nonstationary simulations considering linear acceleration or deceleration, the values of $\dot{\phi}$ and $\ddot{\phi}$ are shown in Eqs. (5.1a)-(5.1c). δ_c and δ_t represent the phase of the imposed unbalance at Node 1 and Node 4 (see Fig. 2.1), respectively. \mathbf{F}_s denotes the static gravitational force vector in the Y direction only. In linear rotordynamics, it is counteracted by the static forces given by the bearing force linearization, and, normally, is not shown in Eq. (2.1).

$$\mathbf{F}_{\text{ub}_c} = \begin{Bmatrix} F_{ub_{xc}} \\ F_{ub_{yc}} \end{Bmatrix} = \begin{Bmatrix} m_c e \dot{\phi}^2 \cos(\phi + \delta_c) + m_c e \ddot{\phi} \sin(\phi + \delta_c) \\ m_c e \dot{\phi}^2 \sin(\phi + \delta_c) - m_c e \ddot{\phi} \cos(\phi + \delta_c) \end{Bmatrix} \quad (2.2a)$$

$$\mathbf{F}_{\text{ub}_t} = \begin{Bmatrix} F_{ub_{xt}} \\ F_{ub_{yt}} \end{Bmatrix} = \begin{Bmatrix} m_t e \dot{\phi}^2 \cos(\phi + \delta_t) + m_t e \ddot{\phi} \sin(\phi + \delta_t) \\ m_t e \dot{\phi}^2 \sin(\phi + \delta_t) - m_t e \ddot{\phi} \cos(\phi + \delta_t) \end{Bmatrix} \quad (2.2b)$$

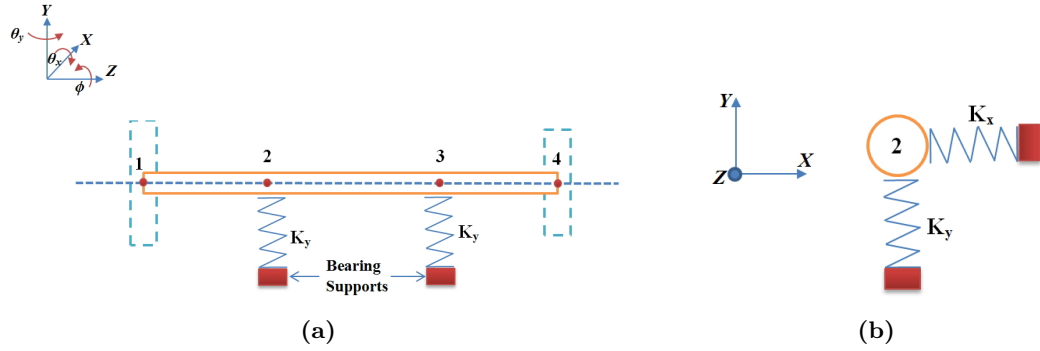


Fig. 2.2. TC rotor with constant stiffness bearing supports: (a) the front view, (b) the side view at Node 2.

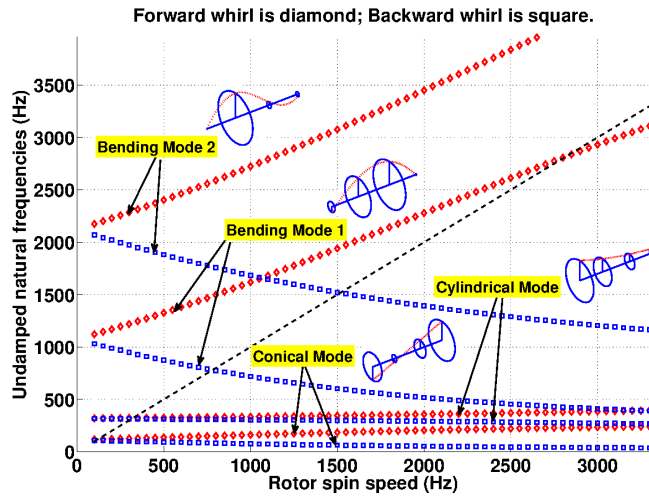


Fig. 2.3. Campbell diagram (isotropic spring with stiffness of 1×10^6 N/m), the dash line is the synchronous line; mode shape plots are obtained at 1000 Hz.

2.2 Isotropic Spring Supports

For simplicity, both FRBs are replaced by identical isotropic spring supports in this section as shown in Fig. 2.2. The Campbell diagram depicted in Fig. 2.3 is calculated when the stiffness of both springs is 1×10^6 N/m. The mode shapes at 1000 Hz of rotor speed are plotted. It is clear that the first two modes are mostly rigid modes. The first mode is a conical mode, in which the orbits of the compressor centre and turbine centre are out-of-phase by 180 degrees. The orbits of Node 2 and Node 3, where the bearings locate, are out-of-phase as well. By contrast, the orbits of all the four nodes are in-phase in Mode 2, which is labelled by *cylindrical mode* in Fig. 2.3. Note that the vibration amplitudes of the four nodes follow a descending trend along the shaft. Two bending modes with higher frequencies are also depicted in Fig. 2.3. It should be mentioned that there are three intersection points of the dashed synchronous line and those forward modes within the considered speed range, which indicate three critical speeds in the linearized system.

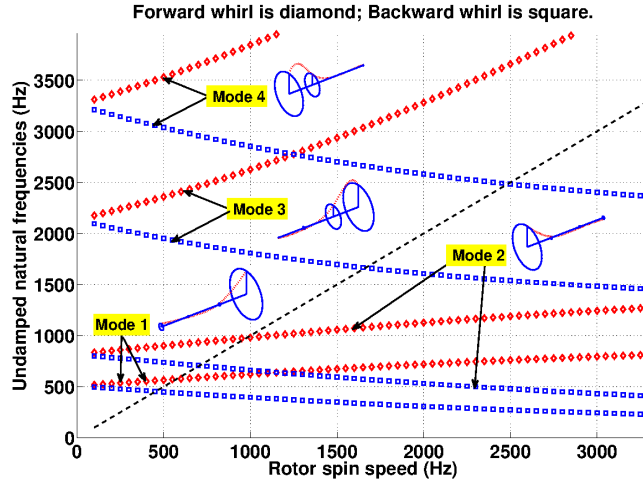


Fig. 2.4. Campbell diagram (isotropic spring with stiffness of 1×10^8 N/m), the dash line is the synchronous line; mode shape plots are obtained at 1000 Hz.

The first two are located lower than 500 Hz, while the third one is approximately at 2800 Hz. The third critical speed evidences that the rotor will be operated higher above the first bending mode over the higher end of the considered speed range.

Fig. 2.4 presents the results with spring stiffness of 1×10^8 N/m, which corresponds to extremely stiff bearings. It is seen that all the modes are moved to higher frequency locations as compared to the case shown in Fig. 2.3. Owing to the considerable increase of bearing stiffness, the first two rigid modes in Fig. 2.3 become bending modes in Fig. 2.4, and the phase differences of the orbits of the four nodes are also altered. For example, the orbits of the compressor and turbine centres of Mode 1 are in-phase in Fig. 2.4, although the orbits of the two bearing nodes are still out-of-phase. Furthermore, due to the frequency increases of all modes, there are only two critical speeds in Fig. 2.4, although both of them are higher than those in Fig. 2.3.

2.3 Anisotropic Spring Supports

In this section, the stiffness of the spring supports shown in Fig. 2.2 is assumed to be anisotropic, i.e. $K_x \neq K_y$, since the linearization of the nonlinear forces of the fluid lubricated bearings can always introduce anisotropic stiffness in the X and the Y directions, which will be detailed in Section 2.4 and Section 2.6. Fig. 2.5 shows the Campbell diagram obtained under the condition that $K_x = 1 \times 10^6$ N/m and $K_y = 2 \times 10^6$ N/m. Unlike the circular orbits shown in Fig. 2.3 and Fig. 2.4, the orbits with anisotropic supports are elliptical, especially the lower modes. In addition, one can also see the existence of the so-called mixed whirl introduced by the complexity of the anisotropic supports. This means

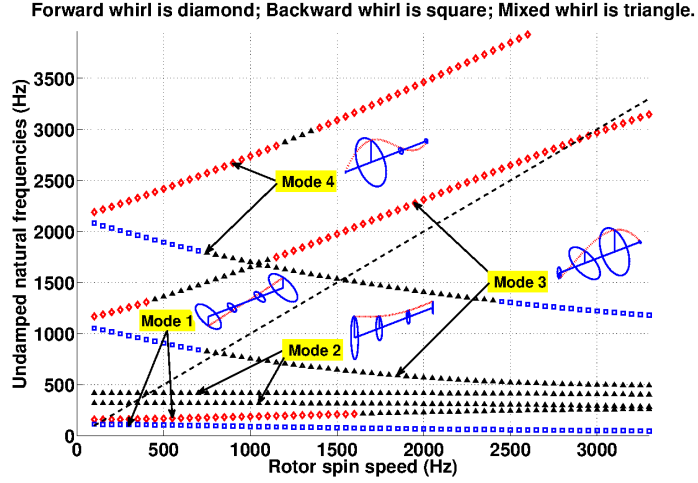


Fig. 2.5. Campbell diagram (anisotropic spring supports with stiffness of 1×10^6 N/m in the X direction and 2×10^6 N/m in the Y direction), the dash line is the synchronous line; mode shape plots are obtained at 1000 Hz.

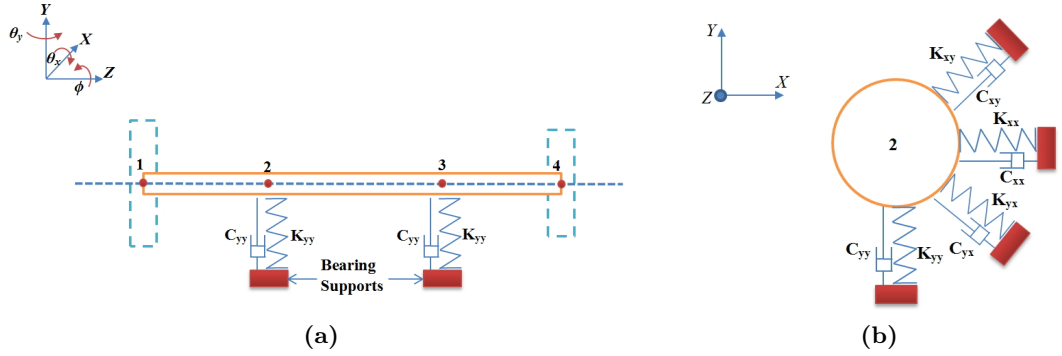


Fig. 2.6. TC rotor supported by linearized journal bearings

that the whirling directions of all the four nodes are not exactly the same. Some portions of the nodes are in forward whirl, but the other are in backward whirl. Although this phenomenon is counter-intuitive, it can appear as a result of the anisotropic properties of the bearings [1, 27]. In contrast to Fig. 2.3, the biggest difference is that the forward whirl and backward whirl of Mode 2 are totally changed to mixed whirl over the considered speed range in Fig. 2.5.

2.4 Linearized Journal Bearings

The investigated TC rotor is assumed to be supported by a pair of normal journal bearings in this section. The bearing structural parameters are assumed to be the same as the FRB outer clearances, which are given in Table 2.1c. As shown in Fig. 2.6, the linearization of journal bearing will lead to the appearance of damping coefficients in the X and Y directions, respectively. In the meantime, the cross coupling stiffness and damping coefficients

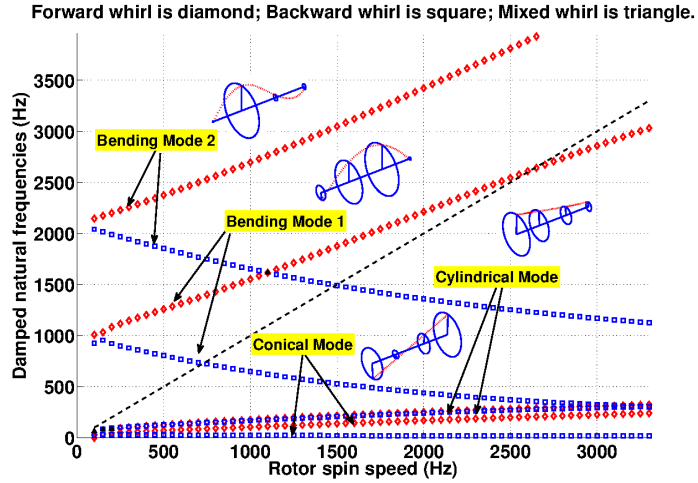


Fig. 2.7. Campbell diagram with linearized journal bearings, the dash line is the synchronous line; mode shape plots are obtained at 1000 Hz.

are produced by the linearization as well [1, 27, 28]. Since the bearing is relatively short ($L_o/d < 1$), the classical short bearing approximation theory [27, 33] can be employed to obtain the needed bearing stiffness and damping coefficients in closed form equations without numerically solving the Reynolds' equation. The Campbell diagram is presented in Fig. 2.7, which reveals a significant difference with Fig. 2.3 in the rigid modes. It is seen the frequency of the backward whirl of the cylindrical mode gradually ascends with increasing rotor speed, which leads to the very small difference with the forward whirl of the cylindrical mode.

It should be mentioned that the cross coupling stiffness coefficients exert a destabilising effect on the rotor-bearing system, which means eigenvalues with positive real parts would be encountered during calculations. The results of stability analysis are shown in Fig. 2.8. Fig. 2.8a is an enlarged version of Fig. 2.7 over the low speed range, but the imaginary parts of all the stable modes are set to zero to bring out the unstable modes. It is evident that there are two unstable modes within the entire speed range up to 3300 Hz. The Unstable Mode 1 becomes unstable at the start of calculation, and it is a conical forward mode. The cylindrical Unstable Mode 2 sets in at 200 Hz, and it is also in forward whirl over the speed range from 250 Hz to 3300 Hz. Fig. 2.8b and c show the stability map and damping factor plot of the investigated TC rotor-journal bearing system, respectively. The mode is unstable on condition that its logarithmic decrement is below zero. Moreover, it is considered that the less the logarithmic decrement is, the more likely the unstable mode is to be excited in the simulations with nonlinear oil-film forces. In this case, it is observed the Unstable Mode 2 is more likely to occur over the high speed range from 400 Hz to 3300 Hz. What can also be appreciated is that the journal bearing can hardly affect

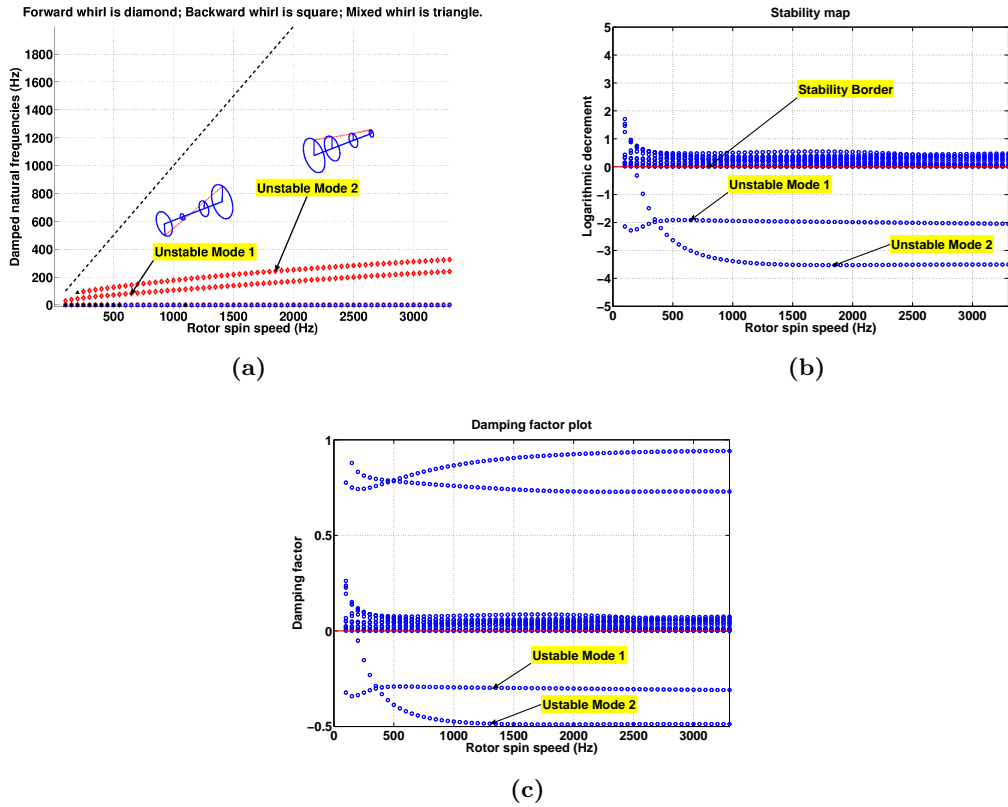


Fig. 2.8. Stability analysis with journal bearings: (a) Campbell diagram with unstable modes, (b) stability map and (c) damping factor plot.

the stability characteristics at rotor speeds higher than 1000 Hz, since the logarithmic decrements of both unstable modes cannot be influenced with varying rotor speed.

2.5 Isotropic Spring Supports with Ring Masses

The floating ring masses are added to the linear model to investigate its effects on the linear rotordynamic characteristics of the system. As shown in Fig. 2.9, the floating rings are modelled as pedestals connected by flexible supports with constant stiffness. The Campbell diagram shown in Fig. 2.10 demonstrates that the added ring masses can hardly affect the rigid modes at relatively low frequencies, but one can see the forward whirl of the second bending mode will be considerably affected by the increasing rotor speed as compared to Fig. 2.3. Moreover, two forward whirals and two backward whirals are introduced over the higher end of the considered frequency range. The mode shapes of the forward whirals are depicted in Fig. 2.11, in which the ring orbits are also shown. It is observed the ring orbits are in-phase with the corresponding node orbits on the rotor shaft in the first three forward whirals. The fourth forward whirl, i.e. the forward whirl of the second bending mode, is dominated by the ring vibration amplitude on the compressor

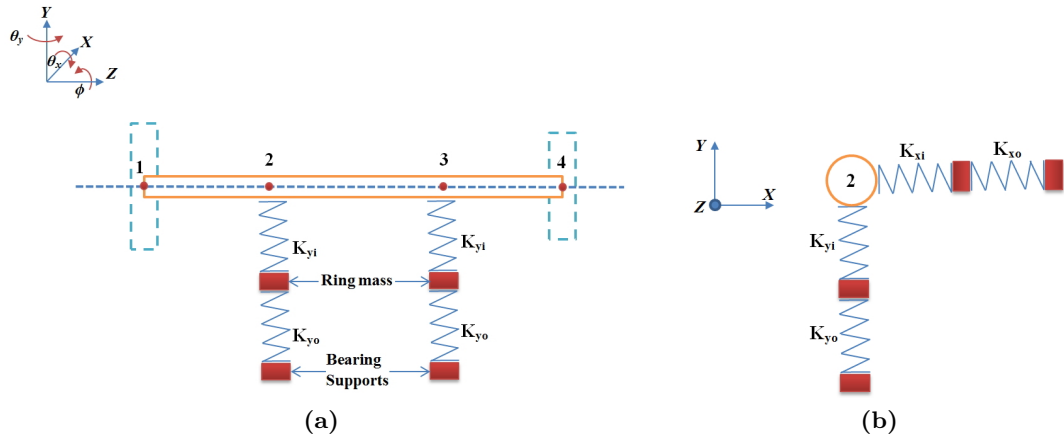


Fig. 2.9. TC rotor with constant stiffness bearing supports including floating ring masses; $K_{xi} = K_{xo} = K_{yi} = K_{yo} = 1 \times 10^6$ N/m.

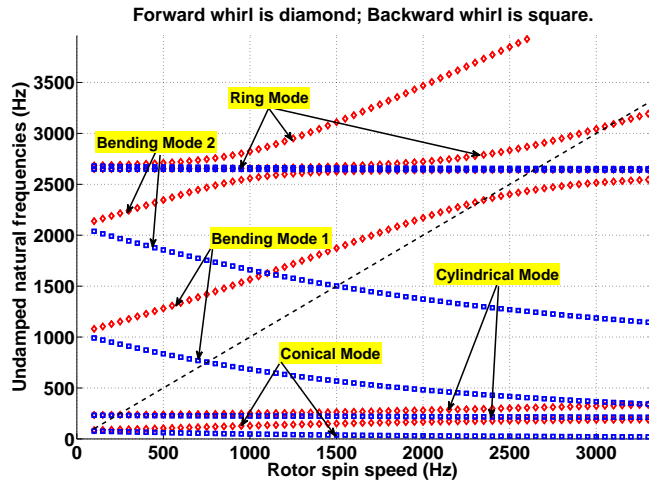


Fig. 2.10. Campbell diagram with linearized journal bearings, the dash line is the synchronous line; mode shape plots are obtained at 1000 Hz.

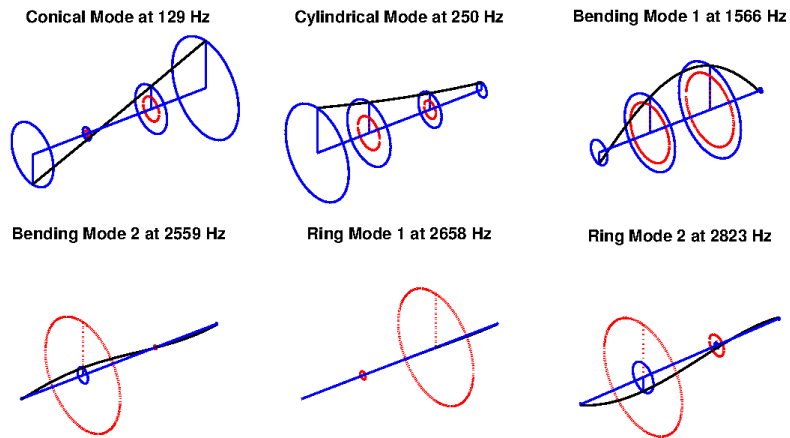


Fig. 2.11. Mode shapes of forward whirls when the ring masses are considered and connected by constant stiffness supports; ring orbits are represented by the red dotted circles; the rotor speed is set to be 1000 Hz.

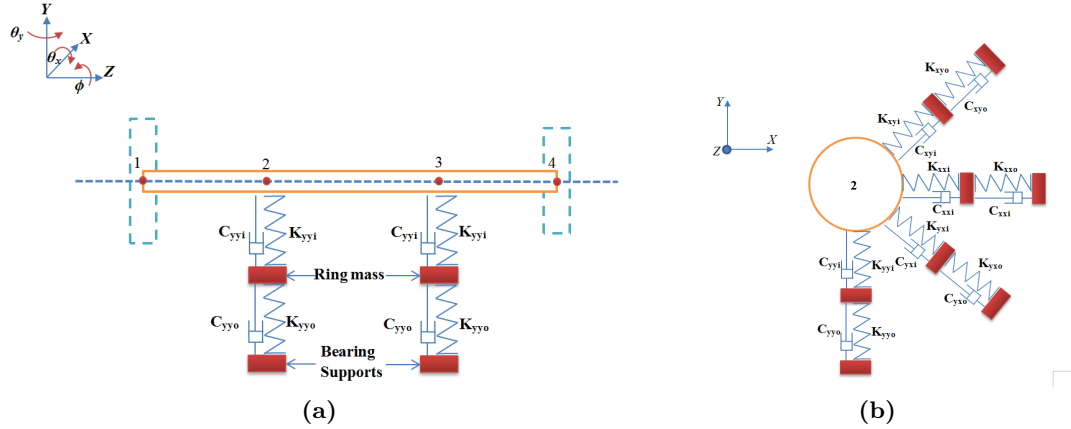


Fig. 2.12. TC rotor supported by linearized FRBs including floating ring masses

side, which confirms that the influence of the floating rings on the higher modes. By contrast, in the forward ring mode 1 at 2658 Hz, the ring on the turbine side produces the highest vibration amplitude, although the ring on the compressor side establishes the dominance again in the forward ring mode 2 at 2823 Hz.

2.6 Linearized FRBs

In this section, based upon the short-bearing approximation, the linearization of the FRB is realised by linearizing the inner and outer oil-film forces to bearing stiffness and damping coefficients around the static equilibrium, as shown in Fig. 2.12. Firstly, the ring masses is considered to be negligible, and, therefore, the stiffness and damping coefficients of the inner and outer films are combined to get the total impedance. Thus, the two films are reduced to one, and the FRBs are modelled as normal journal bearings (see Fig. 2.6). The results of this case are shown in Section 2.6.1. The ring masses are included in Section 2.6.2, and the effects of the outer clearance on the linear rotordynamic characteristics of the investigated system are also shown.

2.6.1 Linearization without ring mass

The Campbell digram of the predicted unstable modes with linearized FRBs but without ring masses is shown in Fig. 2.13a. In comparison with Fig. 2.8, the results also demonstrate two unstable modes, although the logarithmic decrement can be considerably affected by the increasing rotor speed, especially the logarithmic decrement of the unstable Mode 1. As the rotor speed climbs up, one can see that the logarithmic decrement of the unstable Mode 1 clearly follows a descending trend, which implies the unstable Mode 1

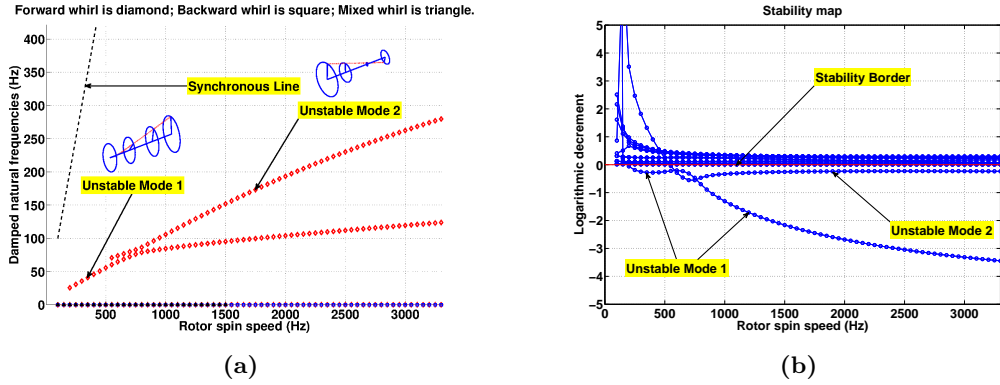


Fig. 2.13. Stability analysis with linearized FRBs without ring masses: (a) Campbell diagram with unstable modes, (b) stability map. Both ring speed ratios are assumed to be 0.2.

are highly likely to be excited within the high speed range. By contrast, the logarithmic decrement of the unstable Mode 2 is much smaller than that of the unstable Mode 1, and it is very close to the stability border. Therefore, unstable Mode 2 may not appear in the nonlinear simulations or measurements.

2.6.2 Linearization with ring mass

The ring masses are included in this section, and the two FRBs are modelled as two journal bearings in series. Several bearing outer clearance values are selected to investigate the influence of bearing outer clearance on the linear rotordynamic characteristics of the investigated system. Fig. 2.14 shows the Campbell diagrams with varying FRB outer clearances. It should be mentioned that, similar to Fig. 2.8 and Fig. 2.13a, only the predicted unstable modes are shown in Fig. 2.14, and they are labelled with respect to the occurrence in the run-up time sequence. The imaginary parts of all the stable modes are set to be zero and plotted on the horizontal axis. It is seen that the inclusion of ring mass introduces additional unstable modes as compared to the single oil film linearization (see Fig. 2.8 and Fig. 2.13a). Moreover, Fig. 2.14 shows there are mainly four unstable modes for all the considered FRB outer clearances over the entire speed range, although the unstable Mode 5 is observed over the higher end of the considered speed range with the widest outer clearance, 74 μm . Their mode shapes, including the floating ring orbits, are obtained when both FRB outer clearances are 44 μm , and they are presented in Fig. 2.15 as an example. The corresponding stability maps are depicted in Fig. 2.16. The mode is considered to be unstable when its logarithmic decrement is below zero. The obtained results are in good agreement with the unstable modes shown in Ref. [35, 52] and are summarised as follows.

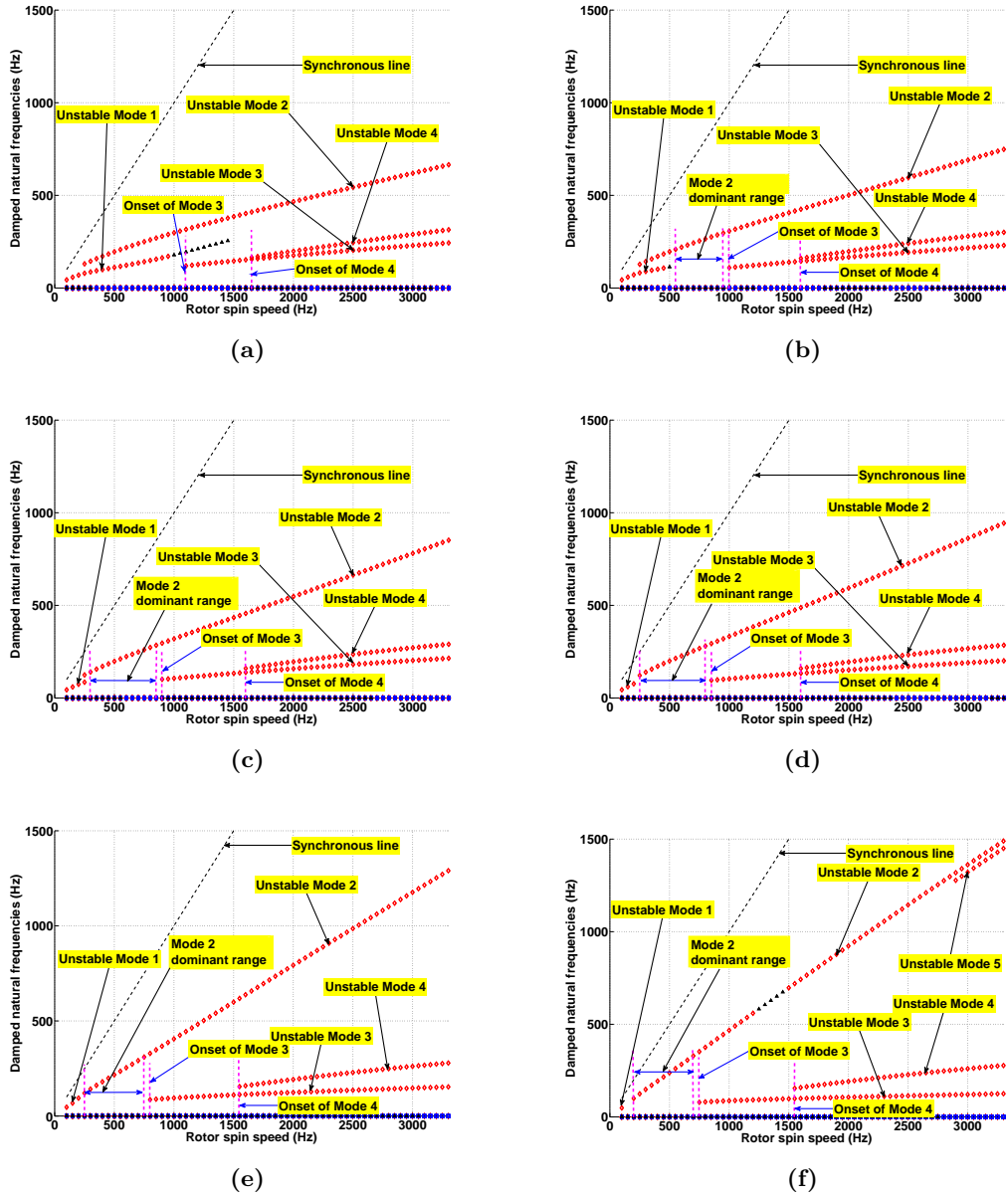


Fig. 2.14. Campbell diagrams (two oil films in series) with the identically varying FRB outer clearances: (a) 30 μm , (b) 35 μm , (c) 40 μm , (d) 44 μm , (e) 60 μm and (f) 74 μm . Forward whirl is diamond; backward whirl is square; mixed whirl is triangle. Both ring speed ratios are assumed to be 0.2.

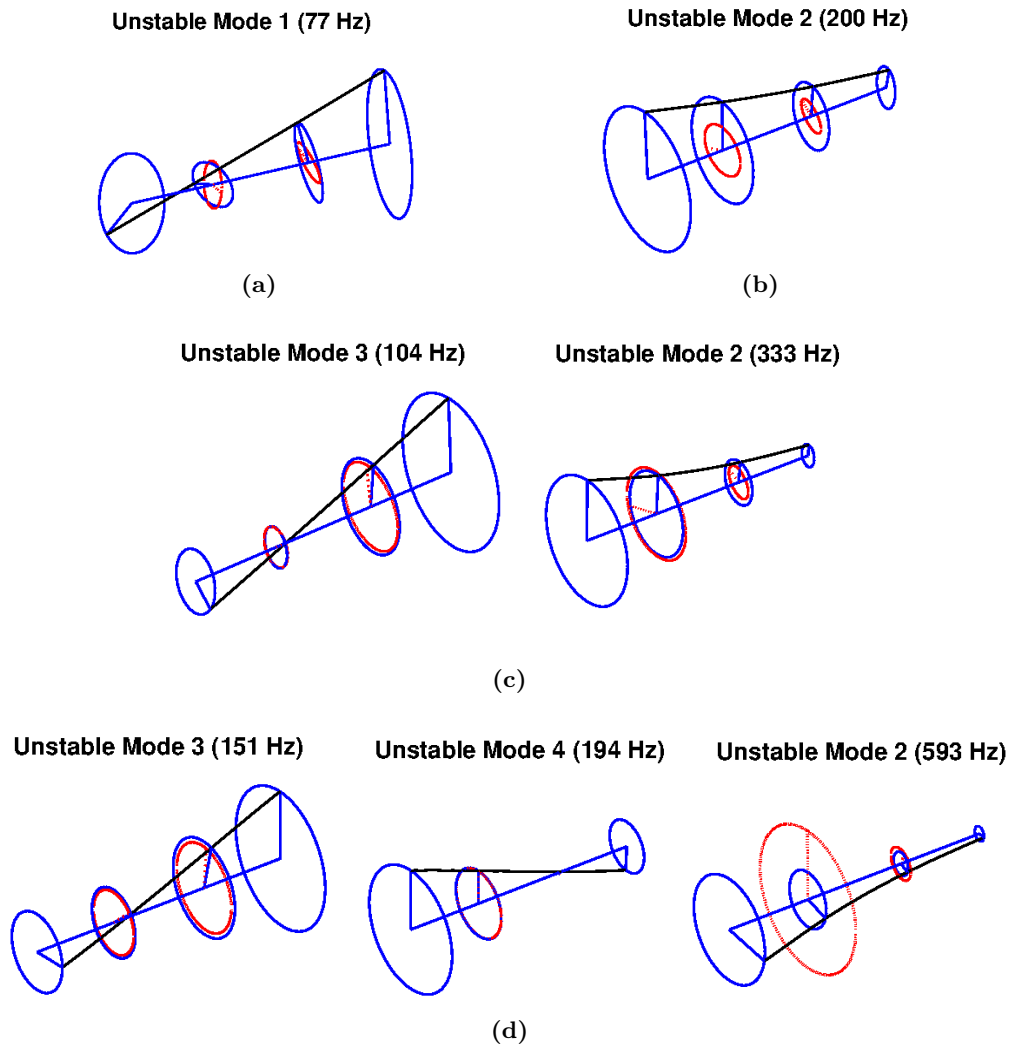


Fig. 2.15. Mode shapes of the unstable modes at four different speeds when both FRB clearances are $44 \mu\text{m}$: (a) 200 Hz, (b) 500 Hz, (c) 1000 Hz and (d) 2000 Hz. The floating ring orbits are represented by the dotted circles, while the dashed lines in mode shapes indicate the positions of the four nodes at a certain moment. Both ring speed ratios are assumed to be 0.2.

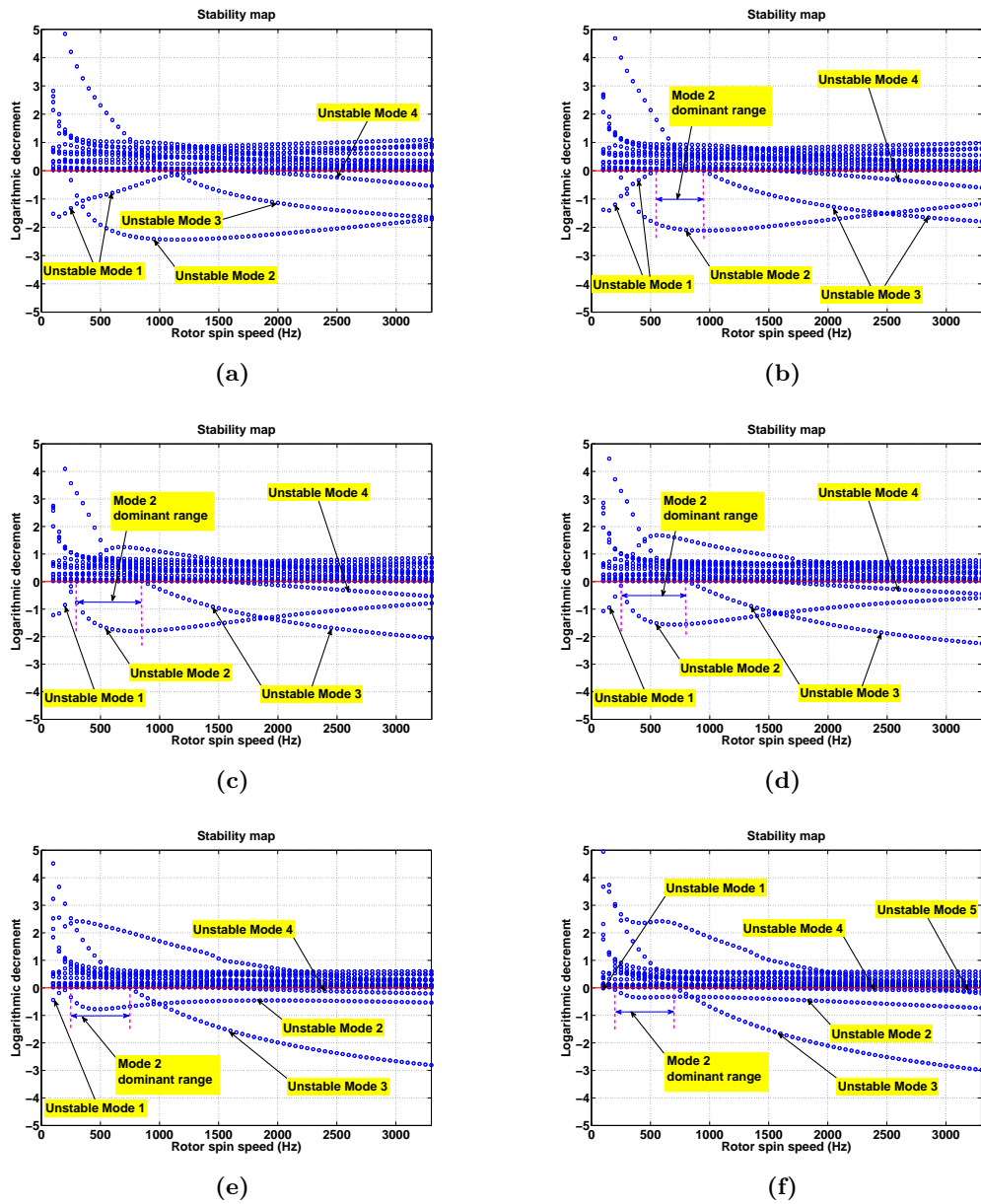


Fig. 2.16. Stability maps with the identically varying FRB outer clearances: (a) 30 μm , (b) 35 μm , (c) 40 μm , (d) 44 μm , (e) 60 μm and (f) 74 μm .

- (a) Fig. 2.14 shows the unstable speed range of Mode 1 can considerably be reduced by increasing the FRB outer clearance. When the outer clearances are 30 μm , Mode 1 is unstable up to 1450 Hz. It is a conical mode as shown in Fig. 2.15a. It should be mentioned that although Fig. 2.15 is obtained when $C_2 = 44 \mu\text{m}$, calculation results show that it can adequately represent the mode shapes of the unstable modes when C_2 is varying in the considered size range. The phases of the two floating rings are also out-of-phase, whereas they are almost 90 degrees behind the phases of the Node 1 and 2 on the rotor shaft. Note that it is changed from forward whirl to mixed whirl at 1000 Hz. This means the whirl directions of the four nodes are not the same. In other words, some portions of the four nodes are in forward whirl, while the others go into backward orbits. Further observations show the orbits at Node 1, 3 and 4 are forward, but the orbit at Node 2 (the location of FRB 1, see Fig. 2.1) is backward with a much smaller amplitude than the other nodes. Although it is counter-intuitive, this phenomenon can appear in a rotor-bearing system as a result of the bearing anisotropic characteristics [1, 27]. The effect of bearing outer clearance on the stability characteristics of Mode 1 can also be appreciated from the stability map plots given in Fig. 2.16, in which the less the logarithmic decrement is, the more likely it is for the unstable mode to be excited in the nonlinear simulations.
- (b) The onset speed of the unstable Mode 2 can hardly be affected by changing the FRB outer clearance, whereas increasing the bearing outer clearance can gradually lift the logarithmic decrement of the unstable Mode 2, which means unstable Mode 2 is weakened by the increase of outer clearance, especially Fig. 2.16e and f. However, owing to the shrink of the unstable Mode 1 caused by the growth of outer clearance, there is a speed range in which only Mode 2 is unstable, as shown in Fig. 2.14b through f as well as Fig. 2.16b-f. It is labelled by “Mode 2 dominant range”, which indicates there might be two nonlinear jumps. The first one is the jump from unstable Mode 1 to unstable Mode 2 at the start of the range. The other is the jump from unstable Mode 2 to unstable Mode 3 at the end of the range. The mode shapes given in Fig. 2.15b through d show Mode 2 is a cylindrical forward mode and the amplitudes of the orbits follow a descending trend along the shaft axis. The orbits of the two floating rings are also in-phase, although they are still 90 degrees behind the shaft orbits. With increasing rotor speed, the amplitude of the floating ring orbit at FRB 1 becomes even higher than all the shaft orbits, which is evident in Fig. 2.15d. In addition, the frequency location of the unstable Mode 2 becomes higher as the

outer clearance becomes wider.

- (c) As can be seen from Fig. 2.15c and d, the unstable Mode 3 is a conical forward mode, but it can clearly be differentiated from the unstable Mode 1, as the ring orbits are almost in phase with the shaft orbits at FRB 1 and FRB 2, respectively. Fig. 2.14 reveals increasing the outer clearance can result in the reduction of the onset speed of unstable Mode 3. Fig. 2.16 shows the increase of outer clearance can generally lower the logarithmic decrement of the unstable Mode 3 as well, which means the unstable Mode 3 is enhanced. Eventually, together with its influence on the logarithmic decrement of the unstable Mode 2, one can see that the intersection of the unstable Mode 2 and 3 becomes earlier with increasing FRB outer clearance. This means that the possibility of the emergence of the unstable Mode 2 is suppressed within the relatively high speed range, and the unstable Mode 3 is very likely to be excited earlier after the intersection.
- (d) Fig. 2.15d additionally shows the unstable Mode 4 is also a conical mode, which becomes unstable at relatively high rotor speeds. The orbits of the two floating rings are still in phase with the corresponding orbits of Node 2 and 3 on the shaft as unstable Mode 3. However, it can readily be distinguished from the unstable Mode 3 by the extremely low amplitudes of the shaft and ring orbits at Node 3. Neither the occurring speed of this unstable mode nor the logarithmic decrement can be significantly affected by the varying bearing outer clearance, which can be appreciated from Fig. 2.14 and Fig. 2.16. Since the unstable Mode 4 is quite close to the stability border, it might not be excited in the nonlinear simulations and experiments.

2.7 Synchronous Response

In this section, based upon the linear model described in Section 2.6.2, 30 μm in-phase unbalance offset is added to the compressor disk and turbine disk, i.e., Node 1 and Node 4, respectively. The computed rotor response of the compressor centre (Node 1) over the considered rotor speed range is shown in Fig. 2.17. It can be seen that the amplitudes of x_1 and y_1 reaches their maxima at 2650 Hz, which should be the critical speed of the investigated system. The calculated results agree well with the Campbell diagram shown in Fig. 2.18, which is the full version of the unstable Campbell diagram given in Fig. 2.14f and shows there is an intersection between the calculated eigenvalues and the synchronous

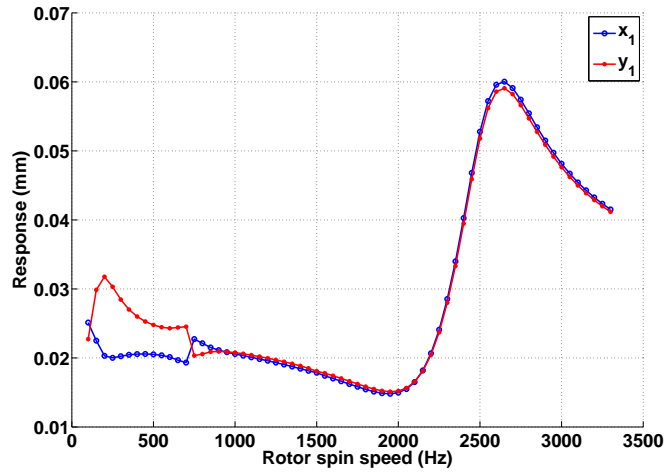


Fig. 2.17. Predicted synchronous response of the compressor centre in the X and the Y directions

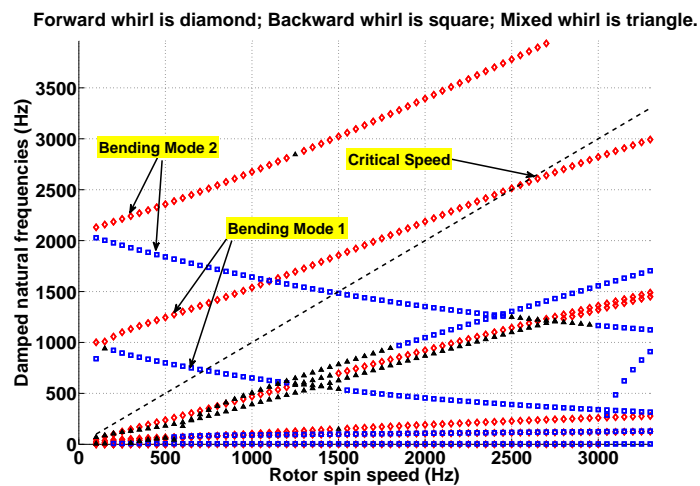


Fig. 2.18. Campbell digram of linearized FRBs when the ring masses are included and the bearing outer clearance is $74 \mu\text{m}$; the dashed line is the synchronous line.

line at 2650 Hz. It is observed that the first bending mode is excited at the critical speed, 2650 Hz. At lower rotor speeds, due to the complexity introduced by the linearization of FRBs, no noticeable critical speed is obtained.

Chapter 3

Stationary Nonlinear Analysis

The calculation of nonlinear oil-film forces at each time step is the heart of TC nonlinear rotordynamic analysis. Currently, the finite bearing solutions, i.e. the finite difference method and the finite element method, can produce the most accurate results, although the calculation process is quite time consuming. Alternatively, based upon the short-bearing approximation, the desired bearing forces can be obtained and expressed in a closed form, which can significantly reduce the computation time, and ensure sufficient accuracy [11, 43, 57, 75]. A newly proposed nonlinear FRB model extended from Capone’s journal bearing model [2, 18] is presented in Section 3.1. The governing equations of motion of the two floating rings are introduced in Section 3.2. In Section 3.3 the model detailed in Section 3.1 is validated through comparisons with the results shown in Refs. [11, 59]. In-phase unbalance is added to the compressor disk and the turbine disk of the finite element model in Section 3.4 to preliminarily investigate the influence of unbalance on the system response. The results shown in Section 3.3 and Section 3.4 are obtained at constant rotor speeds, which, in other words, means the rotor speed variation is not considered. Therefore, the nonlinear analysis shown in this chapter is termed “Stationary Nonlinear Analysis”.

3.1 Nonlinear FRB Model

The FRB model described in this section has been previously presented and validated in Ref. [95]. The model is developed from Capone’s method applied to normal journal bearings and elliptical bearings whose validity and efficiency have been proved and confirmed in Ref. [2, 3, 101]. Meanwhile, in Ref. [75], Rübél concludes that the short journal bearing model is a good compromise after comparison with results obtained from more

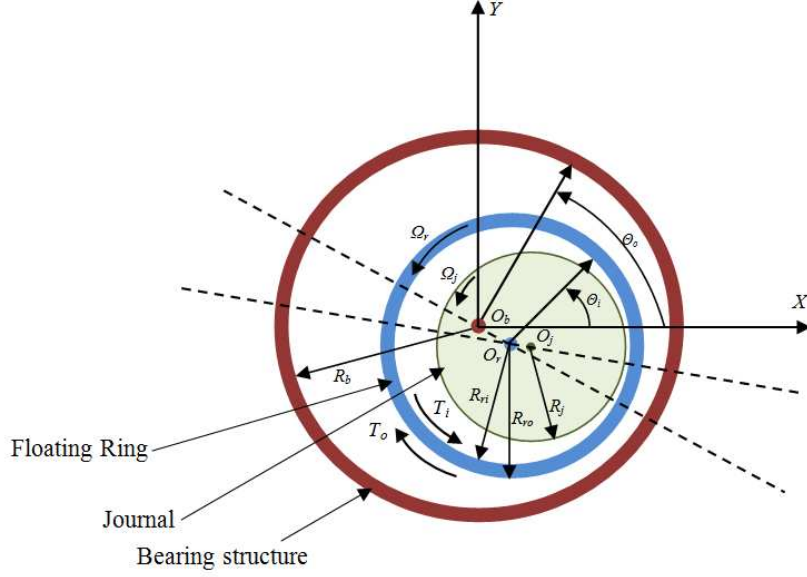


Fig. 3.1. FRB middle plane and reference frame

time-consuming finite bearing solutions, i.e. finite element method as well as finite difference method. Recently, the FRB model based upon the short journal bearing theory developed by Inagaki et al. [43] shows that the obtained results agree with the experimental results quite well. In addition, the capability of Capone's method to be used in rotor-journal bearing system rundown simulations is shown in Ref. [23]. Therefore, the proposed model is entirely feasible to carry out the nonlinear rotordynamic analysis for the described rotor-FRB system in Section 2.1.

Fig. 3.1 shows the cross section at the middle plane of one of the two identical FRBs. The fixed reference frame O_bXYZ is in agreement with the inertia frame given in Fig. 2.1, where O_b denotes the bearing origin. The O_bZ axis cannot be shown as it is perpendicular to the depicted plane. For the purpose of simplicity, the bearing feeding holes are not included in Fig. 3.1 and the oil feeding conditions will not be considered in the FRB model. The variations of oil feeding pressure and temperature can lead to the changes of onset speeds of relevant nonlinear jumps and possibly to the occurrence of new subsynchronous component. For more detailed information, the reader is referred to Refs. [72, 87, 88, 100]. In addition, the isothermal fluid flow condition is assumed for the proposed model. Corresponding to the reference frame, the Reynolds equations for the inner and outer oil films can be written as follows [93]:

$$\frac{1}{R_j^2} \frac{\partial}{\partial \Theta_i} \left(\frac{h_i^3}{12\mu_i} \frac{\partial p_i}{\partial \Theta_i} \right) + \frac{\partial}{\partial Z_i} \left(\frac{h_i^3}{12\mu_i} \frac{\partial p_i}{\partial Z_i} \right) = \frac{\Omega_j + \Omega_r}{2} \frac{\partial h_i}{\partial \Theta_i} + \frac{\partial h_i}{\partial t} \quad (3.1a)$$

$$\frac{1}{R_{ro}^2} \frac{\partial}{\partial \Theta_o} \left(\frac{h_o^3}{12\mu_o} \frac{\partial p_o}{\partial \Theta_o} \right) + \frac{\partial}{\partial Z_o} \left(\frac{h_o^3}{12\mu_o} \frac{\partial p_o}{\partial Z_o} \right) = \frac{\Omega_r}{2} \frac{\partial h_o}{\partial \Theta_o} + \frac{\partial h_o}{\partial t} \quad (3.1b)$$

where the subscripts i and o identify the parameters of the inner oil film and outer oil film, respectively. The subscripts j and r distinguish the parameters between journal and floating ring. p is the oil film pressure, and μ denotes the lubricating oil viscosity. R_j and R_{ro} correspond to the journal radius and floating ring outer radius, respectively. Since the inner film radial clearance $C_1 \ll R_j$, the difference between R_j and the floating ring inner radius R_{ri} is considered negligible. Θ is the angular coordinate for the inner and outer oil films corresponding to the fixed frame given in Fig. 3.1. Z_i and Z_o denote the axial coordinates of the inner and outer films, respectively. Ω denotes the angular velocity of the journal and ring. The oil film thicknesses h_i , h_o and the squeezed terms $\partial h_i/\partial t$, $\partial h_o/\partial t$ can be expressed by coordinates as follows.

$$h_i(\Theta_i, t) = C_1 - x_j \cos \Theta_i - y_j \sin \Theta_i \quad (3.2a)$$

$$h_o(\Theta_o, t) = C_2 - X_r \cos \Theta_o - Y_r \sin \Theta_o \quad (3.2b)$$

$$\frac{\partial h_i}{\partial t} = -(\dot{x}_j \cos \Theta_i + \dot{y}_j \sin \Theta_i) \quad (3.2c)$$

$$\frac{\partial h_o}{\partial t} = -(\dot{X}_r \cos \Theta_o + \dot{Y}_r \sin \Theta_o) \quad (3.2d)$$

$$x_j = X_j - X_r \quad (3.2e)$$

$$y_j = Y_j - Y_r \quad (3.2f)$$

$$\dot{x}_j = \dot{X}_j - \dot{X}_r \quad (3.2g)$$

$$\dot{y}_j = \dot{Y}_j - \dot{Y}_r \quad (3.2h)$$

where C_1 and C_2 represent the radial clearance of the inner and outer oil film, respectively. As shown in Fig. 3.1, (X_j, Y_j) are the displacement vector of the journal center O_j in the

fixed reference frame. They are equivalent to the coordinates (x_2, y_2) , (x_3, y_3) in Eq. (2.1) for the nodes where the two FRBs are located. (X_r, Y_r) are the absolute displacement components of the floating ring center O_r . (\dot{X}_j, \dot{Y}_j) and (\dot{X}_r, \dot{Y}_r) are the absolute velocities of O_j and O_r , while the lowercase letters (x_j, y_j) , (\dot{x}_j, \dot{y}_j) denote the displacement and velocity components of O_j relative to O_r .

Therefore, following the given symbol definition, the inner film eccentricity ϵ_i and outer film eccentricity ϵ_o are developed as

$$\epsilon_i = \frac{\sqrt{x_j^2 + y_j^2}}{C_1}, \quad \epsilon_o = \frac{\sqrt{X_r^2 + Y_r^2}}{C_2} \quad (3.3)$$

With the assumption of iso-viscous Newtonian lubricating oil and the infinite short bearing theory for both films, the analytical solution of the Reynolds Eqs. (3.1a) and (3.1b) can be simplified as follows:

$$\frac{\partial}{\partial Z_i} \left(\frac{h_i^3}{12\mu_i} \frac{\partial p_i}{\partial Z_i} \right) = \frac{\Omega_j + \Omega_r}{2} \frac{\partial h_i}{\partial \Theta_i} + \frac{\partial h_i}{\partial t} \quad (3.4a)$$

$$\frac{\partial}{\partial Z_o} \left(\frac{h_o^3}{12\mu_o} \frac{\partial p_o}{\partial Z_o} \right) = \frac{\Omega_r}{2} \frac{\partial h_o}{\partial \Theta_o} + \frac{\partial h_o}{\partial t} \quad (3.4b)$$

Using the Eqs. (3.2a) to (3.2d) to substitute the oil film thicknesses and squeeze terms in above Eqs. (3.4a) and (3.4b), they can also be expressed in the following format:

$$\begin{aligned} \frac{\partial^2 p_i}{\partial Z_i^2} &= \frac{6\mu_i}{(C_1 - x_j \cos \Theta_i - y_j \sin \Theta_i)^3} \\ &\cdot \{[(\Omega_j + \Omega_r) x_j - 2\dot{y}_j] \sin \Theta_i - [(\Omega_j + \Omega_r) y_j + 2\dot{x}_j] \cos \Theta_i\} \end{aligned} \quad (3.5a)$$

$$\begin{aligned} \frac{\partial^2 p_o}{\partial Z_o^2} &= \frac{6\mu_o}{(C_2 - X_r \cos \Theta_o - Y_r \sin \Theta_o)^3} \\ &\cdot \left[(\Omega_r X_r - 2\dot{Y}_r) \sin \Theta_o - (\Omega_r Y_r + 2\dot{X}_r) \cos \Theta_o \right] \end{aligned} \quad (3.5b)$$

The boundary conditions for Eqs. (3.5a) and (3.5b) are given as follows.

$$p_i \left(\Theta_i, Z_i = -\frac{L_i}{2} \right) = p_i \left(\Theta_i, Z_i = +\frac{L_i}{2} \right) = 0 \quad (3.6a)$$

$$p_o \left(\Theta_o, Z_o = -\frac{L_o}{2} \right) = p_o \left(\Theta_o, Z_o = +\frac{L_o}{2} \right) = 0 \quad (3.6b)$$

where L_i and L_o denote the inner bearing length and outer bearing length, respectively.

Therefore, the analytical form of p_i and p_o in Eqs. (3.5a) and (3.5b) can be obtained by integration as

$$p_i = \frac{3\mu_i}{h_i^3} \left(Z_i^2 - \frac{L_i^2}{4} \right) \{ [(\Omega_j + \Omega_r) x_j - 2\dot{y}_j] \sin \Theta_i - [(\Omega_j + \Omega_r) y_j + 2\dot{x}_j] \cos \Theta_i \} \quad (3.7a)$$

$$p_o = \frac{3\mu_o}{h_o^3} \left(Z_o^2 - \frac{L_o^2}{4} \right) [(\Omega_r X_r - 2\dot{Y}_r) \sin \Theta_o - (\Omega_r Y_r + 2\dot{X}_r) \cos \Theta_o] \quad (3.7b)$$

For numerical calculation, Eqs. (3.7a) and (3.7b) are non-dimensionalized by introducing the following dimensionless variables:

$$\bar{x}_j = \frac{x_j}{C_1}, \bar{y}_j = \frac{y_j}{C_1}, \bar{z}_i = \frac{Z_i}{L_i}, \bar{x}'_j = \frac{\dot{x}_j}{C_1(\Omega_j + \Omega_r)}, \bar{y}'_j = \frac{\dot{y}_j}{C_1(\Omega_j + \Omega_r)}, \bar{p}_i = \frac{p_i}{6\mu_i(\Omega_j + \Omega_r)(R_j/C_1)^2}$$

$$\bar{x}_r = \frac{X_r}{C_2}, \bar{y}_r = \frac{Y_r}{C_2}, \bar{z}_o = \frac{Z_o}{L_o}, \bar{x}'_r = \frac{\dot{X}_r}{C_2\Omega_r}, \bar{y}'_r = \frac{\dot{Y}_r}{C_2\Omega_r}, \bar{p}_o = \frac{p_o}{6\mu_o\Omega_r(R_{ro}/C_2)^2}$$

Accordingly, the dimensionless inner and outer oil film pressure can be given as follows.

$$\bar{p}_i = \frac{1}{2} \frac{L_i^2}{D_j^2} \frac{(4\bar{z}_i^2 - 1)[(\bar{x}_j - 2\bar{y}'_j) \sin \Theta_i - (\bar{y}_j + 2\bar{x}'_j) \cos \Theta_i]}{(1 - \bar{x}_j \cos \Theta_i - \bar{y}_j \sin \Theta_i)^3} \quad (3.8a)$$

$$\bar{p}_o = \frac{1}{2} \frac{L_o^2}{D_{ro}^2} \frac{(4\bar{z}_o^2 - 1)[(\bar{x}_r - 2\bar{y}'_r) \sin \Theta_o - (\bar{y}_r + 2\bar{x}'_r) \cos \Theta_o]}{(1 - \bar{x}_r \cos \Theta_o - \bar{y}_r \sin \Theta_o)^3} \quad (3.8b)$$

where D_j and D_{ro} denote journal diameter and ring outer diameter, respectively.

The oil film extension for integrating Eqs. (3.8a) and (3.8b) to develop the desired oil film forces is assumed to be located at the intervals $(\alpha_i, \alpha_i + \pi)$ of the angular coordinate Θ_i for the inner film and $(\alpha_o, \alpha_o + \pi)$ of the angular coordinate Θ_o for the outer film. The angles α_i and α_o can be defined as [2]

$$\alpha_i = \arctan \frac{\bar{y}_j + 2\bar{x}'_j}{\bar{x}_j - 2\bar{y}'_j} - \frac{\pi}{2} \operatorname{sgn} \left(\frac{\bar{y}_j + 2\bar{x}'_j}{\bar{x}_j - 2\bar{y}'_j} \right) - \frac{\pi}{2} \operatorname{sgn} (\bar{y}_j + 2\bar{x}'_j) \quad (3.9a)$$

$$\alpha_o = \arctan \frac{\bar{y}_r + 2\bar{x}'_r}{\bar{x}_r - 2\bar{y}'_r} - \frac{\pi}{2} \operatorname{sgn} \left(\frac{\bar{y}_r + 2\bar{x}'_r}{\bar{x}_r - 2\bar{y}'_r} \right) - \frac{\pi}{2} \operatorname{sgn} (\bar{y}_r + 2\bar{x}'_r) \quad (3.9b)$$

Subsequently, the dimensionless oil film forces can be developed following the method described in Ref. [2] as follows.

For the inner oil film, the forces

$$\begin{aligned} \begin{Bmatrix} f_{i_x} \\ f_{i_y} \end{Bmatrix} &= - \frac{\sqrt{(\bar{y}_j + 2\bar{x}'_j)^2 + (\bar{x}_j - 2\bar{y}'_j)^2}}{1 - \bar{x}_j^2 - \bar{y}_j^2} \\ &\cdot \begin{Bmatrix} 3\bar{x}_j \cdot V_i(\bar{x}_j, \bar{y}_j, \alpha_i) - \sin \alpha_i \cdot G_i(\bar{x}_j, \bar{y}_j, \alpha_i) - 2 \cos \alpha_i \cdot S_i(\bar{x}_j, \bar{y}_j, \alpha_i) \\ 3\bar{y}_j \cdot V_i(\bar{x}_j, \bar{y}_j, \alpha_i) + \cos \alpha_i \cdot G_i(\bar{x}_j, \bar{y}_j, \alpha_i) - 2 \sin \alpha_i \cdot S_i(\bar{x}_j, \bar{y}_j, \alpha_i) \end{Bmatrix} \end{aligned} \quad (3.10a)$$

For the outer oil film, the forces

$$\begin{aligned} \begin{Bmatrix} f_{o_x} \\ f_{o_y} \end{Bmatrix} &= - \frac{\sqrt{(\bar{y}_r + 2\bar{x}'_r)^2 + (\bar{x}_r - 2\bar{y}'_r)^2}}{1 - \bar{x}_r^2 - \bar{y}_r^2} \\ &\cdot \begin{Bmatrix} 3\bar{x}_r \cdot V_o(\bar{x}_r, \bar{y}_r, \alpha_o) - \sin \alpha_o \cdot G_o(\bar{x}_r, \bar{y}_r, \alpha_o) - 2 \cos \alpha_o \cdot S_o(\bar{x}_r, \bar{y}_r, \alpha_o) \\ 3\bar{y}_r \cdot V_o(\bar{x}_r, \bar{y}_r, \alpha_o) + \cos \alpha_o \cdot G_o(\bar{x}_r, \bar{y}_r, \alpha_o) - 2 \sin \alpha_o \cdot S_o(\bar{x}_r, \bar{y}_r, \alpha_o) \end{Bmatrix} \end{aligned} \quad (3.10b)$$

Corresponding to inner and outer oil films with the subscripts i and o , the functions $V_i, V_o, G_i, G_o, S_i, S_o$ can be further described as

$$G_i(\bar{x}_j, \bar{y}_j, \alpha_i) = \frac{2}{\sqrt{1 - \bar{x}_j^2 - \bar{y}_j^2}} \left(\frac{\pi}{2} + \arctan \frac{\bar{y}_j \cos \alpha_i - \bar{x}_j \sin \alpha_i}{\sqrt{1 - \bar{x}_j^2 - \bar{y}_j^2}} \right) \quad (3.11a)$$

$$G_o(\bar{x}_r, \bar{y}_r, \alpha_o) = \frac{2}{\sqrt{1 - \bar{x}_r^2 - \bar{y}_r^2}} \left(\frac{\pi}{2} + \arctan \frac{\bar{y}_r \cos \alpha_o - \bar{x}_r \sin \alpha_o}{\sqrt{1 - \bar{x}_r^2 - \bar{y}_r^2}} \right) \quad (3.11b)$$

$$V_i(\bar{x}_j, \bar{y}_j, \alpha_i) = \frac{2 + (\bar{y}_j \cos \alpha_i - \bar{x}_j \sin \alpha_i) \cdot G_i(\bar{x}_j, \bar{y}_j, \alpha_i)}{1 - \bar{x}_j^2 - \bar{y}_j^2} \quad (3.12a)$$

$$V_o(\bar{x}_r, \bar{y}_r, \alpha_o) = \frac{2 + (\bar{y}_r \cos \alpha_o - \bar{x}_r \sin \alpha_o) \cdot G_o(\bar{x}_r, \bar{y}_r, \alpha_o)}{1 - \bar{x}_r^2 - \bar{y}_r^2} \quad (3.12b)$$

$$S_i(\bar{x}_j, \bar{y}_j, \alpha_i) = \frac{\bar{x}_j \cos \alpha_i + \bar{y}_j \sin \alpha_i}{1 - (\bar{x}_j \cos \alpha_i + \bar{y}_j \sin \alpha_i)^2} \quad (3.13a)$$

$$S_o(\bar{x}_r, \bar{y}_r, \alpha_o) = \frac{\bar{x}_r \cos \alpha_o + \bar{y}_r \sin \alpha_o}{1 - (\bar{x}_r \cos \alpha_o + \bar{y}_r \sin \alpha_o)^2} \quad (3.13b)$$

The real oil film forces can be obtained through the following equations:

$$\begin{Bmatrix} F_{i_x} \\ F_{i_y} \end{Bmatrix} = \mu_i(\Omega_j + \Omega_r)R_jL_i \left(\frac{R_j}{C_1}\right)^2 \left(\frac{L_i}{2R_j}\right)^2 \cdot \begin{Bmatrix} f_{i_x} \\ f_{i_y} \end{Bmatrix} \quad (3.14a)$$

$$\begin{Bmatrix} F_{o_x} \\ F_{o_y} \end{Bmatrix} = \mu_o\Omega_rR_{ro}L_o \left(\frac{R_{ro}}{C_2}\right)^2 \left(\frac{L_o}{2R_{ro}}\right)^2 \cdot \begin{Bmatrix} f_{o_x} \\ f_{o_y} \end{Bmatrix} \quad (3.14b)$$

3.2 Equations of Motion for the Floating Rings

The two floating rings are considered as rigid bodies, and equations of motion for one of them are modelled as follows:

$$m_r\ddot{X}_r = F_{o_x} - F_{i_x} \quad (3.15a)$$

$$m_r\ddot{Y}_r = F_{o_y} - F_{i_y} - m_rg \quad (3.15b)$$

$$I_r\dot{\Omega}_r = T_i - T_o \quad (3.15c)$$

where m_r and I_r individually denote the masses and polar moments of inertia of the two floating rings. In Table 2.1c, the subscript c and t of m_r and I_r represents the quantities associated with FRB 1 on the compressor side and FRB 2 on the turbine side, respectively; g is the acceleration of gravity; T_i and T_o are the torques applied to the floating rings derived from the friction of inner and outer films, separately. They can be expressed as follows[11, 17, 74]:

$$T_i = 2\pi \frac{\mu_i R_{ri}^3 L_i (\Omega_j - \Omega_r)}{C_1 \sqrt{1 - \varepsilon_i^2}} + \frac{y_j F_{i_x} - x_j F_{i_y}}{2} \quad (3.16a)$$

$$T_o = 2\pi \frac{\mu_o R_{ro}^3 L_o \Omega_r}{C_2 \sqrt{1 - \varepsilon_o^2}} - \frac{Y_r F_{o_x} - X_r F_{o_y}}{2} \quad (3.16b)$$

where ε_i and ε_o refer to the eccentricity ratio for the journal and floating rings, respectively. R_{ri} denotes the floating ring inner radius.

Rotor parameters		
Rotor mass	$m_{rotor} = 0.5224 \text{ kg}$	
Rotor weight	$W_{rotor} = 5.120 \text{ N}$	
Rotor speed	Ω_{rotor}	
Floating ring parameters		
Ring mass	$m_{ring} = 0.022 \text{ kg}$	
	Inner film	Outer film
Radius	$R_{in} = 5.5 \times 10^{-3} \text{ m}$	$R_{ou} = 7.26 \times 10^{-3} \text{ m}$
Oil film length	$L_{in} = 1.1 \times 10^{-2} \text{ m}$	$L_{ou} = 1.1 \times 10^{-2} \text{ m}$
Clearance	$c_{in} = 3.4 \times 10^{-7} \text{ m}$	$c_{in} = 6.8 \times 10^{-7} \text{ m}$

Table 3.1. Symmetric rigid rotor-FRB system parameters

3.3 Model Validation

3.3.1 Non-dimensional analysis

In order to validate the given FRB model developed in Section 3.1, it is evaluated in the same way as the dimensionless analysis in Ref. [11, 59]. The dimensionless analysis is conducted on a symmetric rigid rotor supported by two identical FRBs at the two ends of the rotor. The parameters of the rotor-FRB system are the same as those in Ref. [11] and listed in Table 3.1. The two non-dimensional parameters λ , ν given in Ref. [59] are rewritten in equations (3.17a) and (3.17b). They are employed to calculate the dynamic response of the symmetric rigid rotor-FRB system. The varying parameter ν has three values, 4.0, 4.5, 5.0, while λ is fixed at 0.1. With each selected ν and the known values in Table 3.1 and the fixed λ , the corresponding values of Ω_{rotor} and oil viscosity μ can be calculated from the relationship defined in equations (3.17a) and (3.17b). Note that the oil viscosities of the inner and outer films are assumed to be the same. After knowing all the parameters in Table 3.1, they are then imported to the nonlinear oil film force model to accomplish the dimensionless analysis. Note that the inner and outer oil films are assumed to have the same value of oil viscosity.

$$\lambda = \frac{\mu}{\pi \sqrt{c_{in} m_{rotor} W_{rotor}}} L_{in} R_{in} \left(\frac{R_{in}}{c_{in}} \right)^2 \left(\frac{L_{in}}{2R_{in}} \right)^2 \quad (3.17a)$$

$$\nu = \Omega_{rotor} \sqrt{\frac{c_{in} m_{rotor}}{W_{rotor}}} \quad (3.17b)$$

The results of the non-dimensional analysis are shown in Fig. 3.2. As all the displacements are defined as non-dimensional to the inner clearance c_{in} , the magnitudes of all the displacements are likely to be greater than one. Despite the slight difference between the results of the current model and those given in Refs. [11, 59], the clearly identified limit cy-

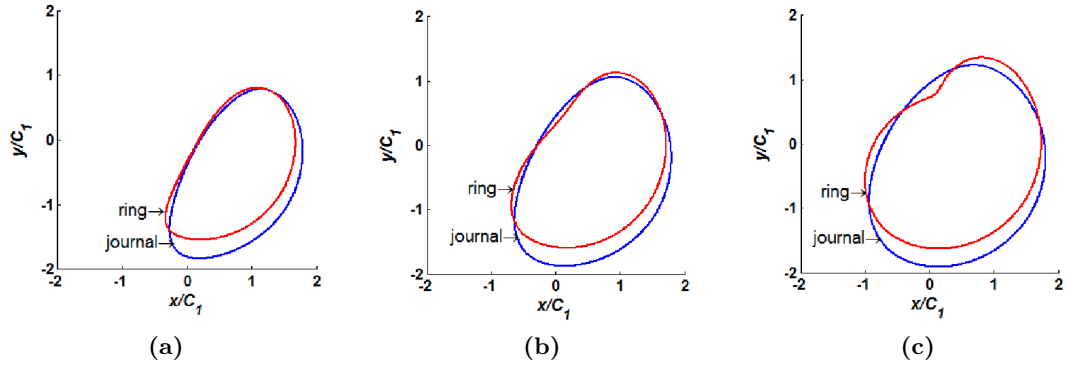


Fig. 3.2. Orbit maps of dimensionless analysis results: (a) $\nu = 4.0$, (b) $\nu = 4.5$ and (c) $\nu = 5.0$.

cles of the journal and ring ensure the validation of the current FRB model. The analytic method detailed in Section 3.1 provides a fast, efficient tool to calculate the demanded forces for the inner and outer oil films.

3.3.2 Perfectly balanced TC rotor

Under the perfectly balanced condition, the dynamic response of the FEM model of the TC rotor-FRB system detailed in Table 2.1 at six different rotor speeds is shown below as a comparison with the model described in Ref. [11]. At each speed, the first 600 revolutions of the rotor response are calculated with appropriate initial conditions set by MATLAB[®] routine `ode15s`[®]. The steady state is assumed to be achieved in the last 100 revolutions, from which the response data are collected and presented in Fig. 3.3. For the results presented in Section 3.4, the same conditions are applied as well.

The results presented in Fig. 3.3b and e show a significant correlation with results at the same speeds given by considering zero cavitation pressure ($p_{cav} = 0$ Pa) in Ref. [11]. Although the orbit maps of TC working at 18000 rpm under zero cavitation pressure were not provided in Ref. [11], it is observed that Fig. 3.3f fully agrees with the orbit map at the same rotational speed when the absolute zero cavitation pressure ($p_{cav} = -1.01 \times 10^5$ Pa) is assumed. Therefore, the current FRB model has been further validated.

Fig. 3.4 presents the non-dimensional waterfall diagrams of Nodes 2 and 3 in the X direction. It can be seen that a dominant subsynchronous component is locked around $0.15\times$, i.e. 0.15 times of rotor speed, throughout the entire rotor speed range. In addition, another subsynchronous component at approximately $0.25\times$ can also be found, although its amplitudes are significantly smaller than those of the $0.15\times$ component. With careful inspection to the waterfall diagram and the mode shape plots, an intriguing phenomenon

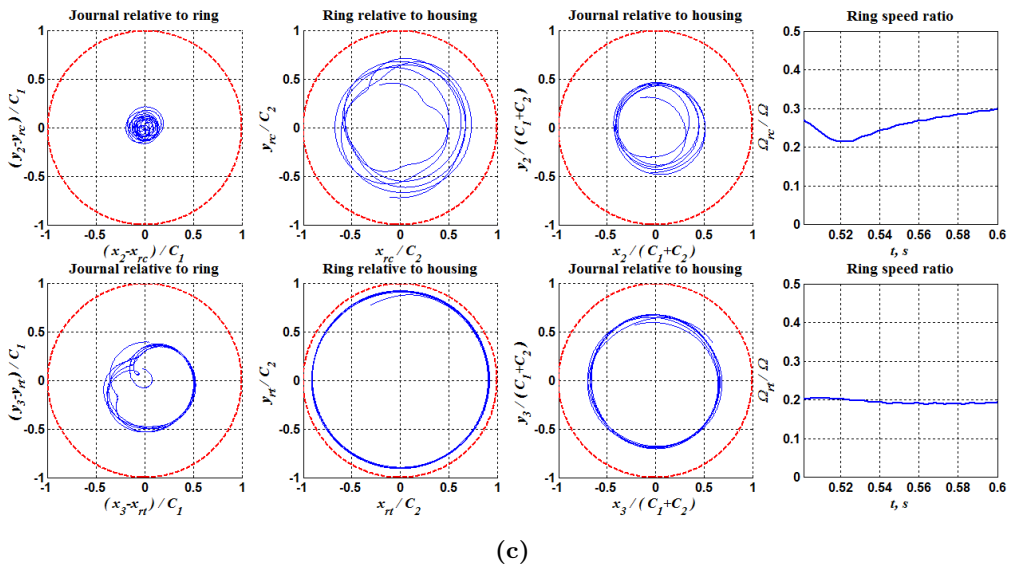
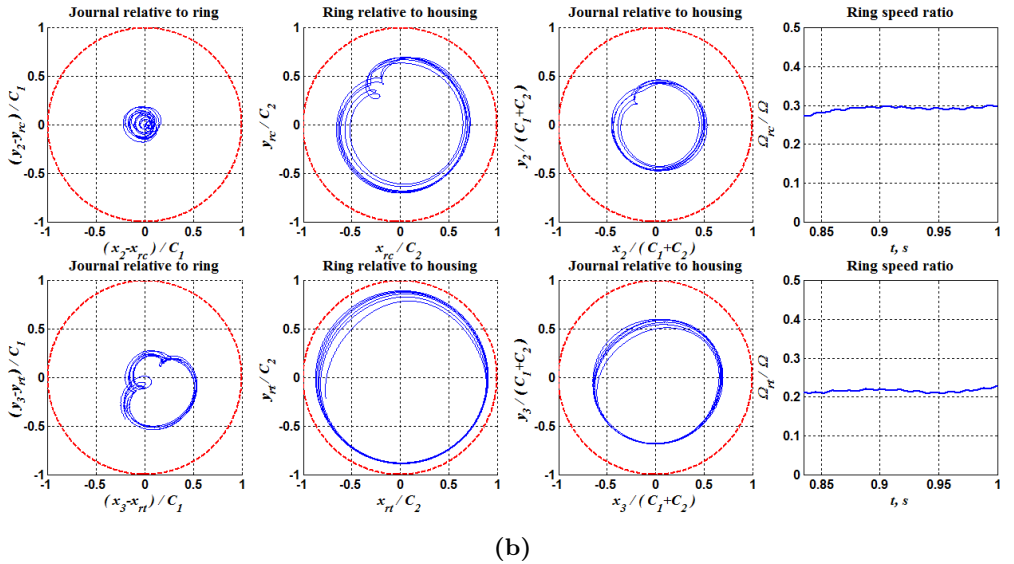
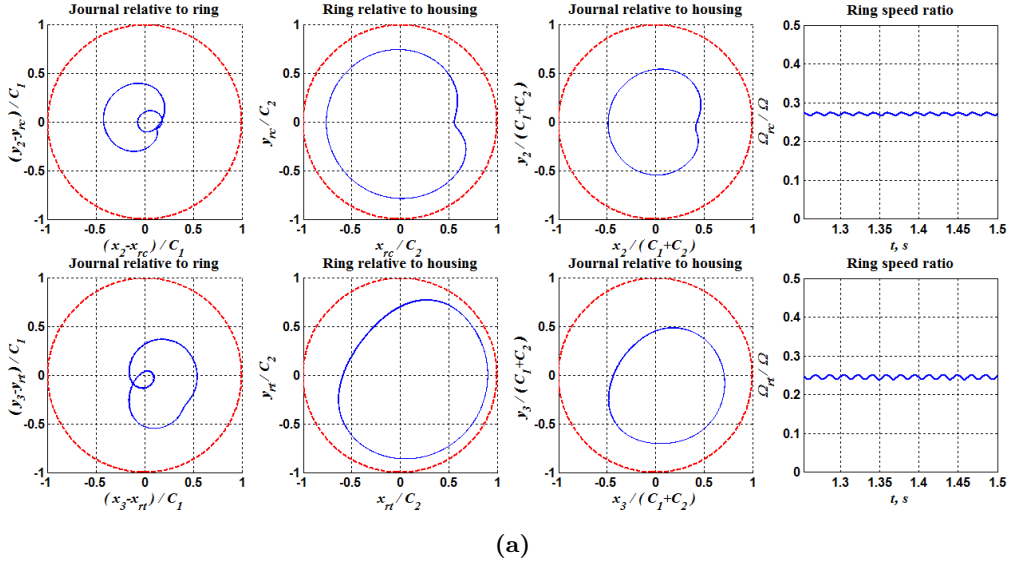


Fig. 3.3. Orbits and ring speed ratios of FRBs without unbalance (FRB1 first row, FRB2 second row), where the outer dashed circles indicate the border of motion. (a) 24,000 rpm, (b) 36,000 rpm, (c) 60,000 rpm, (d) 90,000 rpm, (e) 148,000 rpm and (f) 180,000 rpm.

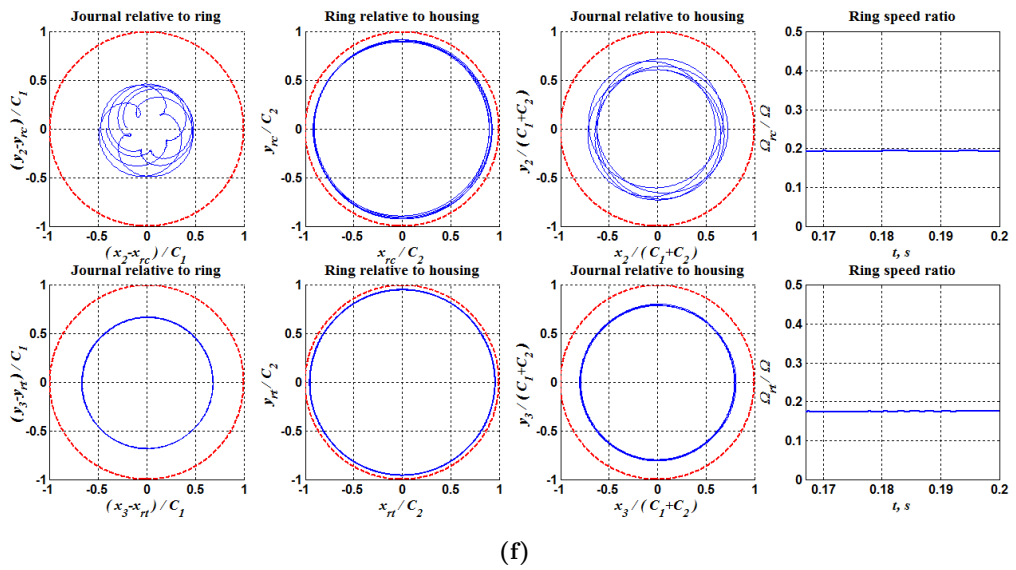
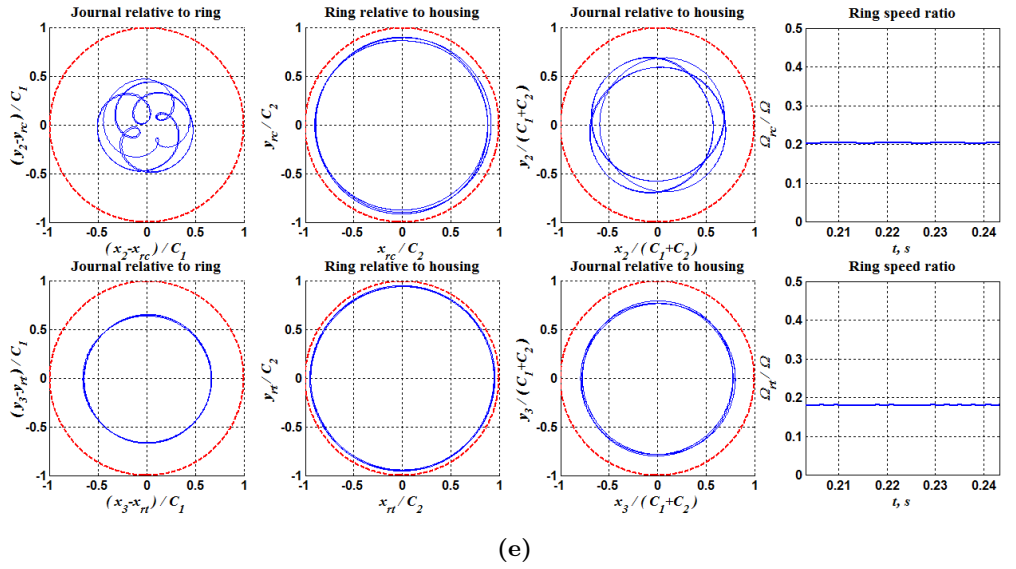
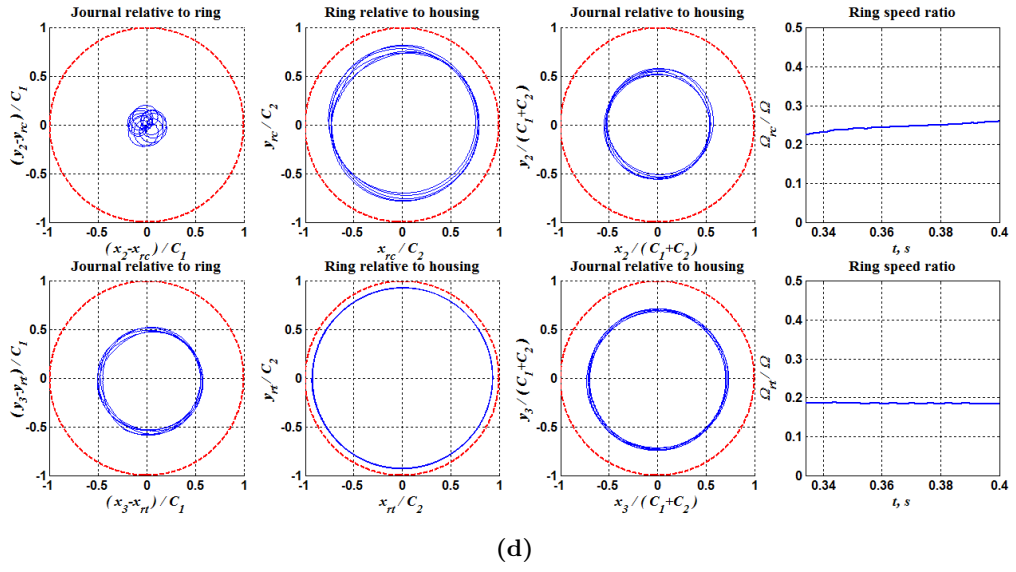
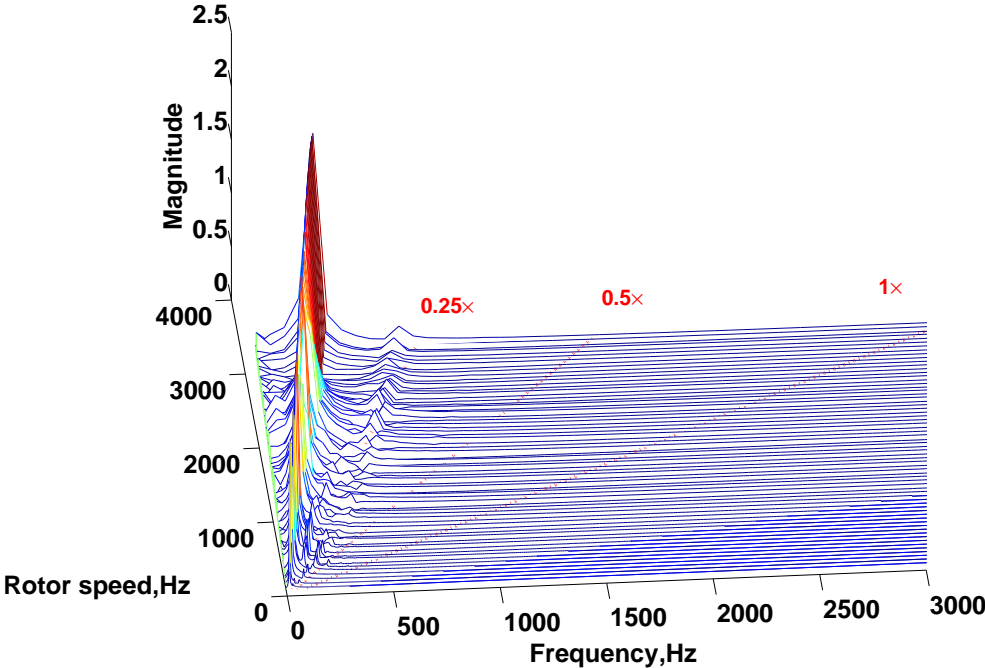
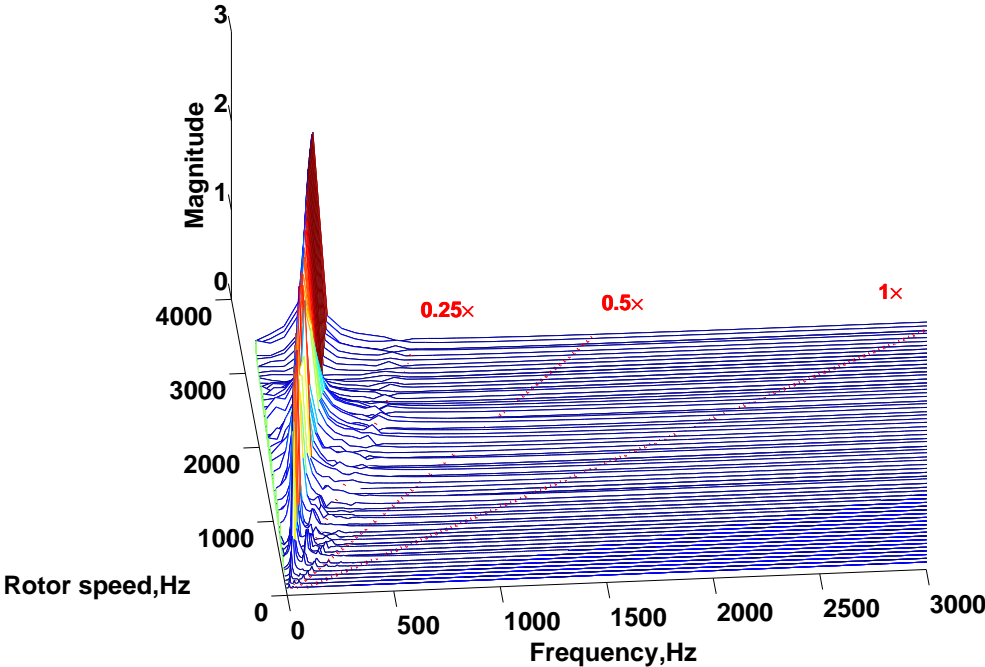


Fig. 3.3. (continued)



(a)



(b)

Fig. 3.4. Waterfall plots under the perfectly balanced condition: (a) x_2/C_1 and (b) x_3/C_1 .

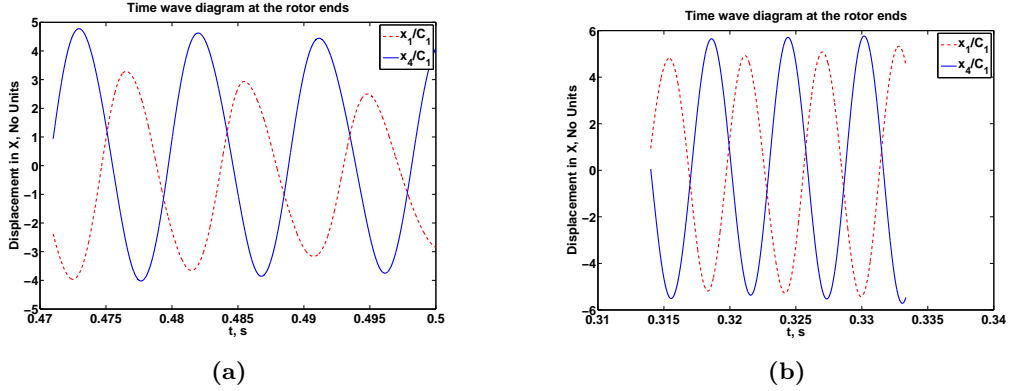


Fig. 3.5. Displacement plot of the two ends of the rotor in the X direction: (a) 60,000 rpm and (b) 90,000 rpm. The dashed line indicates x_1/C_1 ; the solid line indicates x_4/C_1 .

can be observed. In contrast with the linear analysis shown in Section 2.6.2, the $0.15\times$ high amplitude subsynchronous vibrations can be identified as the unstable Mode 3 as shown in Fig. 2.14, although it appears earlier than the linearly predicted results. This might be attributed to the assumption of constant rotor speeds in the nonlinear simulations, and the calculation interval of 600 rotor revolutions provides enough time for the development of limit cycles. The displacement plots of the two ends of the rotor in Fig. 3.5 show the motions of the two ends are out-of-phase by approximately 180 degrees. In other words, one side's top position corresponds to the other's bottom. So far, we can draw the conclusion that, with a perfectly balanced rotor, unstable Mode 3 presented by a conical shape will be excited by the nonlinear subsynchronous vibrations of the FRBs. It appears throughout the operational speed range of the investigated TC. This can be linearly explained by the negative damping effect by the skew-symmetric part of the bearing stiffness matrix on the forward whirling motion. As this destabilizing effect is merely proportional to the whirling orbit area and the stabilizing damping effect is normally proportional to the rotor speed, the lowest-frequency forward whirling mode is usually excited [1].

3.4 Unbalanced TC Rotor

Unbalance as a common defect is usually taken into consideration in rotordynamic analysis. Even though a high degree of balance can be costly achieved in the manufacturing process, the fault derived from unbalance can still be detected during the operation of TC [51, 53]. The unbalance fault can be caused by the oil/dust adhesion and impellers erosion after a period of operation together with the inherent unbalance. Since the data of unbalance is not specified in Ref. [11], as small as $30\ \mu\text{m}$ in-phase unbalance offset is assumed at both

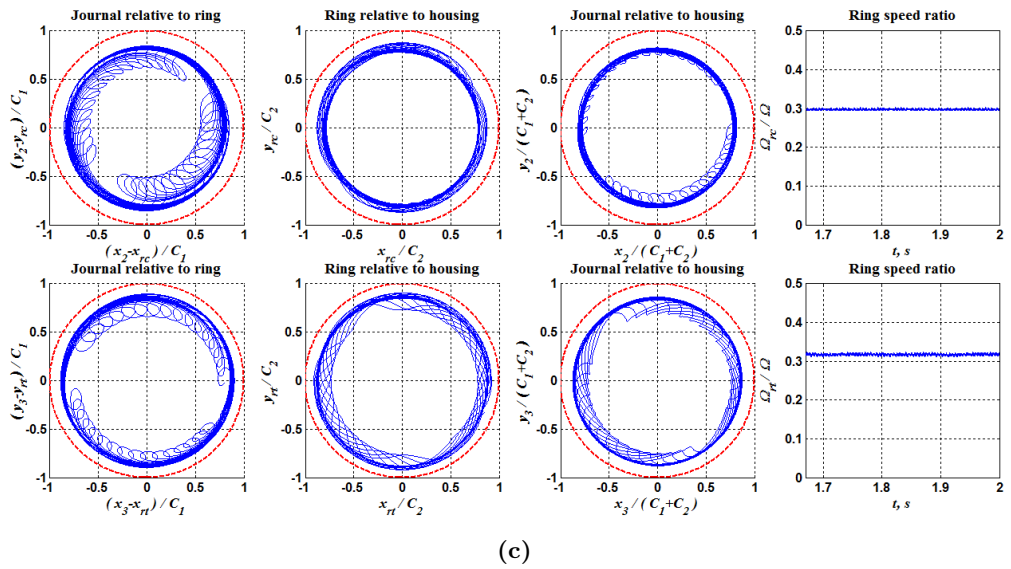
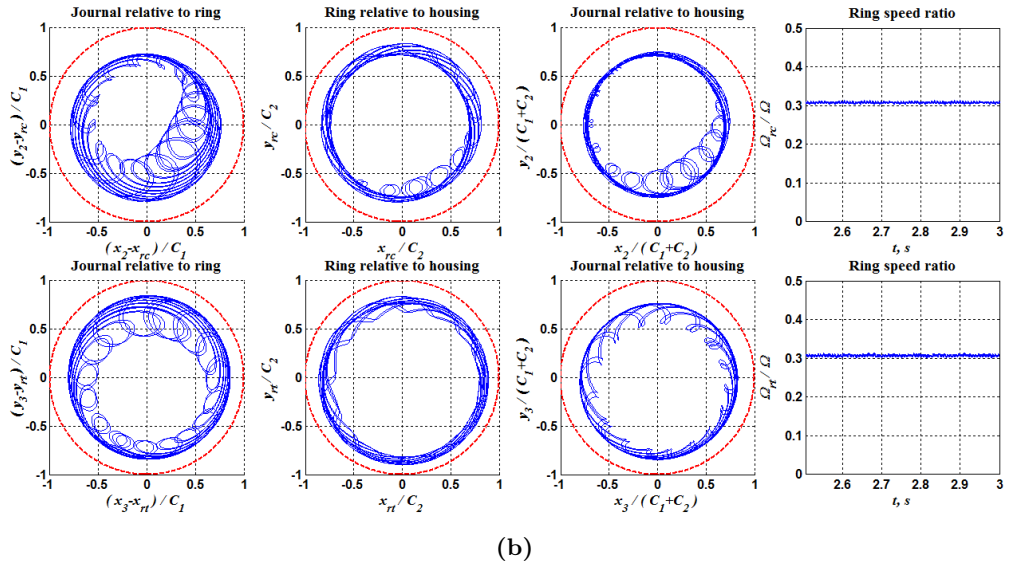
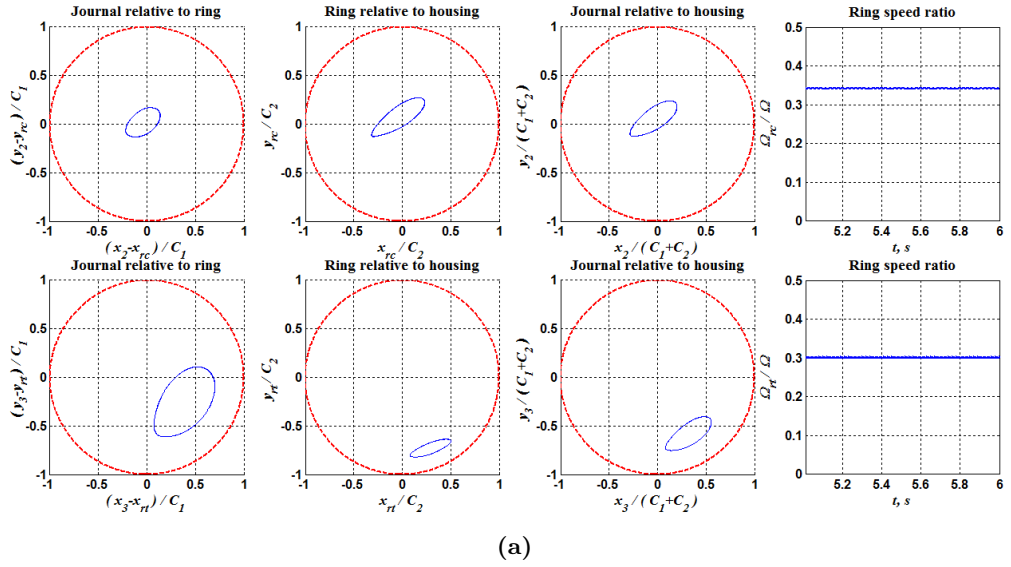


Fig. 3.6. Orbits and ring speed ratios of FRBs subject to unbalance (FRB1 is at first row; FRB2 is at second row), where the outer dashed circles indicate the border of motion. (a) 24,000 rpm, (b) 12,000 rpm, (c) 18,000 rpm, (d) 24,000 rpm, (e) 36,000 rpm, (f) 60,000 rpm, (g) 90,000 rpm, (h) 148,000 rpm and (i) 180,000 rpm.

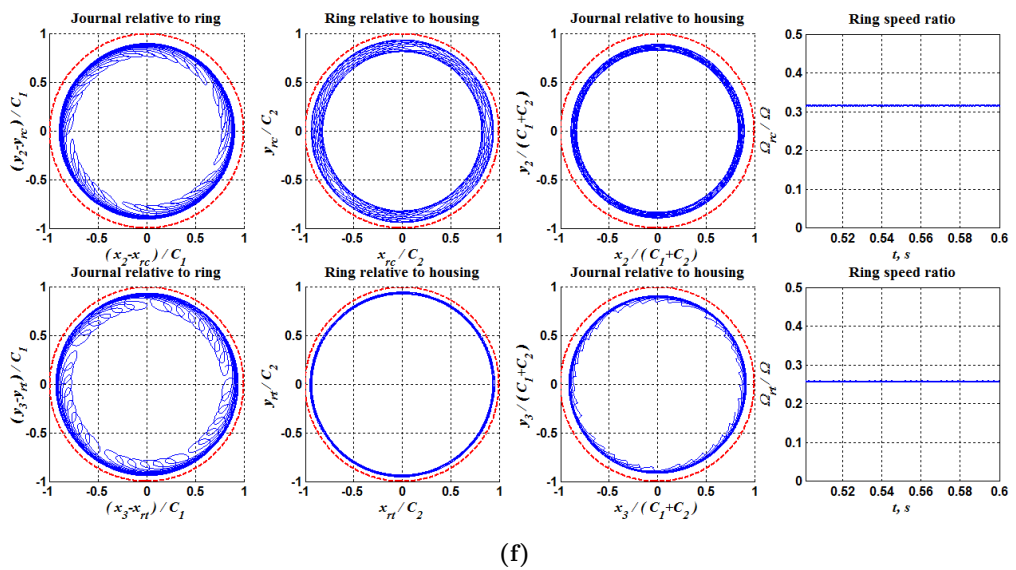
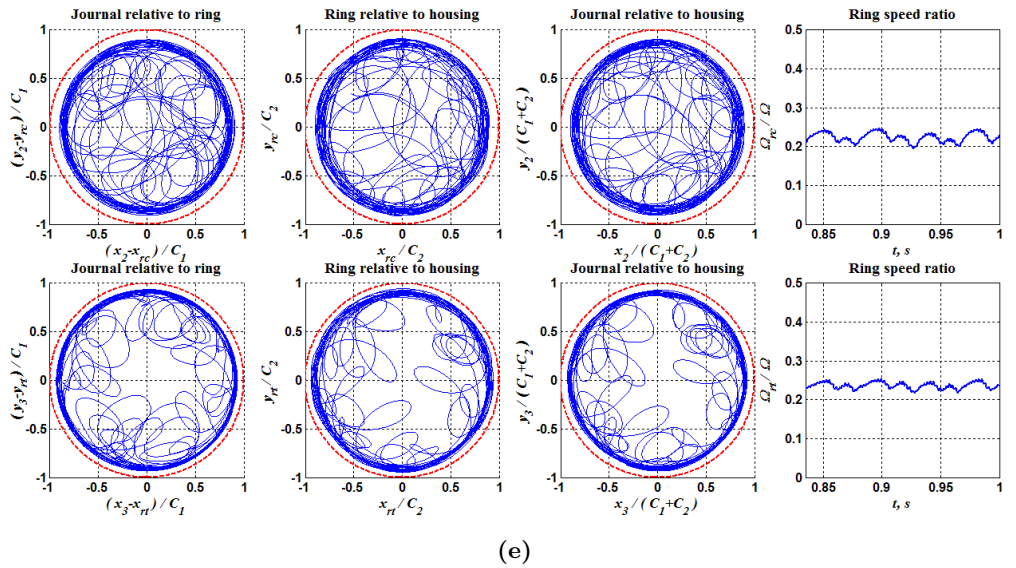
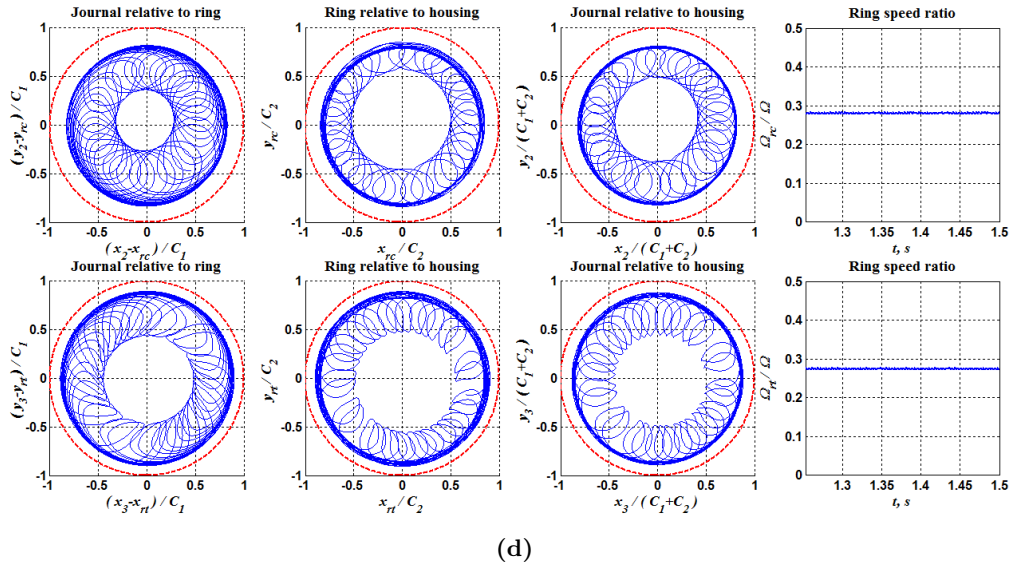


Fig. 3.6. (continued)

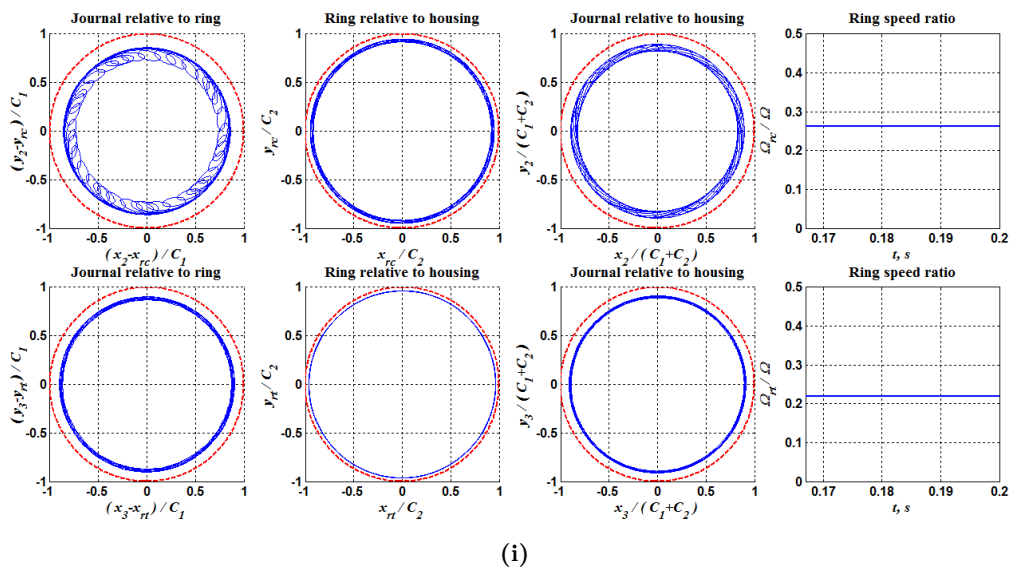
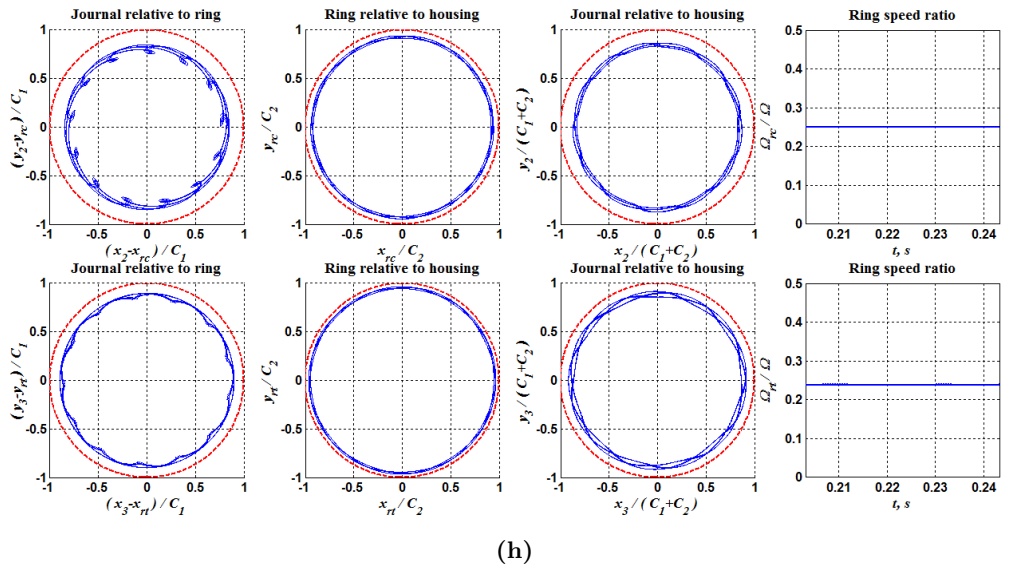
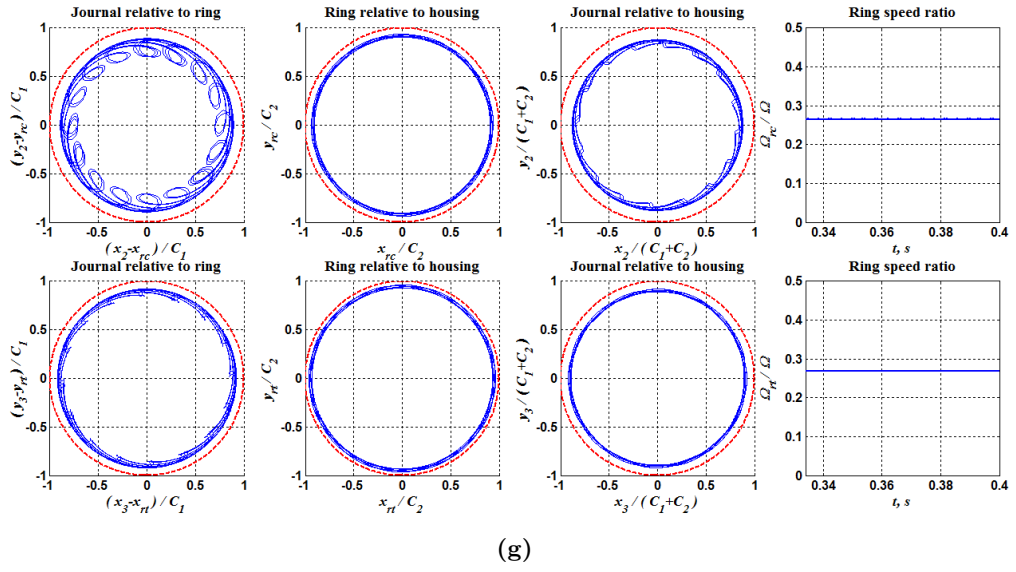
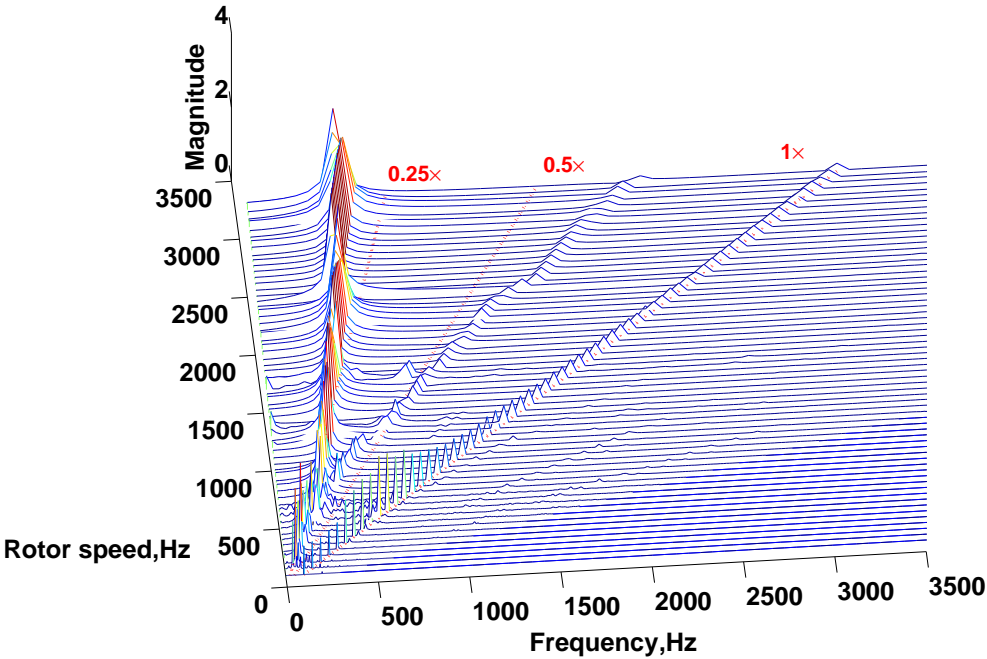
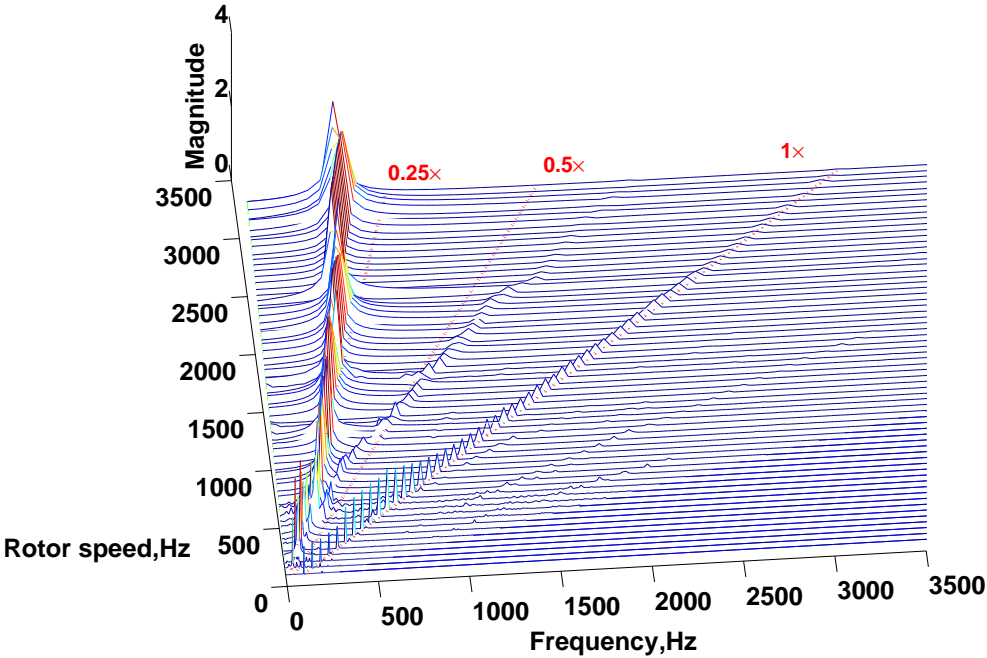


Fig. 3.6. (continued)



(a)



(b)

Fig. 3.7. Waterfall plots at FRB 1 and FRB 2 in the X direction with unbalance: (a) waterfall plot at FRB 1 for x_2/C_1 and (b) waterfall plot at FRB 2 for x_3/C_1 .

the compressor disk and turbine disk as a reasonable value to examine the unbalance effect on the TC rotor behaviour. As can be observed in Fig. 3.6, at a lower operating speed, the unbalance can significantly affect the TC rotor response. At 6000 rpm, the rotor with unbalance undergoes a synchronous whirl (Fig. 3.7), while the subsynchronous component will appear in the situation without unbalance (Fig. 3.4). This means, at a certain speed, the imposed unbalance is able to suppress the sub-synchronous vibrations. Even though the unbalance force imposed on the TC rotor is dramatically increased when the rotor speed moves up, the rotor dynamic response will be dominated by the vibration generated from oil film instability at a higher rotor speed, e.g. 180,000 rpm. The nonlinear effect provided by the inner and outer films will keep the rotor orbiting in the form of limit cycles, which prevent the rotor from undergoing unacceptable large deviation caused by the unbalance force. Even though the TC rotor is operated at a high speed, e.g. 3300 Hz (198,000 rpm), the chaotic motion of the rotor observed in Ref. [102] cannot be identified with the proposed FRB model. This means the results obtained by simplification with the normal journal bearing model in Ref. [102] will deviate from the actual phenomenon held by FRBs, and, therefore, the simplification is not adequate. The above discussion can also be appreciated from the waterfall plots in Fig. 3.7a and b, which clearly show the dominant effect of $0.2\times$ sub-synchronous vibrations along with the increasing rotor speed. The results agree very well with the simulation results given in Ref. [50] and the test results presented in Ref. [38]. Furthermore, the ring speed ratio evidently fluctuates around 0.2 at 36,000 rpm under unbalance. At higher rotor speeds, ring speed ratio becomes stable as without unbalance, whereas its value is kept between 0.2 and 0.3 higher than the results without unbalance.

It can also be seen that, from Fig. 3.7a and b, there are three principal frequency components for the investigated TC rotor-FRB system. The bounded $0.2\times$ sub-synchronous vibrations correspond to the instability developed from the outer oil-films. The frequency is actually higher than the $0.15\times$ component in Fig. 3.4. This may be attributed to the induced imbalance which can affect the whirling shape of the rotor and further the stiffness and damping characteristics of the oil-films. The speed range from 500 Hz to 750 Hz is uncommon in the waterfall diagram. The orbit shapes are quite complex, e.g. Fig. 3.6e, and a frequency spectrum bifurcation will occur. A higher mode will be excited to appear then, and persist until the very end of the considered speed range. A similar type of frequency spectrum bifurcation has been reported in Ref. [87]. The physical parameters of the TC rotor and FRBs should be the determinants of the bifurcation type [87]. It

should be mentioned that the linearly predicted critical speed at 2650 Hz as shown in Fig. 2.17 cannot be identified in Fig. 3.7a and b, as a result of the high amplitude critical limit cycles at the two FRBs, which can stiffen the rotor supports and, therefore, significantly increase the natural frequencies of the higher modes (see Fig. 2.4). The waterfall diagram at FRB 2 is quite similar to the one at FRB 1. Nevertheless, after careful inspection, the slight difference between Fig. 3.7a and b can still be found. In Fig. 3.7b, the $0.5\times$ frequency component almost disappears when the rotor speed approaches the top operating speed 3000 Hz (180,000 rpm). Furthermore, the $1\times$ synchronous response also becomes negligible at the high speed range. The above-mentioned discrepancy may be caused by the heavier static load at the turbine end.

Chapter 4

Effects of Engine Excitation

The TC rotors are normally incorporated by rigid housing connected to the internal combustion engines. The engine induced vibration could place a significant effect on the TC rotor response [60, 79, 102], although FRBs are replaced by two journal bearings in Ref. [102], and a commercial TC-SFRB system is investigated by Maruyama [60], San Andrés et al. [79]. Chapter 4 pioneers the study of the effects of the engine excitation in TC-FRB systems. The modelling of engine vibrations are shown in Section 4.1. Section 4.2 presents the nonlinear simulation results obtained at constant TC rotor speeds.

4.1 Engine Vibration Modelling

For simplicity, the housing can be considered as a rigid body and it moves in the X and Y directions only. The angular movements are neglected. The engine induced vibration will be introduced to the established TC rotor-FRB model only through the FRB-TC support structure connections (Fig. 2.12). In other words, for the oil film force calculation in the outer clearance in Section 3.4, the ring centre velocity (\dot{X}_r, \dot{Y}_r) and displacement (X_r, Y_r) should be redefined as the values relative to the velocity and displacement of the TC housing. From the experimental results of available publications [79, 102], the TC housing displacement can be expressed as a harmonic function of the engine rotating speed ω_e as follows. Note that Eqs. (4.1a) and (4.1b) only consider the housing motions generated from engine's operation, and the more complex state of the road excitation is not considered.

$$X_e = A_{x0} + \sum_{n=1}^N A_{xn} \cos(n\omega_e t + \varphi_{xn}) \quad (4.1a)$$

$$Y_e = A_{y0} + \sum_{n=1}^N A_{yn} \sin(n\omega_e t + \varphi_{yn}) \quad (4.1b)$$

where (X_e, Y_e) denote the housing displacements in the X and the Y directions, respectively. A_{xn} , A_{yn} and φ_{xn} , φ_{yn} are the amplitude and phase angles of the n th order component of the engine crankshaft speed. N is the number of the highest order component. A_{x0} , A_{y0} and φ_{xn} , φ_{yn} can be determined by the initial conditions. In this chapter, the phase angles, i.e. φ_{xn} and φ_{yn} , are assumed to be zero. The velocity components \dot{X}_e , \dot{Y}_e of housing can be simply obtained by derivatives of Eqs. (4.1a) and (4.1b) with respect to time as follows.

$$\dot{X}_e = - \sum_{n=1}^N A_{xn} (n\omega_e) \sin(n\omega_e t + \varphi_{xn}) \quad (4.2a)$$

$$\dot{Y}_e = \sum_{n=1}^N A_{yn} (n\omega_e) \cos(n\omega_e t + \varphi_{yn}) \quad (4.2b)$$

In this chapter, the maximum harmonic components are $4\omega_e$, and the amplitudes of them listed in Table 4.1 are carefully selected referring to the experiment results in Ref. [102] and the FRB parameters in Table 2.1. The $2\omega_e$ and $4\omega_e$ components dominate the engine excitation in the X direction while in the Y direction the largest amplitude is held by the $2\omega_e$ component. The engine is set to work at 3600 rpm ($\omega_e = 60 \times 2\pi$ rad/s) in a full load condition. In reality, the higher engine speed will produce a higher TC rotor speed and the amplitude of the engine frequency harmonic components in Table 4.1 should vary with different engine speed [60]. Nevertheless, for a qualitative investigation, it is still reasonable to assume that the TC rotor of interest operates at low speeds with the same engine excitation inputs as in Table 4.1.

4.2 Stationary Simulation Results

As can be predicted, the engine excitation will definitely change the rotor orbit shape if it is observed in the fixed reference frame XYZ . In order to obtain a deep insight into the response under engine excitation condition, the rotor orbit shapes at FRB 1 and FRB 2 depicted below are observed in a reference frame relative to the TC housing.

Fig. 4.1 shows the orbit maps and ring speed ratios after considering engine excitation effect on the dynamic response of the TC rotor. It can be seen that, at lower speeds, e.g. 24,000 rpm, the orbit shape will be dramatically altered. The introduced engine excitation

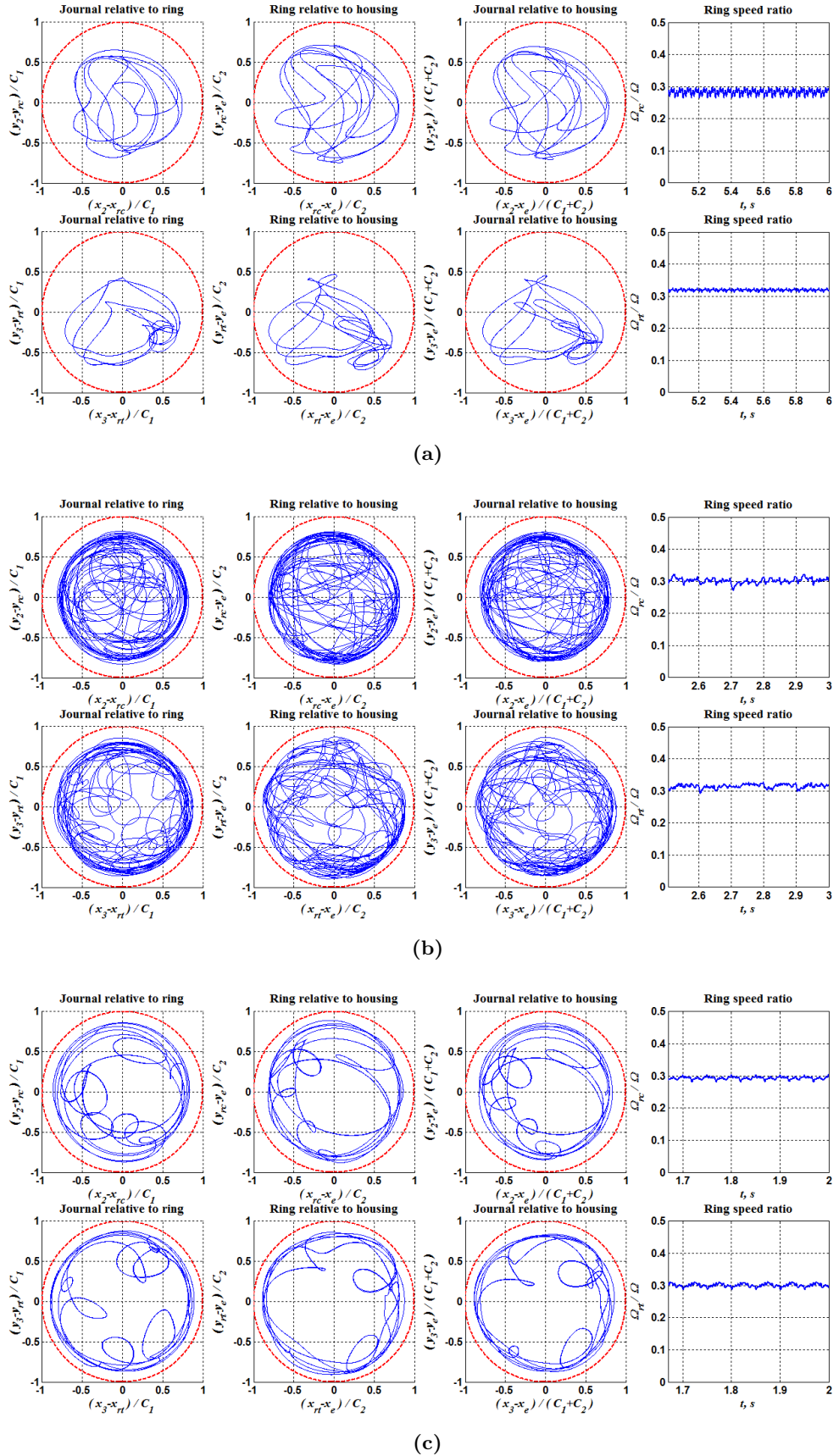


Fig. 4.1. Orbits and ring speed ratios of FRBs subject to unbalance and engine excitation (FRB1 first row, FRB2 second row), where the outer dashed circles indicate the border of motion. x_e , y_e denote the TC housing motions in the X direction and the Y direction, respectively. (a) 6,000 rpm, (b) 12,000 rpm, (c) 18,000 rpm, (d) 24,000 rpm, (e) 36,000 rpm, (f) 60,000 rpm and (g) 90,000 rpm.

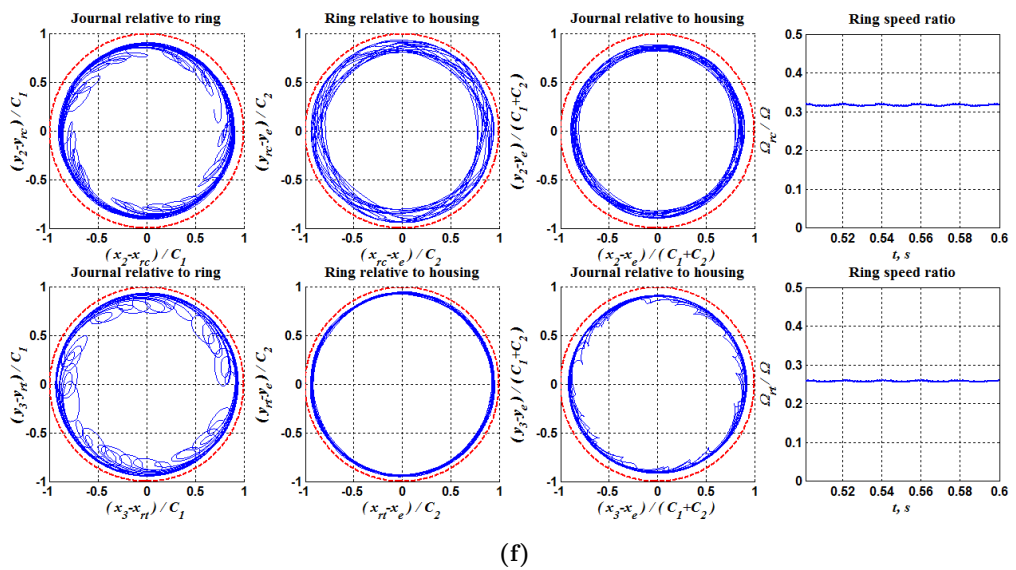
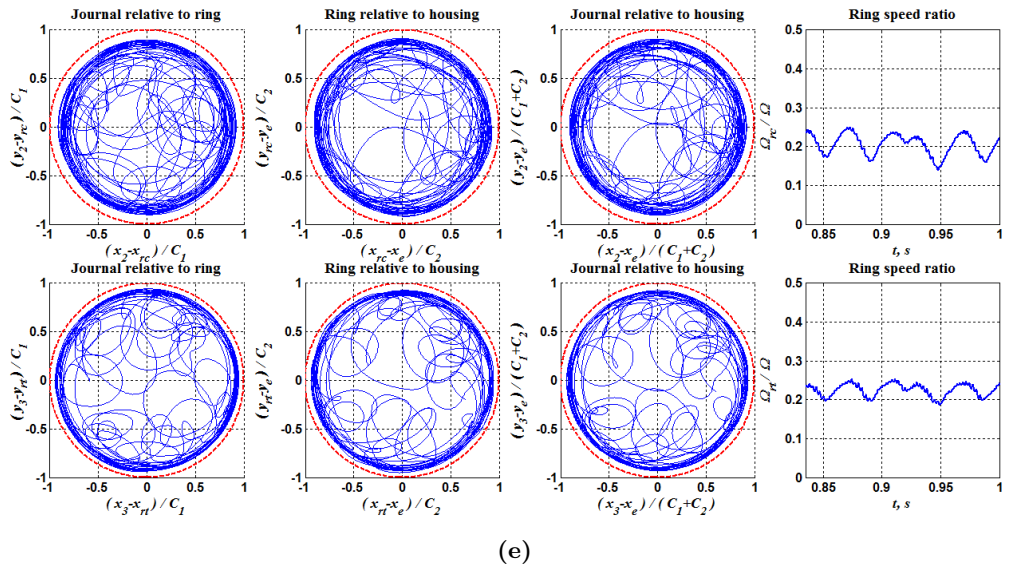
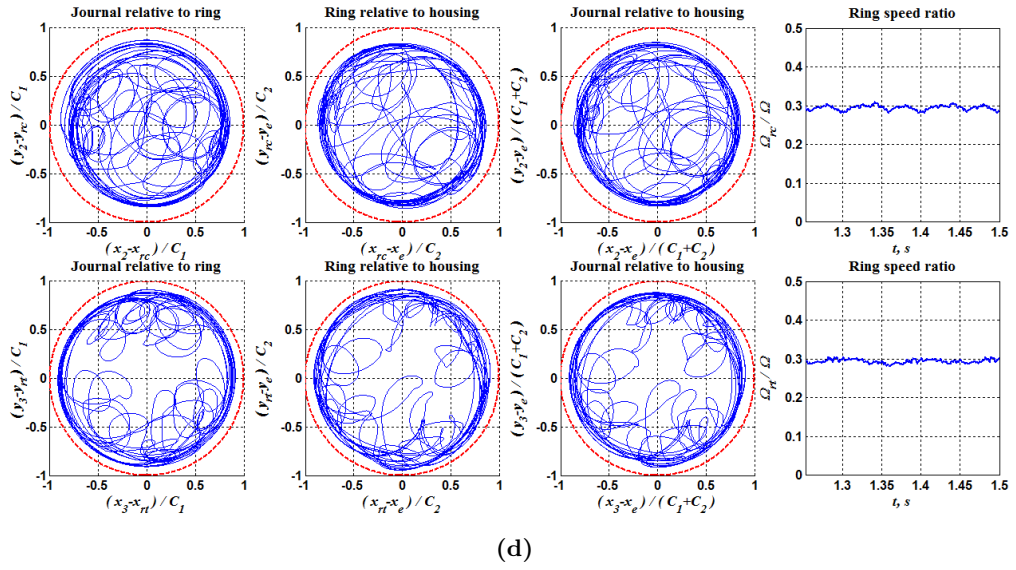


Fig. 4.1. (continued)

Horizontal excitation (m)				Vertical excitation (m)			
A_{x1}	A_{x2}	A_{x3}	A_{x4}	A_{y1}	A_{y2}	A_{y3}	A_{y4}
1E-5	2E-5	1E-5	3E-5	0.3E-5	6E-5	0.5E-5	0.2E-5

Table 4.1. Selected simulation parameters

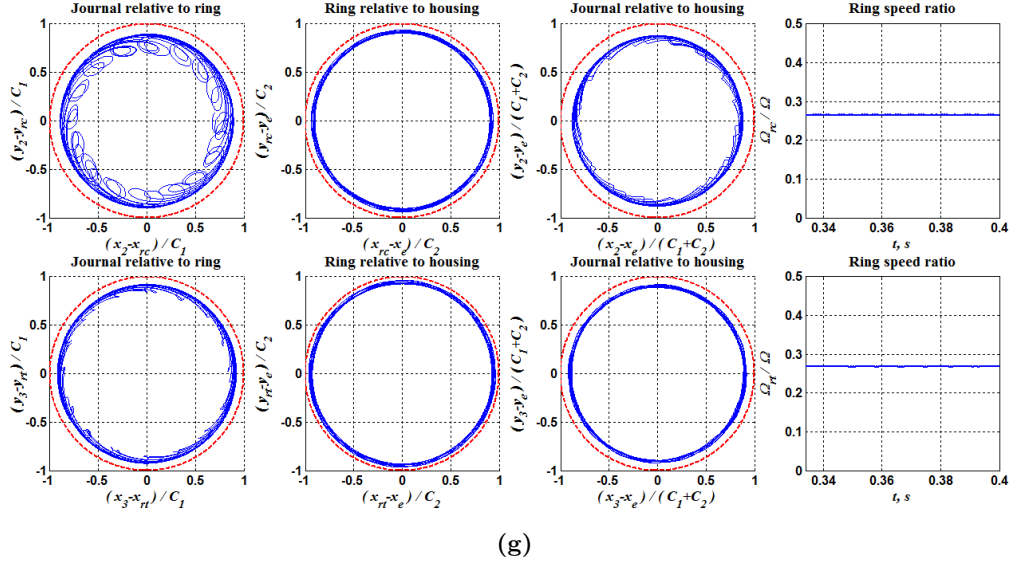
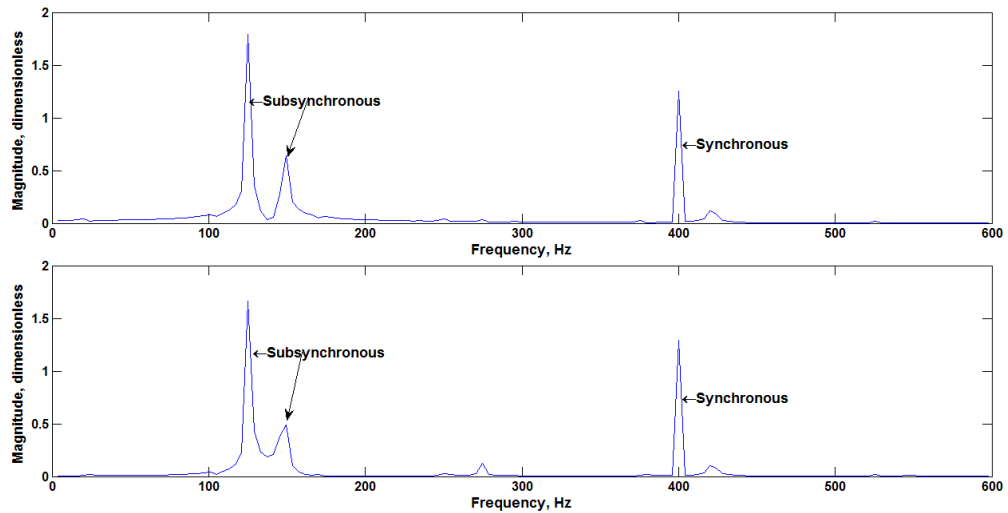


Fig. 4.1. (continued)

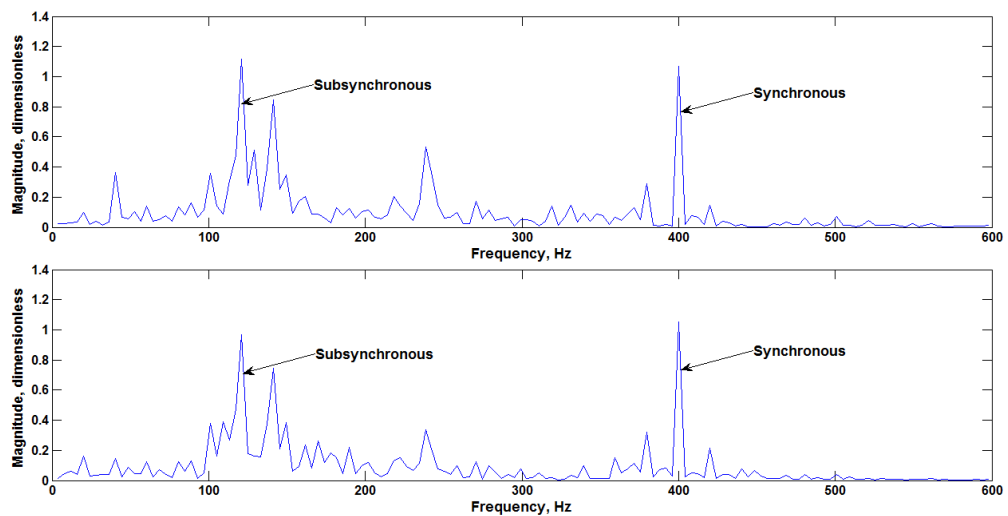
will bring the rotor response to a complex state earlier than the situation without engine excitation. The conclusion can also be appreciated from the difference between Fig. 4.2a and b. The effect of the engine induced vibration will entirely change the appearance of the frequency spectrum. In the state without engine excitation, the rotor only suffers from synchronous vibration induced by the unbalance and subsynchronous vibration originated from the oil film instability. However, the spectrum under the engine excitation will hold much more widely spread frequency components with various amplitudes. It is confused to say which rotor mode has been excited corresponding to linear analysis in Section 2.6.2. The broadband may indicate a chaotic state. Therefore, the engine excitation effect should not be neglected when the TC is in testing phase as well as in actual operation.

Another conclusion which can be drawn from the comparisons between Fig. 4.1 and Fig. 3.6 is that the engine excitation effect can hardly be identified from the rotor orbit maps when rotor rotates at relatively high speeds, e.g. 90,000 rpm. This phenomenon should be attributed to the dominant effect of $0.2\times$ subsynchronous component and the relatively low engine excitation frequencies.

Fig. 4.3 shows the waterfall plot of the TC rotor response at FRB 1 and FRB 2 relative to the TC housing motion in the X direction. The obvious difference between Fig. 3.7 and Fig. 4.3 is the part when the TC rotor operates within the low speed range from 100 Hz

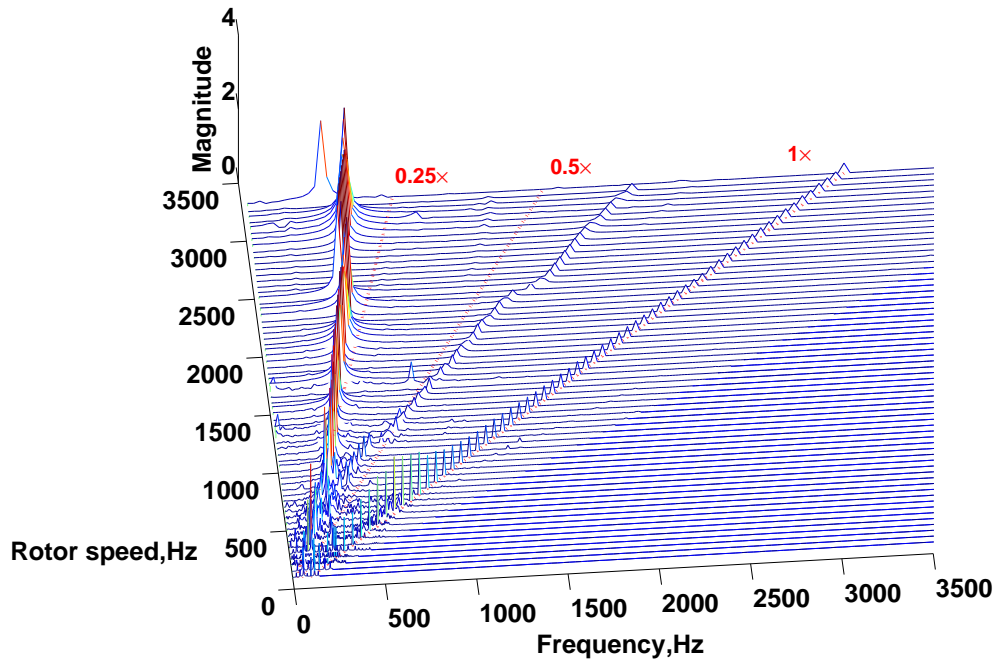


(a)

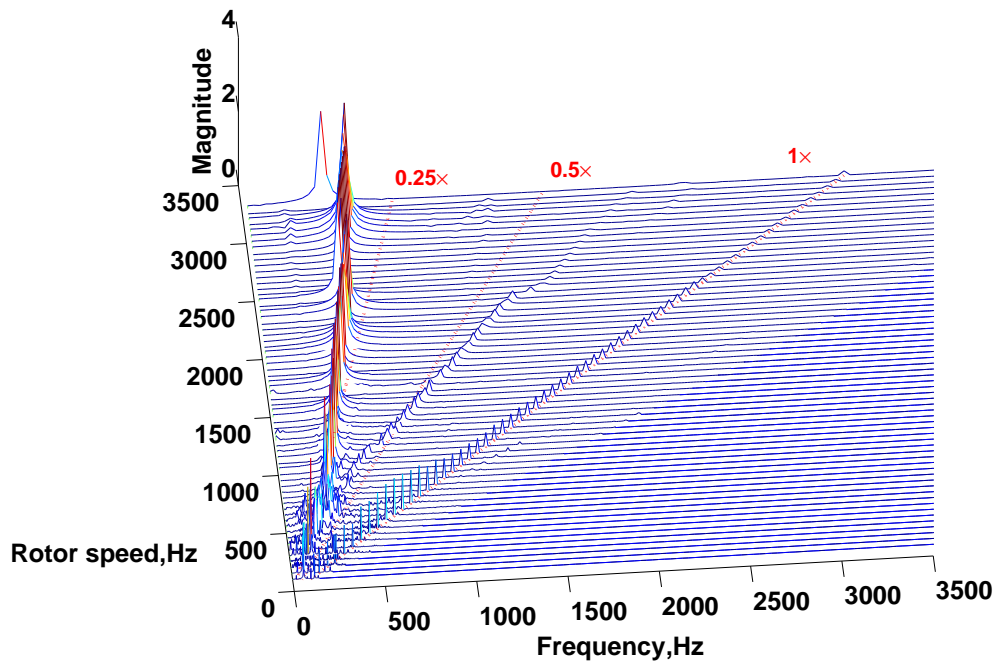


(b)

Fig. 4.2. Frequency spectrum of the journal at FRB1 at 24,000 rpm: (a) upper FFT for x_2/C_1 , lower for y_2/C_1 ; with unbalance only, (b) upper FFT for $(x_2 - x_e)/C_1$, lower for $(y_2 - x_e)/C_1$; with unbalance and engine excitation.

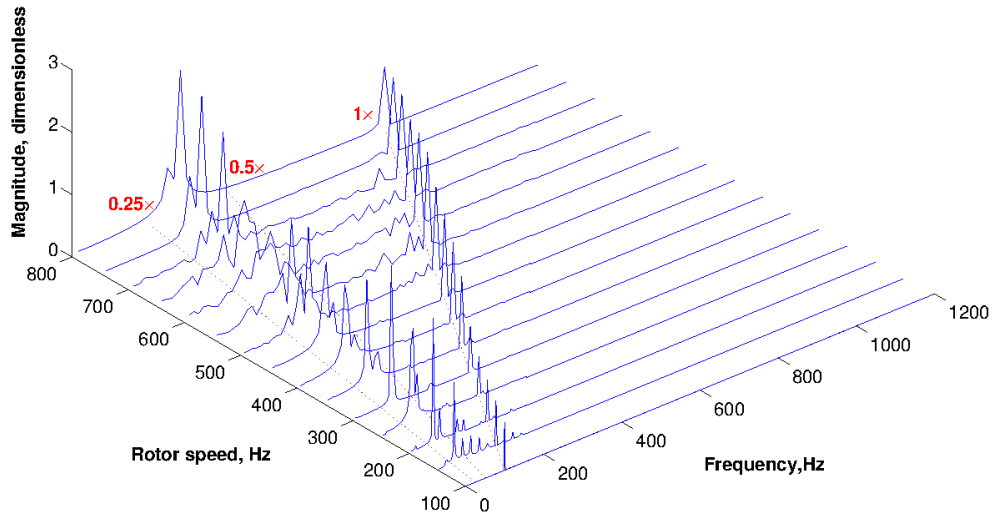


(a)

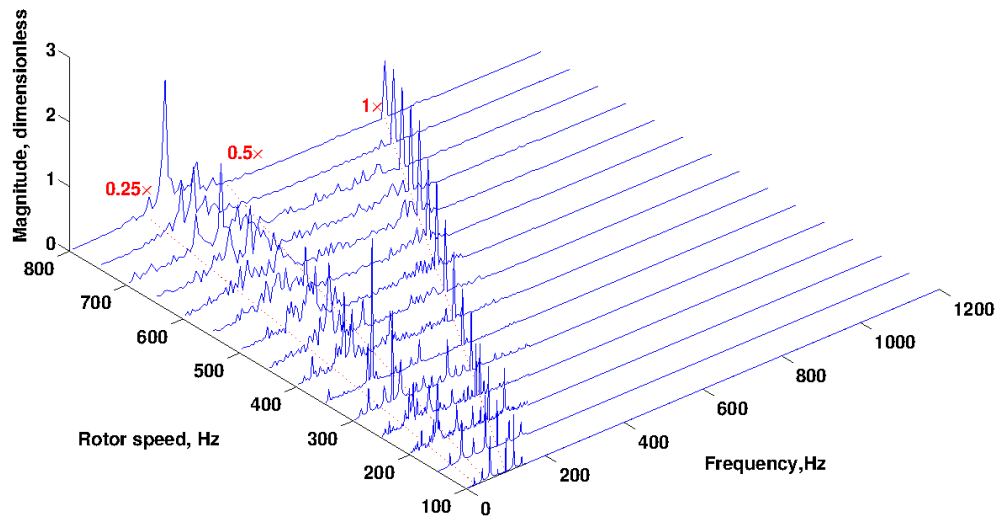


(b)

Fig. 4.3. Waterfall plot at FRB 1 and FRB 2 in the X direction with unbalance and engine excitation: (a) at FRB 1 for $(x_2 - x_e)/C_1$, (b) at FRB 2 for $(x_3 - x_e)/C_1$.



(a)



(b)

Fig. 4.4. Zoomed waterfall plot at low speed range at FRB1 in the X direction: (a) waterfall for x_2/C_1 ; with unbalance only, (b) waterfall for $(x_2 - x_e)/C_1$; with unbalance and engine excitation.

(6000 rpm) to 750 Hz (45,000 rpm). Fig. 4.4 provides a closer visit to the waterfall plot shown in Fig. 3.7a and Fig. 4.3a in the low speed range. What can be clearly observed is that the multiple harmonic components of ω_e raise much more frequency components on the frequency spectrum than the case without engine excitation. Therefore, the dynamic behaviour of TC rotor will be overwhelmingly influenced by the engine movement in the engine starting stage. Surprisingly, the engine induced vibration will be suppressed by the dominant subsynchronous vibrations when the TC rotor speed is above 45,000 rpm.

Chapter 5

Nonlinear Effects of Bearing Outer Clearance

The rotordynamic characteristics of TC rotor-FRB systems are proved to be highly sensitive to the system physical parameters, e.g. the FRB structural parameters [86, 87]. Chapter 5 aims to clarify the effect of FRB outer clearance on the rotordynamic characteristics of TCs by carrying out both run-up and run-down simulations of the practical TC rotor-FRB system shown in Section 2.1 but with varying FRB outer clearance sizes. As can be appreciated from the following sections, the obtained results systematically reveal some intriguing phenomena, which have never been reported in previous publications. This chapter is structured as follows. First, the nonstationary simulation method (run-up or run-down simulation) is introduced in Section 5.1. In order to investigate self-excitation nature of the FRB outer clearance, the simulated results shown in Section 5.2 are obtained under the perfectly balanced condition.

5.1 Nonstationary Simulation Method

The nonlinear simulation results shown in Chapter 3 and Chapter 4 are all obtained based on the assumption that the spin speed of the TC rotor is being maintained constant. By contrast, the rotor speed variation is considered in this chapter. In other words, the rotor acceleration or deceleration term $\ddot{\phi}$ in Eqs. (2.2a) and (2.2b) is not equal to zero any more, and, therefore, the rotor speed $\dot{\phi}$ or Ω_j will vary within the simulation time interval. Accelerating a rotor to its operational speed is normally referred to as run-up, while decelerating a rotor is referred to as run-down. In this chapter and the following Chapter 6, a linear run-up or run-down is considered, which means the rotor speed is a

Parameters	Value
Shaft ramp rate (Hz/s)	$\beta = \pm 300$
Total integration time (s)	10
Total time steps	100,000
Rotor speed range (Hz)	0 ~ 3000

Table 5.1. Parameters for run-up and run-down simulations

Parameters	Value
Hamming window length <i>window</i>	2048
Number of overlapping samples <i>noverlap</i>	1024+512
FFT length <i>nfft</i>	2048
Sampling Frequency <i>fs</i>	10000 Hz

Table 5.2. Parameters for MATLAB spectrogram[®] function

linear function of time. As a result, with respect to the rotor rotation angle ϕ defined in Section 2.1, the following equations are obtained.

$$\phi(t) = \frac{1}{2}\beta t^2 \quad (5.1a)$$

$$\dot{\phi}(t) = \beta t \quad (5.1b)$$

$$\ddot{\phi}(t) = \beta \quad (5.1c)$$

where β represents the rotor acceleration or deceleration. With a modern computer, numerically integrating the system equations of motion Eq. (2.1) can easily be achieved for different values of β . The adopted numerical integration method and the tolerance will be detailed in the following section.

5.2 Simulation Results

In this section, in order to investigate the pure nonlinear nature of the oil film forces, the nonlinear run-up and run-down simulation results of a perfectly balanced TC rotor will be presented. The coupling of unbalance will be considered in Chapter 6 to show various induced complexity and interesting phenomena. Table 5.1 lists the parameters of the performed run-up and run-down simulations. Apart from the identically varying outer clearance of the two FRBs from 30 μm to 50 μm , the TC rotor-FRB system parameters are the same as shown in Table 2.1. Owing to the stiffness of the system equations of motion in Eq. (2.1), the robust MATLAB[®] routine ode15s[®] solver has been employed to

successfully fulfill the simulation objectives throughout this chapter. All simulations have been carried out with a relative error tolerance of 1E-6. To avoid singularities of oil film locators α_i and α_o in Eqs. (3.9a) and (3.9b), a small deviation from the bearing origin, i.e. one thousandth of the bearing outer clearance, is assigned to the displacements of both ring centers in the X axis direction and the negative Y axis direction as the initial conditions of the performed run-up simulations. For the run-down simulations, initial conditions are chosen from the end of the obtained data from the corresponding run-up simulations. As will be seen in s 5.2.1-5.2.4, the changes of outer clearance result in complex phenomena, e.g. various kinds of nonlinear jumps. The simulation results also show that the considered outer clearance range can be further divided into several groups, each of which can be identified and characterized by similar response plots, e.g. waterfall diagrams, displacements plots.

5.2.1 Simulation 1 ($C_2 = 30 \mu\text{m}$)

Fig. 5.1 shows the run-up simulation results when the outer clearances of both oil films are $30 \mu\text{m}$, which is smaller than the inner clearance. The waterfall diagrams of y_1 and y_4 non-dimensionalized by the bearing inner clearance C_1 are depicted in Fig. 5.1a and b. Correspondingly, top-views of the waterfall diagrams are given in Fig. 5.1c and d. The following color pattern corresponds to the ascending order of response magnitude: dark blue, light blue, cyan, yellow, orange and red. The non-dimensional displacement plots of the rotor two ends in Y direction are shown in Fig. 5.1e and f, in which the rotor speed is also shown by a slope leading up to 3000 Hz. Note that the maxima on the magnitude axes in the waterfall diagrams are actually smaller than on the displacement axes in the displacement plots, since the Hamming Window, which is used to draw the waterfall diagrams for selected vibration signals through MATLAB[®] function spectrogram[®] based upon Short-time Fourier Transform, reduces part of the energy of the obtained signals. Nevertheless, it will only slightly and quantitatively affect the displayed results. The selected parameters for the spectrogram[®] function is listed in Table 5.2. For the following simulations given in this chapter and Chapter 6, the same parameters are used. As defined in Eq. (3.3), the bearing eccentricities of FRB 1 and FRB 2 are presented in Fig. 5.1g and h, in which the subscripts c and t denote FRB 1 and FRB 2 respectively. The ring speed ratio plot for the two bearings is depicted in Fig. 5.1i. With the help of the mode filtering method described in Ref. [100], rotor whirling mode shapes related to the interested subsynchronous frequencies at two selected speeds are shown in Fig. 5.2. Fig. 5.3

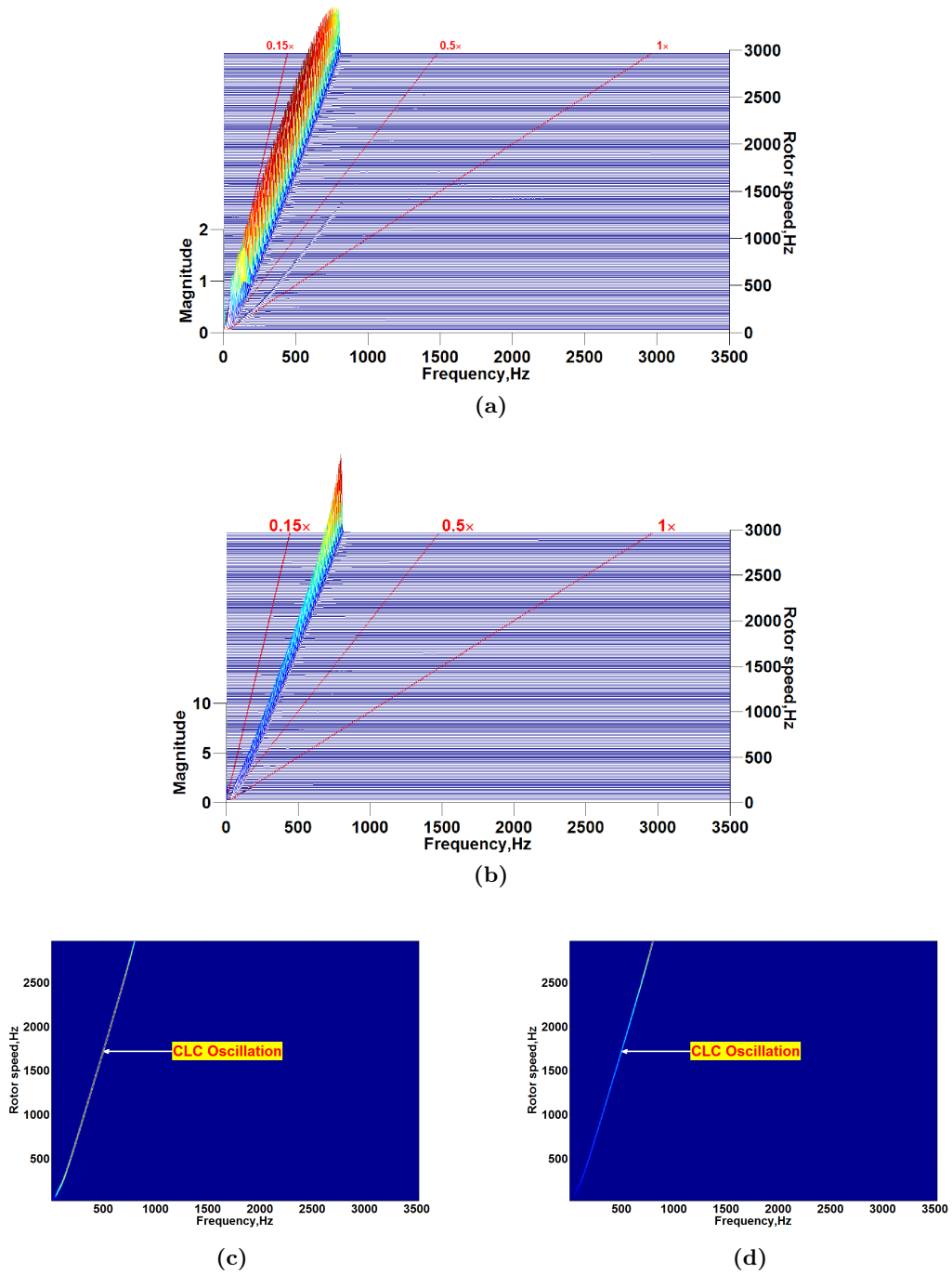
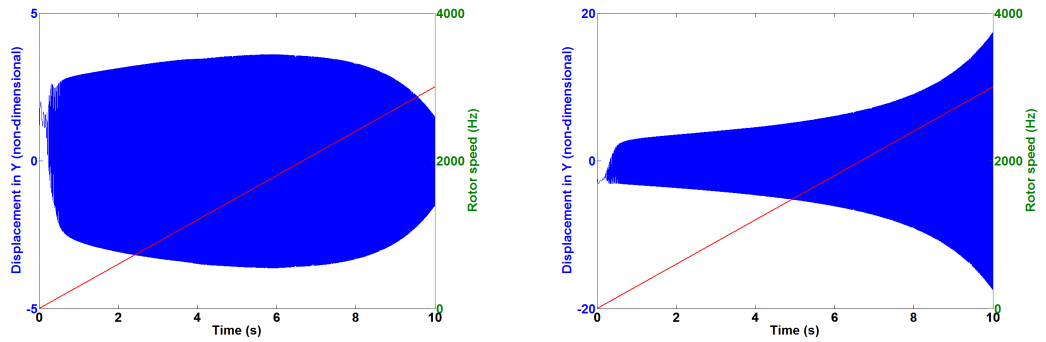
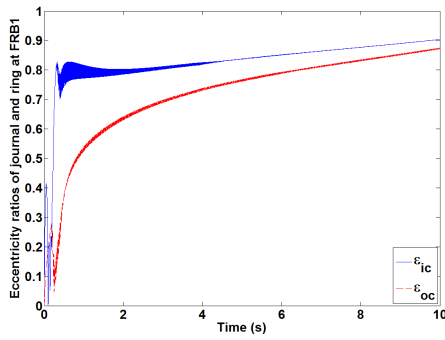


Fig. 5.1. Run-up simulation when the TC rotor is perfectly balanced and $C_2 = 30\mu\text{m}$: (a), (b) waterfall plots of the compressor end y_1/C_1 and turbine end y_4/C_1 in Y axis direction, respectively, (c), (d) top-views of the waterfall diagrams given in (a) and (b), corresponding to y_1/C_1 and y_4/C_1 , respectively, (e) and (f) displacement plots of y_1/C_1 and y_4/C_1 , (g), (h) eccentricity plots of the inner and outer oil films at FRB 1 and FRB 2, respectively, (i) ring speed ratios of FRB 1 and FRB 2.

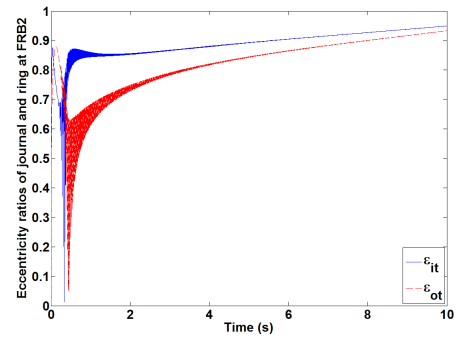


(e)

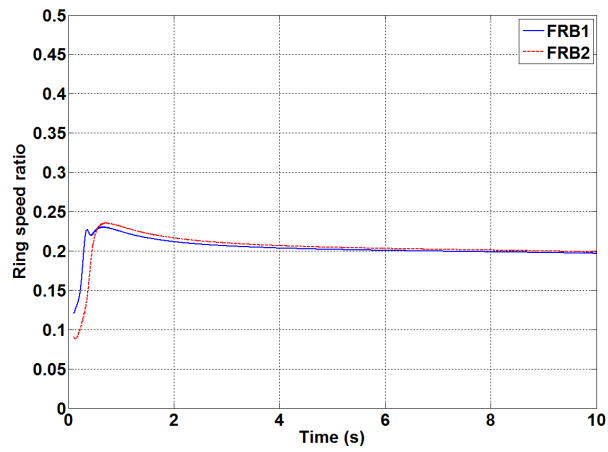
(f)



(g)



(h)



(i)

Fig. 5.1. (continued)

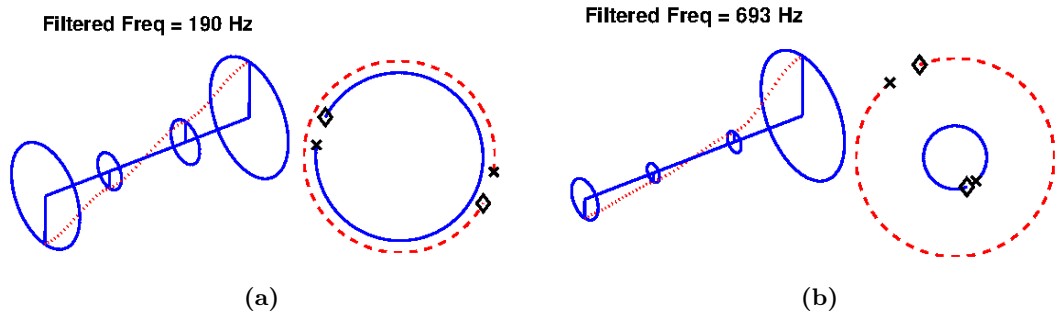


Fig. 5.2. Filtered mode shapes and orbits for Sub 1 when the outer clearances are $30 \mu\text{m}$ at selected rotor speeds: (a) 507 Hz and (b) 2504 Hz.

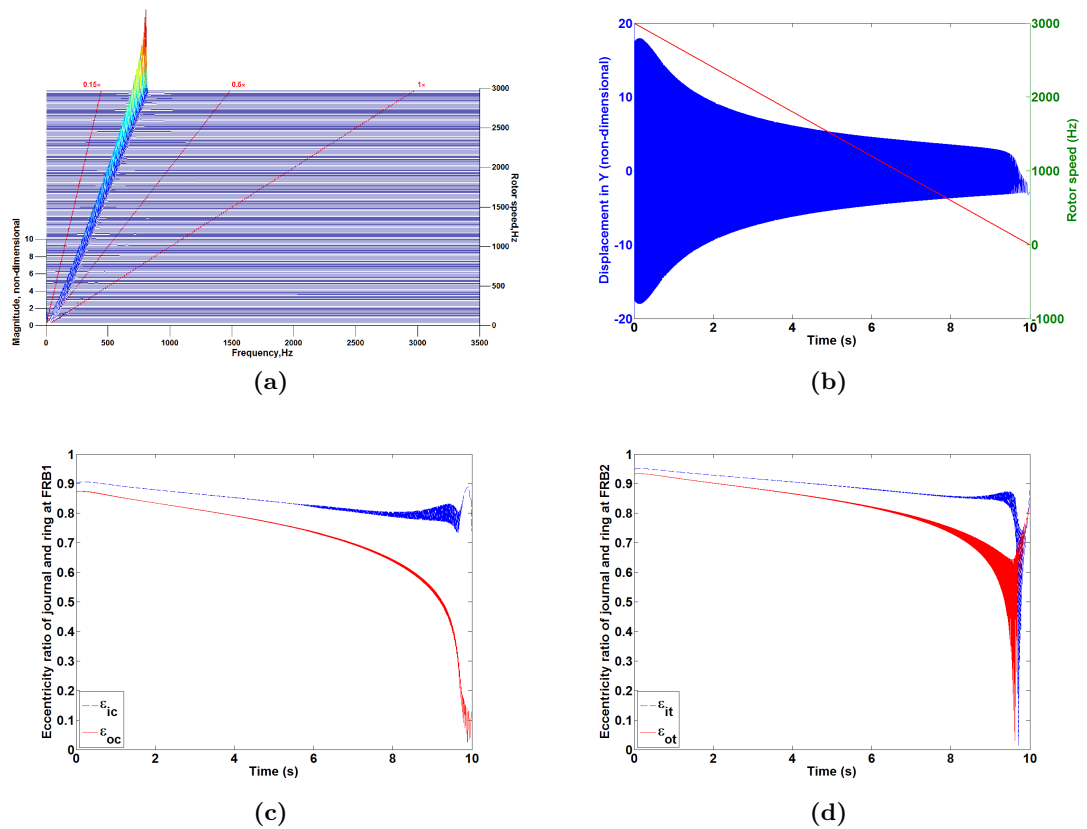


Fig. 5.3. Run-down simulation when the TC rotor is perfectly balanced and $C_2 = 30 \mu\text{m}$: (a) waterfall plot of the turbine end y_4/C_1 in Y axis direction, (b) displacement plot of y_4/C_1 , (c), (d) eccentricity plot of the inner and outer oil films at FRB 1 and FRB 2, respectively.

presents the results of run-down simulation. The observed phenomena can be summarised as follows.

- (a) As can be observed in Figs. 5.1a-d, the system under investigation becomes unstable at the beginning and the Sub¹ vibrations derived from the oil film instability persist throughout the considered rotor operating speed range.
- (b) The displacement plots in Fig. 5.1e and f show the amplitude of y_1 is gently climbing up until the maximum is reached at 6 seconds. Thereafter, it follows a decreasing trend. By contrast, the amplitude of y_4 consistently ascends to an extreme high value, i.e. 17 times bigger than the bearing inner clearance at 3000 Hz. This possibly indicates a failure of the TC, as the blade at the turbine disk would touch the turbine case in this situation.
- (c) As shown in Fig. 5.1g and h, one can see consistent growth of both inner and outer eccentricities of the two FRBs to very high values, although the inner and outer films of FRB 2 become unstable at approximately 0.23 seconds, which is slightly later than the onset of inner film instability at FRB 1. The ascending bearing eccentricities of both FRBs can increasingly stiffen the rotor-FRB system and limit the rotor operation at relatively high speeds, which is very undesirable for the healthy operation of the TC. This phenomenon is termed *Critical Limit Cycle Oscillation* in Ref. [16], which is followed and abbreviated to the *CLC Oscillation* in this thesis. The onset of the *CLC Oscillation* can possibly be attributed to the instability synchronization of the instability of inner and outer films, as stated by Schweizer in Ref. [85, 86], since there is only one evident Sub component on the waterfall diagrams, but the inner and outer films are both unstable, as confirmed by the high bearing eccentricities.
- (d) At FRB 1, the ring speed ratio plot depicted in Fig. 5.1i initially shows a sudden jump, which corresponds to the sharp rise of the eccentricity ϵ_{ic} , when the inner oil film at FRB 1 becomes unstable. The short delay of the ring speed ratio at FRB 2 indicates the slightly late development of the instability of the oil films at the turbine side. Thereafter, following a gradually decreasing trend to approximately 0.2 seconds, the two ratios are almost equal to each other. This is probably helpful for the appearance of the single Sub component observed in Figs. 5.1a-d, as the disagreement between the ring speed ratios can cause instability of the two FRBs

¹For brevity, from this point Sub is used as the abbreviation of 'subsynchronous' throughout this chapter.

individually occurs at different frequencies, and, therefore, the emergence of multiple Sub components on the waterfall diagram.

- (e) The filtered mode shape plots in Fig. 5.2 clearly show the self-excited Sub vibrations are a conical forward mode, in which the compressor disk and the journal at FRB 1 are out-of-phase with the journal at FRB 2 and turbine disk. As the rotor speed moves up, the whirling amplitude of the turbine disk centre is much higher than that of the compressor disk (see Fig. 5.2b), and the conical forward mode becomes a bending mode. This can be attributed to the high bearing eccentricities at both FRBs, which lead to very stiff bearings [16] at higher rotor speeds. Apart from the filtered conical mode shapes, it is difficult to correlate the simulated nonlinear results with any of the linearly predicted unstable modes as shown in Fig. 2.14a. However, the *CLC Oscillation* component might be interpreted as the result of the collaboration between unstable Mode 2 and 3. The stability map presented in Fig. 2.16a demonstrates that those two modes are most likely to be excited over the considered speed range. At a given speed, the frequency of the *CLC Oscillation* component is higher than unstable Mode 3 but smaller than Mode 2.
- (f) Despite the descending rotor speed, the run-down simulation results shown in Fig. 5.3 do not reveal any substantial difference from the results obtained in the run-up simulation.
- (g) Further simulations with slightly bigger outer clearance values, i.e. 31 μm , 32 μm and 33 μm , also show very similar rotor response characteristics as described above, although the following items are slightly smaller: the eccentricities of two inner films, both ring speed ratios and the vibration amplitude of the turbine disk centre.

5.2.2 Simulation 2 ($C_2 = 35 \mu\text{m}$)

In contrast with Simulation 1, the outer clearances of both bearings are increased to 35 μm and the simulation results are shown in Figs. 5.4-5.6. What can clearly be observed are the jump phenomena from Sub 1 to Sub 2 and then from Sub 2 to *CLC Oscillation*, which are the main differences as compared to Simulation 1. This kind of nonlinear jump phenomenon has been reported to be closely related to the sudden increase of TC noise in reported experimental work [57, 100]. The obtained results are listed and summarised as below.

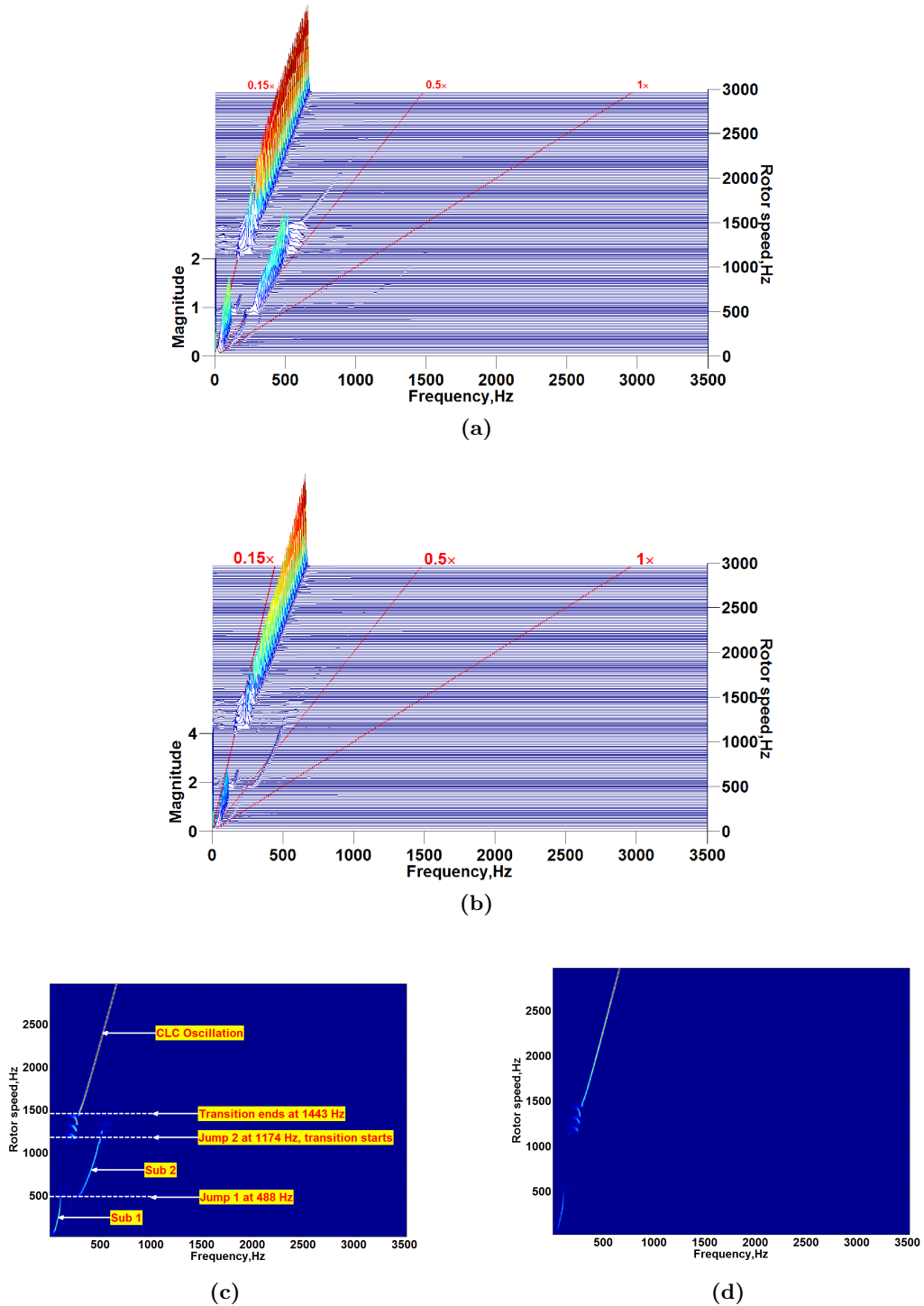
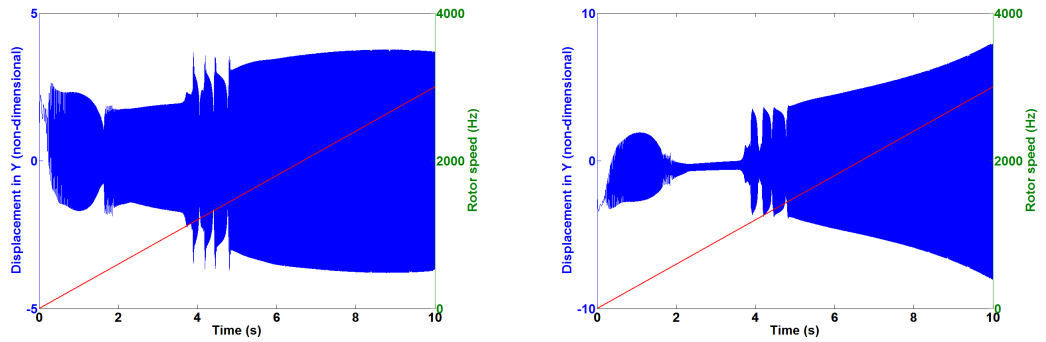
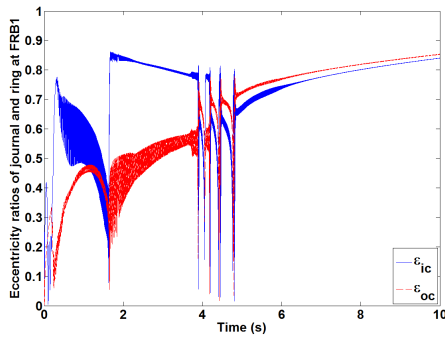


Fig. 5.4. Run-up simulation when the TC rotor is perfectly balanced and $C_2 = 35\mu\text{m}$: (a), (b) waterfall plots of the compressor end y_1/C_1 and turbine end y_4/C_1 in Y axis direction, respectively, (c), (d) top-views of the waterfall diagrams given in (a) and (b), corresponding to y_1/C_1 and y_4/C_1 , respectively, (e) and (f) displacement plots of y_1/C_1 and y_4/C_1 , (g), (h) eccentricity plots of the inner and outer oil films at FRB 1 and FRB 2, respectively, (i) ring speed ratios of FRB 1 and FRB 2.

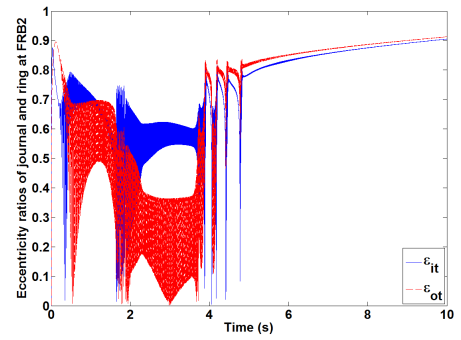


(e)

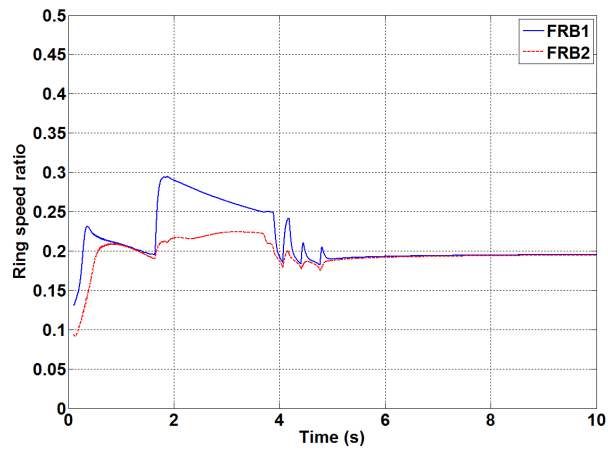
(f)



(g)



(h)



(i)

Fig. 5.4. (continued)

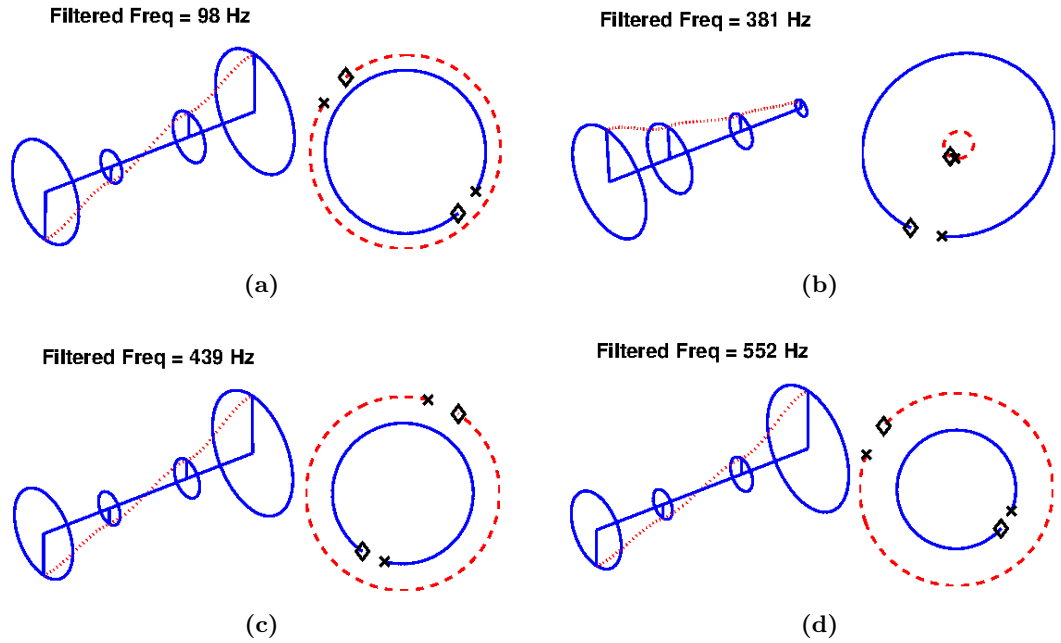


Fig. 5.5. Filtered mode shapes and orbits for Sub 1 and Sub 2 when the outer clearances are $35 \mu\text{m}$ at selected rotor speeds: (a) 307 Hz for Sub 1, (b) 707 Hz for Sub 2, (c) 2012 Hz for Sub 1 and (d) 2504 Hz for Sub 1.

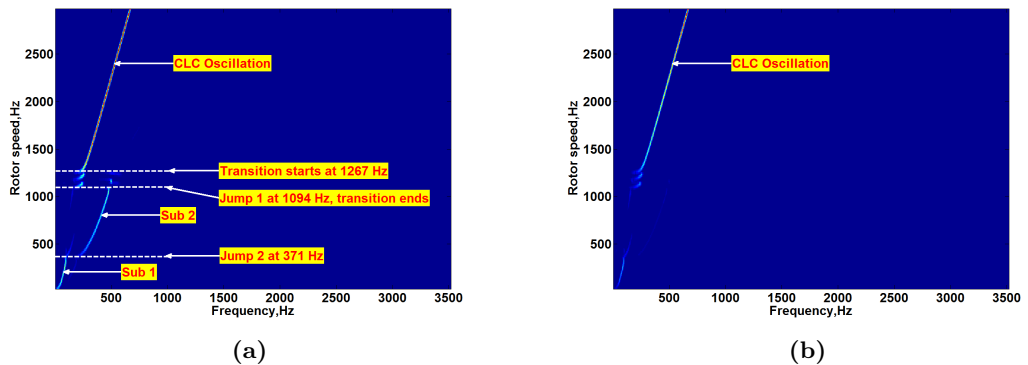


Fig. 5.6. Top-views for the waterfall diagrams of run-down simulation: $C_2 = 35 \mu\text{m}$. (a) for y_1/C_1 and (b) for y_4/C_1 .

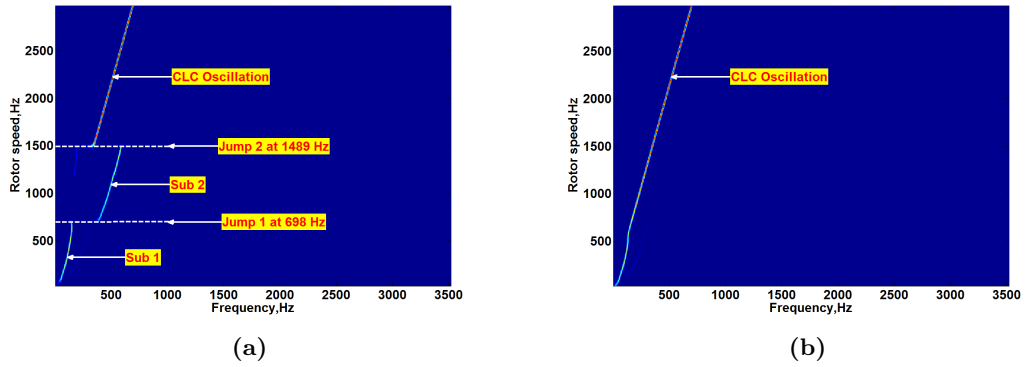


Fig. 5.7. Top-views of the waterfall diagrams of the run-up and run-down simulation results when the outer clearances of both bearings are $34 \mu\text{m}$: (a) run-up simulation results for y_1/C_1 , (b) run-down simulation results for y_1/C_1 .

- (a) Both bearings are unstable from the very beginning to the end of simulation, which can clearly be seen from the given waterfall diagrams in Fig. 5.4a-d. The distinctive characteristic is the dominant Sub component jump from Sub 1 to the higher frequency Sub 2 at 488 Hz. At this stage, what is interesting is the extremely small magnitude of Sub 2 at the turbine end shown in Fig. 5.4b and d. Subsequently, a further jump from Sub 2 to the *CLC Oscillation* occurs at 1174 Hz. However, this jump cannot be quickly accomplished as there is a special transition range from 1174 Hz to 1443 Hz, in which the *CLC Oscillation* component is discontinued by the abruptly short appearances of Sub 2. As will be discussed later, the existence of this transition range leads to a more complex state of the investigated system. At 1443 Hz, Sub 2 completely disappears and the *CLC Oscillation* component solely exists until reaching the top end of rotor speed range.
- (b) The discontinuities in the displacement plots and eccentricity figures evidently indicate the observed frequency jump phenomena. Before the onset of Jump 1 at 488 Hz, the displacement amplitude of the compressor disk is comparable to the turbine end. After the dominance of Sub 2 is established, corresponding to the waterfall diagrams shown in Fig. 5.4a and b, the vibration amplitude at the turbine centre is much smaller than that of the compressor centre. During the transition range, the vibration amplitudes of both ends considerably fluctuate. After the *CLC Oscillation* establishes the dominance at 4.8 seconds, the vibration amplitude of the compressor end goes up slowly to a maximum and then follows a slightly descending trend, while the amplitude at the turbine end continuously moves up, which is very similar to the situation in Simulation 1.

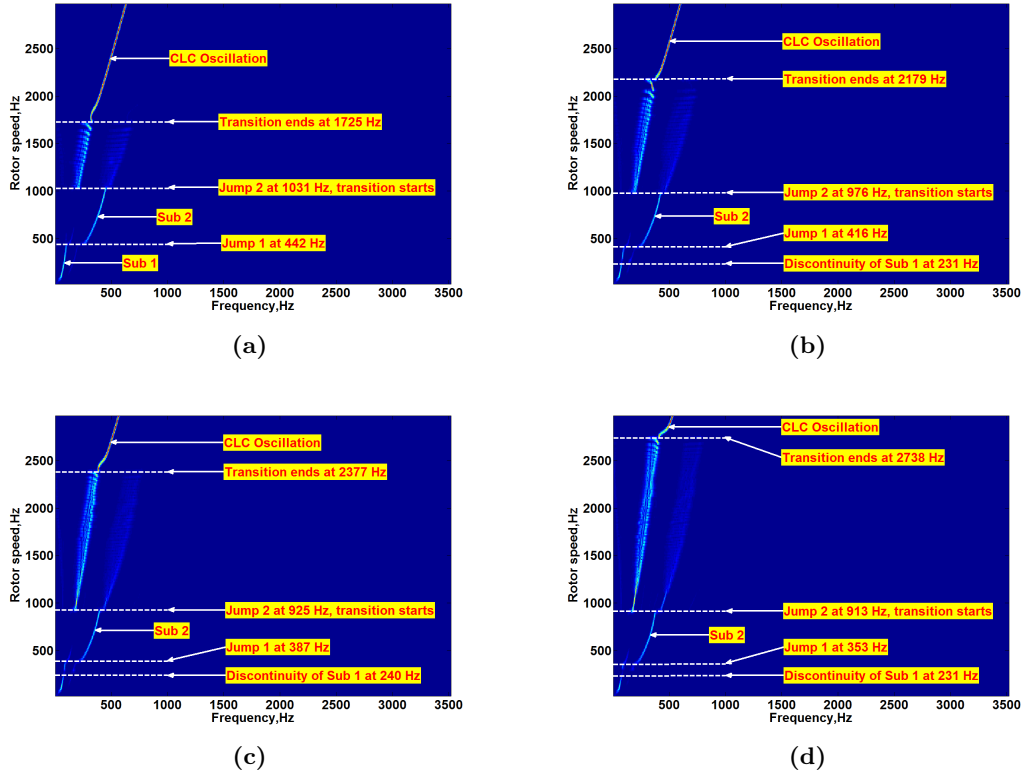


Fig. 5.8. Comparisons of the top-views of waterfall diagrams for y_1/C_1 from run-up simulations: (a) $C_2 = 36 \mu\text{m}$, (b) $C_2 = 37 \mu\text{m}$, (c) $C_2 = 38 \mu\text{m}$ and (d) $C_2 = 39 \mu\text{m}$

- (c) At 0.2 seconds, we see the quantum leap of the inner film eccentricity at FRB 1 (ϵ_{ic}) from a fairly small value to 0.76, which implies the occurrence of Sub 1. The further jump of ϵ_{ic} at 1.6 s displays the onset of the fully developed instability of the inner film, which results in the jump from Sub 1 to Sub 2. In this stage, the eccentricities of both outer films (ϵ_{oc} and ϵ_{ot}) are clearly smaller than those of the corresponding inner films. Corresponding to the wavering of the displacement plots, the transition range starting at 3.9 seconds brings about the violent fluctuations of the inner and outer eccentricities at both bearings. After the disappearance of Sub 2 at 4.8 seconds, the inner and outer bearing eccentricities of FRB 1 and FRB 2 gradually come up to quite high values, which indicates the onset of the *CLC Oscillation*. Nevertheless, unlike Simulation 1, ϵ_{oc} and ϵ_{ot} are bigger than ϵ_{ic} and ϵ_{it} , respectively.
- (d) The occurrence of Jump 1 and Jump 2 can also be appreciated from the ring speed ratio variations in Fig. 5.4i. The greatest discrepancy between the two ring speed ratios can be observed during the dominance of Sub 2. The ratio at FRB 1 is evidently higher than at FRB 2. The following transition range also causes the

wavering of both ratios. Meanwhile, the amplitudes of both ratios, especially the one at FRB 1, clearly follow a decreasing trend. After the *CLC Oscillation* sets in, they are close to each other and slightly below 0.2.

- (e) The filtered mode shapes at four selected speeds in Fig. 5.5 show Sub 1 is a conical forward mode, and Sub 2 is a cylindrical forward mode with smaller amplitude at the turbine end. Comparisons with the linear analysis results given in Fig. 2.14 and Fig. 2.15 show Sub 1 closely corresponds to the linearly predicted unstable Mode 1, while Sub 2 agrees well with the unstable Mode 2. In addition, it should be mentioned that the Mode 2 dominant range on the Campbell diagram in Fig. 2.14b, i.e. from 550 Hz to 950 Hz, are within the nonlinearly simulated Sub 2 dominant range in Fig. 5.4c, i.e. from 488 Hz to 1174 Hz. The good agreement between the linear and nonlinear results evidences the capability of the linear eigenvalue analysis to predict the nonlinear jump from Sub 1 to Sub 2. Similar to Simulation 1, the mode shape of the *CLC Oscillation* filtered at 2012 Hz shows it is a conical mode. However, at even higher rotor speeds, it becomes bent owing to the excessive growth of the displacement amplitude of the turbine centre (see Fig. 5.5d). It can possibly be linearly interpreted as the result of the cooperation between the unstable Mode 2 and the unstable Mode 3, as those two modes are highly likely to be excited at higher rotor speeds.
- (f) The run-down simulation results given in Fig. 5.6 show that the transition from the *CLC Oscillation* to Sub 2 starts at 1267 Hz, corresponding to the transition end at 1443 Hz in the run-up simulation. This means that the *CLC Oscillation* component at the high speed range will stay over a longer speed span in the run-down simulation than when the rotor accelerates, which can be attributed to the well-known hysteresis characteristic found in the nonlinear response of rotor-journal bearing systems. Surprisingly, the length of transition range is much smaller in the run-down simulation than in the run-up. The rotor speed 1094 Hz, at which the jump from the *CLC Oscillation* to Sub 2 happens, is also lower than the corresponding rotor speed 1174 Hz in the run-up simulation. The jump from Sub 2 back to Sub 1 (Jump 2 in run-down simulation) occurs at 371 Hz, significantly smaller than the frequency 488 Hz of Jump 1 when the rotor speed moves up. The lower jump speed leads to the slightly longer existence of Sub 2 in the run-down waterfall diagram, which results from the hysteresis characteristic as well.

- (g) Fig. 5.7 depicts the simulated results when both outer clearances are reduced to 34 μm . In comparison to the presented run-up simulation results in Fig. 5.4, Fig. 5.7a show the onset speeds of Jump 1 and Jump 2 are higher than in Fig. 5.4. In addition, the transition range in Fig. 5.4 cannot be observed in Fig. 5.7a, which means that the dominant frequency transition from Sub 2 to *CLC Oscillation* can be completed as soon as Jump 2 occurs. By contrast, surprisingly, the run-down simulation results in Fig. 5.7b, which are quite similar to the results presented in Fig. 5.1, do not show any jump phenomenon, and Sub 2 disappears.
- (h) The results of run-ups with wider outer clearances given in Fig. 5.8 show similar response characteristics as the presented simulation results in Figs. 5.4-5.6. However, the differences emerging from the increased bearing outer clearance can also clearly be observed. The speeds, at which Jump 1 and Jump 2 occur, evidently follow a decreasing trend. Meanwhile, as the value of outer clearance goes up, the length of the transition range also becomes longer. Another interesting phenomenon is the discontinuity of Sub 1 in the low-speed range, which can be found when the value of outer clearance is higher than 36 μm .

5.2.3 Simulation 3 ($C_2 = 40 \mu\text{m}$)

The outer clearances of two bearings are further increased to 40 μm in this subsection. The simulation results are presented in Fig. 5.9 to Fig. 5.11. In comparison with the aforementioned two simulations, the observed major difference is the sudden jump of the vibration amplitudes at both sides to a relatively small value when the rotor speed is higher than 1754 Hz. This interesting phenomenon indicates the unwelcome Sub vibrations can be suppressed by adjusting the size of FRB outer clearance. The simulated results are summarised as follows.

- (a) The waterfall diagrams (Figs. 5.9a-d) show there are three jumps from the beginning to the end of simulation. The jump sequence of dominant frequency is from Sub 1 to Sub 2, from Sub 2 to Sub 1 and finally from Sub 1 to Sub 3. The perfectly balanced system quickly runs to an unstable state, which is represented by the appearance of Sub 1, after the simulation starts. At 227 Hz, the rotor becomes stable and after a small speed span, at 332 Hz, the instability state appears again. However, instead of Sub 1, the dominant Sub component is Sub 2 with a bigger frequency than Sub 1. Thereafter, at 850 Hz, the dominant frequency jumps back to Sub 1 accompanied

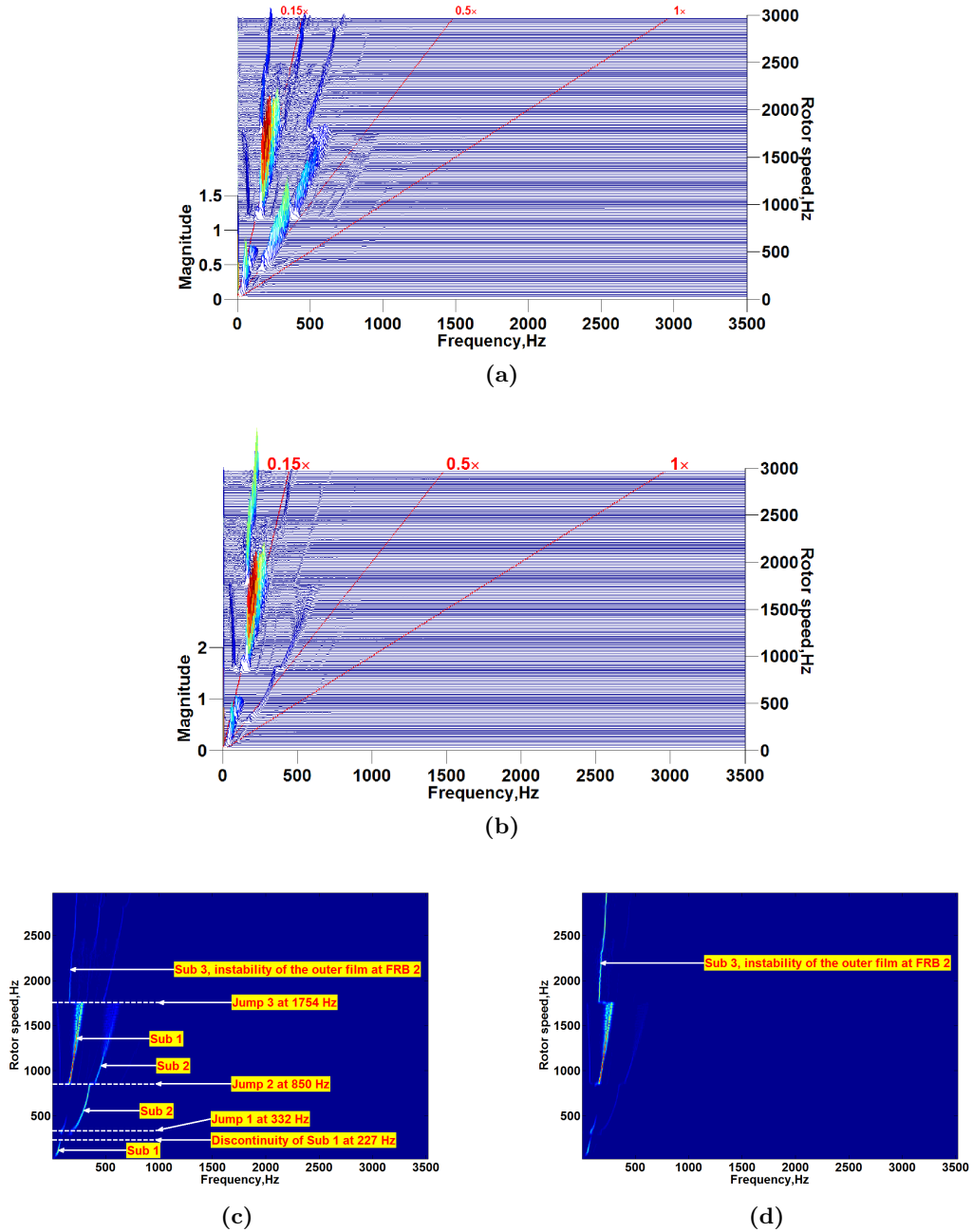
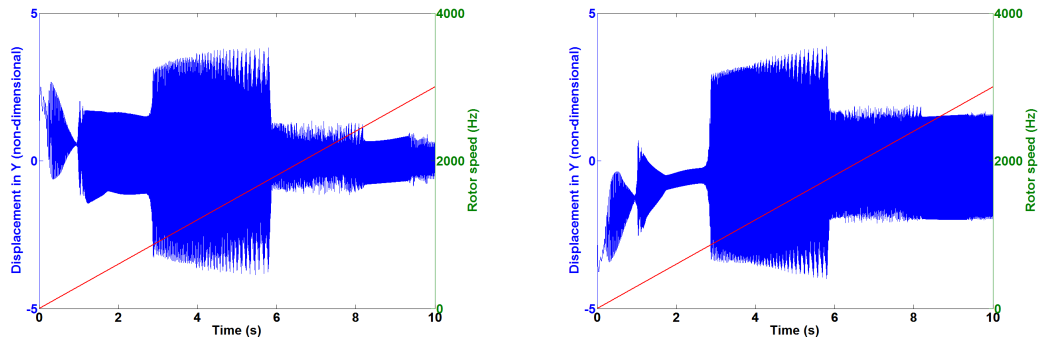
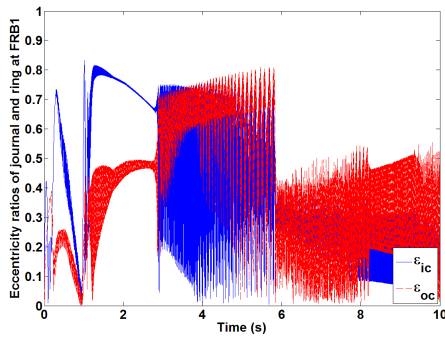


Fig. 5.9. Run-up simulation when the TC rotor is perfectly balanced and $C_2 = 40 \mu\text{m}$: (a), (b) waterfall plots of the compressor end y_1/C_1 and turbine end y_4/C_1 in Y axis direction, respectively, (c), (d) top-views of the waterfall diagrams given in (a) and (b), corresponding to y_1/C_1 and y_4/C_1 , respectively, (e) and (f) displacement plots of y_1/C_1 and y_4/C_1 , (g), (h) eccentricity plots of the inner and outer oil films at FRB 1 and FRB 2, respectively, (i) ring speed ratios of FRB 1 and FRB 2.

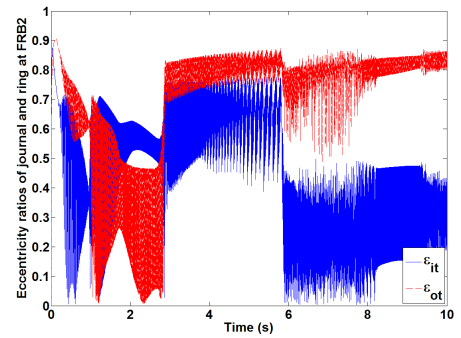


(e)

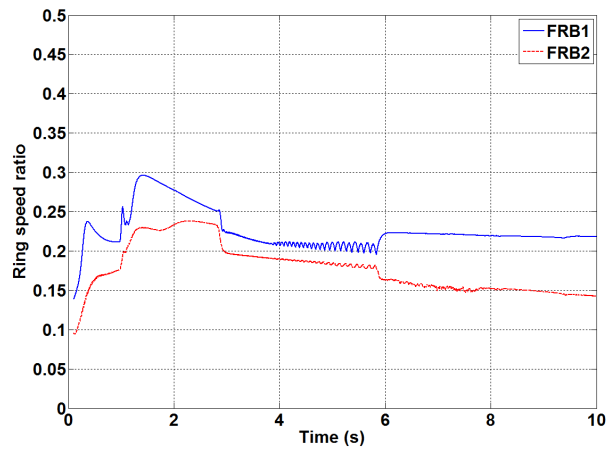
(f)



(g)



(h)



(i)

Fig. 5.9. (continued)

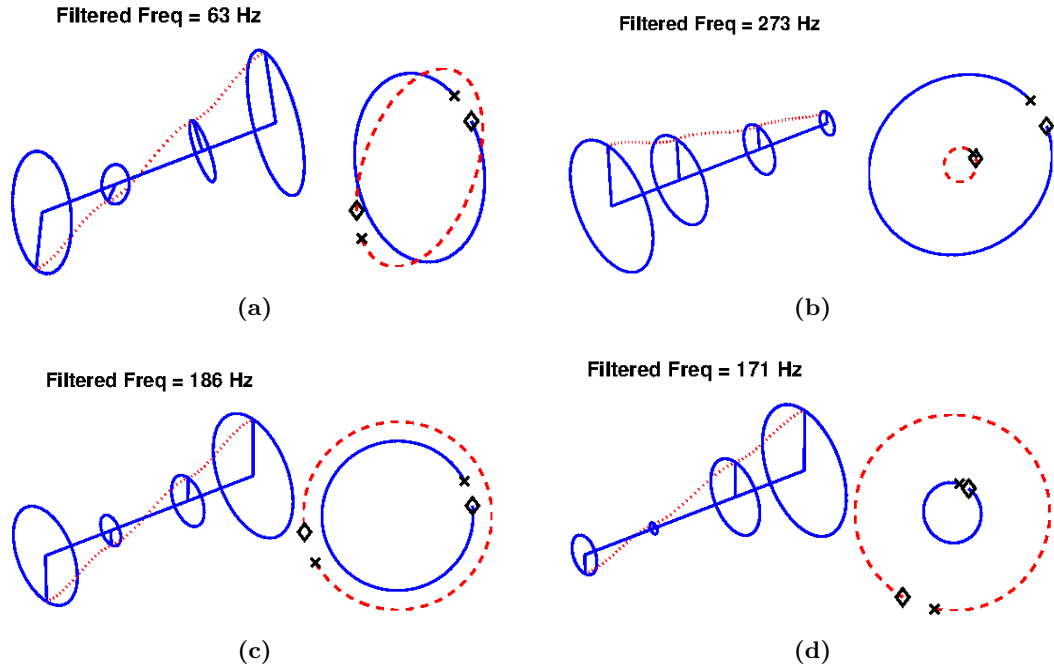


Fig. 5.10. Filtered mode shapes and orbits for Sub 1, Sub 2 and Sub 3 when the outer clearances are $40\ \mu\text{m}$ at selected rotor speeds: (a) 169 Hz for Sub 1, (b) 507 Hz for Sub 2, (c) 998 Hz for Sub 1 and (d) 2012 Hz for Sub 3.

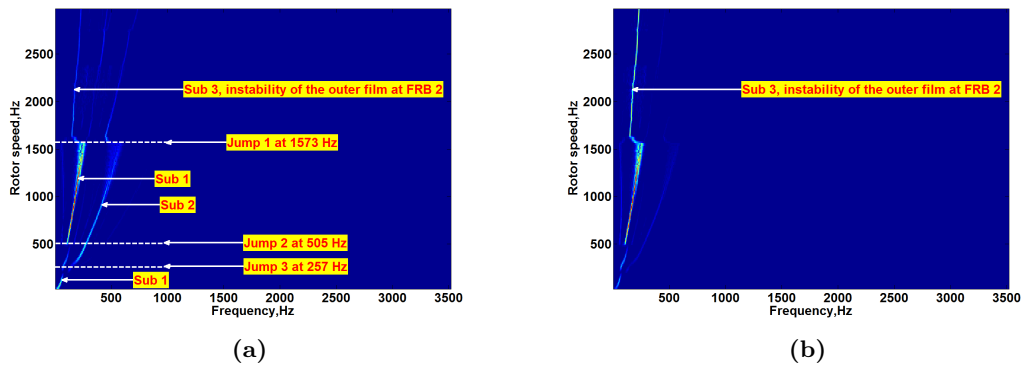


Fig. 5.11. Top-views for the waterfall diagrams of run-down simulation when $C_2 = 40\ \mu\text{m}$: (a) for y_1/C_1 and (b) for y_4/C_1 .

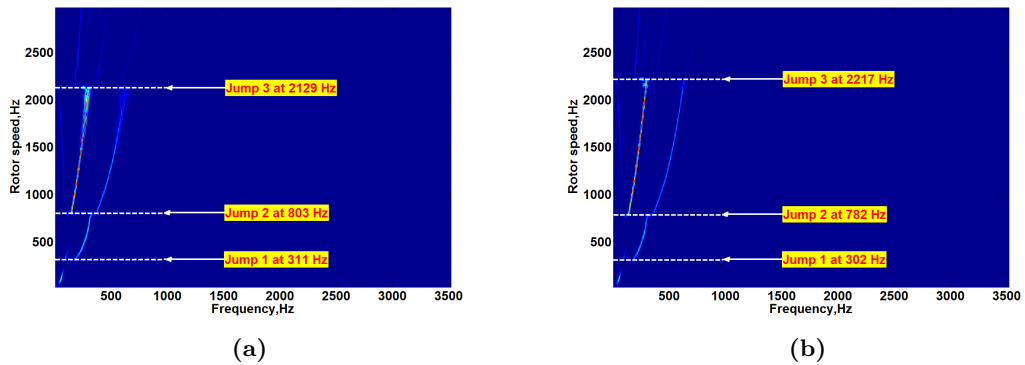


Fig. 5.12. Comparisons of the top-views of waterfall diagrams for y_1/C_1 from run-up simulations: (a) $C_2 = 42\ \mu\text{m}$, (b) $C_2 = 43\ \mu\text{m}$

by Sub 2 with a smaller magnitude. One can also appreciate a sudden frequency increase of Sub 2 then. The further jump from Sub 1 to Sub 3 at 1754 Hz can clearly be observed in Fig. 5.9c.

- (b) Corresponding to the above-mentioned waterfall plots, the observed three jumps can be identified from the considerable variations in the displacement plot depicted in Fig. 5.9e and f. The coexistence of Sub 1 and Sub 2, after the onset of Jump 2 and before the appearance of Jump 3, forces the rotor to work with the highest vibration amplitude. The vibration amplitudes of both ends are comparable with each other then, albeit the displacement plot at the compressor centre is not given. The onset of Jump 3 leads to dramatic decreases of the vibration amplitudes at both ends, although amplitude at the turbine centre is higher than that at the compressor centre. What can also be observed is that the existence of Sub 3 is not able to further increase the vibration amplitude at the turbine centre as the rotor speed moves up, which is a major difference as compared to the characteristics of the *CLC Oscillation* observed in Simulation 1 and Simulation 2 over the relatively high speed range.
- (c) The eccentricity plots in Fig. 5.9g and h show, regarding to the Sub 1 at the lower end of the speed range, ϵ_{ic} is clearly higher than ϵ_{oc} at FRB 1, while ϵ_{it} is actually smaller than ϵ_{ot} at FRB 2. At 227 Hz, the system becomes temporarily stable as indicated by the short line connecting the Sub 1 dominant range with the Sub 2 dominant range. When the dominance of Sub 2 is established after Jump 1, it is evident the eccentricities of both inner films are bigger than those of the corresponding outer films, which indicates the dominant instabilities of inner films. Thereafter, when Sub 1 rebuilds the dominant position, violent fluctuations can be found for the eccentricities of both FRBs. Meanwhile, the mean values of ϵ_{oc} and ϵ_{ot} are higher than those of ϵ_{ic} and ϵ_{it} , respectively. Interestingly, after the occurrence of Jump 3, all of the four eccentricities suddenly climb down, although only ϵ_{ot} retains its high-amplitude position. This means, following Jump 3, the instability of the outer film at FRB 2 is dominant.
- (d) The discontinuities in the ring speed ratio plot given in Fig. 5.9i also strongly imply the onset of the dominant frequency component jumps. The dominance of Sub 2 brings out the highest ratio values for both bearings, although the ratio at FRB 1 is bigger than at FRB 2. In contrast to Simulation 1 and 2, the major discrepancy is the emergence of Sub 3 can enlarge the difference between the two speed ratios.

- (e) As indicated by the filtered mode shape plots in Fig. 5.10, Sub 1 is a conical forward mode, in which the two nodes on the left-hand side are out of phase by 180 degrees with those two on the right-hand side. Sub 2 is a slightly bent cylindrical mode with the smallest amplitude at the turbine end. After Jump 2, accompanied by Sub 2, the dominant Sub 1 is still in a conical shape. The phase differences between the four nodes are exactly the same as Sub 1 at the start of simulation. This is the reason for us to give both Sub components the same name. However, even though Sub 3 is also a conical mode, after zooming in on Fig. 5.10d, it has been observed that Node 2 is actually in phase with Node 3 and 4 and out of phase with Node 1. Similar to the results given in Simulation 2, Sub 1 appearing at the beginning of the simulation and Sub 2 correlate well with the linearly predicted unstable Mode 1 and Mode 2, respectively, as compared to the linear predictions shown in Fig. 2.14 and Fig. 2.15. The unstable Mode 2 dominant range in Fig. 2.14c is from 300 Hz to 850 Hz, which surprisingly agree well with the nonlinearly simulated Sub 2 dominant range, i.e., from 332 Hz to 850 Hz. This further confirms the benefits of the linear analysis to the understanding of nonlinear results. However, further nonlinear jumps occurring at rotor speeds higher above the Sub 2 dominant range can hardly be linearly predicted. After the onset of Jump 2, one can notice the coexistence of Sub 1 as well as Sub 2, which evidences the instability of outer and inner films, respectively. This means the coexistence of inner and outer film instability does not necessarily bring about the occurrence of the *CLC Oscillation*. The two Sub components which clearly indicate their instability are not synchronized. The Sub 1 component appearing after Jump 2 might correspond to the unstable Mode 3, but its frequency is actually higher than that of the unstable Mode 3, probably caused by the influence of the inner film instability. With increasing rotor speed from 850 Hz to 1754 Hz, the magnitude of the Sub 2 component follows a descending trend until Jump 3 occurs, which can be linearly explained as the increase of the logarithmic decrement in Fig. 2.16c. The following Sub 3 correlates well with the unstable Mode 3.
- (f) The run-down simulations presented in Fig. 5.11 show the three jump speeds are lower than in the run-up simulation due to the hysteresis characteristic of the fluid film. Another difference is the frequency jump of Sub 2 at the onset of Jump 2 cannot be observed in the run-down simulation.
- (g) Further simulations with higher bearing clearance values, i.e. 41, 42 and 43 μm , have also been carried out by the authors and the results of the last two are shown in

Fig. 5.12. As can be seen, the onset speeds of Jump 1 and Jump 2 become slightly smaller when the value of outer clearance is increased. What can also be observed is the considerable change of the onset speed of Jump 3 to higher values, in comparison with the simulation results given in Fig. 5.9.

5.2.4 Simulation 4 ($C_2 = 44 \mu\text{m}$)

In this subsection, we present and discuss the simulation results (Figs. 5.13-5.15) when both bearing clearances are increased to $44 \mu\text{m}$. In comparison to the results of Simulation 3, the obvious difference is the dominance of Sub 1 cannot be established, and it is replaced by Sub 3 directly after the occurrence of Jump 2. The dominant frequency jump sequence is Sub 1 to Sub 2 and subsequently Sub 2 to Sub 3. The summary of the obtained results is given as follows.

- (a) The waterfall plots depicted in Figs. 5.13a-d show that there are two jumps in the system under investigation. Similar to Simulation 3, the component Sub 1, firstly, appears at a quite low rotor speed and disappears when the rotor speed goes up to 193 Hz. At 299 Hz, the dominant frequency jumps to Sub 2 although Sub 1 still exists until at 427 Hz it disappears again. Subsequently, at 787 Hz, the dominant frequency further jumps to Sub 3 from Sub 2. Following a magnitude decreasing trend, the Sub 2 component with a higher frequency can still be identified on the waterfall diagram at the compressor end.
- (b) Fig. 5.13e and f present the displacement plots of the compressor and turbine centres, the discontinuities in which clearly indicate the onset of the nonlinear jumps found in the waterfall plots. Prior to Jump 2, the mean value of y_4/C_1 is negative, corresponding to the direction of the static load on FRB 2. Since Jump 2 brings about Sub 3 directly rather than Sub 1, after the occurrence of Jump 2, the maximum vibration amplitudes of both ends are smaller than in Simulation 3. Similar to Simulation 3, Sub 3 cannot further increase the vibration amplitude on the turbine side, which is approximately constant, though the rotor speed continuously ascends. By contrast, displacement at the compressor end descends generally as the rotor speed climbs up.
- (c) The eccentricity plots are shown in Fig. 5.13g and h. Earlier than the onset of Jump 2 at 787 Hz, the plots are quite similar to Simulation 3. The major difference is, after the occurrence of Jump 2, both inner and outer eccentricities at FRB 1 are following a decreasing trend and finally fluctuate around a small mean value. However, the

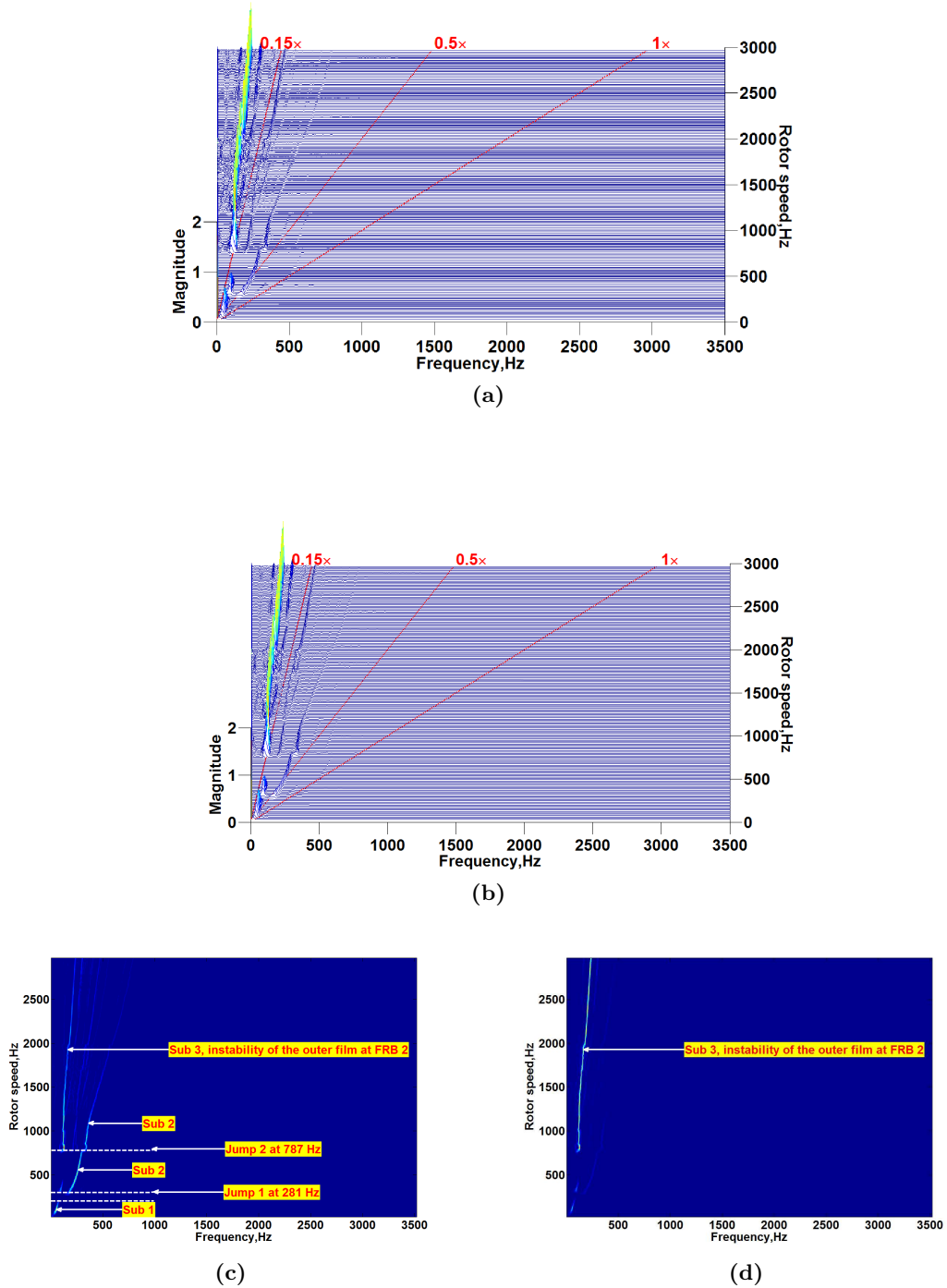


Fig. 5.13. Run-up simulation when the TC rotor is perfectly balanced and $C_2 = 44 \mu\text{m}$: (a), (b) waterfall plots of the compressor end y_1/C_1 and turbine end y_4/C_1 in Y axis direction, respectively, (c), (d) top-views of the waterfall diagrams given in (a) and (b), corresponding to y_1/C_1 and y_4/C_1 , respectively, (e) and (f) displacement plots of y_1/C_1 and y_4/C_1 , (g), (h) eccentricity plots of the inner and outer oil films at FRB 1 and FRB 2, respectively, (i) ring speed ratios of FRB 1 and FRB 2.

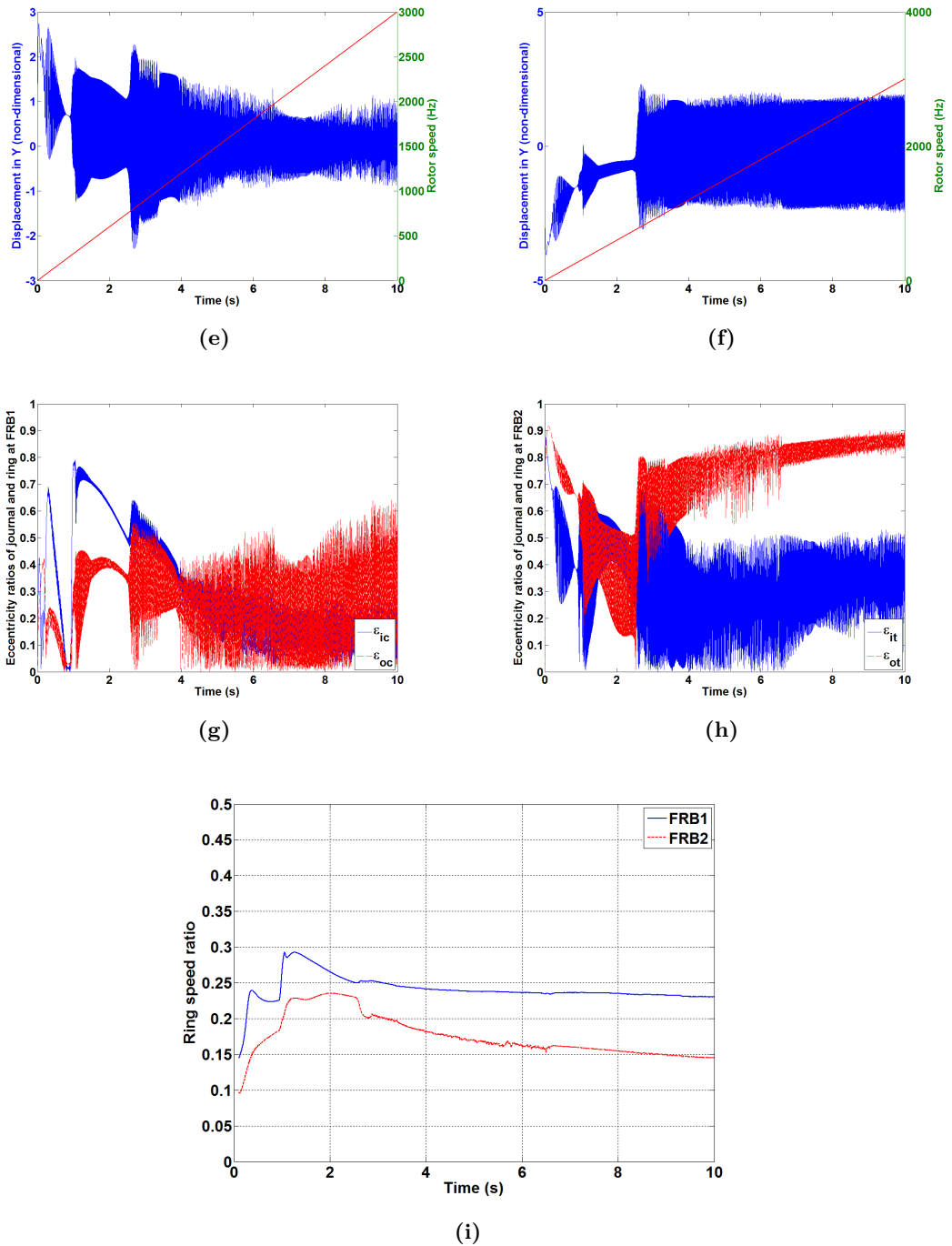


Fig. 5.13. (continued)

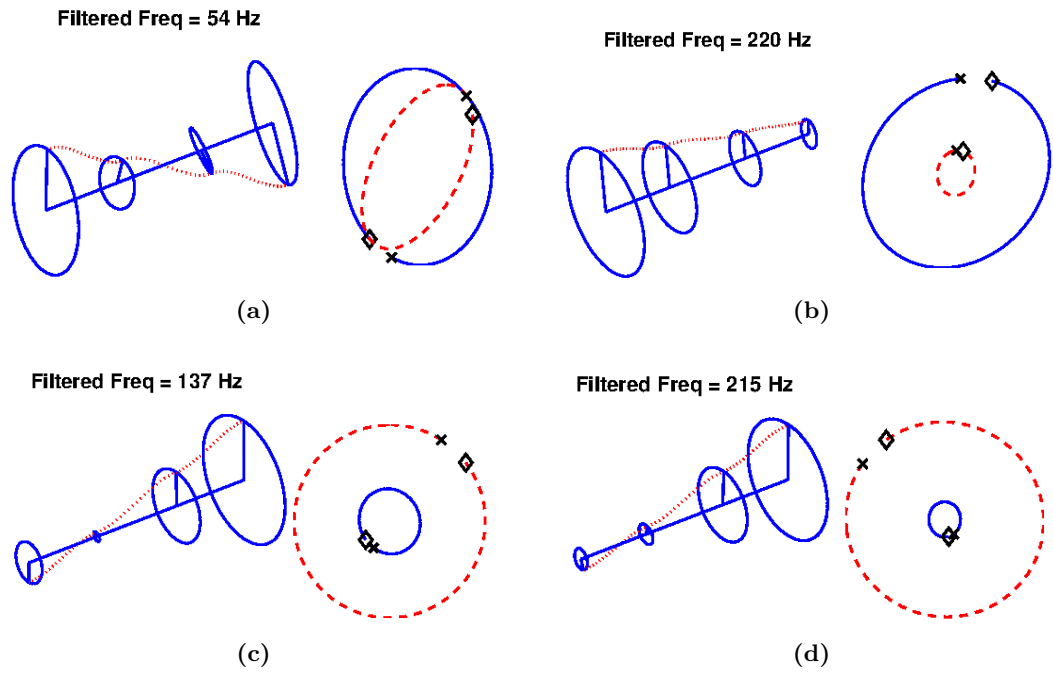


Fig. 5.14. Filtered mode shapes and orbits for Sub 1, Sub 2 and Sub 3 when the outer clearances are $44 \mu\text{m}$ at selected rotor speeds: (a) 108 Hz for Sub 1, (b) 399 Hz for Sub 2, (c) 1505 Hz for Sub 3 and (d) 2611 Hz for Sub 3.

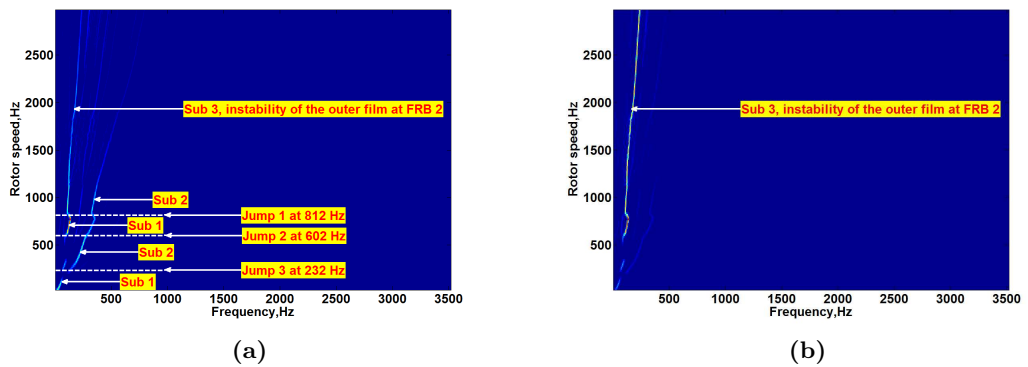


Fig. 5.15. Top-views for the waterfall diagrams of run-down simulation: $C_2 = 44 \mu\text{m}$. (a) for y_1/C_1 and (b) for y_4/C_1 .

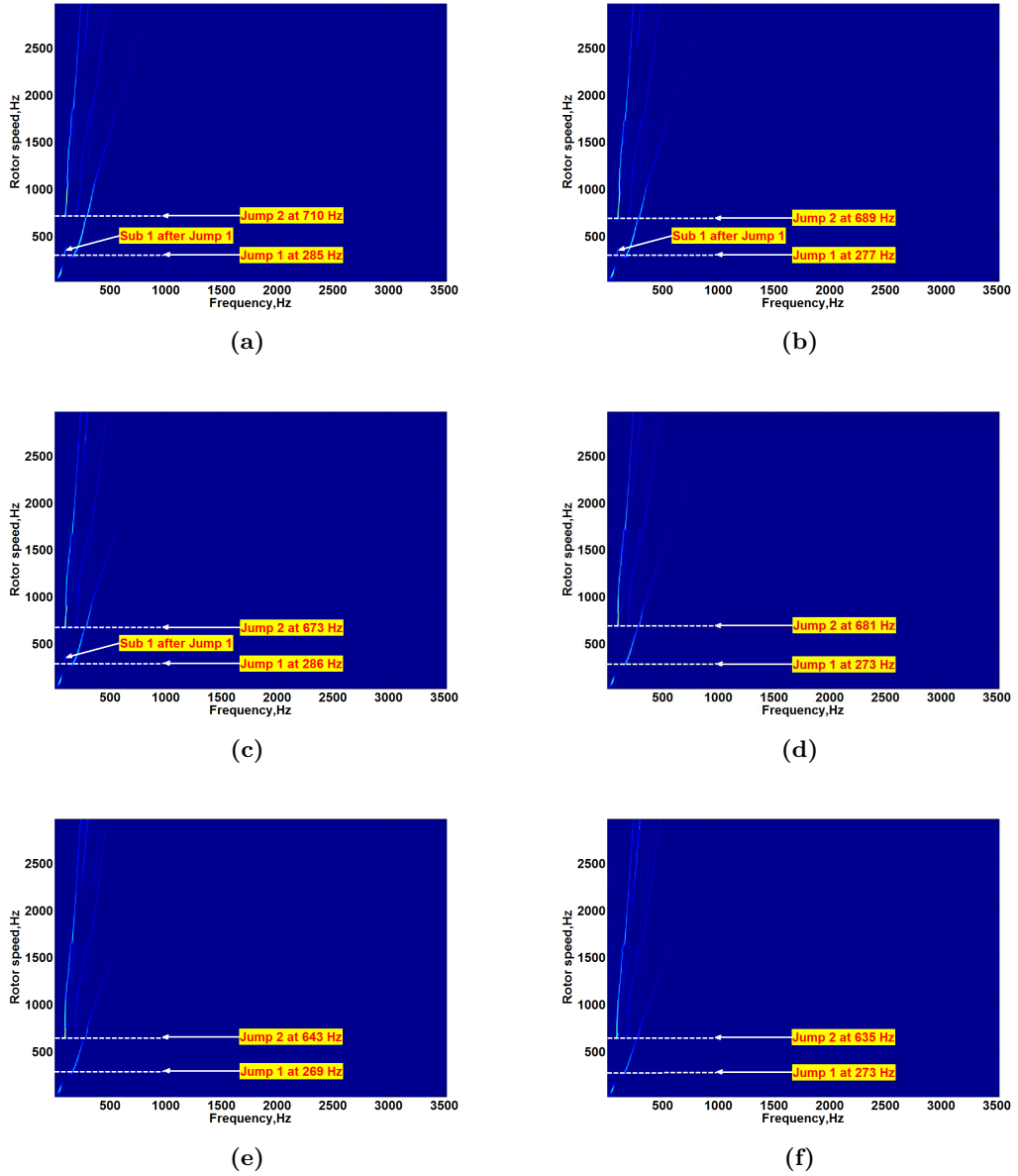


Fig. 5.16. Comparisons of the top-views of waterfall diagrams for y_1/C_1 from run-up simulations: (a) $C_2 = 45 \mu\text{m}$, (b) $C_2 = 46 \mu\text{m}$, (c) $C_2 = 47 \mu\text{m}$, (d) $C_2 = 48 \mu\text{m}$, (e) $C_2 = 49 \mu\text{m}$ and (f) $C_2 = 50 \mu\text{m}$

outer eccentricity at the FRB 2 suddenly leaps up to a high value then. Thereafter, the mean value of ϵ_{ot} consistently moves up with the ascending rotor speed. This phenomenon clearly implies the well-developed instability at the outer clearance of FRB 2 dominates the rotor response, which can also be appreciated in Fig. 5.13b and d.

- (d) Apart from the transient start, the plot of ring speed ratios given in Fig. 5.13i shows the ratio of FRB 1 is higher than that of FRB 2 throughout the whole speed range. Corresponding to the two rises of ϵ_{ic} in Fig. 5.13g, there are two leaps of the ring speed ratio at FRB 1. The maximum of the ratio at FRB 1 is reached at the onset of Jump 1, at which ϵ_{ic} is also maximum, and it follows a decreasing trend afterwards. The dominance of Sub 2 also results in the top position of the ratio at FRB 2. The subsequent occurrence of Sub 3 also leads to a descending trend of the ratio at FRB 2.
- (e) Fig. 5.14 shows the filtered mode shapes and orbits at four selected speeds. One can appreciate the similarities between Fig. 5.14 and Fig. 5.10 in the mode shapes of Sub 1, Sub 2 and Sub 3. In comparison with the linear results shown in Fig. 2.14d and Fig. 2.15, they correspond to the unstable Modes 1, 2 and 3, respectively. The linearly predicted unstable Mode 2 dominant range is from 250 Hz to 800 Hz, which is in good agreement with the nonlinearly simulated Sub 2 dominant range from 299 Hz to 787 Hz. After Jump 2, the major discrepancy between Simulation 4 and 3 can possibly be attributed to the weaker unstable Mode 2 and stronger unstable Mode 3 in Fig. 2.16d as compared to Fig. 2.16c.
- (f) The top-views of waterfall plots derived from the run-down simulation are given in Fig. 5.15. As the rotor speed goes down, one major difference is identified. There is one more jump from Sub 3 to Sub 1 at 812 Hz in the run-down simulation, which excites the maximum magnitudes shown in the two figures. The established Sub 1 disappears shortly at 602 Hz when Jump 2 sets in. The onset speed is actually lower than in the run-up simulation as a result of the hysteresis characteristic. Corresponding to Jump 1 in the run-up simulation, for the same reason, the onset speed of Jump 3 in the run-down simulation is smaller than in the run-up simulation as well.
- (g) The results of further simulations with bigger outer clearance values are depicted in Fig. 5.16. Despite some small differences, they are quite similar to the results when the bearing outer clearances are 44 μm . One of the differences is the appearance of

Sub 1 after Jump 2 cannot be observed with the last three bearing clearance values. Another is the onset speed of Jump 2 descends when the outer clearance value is increased, although the influence on the onset speed of Jump 1 is negligible.

5.2.5 Discussions

The presented simulation results in s 5.2.1-5.2.4 show that the considered bearing outer clearance range can be subdivided into four ranges:

- (a) Range 1: 30 μm to 33 μm . The dominant Sub frequency is the *CLC Oscillation* throughout the considered speed range. Nonlinear jump has not been observed. No major difference has been found in the run-down simulation when both bearing outer clearances are 30 μm . In further run-up simulations, increasing the bearing clearance size within the range will lead to the decrease of eccentricities, ring speed ratios as well as vibration amplitude at the turbine end.
- (b) Range 2: 34 μm to 39 μm . Nonlinear jumps are identified and follow the sequence: Sub 1 \rightarrow Sub 2 and subsequently Sub 2 \rightarrow *CLC Oscillation*. The run-down simulation with 35 μm bearing outer clearance size shows that the dominant frequency follows the same track to come back but the transition range is shorter than in the run-up simulation. Meanwhile, the onset speeds of Jump 1 and 2 are smaller than those of the corresponding Jump 2 and Jump 1 in the run-up. However, the run-down simulation, when bearing outer clearances are 34 μm , does not reveal any frequency jump and is analogous to the simulation results in Range 1. Run-up simulations with bigger outer clearance sizes in the range result in the earlier occurrences of nonlinear jumps as well as longer transition ranges.
- (c) Range 3: 40 μm to 43 μm . Nonlinear jumps are observed, and the jump sequence of dominant frequency is: Sub 1 \rightarrow Sub 2, Sub 2 \rightarrow Sub 1 and then Sub 1 \rightarrow Sub 3. For the run-down simulation with 40 μm bearing outer clearances, the dominant frequency jump sequence is the same as in run-up simulation, although the onset speeds of the three jumps become smaller than those in the run-up. Further run-up simulations show that, in the considered range, increasing the bearing outer clearances will lead to the increase of the onset speed of Sub 3.
- (d) Range 4: 44 μm to 50 μm . The results with the bearing clearance values in this range also display nonlinear jumps, following the sequence: Sub 1 \rightarrow Sub 2 and Sub 2 \rightarrow Sub 3. Other than Range 1 to Range 3, the performed run-down simulation

with $C_2 = 44\ \mu\text{m}$ reveals a different jump track: Sub 3 \rightarrow Sub 1, then Sub 1 \rightarrow Sub 2 and finally Sub 2 \rightarrow Sub 1. Run-up simulations with ascending bearing outer clearance values cause the earlier onset of Sub 2 as well as the disappearance of Sub 1 after Jump 2 when the bearing clearance values are greater than $47\ \mu\text{m}$.

Chapter 6

Nonlinear Effects of Unbalance

As shown earlier in the preliminary study in Section 3.4, the TC rotor response can be considerably affected by the introduced 30 μm in-phase unbalance offsets, which correspond to the heavily unbalanced condition. Using the run-up and run-down simulation method shown in Chapter 5, this chapter aims to thoroughly investigate the influence of imbalance magnitude and distribution on the dynamic response of the TC rotor-FRB system. Variations of the imbalance magnitude as well as distribution are considered in the performed simulations. The magnitude of imposed unbalance changes through varying the offset displacement e (see Eqs. (2.2a) and (2.2b)) from 0 μm to 30 μm with an increment of 5 μm for both disks, while two types of unbalance distribution are considered, i.e., in-phase unbalance ($\delta_c = \delta_t = 0$) as well as out-of-phase unbalance ($\delta_c = 0, \delta_t = \pi$). The simulation parameters of the nonstationary simulations are listed in Table 6.1. In comparison with the nonstationary simulations shown in Chapter 5, the shaft ramp rate is increased to 500 Hz in the run-ups and decreased to -500 Hz in the run-downs. Moreover, the rotor speed range is enlarged up to 3500 Hz to investigate the rotor response at even higher rotor speeds. In consideration of the stiffness of the system equations of motion given in Eq. (2.1), the robust MATLAB[®] routine ode15s[®] solver has been employed to successfully fulfil the simulation objectives throughout this chapter. All simulations have been carried out with a relative error tolerance of 1E-6. To avoid singularities of oil film locators α_i and α_o in Eqs. (3.9a) and (3.9b), a small deviation from the bearing origin, i.e., one-thousandth of the bearing outer clearance, is assigned to the displacements of both ring centres in the X axis direction and the negative Y axis direction as the initial conditions of the performed run-up simulations. All elements in the displacement vector \mathbf{q} (see Section 2.1) are assumed to be zero at the start of simulation. Initial conditions for run-down simulations are selected as the end of the run-up data simulated with the

Parameters	Value
Shaft ramp rate (Hz/s)	$\beta = \pm 500$
Total integration time (s)	7
Total time steps	70,000
Rotor speed range (Hz)	0 ~ 3500

Table 6.1. Parameters for run-up and run-down simulations

same parameters. As can be seen from the following, the obtained results systematically reveal the effects of imposed unbalance on the dynamic behaviour of the investigated TC rotor-FRB system. In the performed simulations, with varying unbalance magnitude and distribution, intriguing, distinct phenomena, which have not been reported previously, will occur. It is structured as follows. The results of nonlinear simulations with three selected bearing outer clearance sizes are presented in Sections 6.1-6.3. The results are further discussed in Section 6.4.

6.1 Simulation 1 ($C_2 = 35 \mu\text{m}$)

In this section, the results of the run-up and run-down simulations are presented when both bearing outer clearances are $35 \mu\text{m}$. The results of the perfectly balanced rotor will be shown first as a reference simulation, while the results considering the variable unbalance offset are given afterwards.

6.1.1 Perfectly balanced rotor: $e = 0$

Fig. 6.1 shows the run-up simulation results when the rotor is in a perfectly balanced condition. The waterfall diagrams of the non-dimensionalized displacements of the compressor centre and turbine centre, i.e. y_1/C_1 and y_4/C_1 , are given in Fig. 6.1a and b, respectively. The top-view of Fig. 6.1a are depicted in Fig. 6.1c. Fig. 6.1d shows the displacement plot of y_4/C_1 . The eccentricity plot of the two oil films at FRB 1 are given in Fig. 6.1e, which is followed by the ring speed ratio plot of FRB 1 and FRB 2 in Fig. 6.1f. Corresponding to the run-up simulation, the results of run-down simulation are depicted in Fig. 6.2. Moreover, the filtered mode shapes of the interested subsynchronous component at selected four rotor speeds during the run-up are given in Fig. 6.3. The obtained results are similar to those shown in Fig. 5.4 and are briefly summarised as follows.

- (a) Fig. 6.1a and b clearly shows the TC rotor-FRB system becomes unstable at the start of simulation. Fig. 6.1e indicates that it is because of the onset of inner film

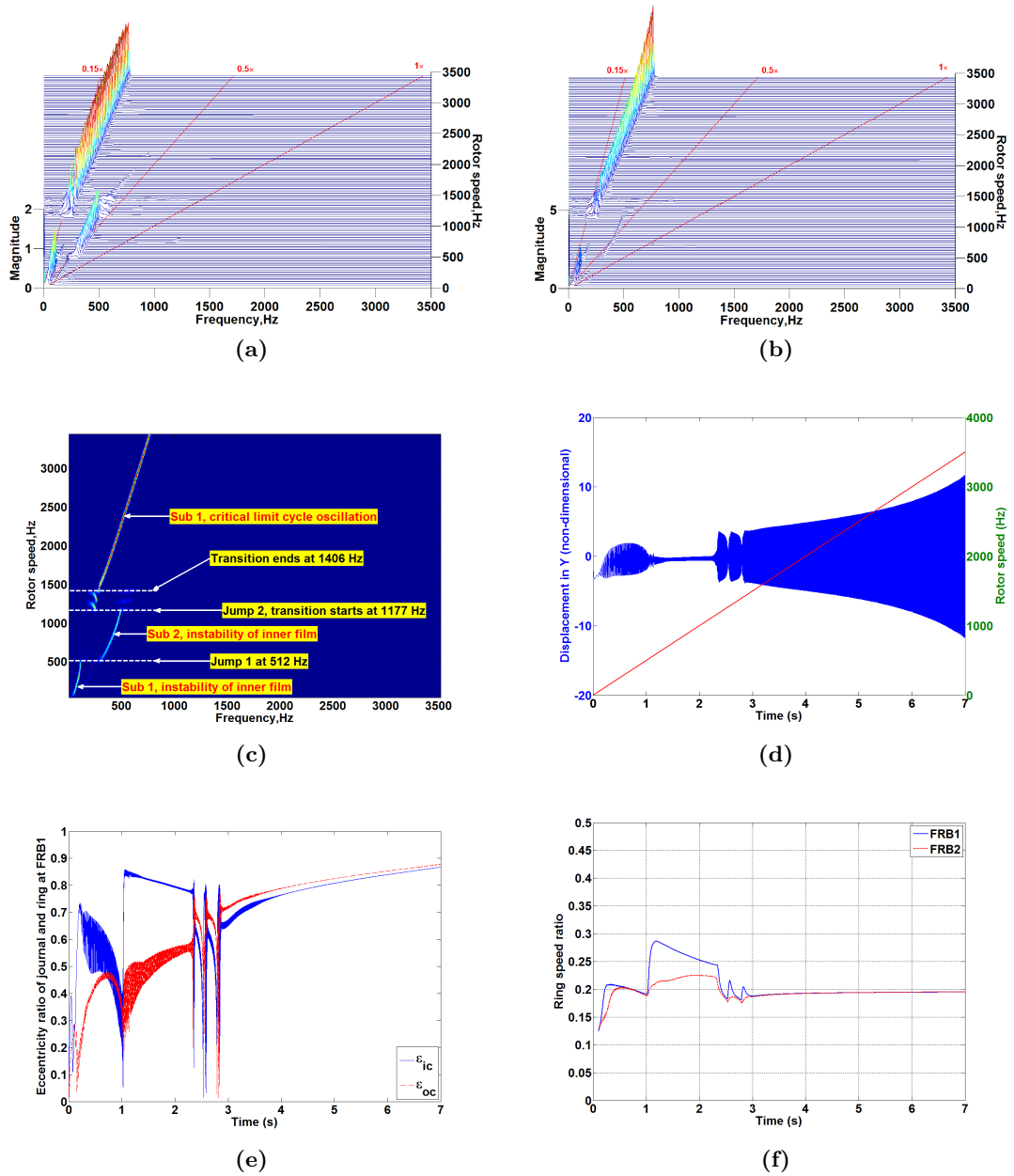


Fig. 6.1. Run-up simulation when the TC-FRB system is in a perfectly balanced condition ($e = 0$) and $C_2 = 35 \mu\text{m}$: (a), (b) non-dimensional waterfall plots for the displacements of the compressor end and turbine end in Y axis direction, i.e., y_1/C_1 and y_4/C_1 , respectively, (c) top-view of (a), (d) displacement plot of y_4/C_1 , (e) eccentricity plot of the inner and outer oil films at FRB 1, (f) ring speed ratio plot of FRB 1 and FRB 2.

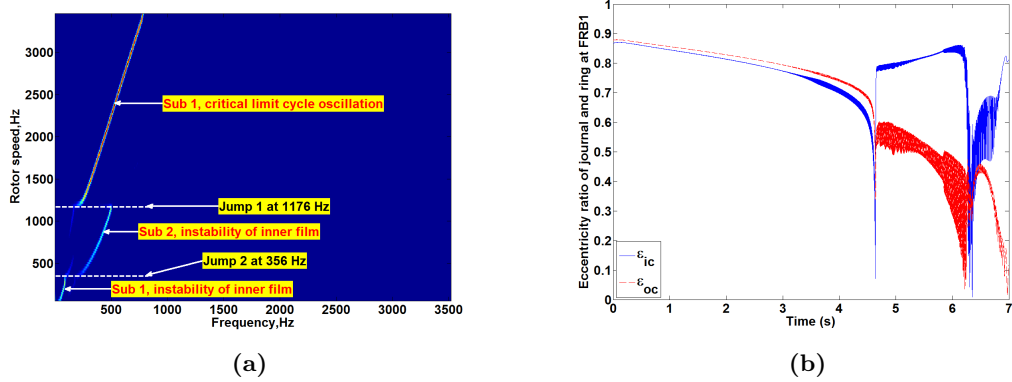


Fig. 6.2. Run-down simulation when the TC-FRB system is in a perfectly balanced condition ($e = 0$) and $C_2 = 35 \mu\text{m}$: (a) top-view of the waterfall diagram of y_1/C_1 , (b) eccentricity plot of the inner and outer oil films at FRB 1.

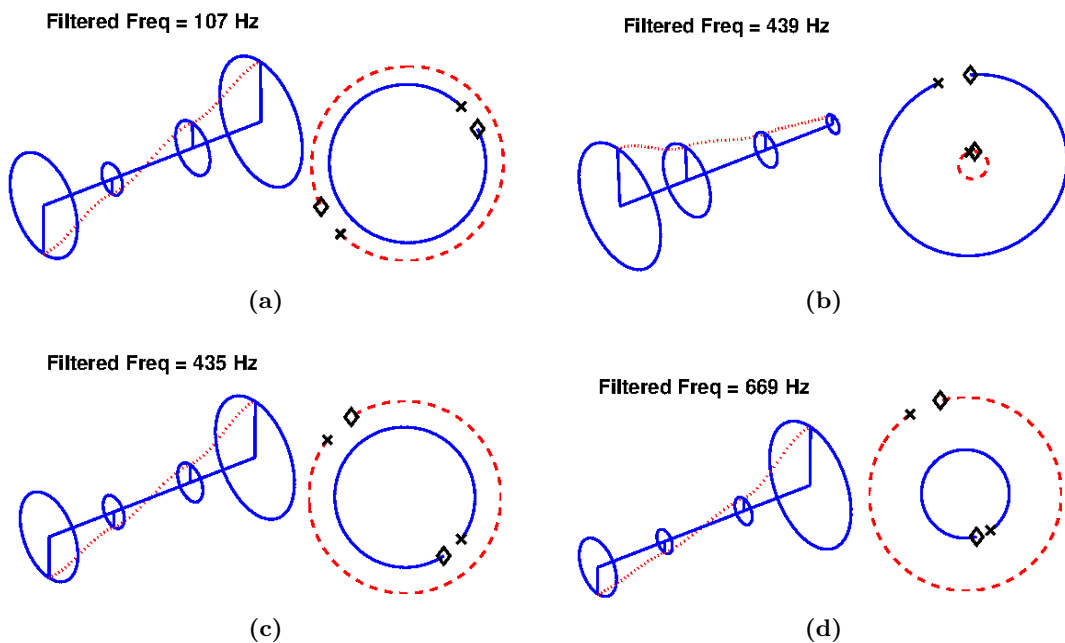


Fig. 6.3. Filtered mode shapes and orbits for Sub 1 and Sub 2 of run-up simulation when the outer clearances are $35 \mu\text{m}$ and the rotor is perfectly balanced at selected rotor speeds: (a) 409 Hz, (b) 896 Hz, (c) 1997 Hz and (d) 2995 Hz.

instability at FRB 1. The mode shape plot of Sub 1 at 409 Hz given in Fig. 6.3a shows Sub 1 is a conical forward mode.

- (b) At 512 Hz, the nonlinear Jump 1 takes place, leading to the shift of dominant subsynchronous component from Sub 1 to Sub 2. Fig. 6.1e shows Sub 2 is originated from the further developed instability of the inner oil films. Fig. 6.3b clearly shows that Sub 2 is in cylindrical shape, although the displacement at the compressor end is bigger than at the turbine end.
- (c) At 1177 Hz, the occurrence of Jump 2 brings about the onset of *CLC Oscillation* until the very end of the simulation. It should be noted that Jump 2 cannot be completed quickly as soon as it occurs, as a transition range, i.e. the situation of the coexistence of Sub 1 and Sub 2, is initiated first until 1406 Hz.

In comparison with the run-up, the run-down simulation results given in Fig. 6.2 show the transition range disappears. What can also be observed is the onset speed of Jump 2 (356 Hz) is smaller than that of the corresponding Jump 1 (512 Hz) in the run-up simulation, owing to the hysteresis effect of the oil film.

6.1.2 Out-of-phase unbalance: $\delta_c = 0, \delta_t = \pi$

The run-up and run-down simulation results of the case that the variable out-of-phase unbalance offsets are equally added to the compressor and turbine disks are presented in Figs. 6.4-6.6. The main characteristics of the obtained results are given as follows.

- (a) In the run-up simulations, as shown in Fig. 6.4a and b, when relatively small unbalance offset is added, i.e., 5 μm and 10 μm , the results still retain the significant features of the perfectly balanced simulation. However, one can also notice the onset speed of Jump 2 actually becomes smaller. The interesting situation is when higher unbalance offsets are applied, i.e., 15 μm , 20 μm , 25 μm and 30 μm , the waterfall plots in Figs. 6.4c-f deviate considerably from the perfectly balanced condition in the low rotor speed range and Sub 2 completely disappears. What can also be imagined and observed is the bigger the unbalance offset, the clearer the synchronous component is shown in the figures. When the offset is higher than 10 μm , Sub 1 derived from the inner oil film instability at the start of simulation can be suppressed by the imposed unbalance, and the TC rotor is oscillating around the static equilibrium with a frequency equal to the rotor running speed (see Fig. 6.5a and b from 0 s to approximately 0.5 s). After a short period, the system becomes unstable and the

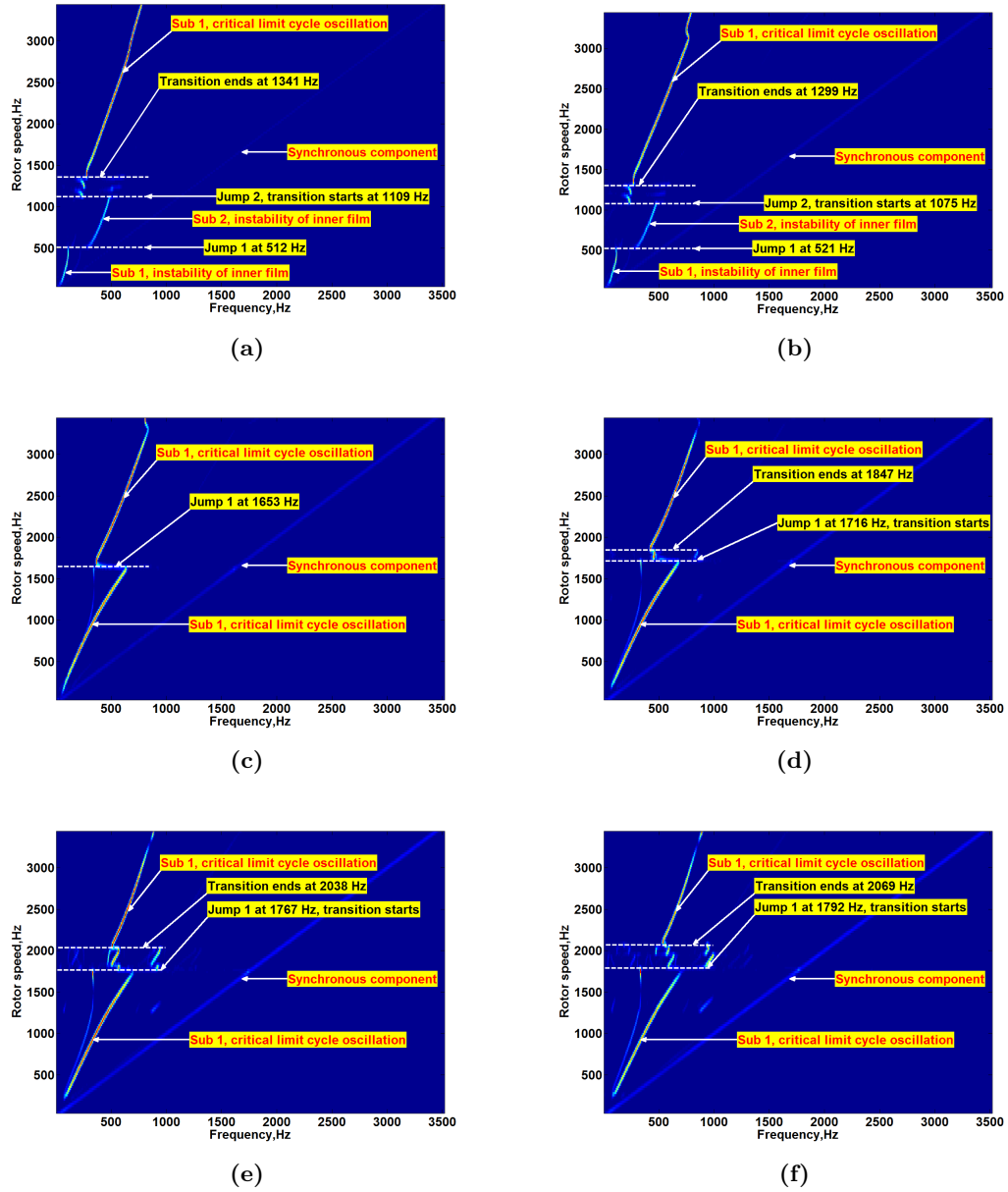


Fig. 6.4. Top-views of the waterfall plots of y_1/C_1 in run-up simulations when the out-of-phase unbalance is imposed ($\delta_c = 0$, $\delta_t = \pi$) and $C_2 = 35 \mu\text{m}$: (a) $e = 5 \mu\text{m}$, (b) $e = 10 \mu\text{m}$, (c) $e = 15 \mu\text{m}$, (d) $e = 20 \mu\text{m}$, (e) $e = 25 \mu\text{m}$ and (f) $e = 30 \mu\text{m}$.

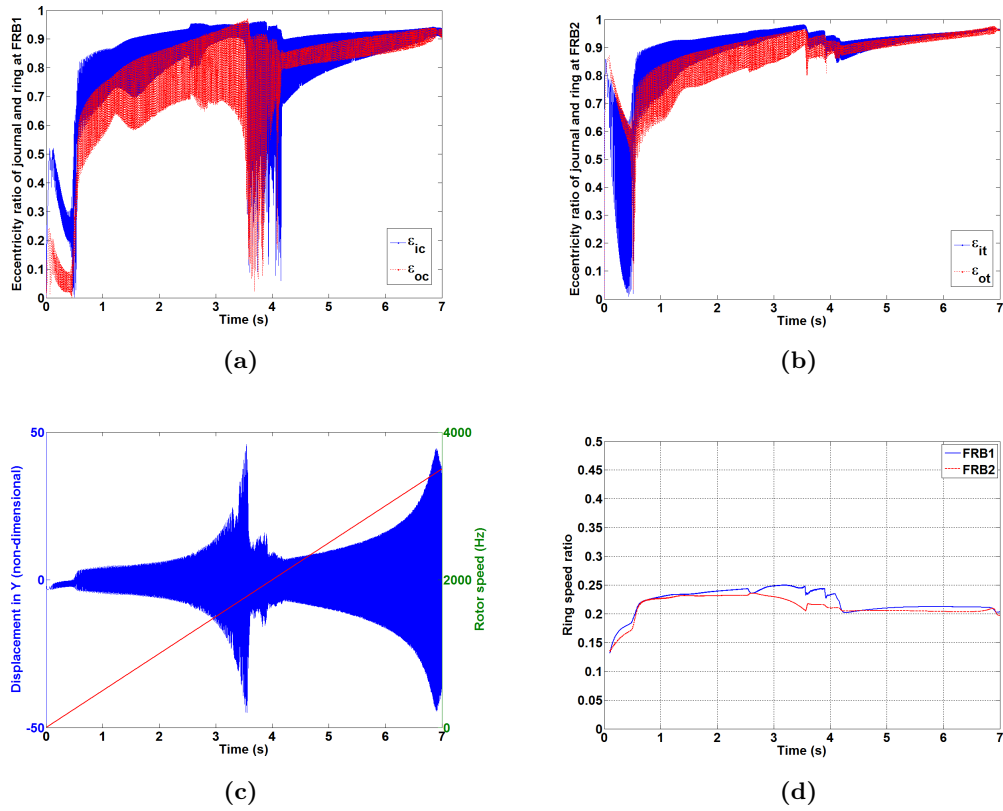


Fig. 6.5. Run-up simulation results when $C_2 = 35 \mu\text{m}$ and the $30 \mu\text{m}$ out-of-phase unbalance offset is imposed: (a) eccentricity plot of the inner and outer oil films at FRB 1, (b) eccentricity plot of the inner and outer oil films at FRB 2, (c) displacement plot of y_4/C_1 and (d) ring speed ratio plot of FRB 1 and FRB 2.

instability is characterised by the the quantum leaps of inner film and outer film eccentricities of both FRBs, although the mean values of the inner film eccentricities is actually bigger than the ones of outer films (see Fig. 6.5a and b), respectively. It is highly likely the *CLC Oscillation* has been excited. On the waterfall diagram, this instability is labelled by “Sub 1, critical limit cycle oscillation” in the relatively low-speed range (see Figs. 6.4c-f). It should be noted that the earlier emergence of the *CLC Oscillation* is extremely harmful to the safe operation of the TC under investigation, as the consistently and rapidly rising amplitude of y_4/C_1 may damage the rotor at a relatively low rotor speed (see Fig. 6.5c). Interestingly, one can still clearly observe one jump when those higher unbalance values are added. Instead of switching between Sub 1 and Sub 2 when the unbalance offsets are $5 \mu\text{m}$ and $10 \mu\text{m}$, the jump with unbalance offsets higher than $10 \mu\text{m}$ is actually from one *CLC Oscillation* component to another *CLC Oscillation* component starting with lower frequency at the onset speed. This jump cannot be completed quickly, and a special transition range is identified when the unbalance offset is above $15 \mu\text{m}$ (see Figs.

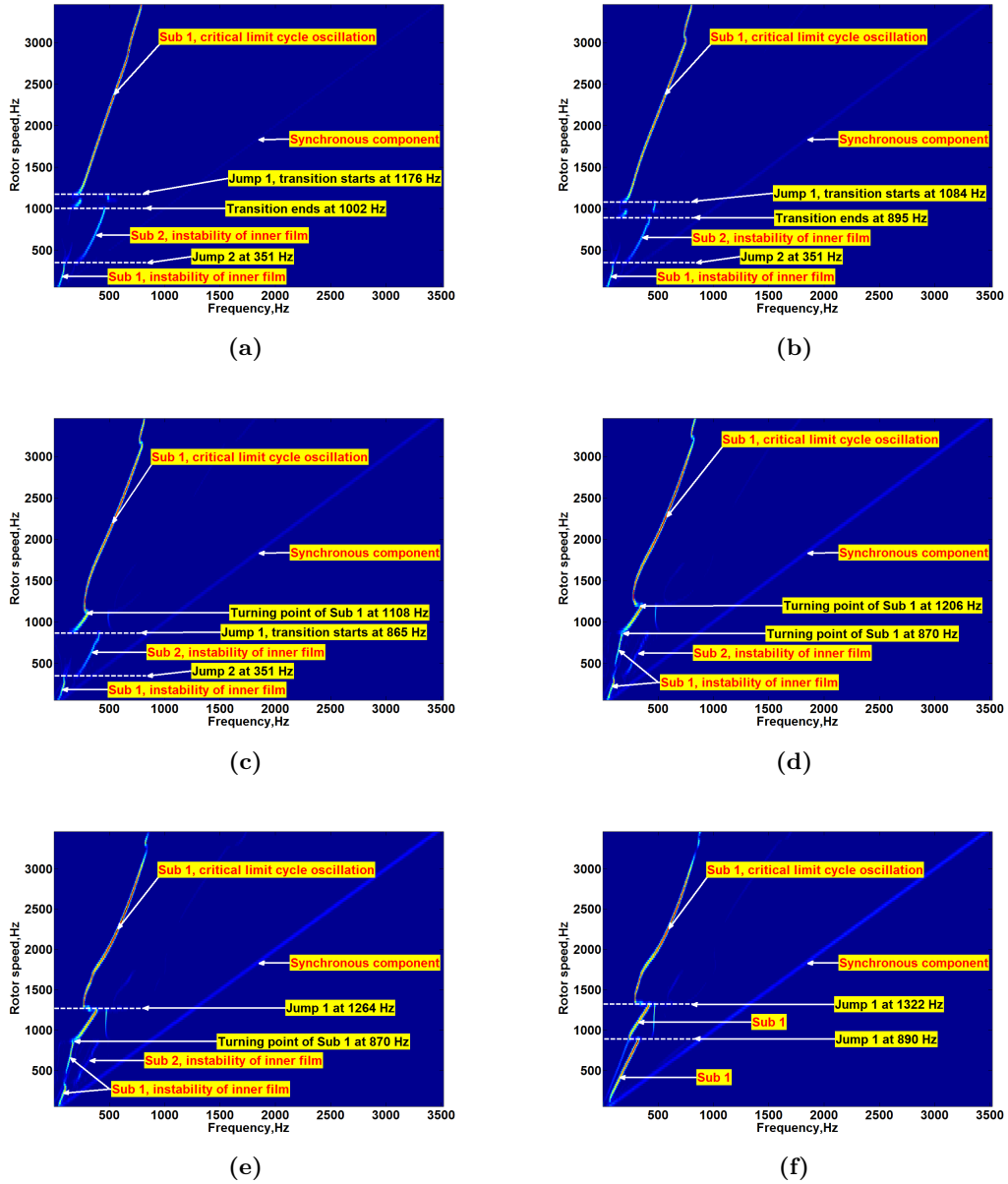


Fig. 6.6. Top-views of the waterfall plots of y_1/C_1 in run-down simulations when the out-of-phase unbalance is imposed ($\delta_c = 0$, $\delta_t = \pi$) and $C_2 = 35 \mu\text{m}$: (a) $e = 5 \mu\text{m}$, (b) $e = 10 \mu\text{m}$, (c) $e = 15 \mu\text{m}$, (d) $e = 20 \mu\text{m}$, (e) $e = 25 \mu\text{m}$ and (f) $e = 30 \mu\text{m}$.

6.4d-f). This jump may result from the branches of the ring speeds of two FRBs in the low speed range, which can probably lead to the break of instability synchronization of the two bearings. The disagreement of the two ring speed ratios also results in another subsynchronous component branching out from Sub 1. With increasing unbalance offsets in the 15 μm to 30 μm range, the onset speed of Jump 1 is slightly delayed.

- (b) In comparison with the results of the out-of-phase unbalanced run-ups as well as the perfectly balanced run-down, the out-of-phase unbalanced run-downs given in Fig. 6.6 exhibits some distinct phenomena. In contrast with the run-ups in Fig. 6.4, the existence of Sub 2 can clearly be identified even though the considerably high unbalance offset, i.e. 25 μm , is added to both disks, which is the main difference from the run-up simulation in the low-speed range. However, with the ascending unbalance offset, the magnitude of Sub 2 follows a descending trend. In Fig. 6.6f, when $e = 30 \mu\text{m}$, Sub 2 completely disappears and is replaced by Sub 1 derived from the instability of both inner and outer oil films at FRB 1 as well as FRB 2. It is clear that the threshold value of the induced out-of-phase unbalance offset to initiate the *CLC Oscillation* at the lower end of the TC rotor speed in run-down simulation is much higher than in the run-up. Compared to the perfectly balanced run-down case shown in Fig. 6.6, a short transition range from Sub 1 (*CLC Oscillation*) to Sub 2 is again observed, provided the unbalance offset is small enough, e.g. 5 μm and 10 μm .

6.1.3 In-phase unbalance: $\delta_c = \delta_t = 0$

The run-up and run-down simulation results under in-phase unbalanced condition are presented in Figs. 6.7-6.9, in which only four unbalance off-sets, i.e., 5 μm , 10 μm , 15 μm and 20 μm are selected from the performed simulations for brevity. The results are summarised as follows.

- (a) In the run-up simulations, the in-phase unbalance can affect the rotor response considerably, even though the imposed unbalance offset is as small as 5 μm . The dominance of Sub 2 brought out by Jump 1 when the rotor is perfectly balanced is replaced by the continuous Sub 1 since following the leap of ϵ_{ic} , considerable increase of ϵ_{oc} can be observed in Fig. 6.8a as well, despite the fact that the existence of Sub 2 can also be identified after close inspection. Together with the lift of the outer

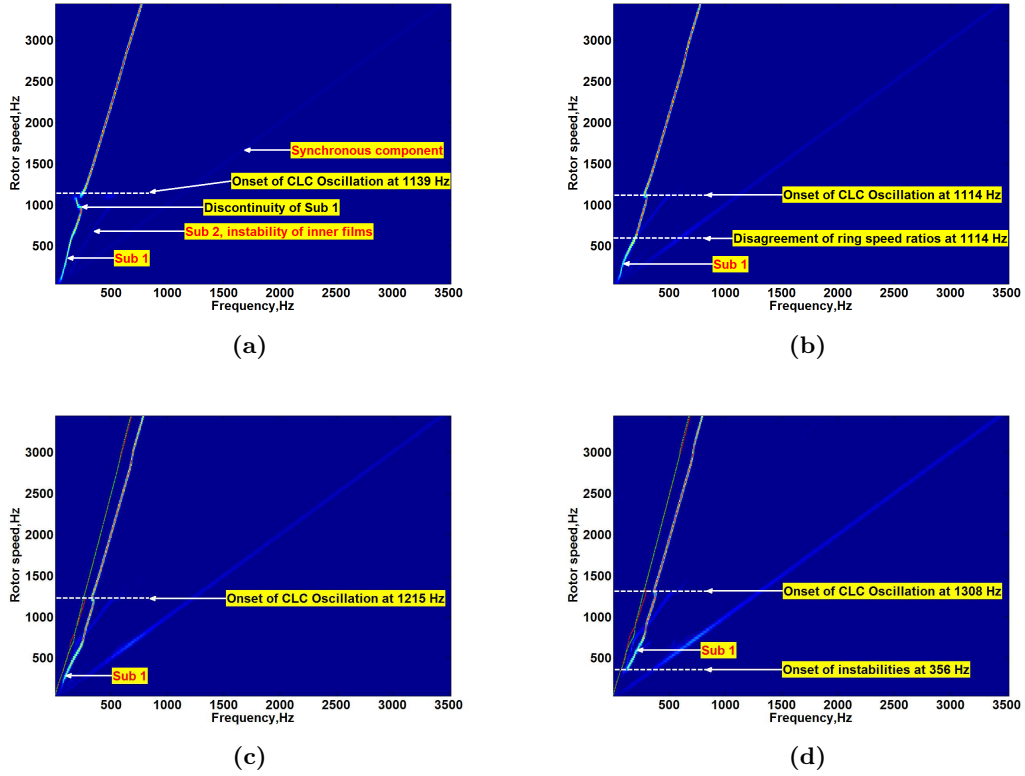


Fig. 6.7. Top-views of the waterfall plots of y_1/C_1 in run-up simulations when the in-phase unbalance is imposed ($\delta_c = 0, \delta_t = 0$) and $C_2 = 35 \mu\text{m}$: (a) $e = 5 \mu\text{m}$, (b) $e = 10 \mu\text{m}$, (c) $e = 15 \mu\text{m}$, (d) $e = 20 \mu\text{m}$, the red as well as green lines in (c) and (d) correspond to the ring speeds at FRB 1 as well as FRB 2, respectively.

eccentricity at FRB 2, i.e., ϵ_{ot} , the early onset of the instability of both outer films is marked, which prohibits the jump from Sub 1 to Sub 2 occurring. Interestingly, in Fig. 6.7a, at approximately 1000 Hz, a discontinuity can be observed between the Sub 1 derived from the outer oil film instability and the following Sub 1 of the *CLC Oscillation*. Correspondingly, sudden drops of the inner and outer eccentricities can also be found in Fig. 6.8a. The occurrence of *CLC Oscillation* leads to the consistently uprising of inner and outer eccentricities at both FRBs, of which only the ones at FRB 1 are given in Fig. 6.8a.

- (b) With higher unbalance offsets, i.e., $10 \mu\text{m}$, $15 \mu\text{m}$ and $20 \mu\text{m}$, the discontinuity disappears and the smooth transition of the two different Sub 1 can be observed. The weak existence of Sub 2 can also be observed until it completely disappears when the $20 \mu\text{m}$ offset is added. Before the *CLC Oscillation* takes place, the disagreement between the two ring speeds leaves another subsynchronous component with lower magnitude intersecting with Sub 1, which can be confirmed by the ring speed ratio lines alongside the subsynchronous lines in Fig. 6.7c and d. The discrepancy between

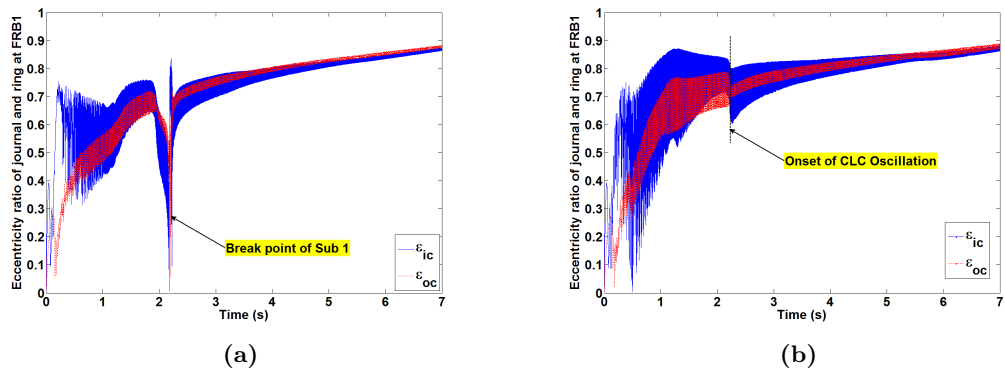


Fig. 6.8. Eccentricities of FRB 1 in run-up simulations when the in-phase unbalance is imposed ($\delta_c = 0$, $\delta_t = 0$) and $C_2 = 35 \mu\text{m}$: (a) $e = 5 \mu\text{m}$, (b) $e = 10 \mu\text{m}$

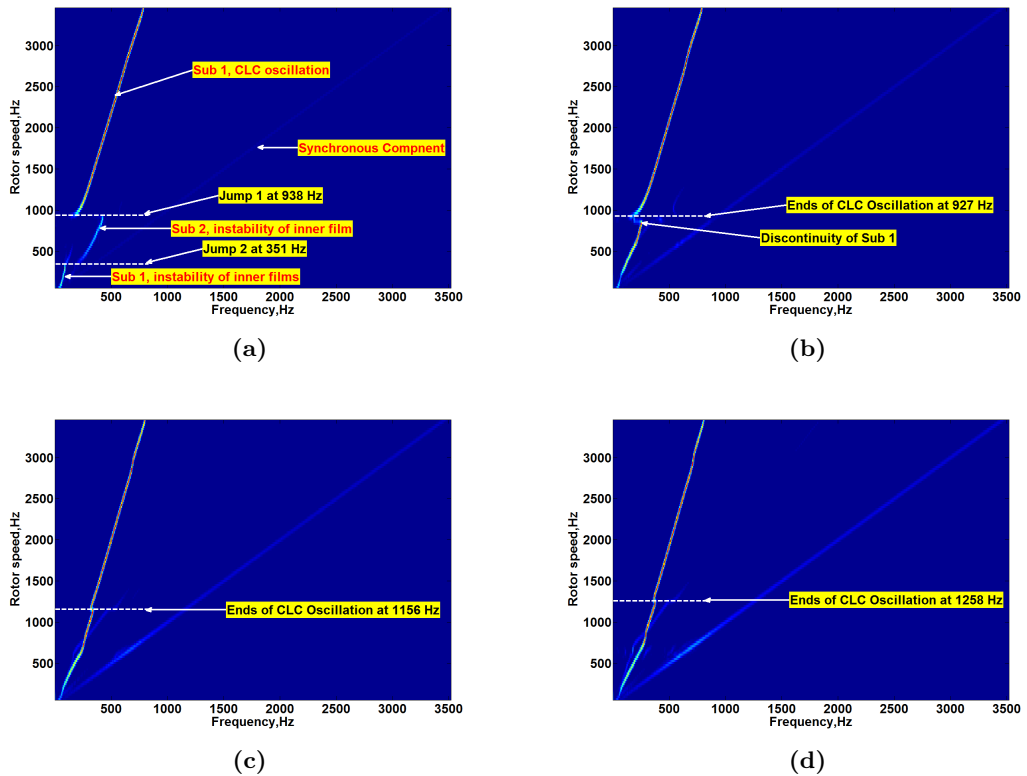


Fig. 6.9. Top-views of the waterfall plots of y_1/C_1 in run-down simulations when the in-phase unbalance is imposed ($\delta_c = 0$, $\delta_t = 0$) and $C_2 = 35 \mu\text{m}$: (a) $e = 5 \mu\text{m}$, (b) $e = 10 \mu\text{m}$, (c) $e = 15 \mu\text{m}$, (d) $e = 20 \mu\text{m}$.

the ring speeds results in the non-synchronization of the instability at the two FRBs. What can also be identified is the onset speed of Sub 1 is increased or delayed by the ascending unbalance offsets. Especially, in Fig. 6.7d, subsynchronous components cannot be observed until 356 Hz. Additionally, with increasing unbalance offsets, the rotor speed, at which *CLC Oscillation* sets in, becomes higher as well (see Figs. 6.7b-d).

- (c) As shown in Fig. 6.9a, when the investigated TC rotor undergoes a run-down, the simulation with 5 μm offset still shows the existence of two jumps and Sub 2 as the perfectly balanced run-down in Fig. 6.2a, although the onset speed of Jump 1 is much lower than in Fig. 6.2a. When the offset value becomes bigger, i.e., 10 μm , the waterfall plot in Fig. 6.9b resembles Fig. 6.7a and a discontinuity is observed after the *CLC Oscillation* terminates. Even higher unbalance offsets, i.e., 15 μm and 20 μm , also result in the disappearance of the above-mentioned discontinuity as in the run-ups. However, the ending speeds of *CLC Oscillation* in Fig. 6.9c and d are smaller than in Fig. 6.7c and d, respectively, due to the well-known hysteresis effect.

6.2 Simulation 2 ($C_2 = 40 \mu\text{m}$)

In this section, the outer clearances of both FRBs are now increased to 40 μm . Following the style of Section 6.1, the simulation results of the perfectly balance TC rotor will be presented first as a reference case, while the results considering the imposed out-of-phase and in-phase unbalances will be shown subsequently.

6.2.1 Perfectly balanced rotor: $e = 0$

Under the perfectly balanced condition, the run-up simulation results are depicted in Fig. 6.10, in which Fig. 6.10a and b are the waterfall plots of the non-dimensionalized y_1/C_1 and y_4/C_1 , respectively. Fig. 6.10c and d show the top-views of the corresponding waterfall diagrams given in Fig. 6.10a and b. The eccentricities of inner and outer films at both FRBs are presented in Fig. 6.10e and f. Fig. 6.10g shows the displacement plot of y_4/C_1 , and the ring speed ratio plot is given in Fig. 6.10h. The obtained simulation results are summarised as follows.

- (a) The TC rotor-FRB system becomes unstable at the start of simulation, which is confirmed by Figs. 6.10a-d. This instability is originated from the instability of both inner films, and Fig. 6.11a shows that a conical mode is excited. With increasing

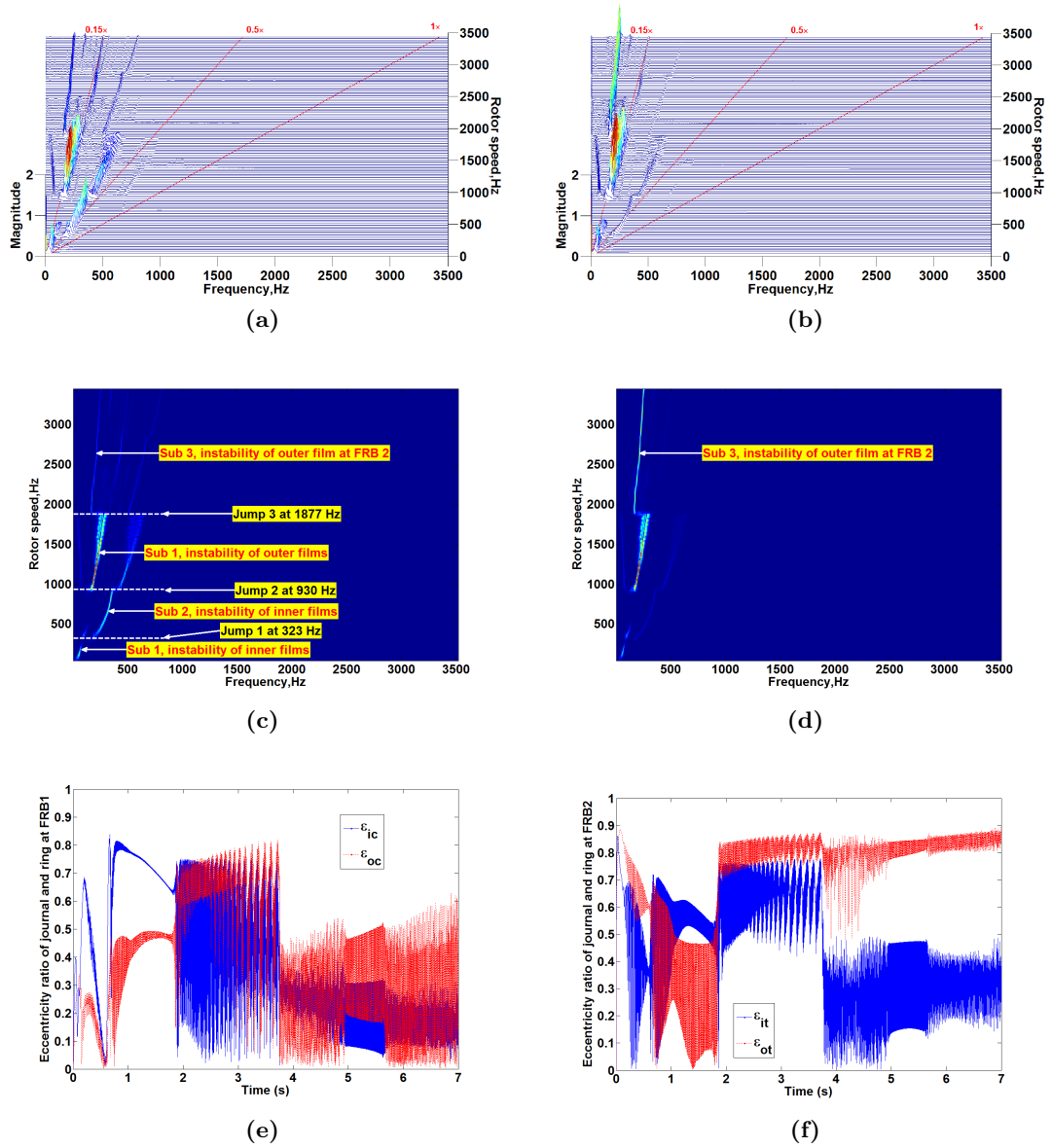


Fig. 6.10. Run-up simulation when the TC-FRB system is in a perfectly balanced condition ($e = 0$) and $C_2 = 40 \mu\text{m}$: (a), (b) non-dimensional waterfall plots for the displacements of the compressor end and turbine end in Y axis direction, i.e., y_1/C_1 and y_4/C_1 , respectively, (c), (d) top-views of (a) and (b), respectively, (e), (f) eccentricity plot of the inner and outer oil films at FRB 1 and FRB 2, (g) displacement plot of y_4/C_1 , (h) ring speed ratio plot of FRB 1 and FRB 2.

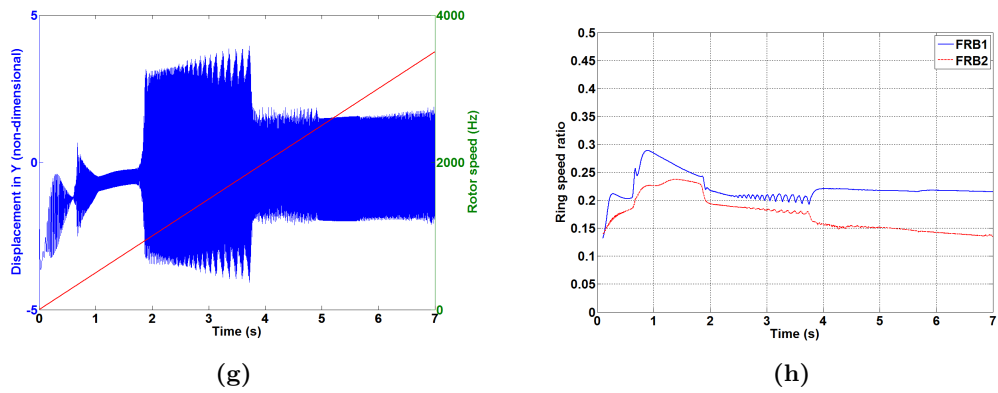


Fig. 6.10. (continued)

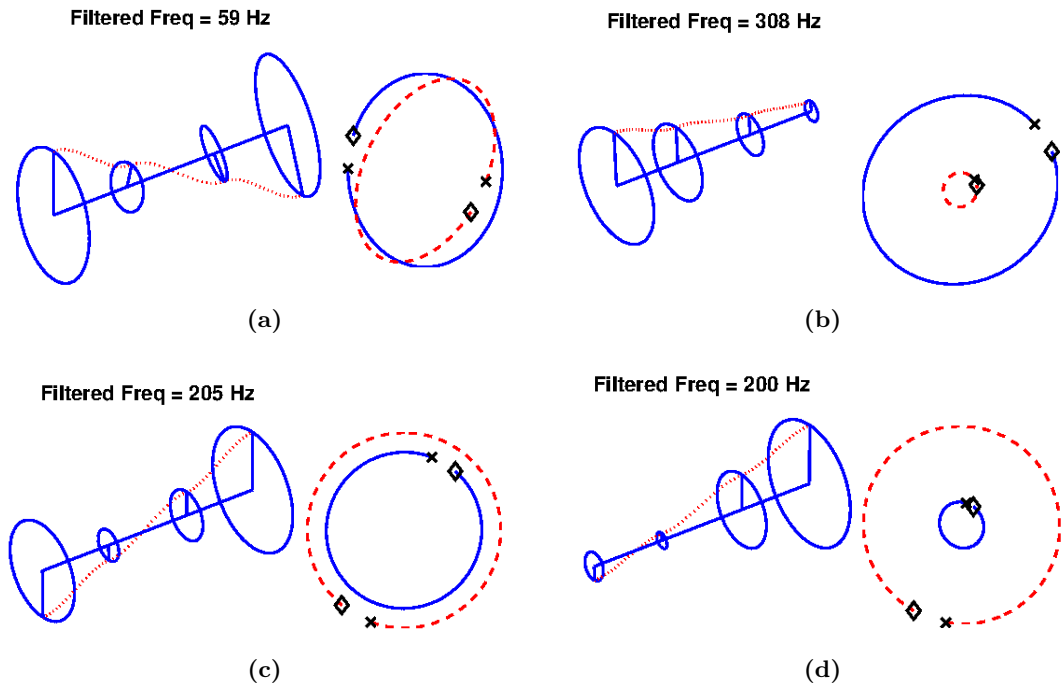


Fig. 6.11. Filtered mode shapes and orbits for Sub 1, Sub 2 and Sub 3 of run-up simulation when the outer clearances are $40 \mu\text{m}$ and the rotor is perfectly balanced at selected rotor speeds: (a) 128 Hz, (b) 589 Hz, (c) 1178 Hz and (d) 2458 Hz.

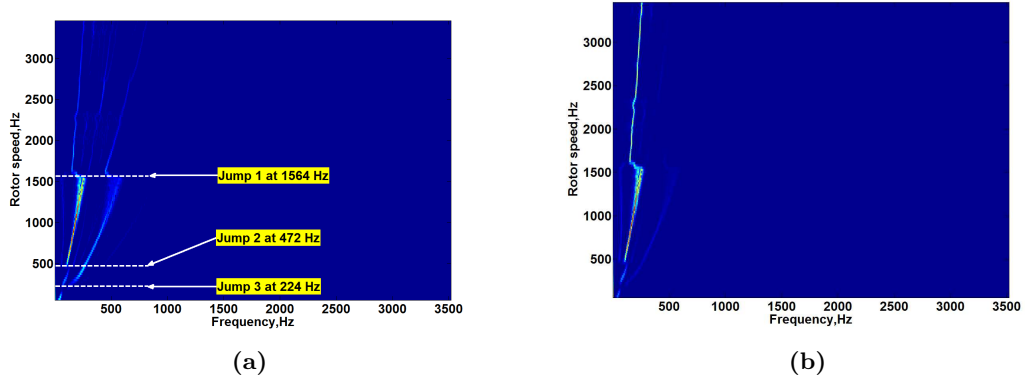


Fig. 6.12. Run-down simulation when the TC-FRB system is in a perfectly balanced condition ($e = 0$) and $C_2 = 40 \mu\text{m}$: (a), (b) top-view of the waterfall diagram of y_1/C_1 and y_4/C_1 , respectively.

rotor speed, this instability can be passed through, and the system becomes intermittently stable approximately at 0.6 s.

- (b) At 323 Hz, the inner films become unstable again. This instability gives rise to the onset of subsynchronous component Sub 2, which is actually a bended cylindrical mode shown in Fig. 6.11b.
- (c) At 930 Hz, the dominant Sub 2 is taken over by the newly developed outer-film instability, which is labelled again by “Sub 1”, since it is also a conical forward mode as shown in Fig. 6.11c. In the meantime, the presence of Sub 2 can be identified as well but at higher frequency locations.
- (d) At 1877 Hz, the dominant frequency component jumps from Sub 2 to Sub 3. Figs. 6.10e and f show that Sub 3 mainly results from the instability of outer film at FRB 2. Fig. 6.11d demonstrates that Sub 3 is also a conical forward mode, although Node 2 is in-phase with Node 3 and Node 4 but out-of-phase with Node 1.

The corresponding run-down simulation shows that the occurring speeds of the corresponding jumps in run-down become smaller than those in the run-up, due to the well-known hysteresis effect.

6.2.2 Out of phase unbalance: $\delta_c = 0$, $\delta_t = \pi$

Figs. 6.13-6.15 show the run-ups as well as run-downs when the variable values of the out-of-phase unbalance offset are imposed. In comparison with the perfectly balanced case described in Section 6.2.1, the conclusion of the obtained results are generally drawn as follows.

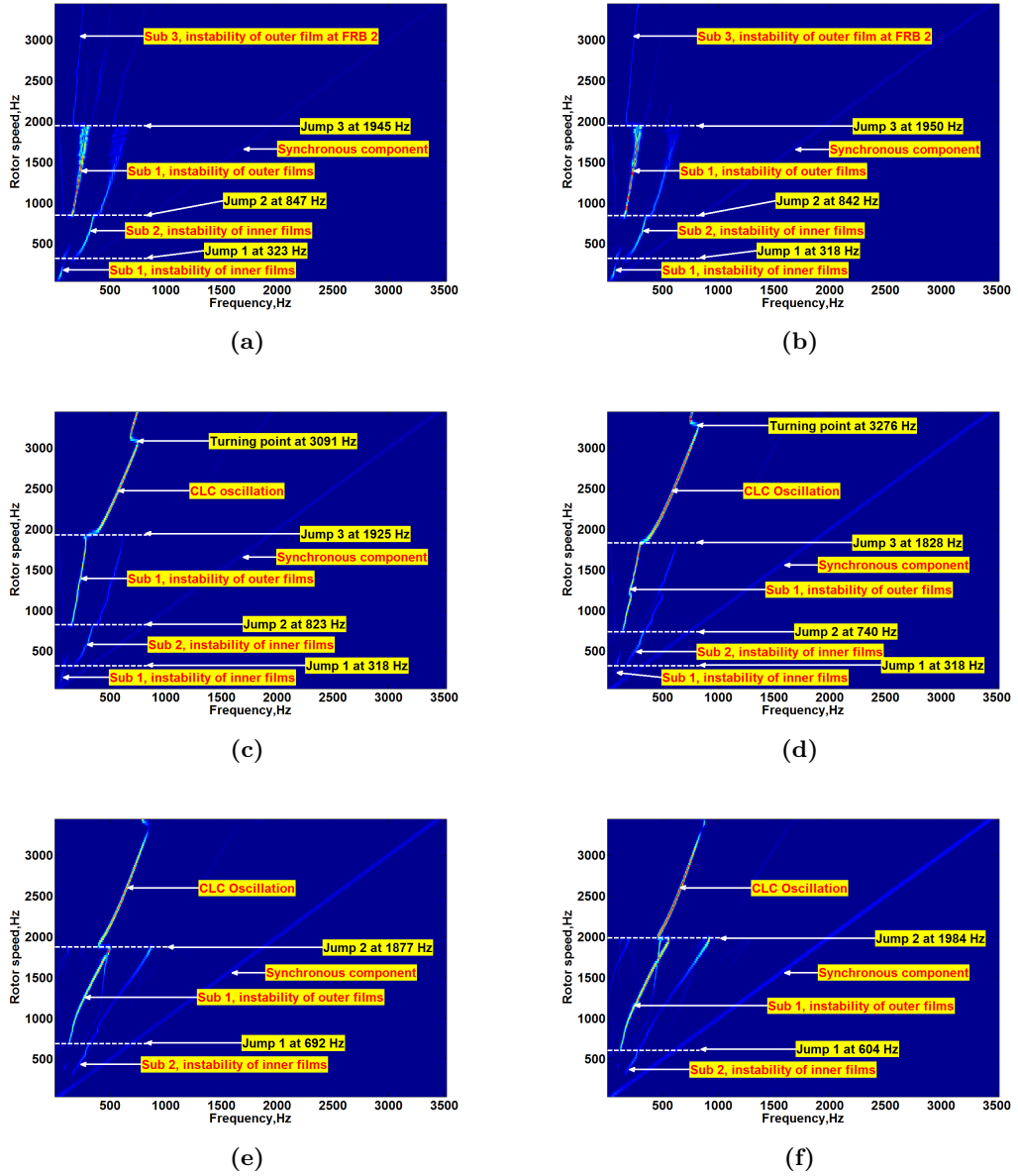


Fig. 6.13. Top-views of the waterfall plots of y_1/C_1 in run-up simulations when the out-of-phase unbalance is imposed ($\delta_c = 0$, $\delta_t = \pi$) and $C_2 = 40 \mu\text{m}$: (a) $e = 5 \mu\text{m}$, (b) $e = 10 \mu\text{m}$, (c) $e = 15 \mu\text{m}$, (d) $e = 20 \mu\text{m}$, (e) $e = 25 \mu\text{m}$ and (f) $e = 30 \mu\text{m}$.

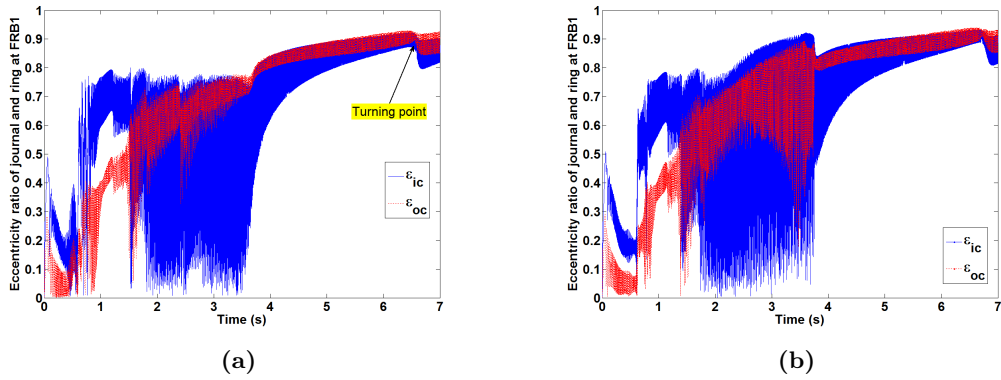


Fig. 6.14. Eccentricities of the inner and outer films at FRB 1 during run-up simulation when $C_2 = 40 \mu\text{m}$ and out-of-phase unbalance is imposed: (a) $e = 20 \mu\text{m}$, (b) $e = 25 \mu\text{m}$.

- (a) In the run-up simulations presented in Fig. 6.13, it is shown the main characteristics of the perfectly balanced run-up can be retained, provided that the imposed unbalance offset is low enough, e.g., $5 \mu\text{m}$ and $10 \mu\text{m}$. It should be mentioned that the added unbalance will reduce the onset speed of Jump 2 and retard the occurrence of Jump 3, although the influence on the onset speed of Sub 2 is negligible. When higher unbalance offset values are introduced, e.g., $15 \mu\text{m}$ and $20 \mu\text{m}$ (Fig. 6.13c and d), it is interesting to see Jump 3 brings out the *CLC Oscillation* until the very end of simulation, instead of leading to the occurrence of Sub 3 observed in the perfectly balanced run-up. Before the rotor is accelerated to the top value of the considered speed range, one can also observe a turning point of the *CLC Oscillation* component accompanied by the slight decrease of the mean values of the inner and outer film eccentricities at both FRBs (see Fig. 6.14a). Thus, under the circumstances, the added out-of-phase unbalance will significantly affect the dynamic response of the investigated system, especially in the high speed range. In the low speed range, one can appreciate the further decrease of occurring speed of Jump 2 as well as Jump 3. Fig. 6.13e and f show even higher unbalance offsets, e.g., $25 \mu\text{m}$ and $30 \mu\text{m}$ can also place considerable influence on the response of the investigated TC rotor-FRB system in the low speed range, since the observed Sub 1 at the beginning of run-up simulations in Figs. 6.13a-d cannot be identified. This means high-value unbalance can effectively suppress the conical forward instability of the inner films (see Fig. 6.11a) and the rotor undergoes purely unbalance induced vibration at the start of run-up. Thereafter, Sub 2 appears but the dominance will be ended much earlier by the onset of outer film instability than the cases with smaller unbalance offsets (Figs. 6.13a-d). The appearance of Sub 2 can still be observed as in Figs. 6.13a-d. What is

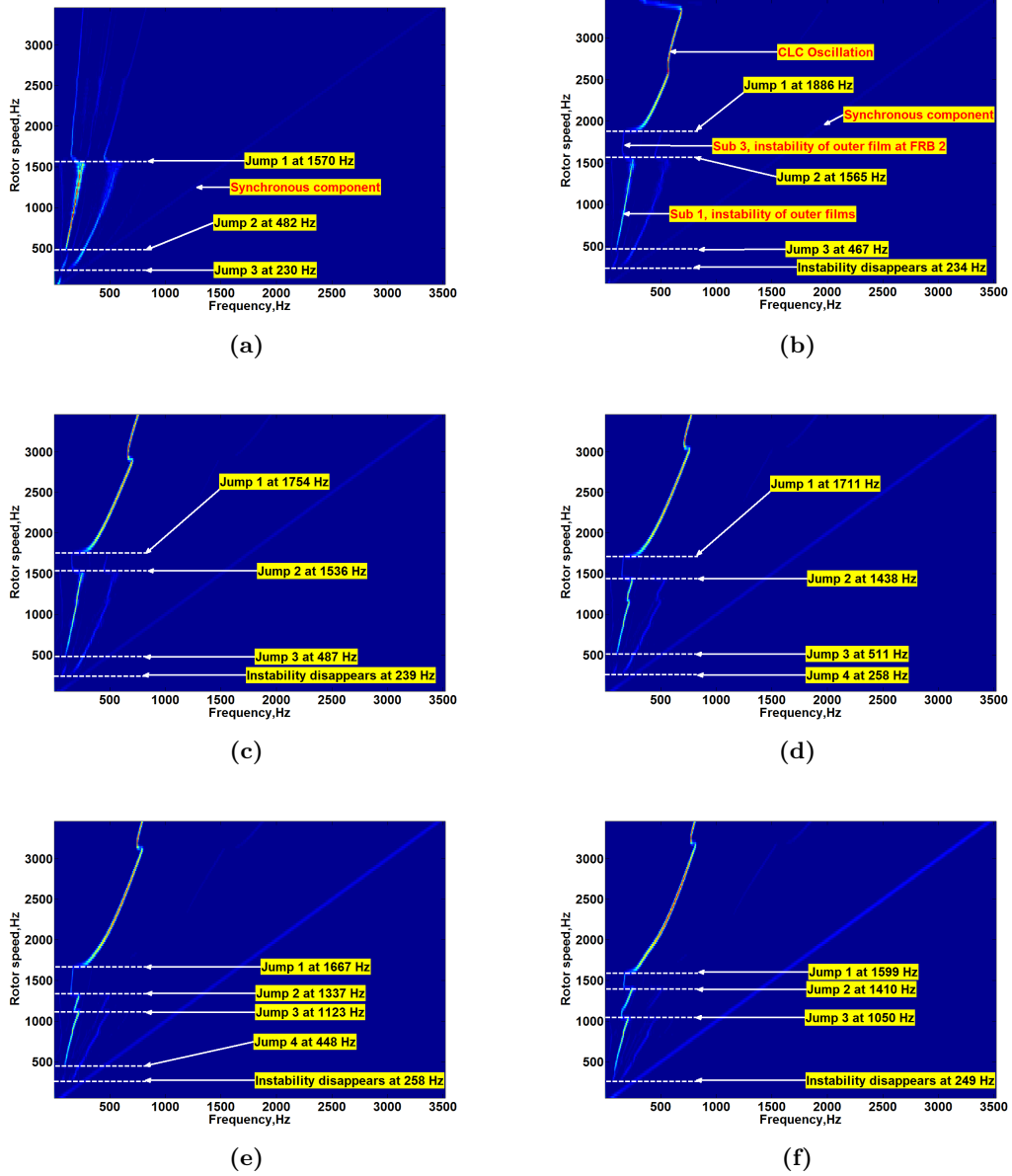


Fig. 6.15. Top-views of the waterfall plots of y_1/C_1 in run-down simulations when the out-of-phase unbalance is imposed ($\delta_c = 0$, $\delta_t = \pi$) and $C_2 = 40 \mu\text{m}$: (a) $e = 5 \mu\text{m}$, (b) $e = 10 \mu\text{m}$, (c) $e = 15 \mu\text{m}$, (d) $e = 20 \mu\text{m}$, (e) $e = 25 \mu\text{m}$ and (f) $e = 30 \mu\text{m}$.

interesting is Sub 1 as well as Sub 2 will be shifted to higher-frequency locations on the waterfall diagrams (see Fig. 6.13e and f). This phenomenon can be attributed to the ascending mean values of both inner film eccentricities (see Fig. 6.14b) caused by the high unbalance offsets, which cannot be observed in the run-ups with lower unbalance offsets (see Fig. 6.14a).

- (b) Fig. 6.15 shows the run-down simulation results with respect to the run-up simulations given in Fig. 6.13. Compared to Fig. 6.13b, i.e., $e = 10\ \mu\text{m}$, Fig. 6.15b exhibits a dramatic difference in the high speed range. Even though the simulation initially starts with the displacement data obtained from the end of the corresponding run-up, one can clearly observe the sudden jump from the initial conditions to the *CLC Oscillation*. Surprisingly, when the rotor is decelerated to 1886 Hz, another jump from *CLC Oscillation* to Sub 3 sets in, which is the major difference between the run-up and run-down simulations when the out-of-phase unbalance is employed.

6.2.3 In-phase unbalance: $\delta_c = \delta_t = 0$

The top-view waterfalls of the run-ups with variable in-phase unbalance offsets are shown in Fig. 6.16. In comparison with the perfectly balanced run-up and the run-ups with out-of-phase unbalance offsets, the main characteristics of the obtained results are described as follows.

- (a) As can be seen in Fig. 6.16a, the run-up with the smallest in-phase unbalance offset, i.e., $e = 5\ \mu\text{m}$, shows the onset speed of Jump 3 is dramatically reduced to 1595 Hz, compared with 1877 Hz in the perfectly balanced case depicted in Fig. 6.10a and 1945 Hz when the same amount of out-of-phase unbalance is applied in Fig. 6.13a. However, the speed when Jump 2 takes place is the same as in Fig. 6.13a, which is lower than the case without unbalance. Additionally, it is interesting to see the appearance of another jump occurring at 3232 Hz, following which the dominant subsynchronous component Sub 3 abruptly switches to a higher-frequency component because the *CLC Oscillation* occurs. This sudden jump from Sub 3 to the *CLC Oscillation* is, firstly, reported in Ref. [85, 86] and is termed *Total Instability*. Following the description in Ref. [16], only the *CLC Oscillation* is used in this thesis. The bifurcation from Sub 3 to *CLC Oscillation* can cause catastrophic failure of a TC, since the high-amplitude displacements of rotor ends will easily exceed the design limits, and the unavoidable rotor-stator rubbing is quite possible to take place. In

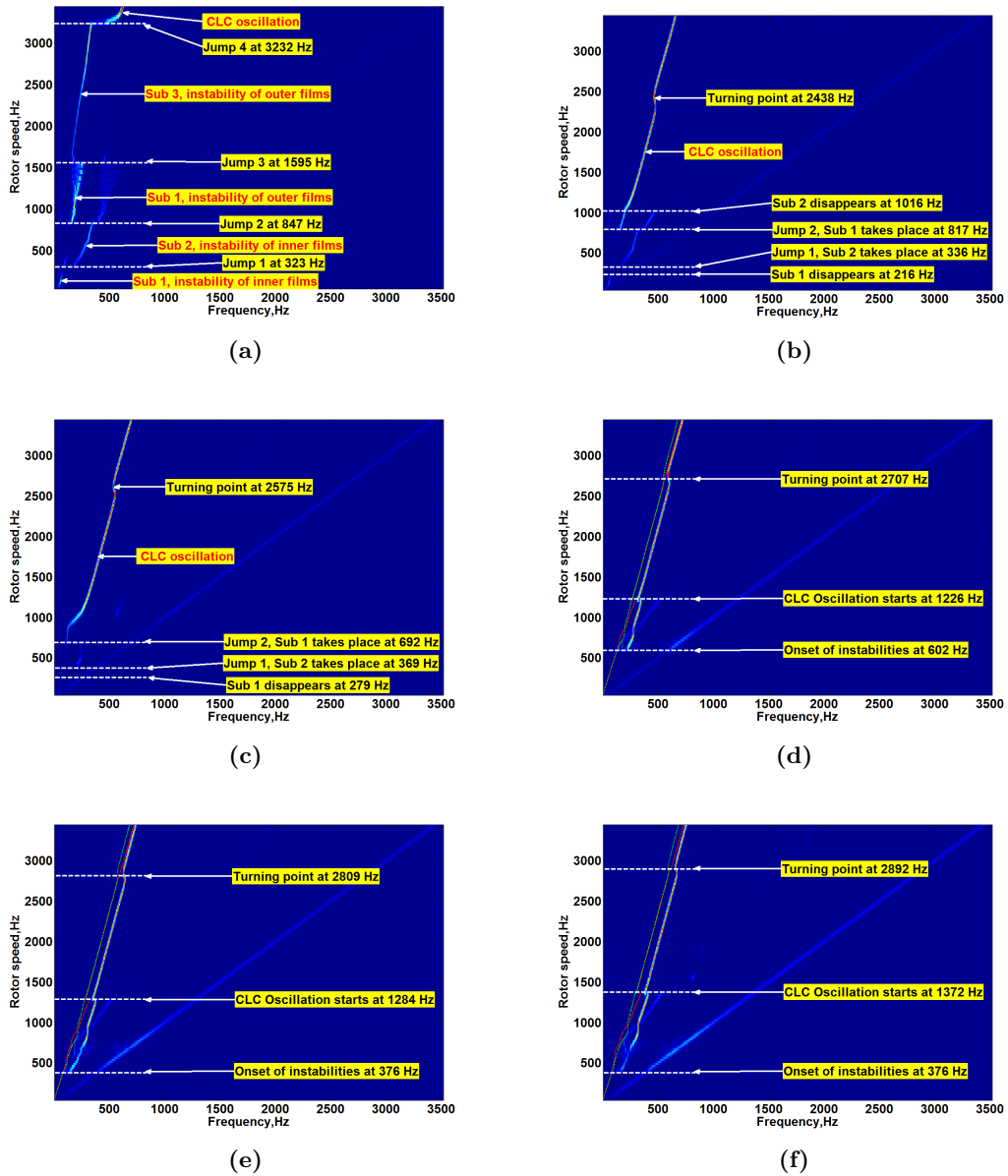


Fig. 6.16. Top-views of the waterfall plots of y_1/C_1 in run-up simulations when the in-phase unbalance is imposed ($\delta_c = 0$, $\delta_t = 0$) and $C_2 = 40 \mu\text{m}$: (a) $e = 5 \mu\text{m}$, (b) $e = 10 \mu\text{m}$, (c) $e = 15 \mu\text{m}$, (d) $e = 20 \mu\text{m}$, (e) $e = 25 \mu\text{m}$ and (f) $e = 30 \mu\text{m}$, the red as well as green lines in (d), (e) and (f) correspond to the ring speeds at FRB 1 as well as FRB 2, respectively.

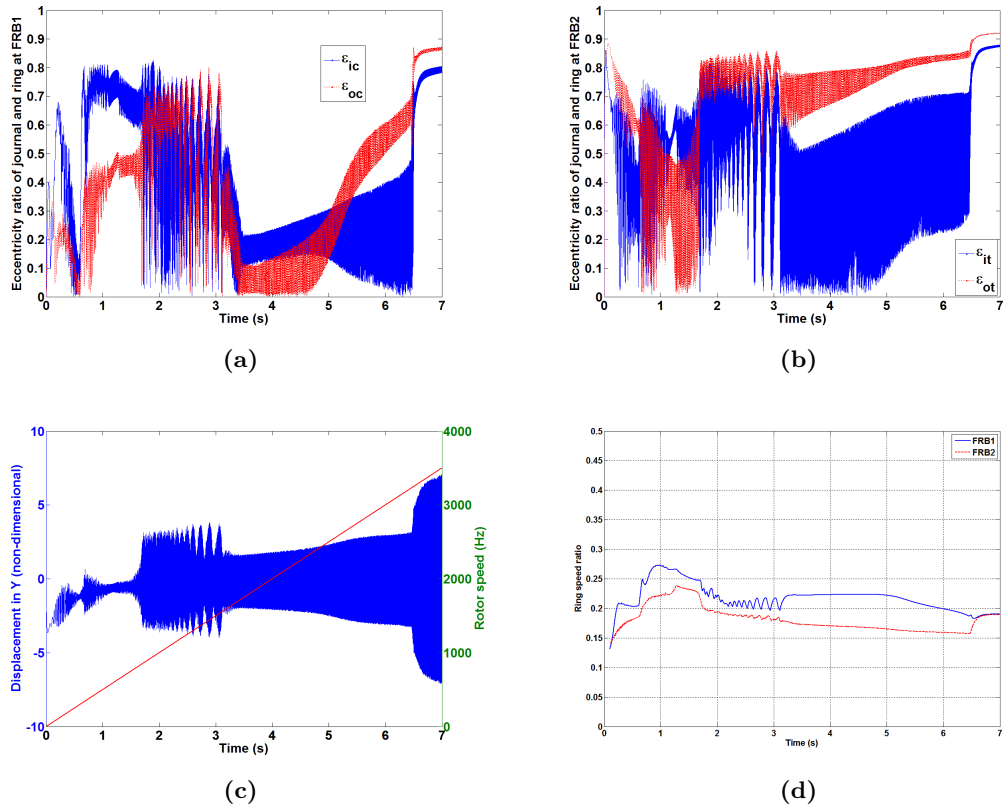


Fig. 6.17. Run-up simulation results when $C_2 = 40\mu\text{m}$ and $5\mu\text{m}$ in-phase unbalance is imposed: (a), (b) inner and outer films eccentricities of FRB 1 and FRB 2, respectively, (c) displacement plot of y_4/C_1 and (d) ring speed ratio plot.

Fig. 6.17a and b, prior to the occurrence of *CLC Oscillation* at approximately 6.5 s, one sees the consistent and significant increase of the mean value of ϵ_{oc} . In addition, the steady increases of the mean values of the inner as well as outer film eccentricities at FRB 2 can also be observed. The mean value of the inner film eccentricity at FRB 1 slightly grows before the *CLC Oscillation* sets in, while the amplitude clearly follows an ascending trend. When Jump 4 takes place, simultaneous leaps of the inner and outer bearing eccentricities at both FRBs are identified, which means the instantaneous occurrence of the inner and outer film instability at FRB 1 and FRB 2. Furthermore, the amplitudes of the inner and outer eccentricities of both FRBs are dramatically reduced. In the meantime, the corresponding jumps of the displacements of the compressor and turbine ends can also be seen, but only the latter are given in Fig. 6.17c. Fig. 6.17d shows the agreement of both ring speed ratios at the onset of Jump 4, which confirms the synchronization of the instability of inner and outer films at both bearings.

(b) When higher unbalance offsets are added, i.e., $10\mu\text{m}$ and $15\mu\text{m}$, the onset speed

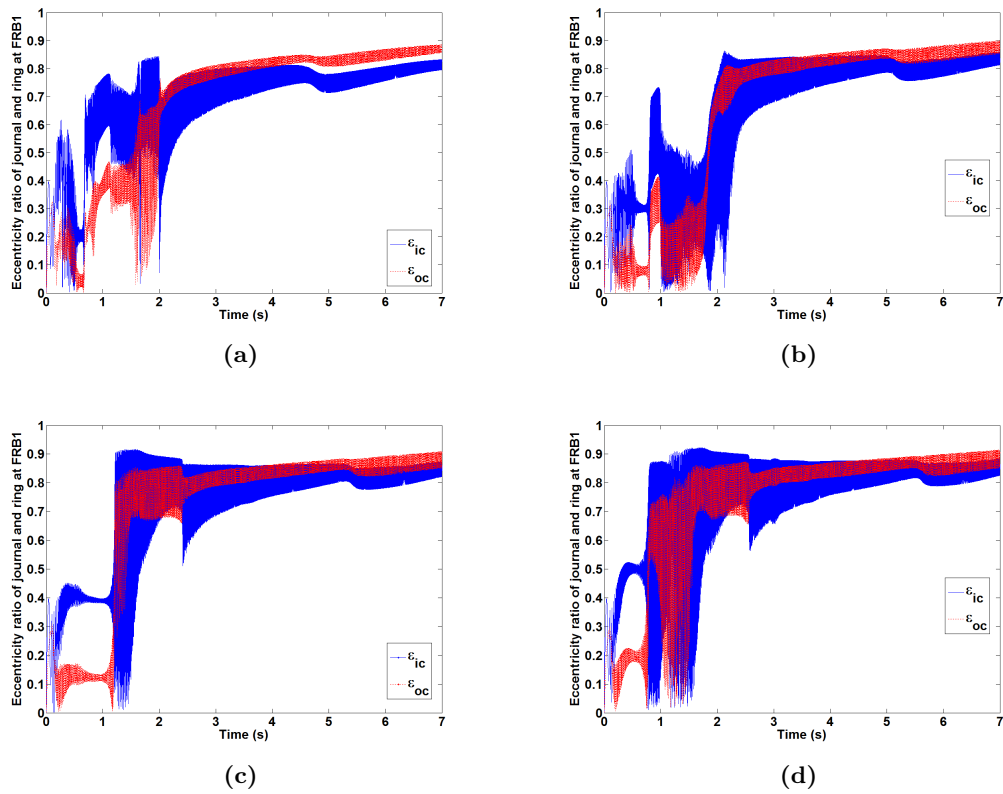


Fig. 6.18. Eccentricities at FRB 1 when $C_2 = 40 \mu\text{m}$ and in-phase unbalance is imposed: (a) $e = 10 \mu\text{m}$, (b) $e = 15 \mu\text{m}$, (c) $e = 20 \mu\text{m}$ and (d) $e = 25 \mu\text{m}$

of Sub 2 is slightly delayed, while the speed when Jump 2 occurs is considerably reduced. The coexistence range of Sub 1 and Sub 2 becomes much shorter until it can hardly be identified with the $15 \mu\text{m}$ unbalance offset. In Fig. 6.16b, at 1016 Hz, the induced unbalance brings out the onset of *CLC Oscillation* characterized by the steady and instantaneous growth of the inner and outer eccentricities of both FRBs to quite high values. The run-ups with even higher unbalance offsets, i.e., $20 \mu\text{m}$, $25 \mu\text{m}$ and $30 \mu\text{m}$ show Sub 1, emerging at the beginning of simulation with lower unbalance offsets (see Figs. 6.16a-c), can no longer be observed. Within the low-speed range, e.g., from 0 Hz to 602 Hz in Fig. 6.16d, the system is subject to vibrations merely induced by the imposed unbalance. It should be noted subsynchronous components derived from oil film instability in the run-up with $20 \mu\text{m}$ unbalance offset actually appears later than in Fig. 6.16e and f with higher unbalance offsets, which implies the complex effect of the induced unbalance on the system response at the lower end of the considered speed range. Prior to the occurrence of *CLC Oscillation*, the system response is placed in a situation similar to Figs. 6.7b-d. Once more, one can see the intersection of Sub 1 and another weak subsynchronous component, with respect to

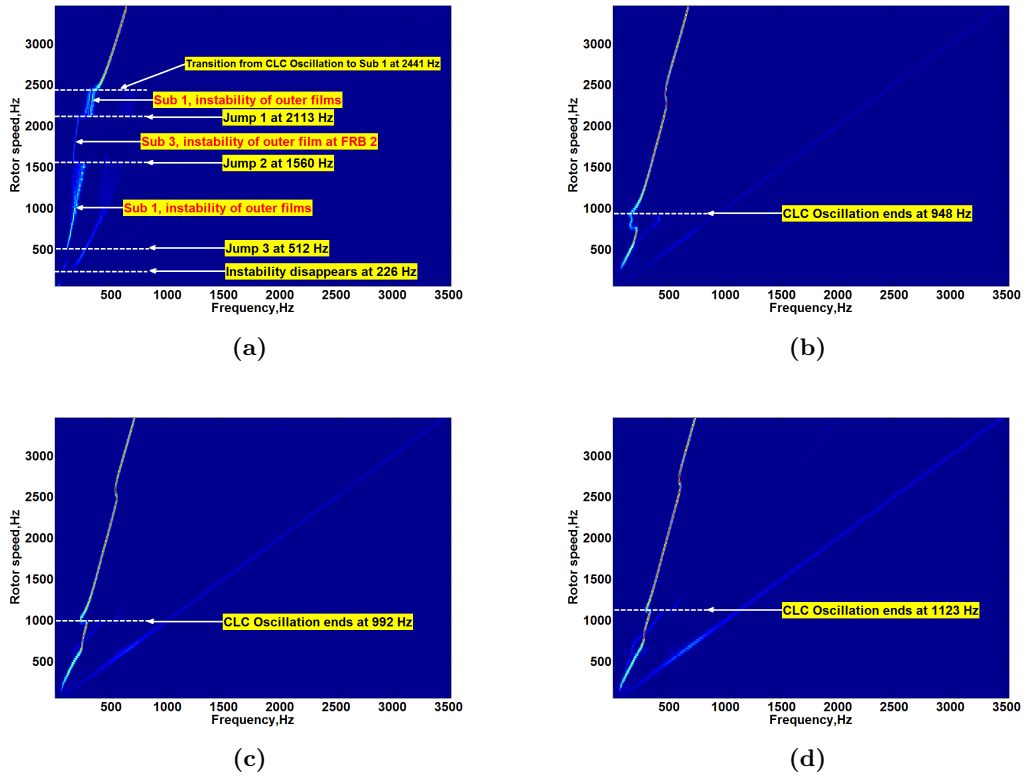


Fig. 6.19. Top-views of the waterfall plots of y_1/C_1 in run-down simulations when the in-phase unbalance is imposed ($\delta_c = 0$, $\delta_t = 0$) and $C_2 = 40 \mu\text{m}$: (a) $e = 5 \mu\text{m}$, (b) $e = 10 \mu\text{m}$, (c) $e = 15 \mu\text{m}$, (d) $e = 20 \mu\text{m}$.

the trends followed by the two ring speeds (see Figs. 6.16d-f). When the rotor speed is accelerated to high value, e.g., 2892 Hz in Fig. 6.16f, the disagreement between the ring speeds brings out the shift of the *CLC Oscillation* component to a lower frequency location in the figure. The rotor speed, at which the shift occurs, is termed the *turning point* in Fig. 6.16. Moreover, the disagreement of the ring speed ratios appears when the *turning point* shows up. In addition, The corresponding declines of the mean values of the inner and outer eccentricities can also be the observed at the *turning point* (see Fig. 6.18). With ascending unbalance offset, Figs. 6.16d-f show that the onset speeds of *CLC Oscillation* and *turning point* both become greater.

- (c) The results of run-down simulations with variable in-phase offsets are given in Fig. 6.19. When the $5 \mu\text{m}$ unbalance offset is added, at the higher end of the speed range, one can see the *CLC Oscillation* continues until the rotor is decelerated to 2441 Hz, which is much lower than the onset speed of *CLC Oscillation* in the corresponding run-up in Fig. 6.16a. Thereafter, instead of jumping back to Sub 3, the dominant subsynchronous component becomes Sub 1, accompanied by the Sub 2 derived from the instability of the inner films. At 2113 Hz, Sub 3 appears and becomes dominant.

Subsequently, Jump 2 takes place at 1506 Hz, which brings back the dominance of Sub 1. Afterwards, the waterfall diagram presented in Fig. 6.19a shows the same characteristics as in run-up, despite the smaller onset speeds of the following two jumps. When the bigger unbalance offsets are imposed, i.e., 10 μm , 15 μm and 20 μm , the *CLC Oscillation* remains until around 1000 Hz as in the run-ups. By contrast, the appearance of Sub 2 within the low-speed range in the corresponding run-ups in Fig. 6.13 b and c cannot be observed in Fig. 6.19b and c.

6.3 Simulation 3 ($C_2 = 50 \mu\text{m}$)

The outer clearances of two FRBs are further increased to 50 μm in this subsection. The results of the run-up and run-down simulations under the perfectly balanced condition are discussed in Section 6.3.1, which is followed by the out-of-phase unbalanced simulations given in Section 6.3.2 and the in-phase unbalanced simulations shown in Section 6.3.3.

6.3.1 Perfectly balanced rotor: $e = 0$

The run-up simulation results of the perfectly balanced rotor are shown in Fig. 6.20 and 6.21. In contrast to the perfectly unbalanced run-up described in Section 6.2.1, the main difference is the occurrence of Jump 2 leads to the sudden transition of the dominant subsynchronous component from Sub 2 to Sub 3, i.e., the instability of the outer film at FRB 2. The results are summarised as follows.

- (a) The instability of the inner films, especially the inner film at FRB 1, can be observed at the very beginning of the performed run-up in Figs. 6.20a-d. Fig. 6.21a indicates that it is a conical forward mode. With increasing rotor speed, this instability can quickly be passed through, and the system becomes stable at approximately 0.45 s.
- (b) At 274 Hz, the system becomes unstable again, resulting from the further developed instability in the inner film of FRB 1. Fig. 6.21b shows the bended cylindrical mode is excited.
- (c) At 697 Hz, the nonlinear jump from Sub 2 to Sub 3 occurs. Figs. 6.20e and f show that the dominance of the instability of the outer film at FRB 2 is established. Fig. 6.20g clearly shows that the onset of Sub 3 gives rise to the highest amplitude of y_4/C_1 . Additionally, dramatic decrease of the ring speed ratio at FRB 2 can be observed in Fig. 6.20h.

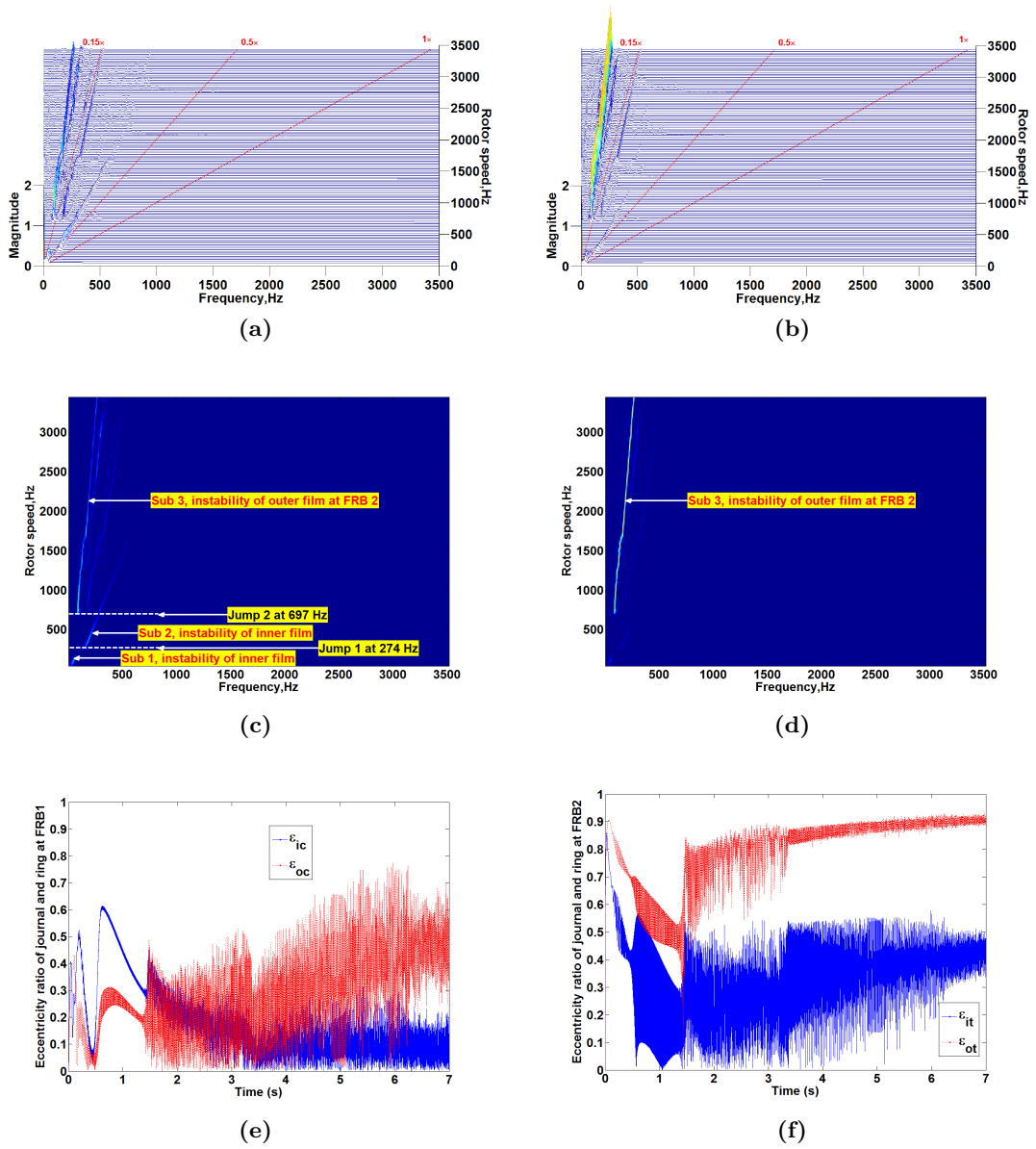


Fig. 6.20. Run-up simulation when the TC-FRB system is in a perfectly balanced condition ($e = 0$) and $C_2 = 50 \mu\text{m}$: (a), (b) non-dimensional waterfall plots for the displacements of the compressor end and turbine end in Y axis direction, i.e., y_1/C_1 and y_4/C_1 , respectively, (c), (d) top-views of (a) and (b), respectively, (e), (f) eccentricity plot of the inner and outer oil films at FRB 1 and FRB 2, (g) displacement plot of y_4/C_1 , (h) ring speed ratio plot of FRB 1 and FRB 2.

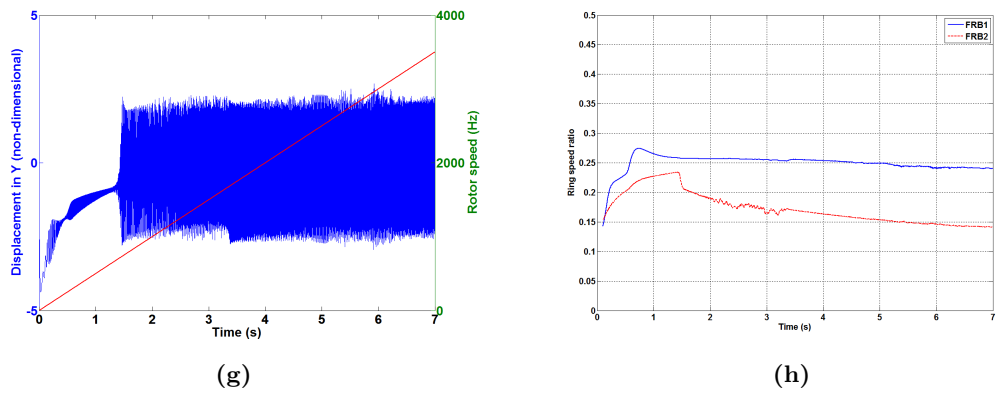


Fig. 6.20. (continued)

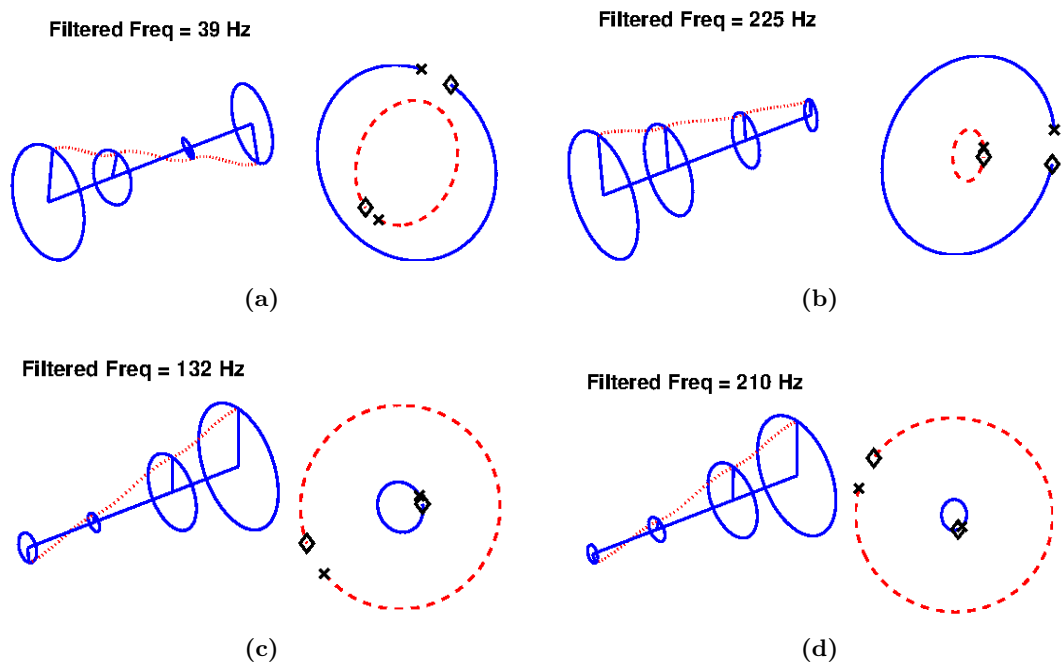


Fig. 6.21. Filtered mode shapes and orbits for Sub 1, Sub 2 and Sub 3 of run-up simulation when the outer clearances are $50 \mu\text{m}$ and the rotor is perfectly balanced at selected rotor speeds: (a) 102 Hz, (b) 512 Hz, (c) 1510 Hz and (d) 2509 Hz.

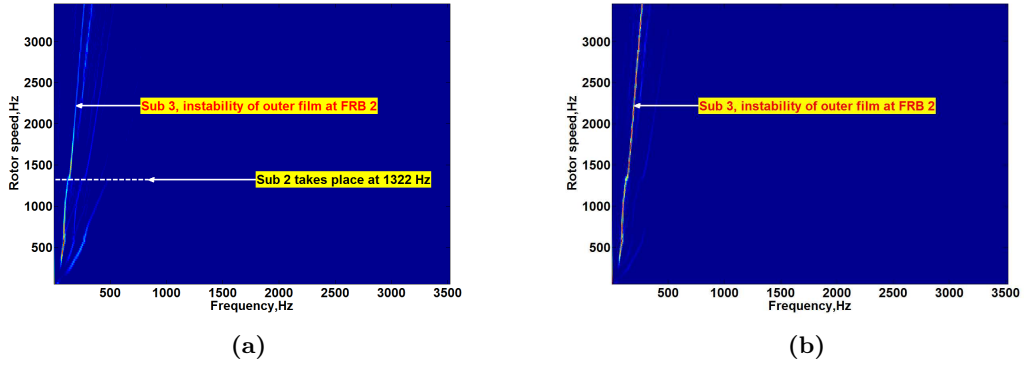


Fig. 6.22. Run-down simulation when the TC-FRB system is in a perfectly balanced condition ($e = 0$) and $C_2 = 50 \mu\text{m}$: (a), (b) top-view of the waterfall diagram of y_1/C_1 and y_4/C_1 , respectively.

The results of the corresponding run-down depicted in Fig. 6.22 show that Sub 3 lasts longer than in the run-up. It can still be identified, even though the rotor speed is below 500 Hz. In addition, the onset speed of Sub 2 in the run-down is actually smaller than the speed when Sub 2 disappears in the run-up.

6.3.2 Out of phase unbalance: $\delta_c = 0, \delta_t = \pi$

Variable out-of-phase unbalance offsets are introduced in this subsection and the run-up as well as run-down simulation results are presented in Figs. 6.23-6.26. The results are characterised as follows.

- (a) When the imposed unbalance offset is as small as $5 \mu\text{m}$, the results shown in Fig. 6.23a resemble the ones of the balanced run-up given in Fig. 6.20, despite the smaller onset speeds of Sub 2 and Sub 3. By contrast, the adoption of bigger unbalance offsets leads to the occurrence of *CLC Oscillation* when the rotor is accelerated to the higher end of the considered speed range (see Figs. 6.23b-f). With increasing unbalance offsets, the onset speed of *CLC Oscillation* follows a descending trend, while the frequency location of the excited *CLC Oscillation* component on the waterfall diagrams becomes higher. It should be mentioned that in Ref. [86] Schweizer concludes the increase of housing stiffness can also effect the growth of the frequency of the *CLC Oscillation* component. With the variable unbalance offsets considered in this thesis, the obtained phenomenon can be explained by the selected eccentricity plots shown in Fig. 6.24. What can clearly be observed is that the higher the unbalance, the bigger the bearing eccentricities when *CLC Oscillation* turns up. Linearly speaking, the increases of bearing eccentricities bring the growth of the

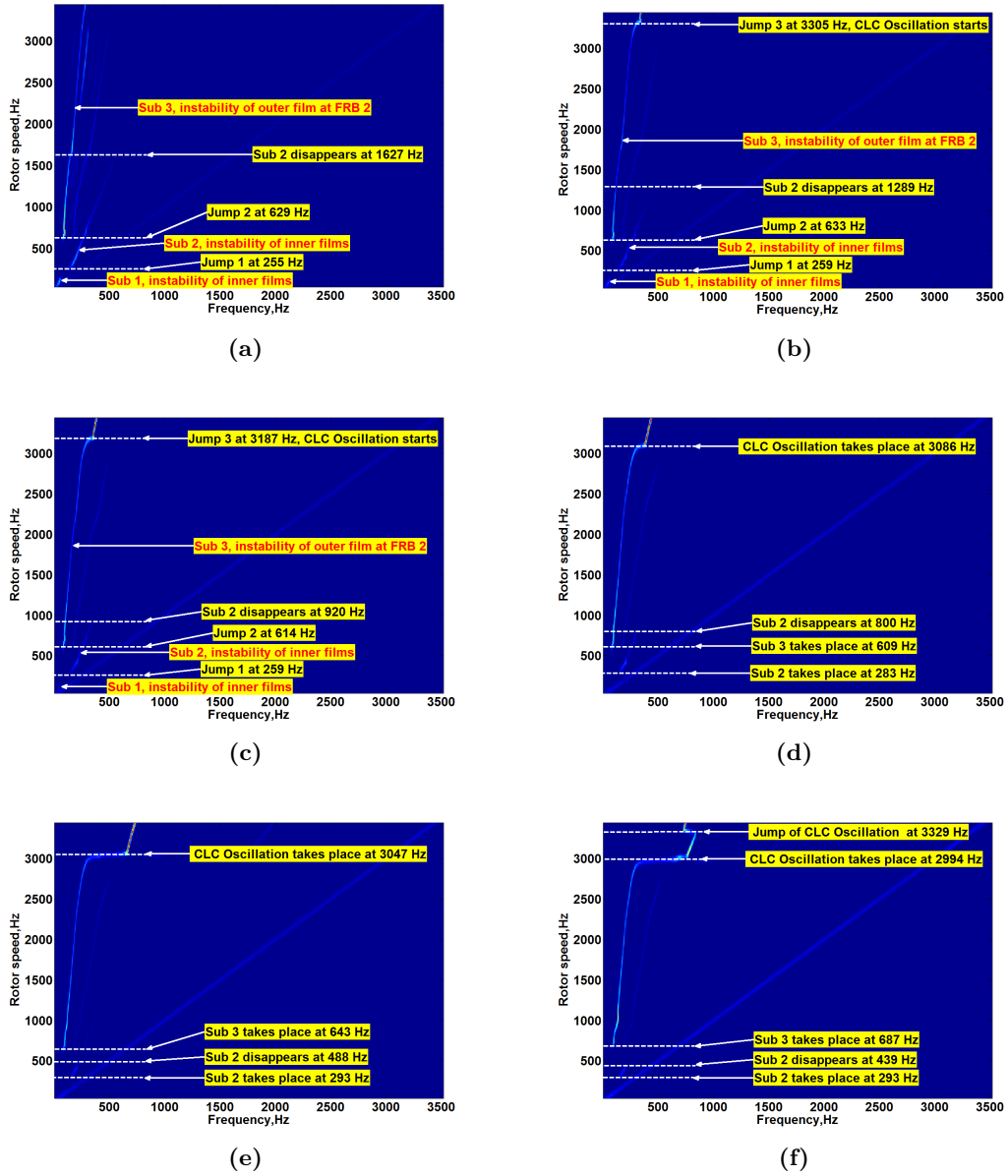


Fig. 6.23. Top-views of the waterfall plots of y_1/C_1 in run-up simulations when the out-of-phase unbalance is imposed ($\delta_c = 0$, $\delta_t = \pi$) and $C_2 = 50 \mu\text{m}$: (a) $e = 5 \mu\text{m}$, (b) $e = 10 \mu\text{m}$, (c) $e = 15 \mu\text{m}$, (d) $e = 20 \mu\text{m}$, (e) $e = 25 \mu\text{m}$ and (f) $e = 30 \mu\text{m}$.

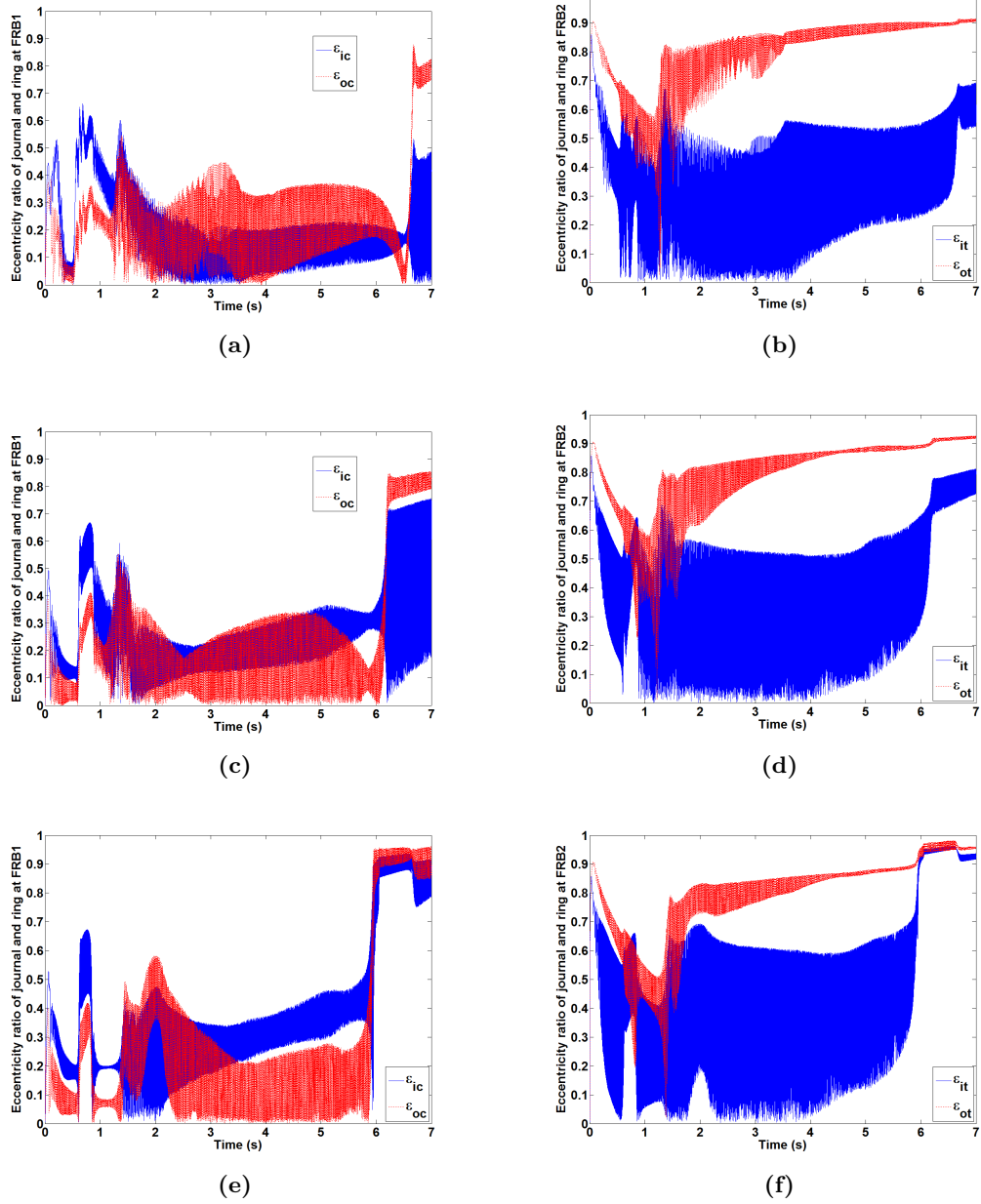


Fig. 6.24. FRB eccentricities in run-up simulations when $C_2 = 50\mu\text{m}$ and out-of-phase unbalance is imposed: (a), (c) and (e) bearing eccentricities at FRB 1 when $e = 10\mu\text{m}$, $e = 20\mu\text{m}$ and $e = 30\mu\text{m}$, respectively, (b), (d) and (f) bearing eccentricities at FRB 2 when $e = 10\mu\text{m}$, $e = 20\mu\text{m}$ and $e = 30\mu\text{m}$ respectively.

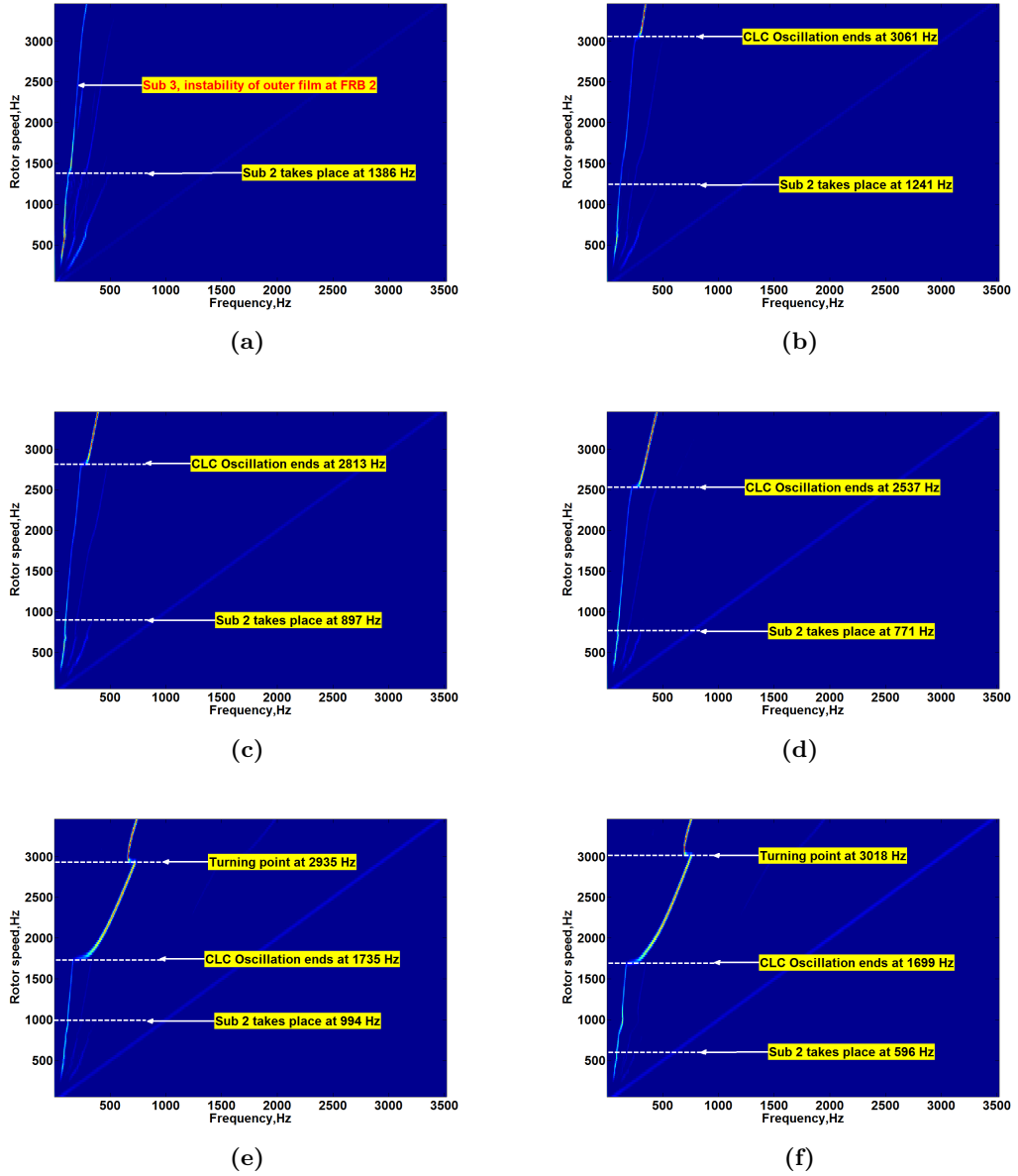


Fig. 6.25. Top-views of the waterfall plots of y_1/C_1 in run-down simulations when the out-of-phase unbalance is imposed ($\delta_c = 0$, $\delta_t = \pi$) and $C_2 = 50 \mu\text{m}$: (a) $e = 5 \mu\text{m}$, (b) $e = 10 \mu\text{m}$, (c) $e = 15 \mu\text{m}$, (d) $e = 20 \mu\text{m}$, (e) $e = 25 \mu\text{m}$ and (f) $e = 30 \mu\text{m}$.

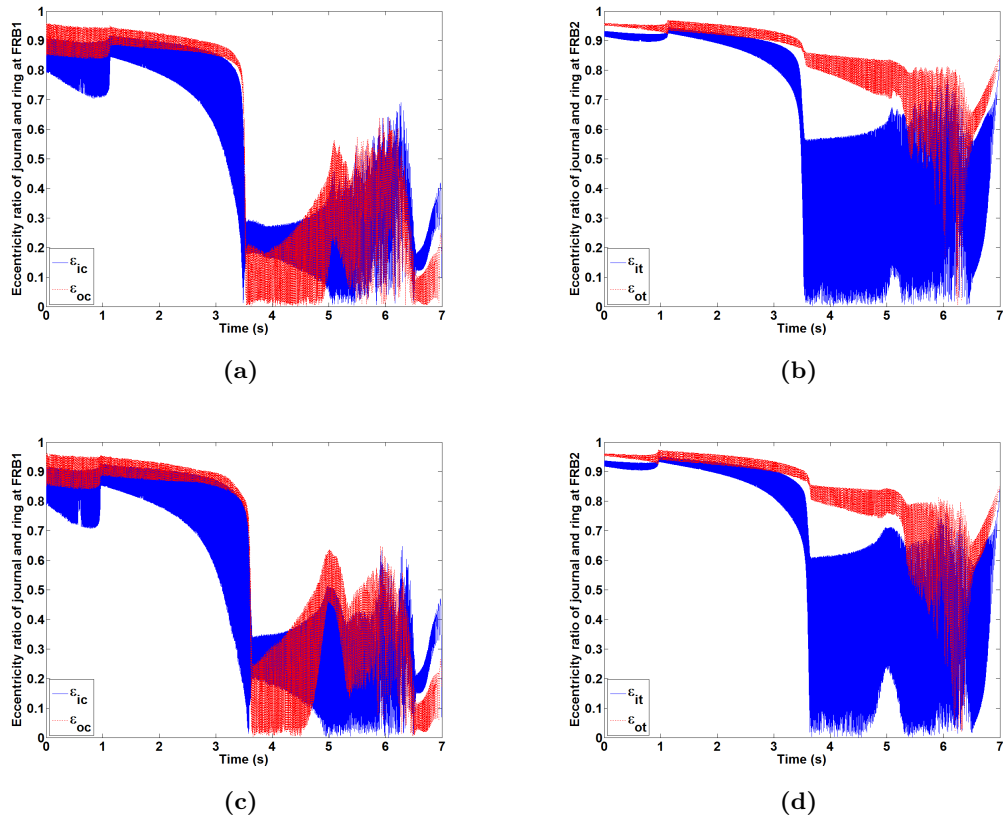


Fig. 6.26. FRB eccentricities in run-down simulations when $C_2 = 50 \mu\text{m}$ and out-of-phase unbalance is imposed: (a), (c) bearing eccentricities at FRB 1 when $e = 25 \mu\text{m}$ and $e = 30 \mu\text{m}$, respectively, (b), (d) bearing eccentricities at FRB 2 when $e = 25 \mu\text{m}$ and $e = 30 \mu\text{m}$, respectively.

corresponding bearing stiffness coefficients [86], especially the mean values of both inner eccentricities. Consequently, the climbing bearing stiffness coefficients of both FRBs bring out the increase of the natural frequency of the TC rotor-FRB system under investigation.

- (b) What can also be seen is that Sub 1 derived from the instability of inner films at the beginning of the perfectly balanced run-up cannot be identified, provided that the unbalance offset is bigger than $15 \mu\text{m}$ (see Figs. 6.23d-f). As mentioned earlier, the introduced high unbalance offset is able to suppress the Sub 1 initiated by the inner film instability. Prior to the rising of Sub 2, the investigated system is merely subject to synchronous vibration.
- (c) The existence of Sub 2 can be observed even though the added unbalance offset is as high as $30 \mu\text{m}$. However, with ascending unbalance offsets, the onset speed of Sub 2 slightly increases. By contrast, the speed at which Sub 2 disappears will be greatly reduced. The range in which Sub 2 as well as Sub 3 coexist cannot be identified any

more. Instead, the earlier disappearance of Sub 2 will leave an intermittent stable range, i.e., from 439 Hz to 687 Hz in Fig. 6.23f, prior to the occurrence of Sub 3.

- (d) It is interesting to see, when the considered highest unbalance offset is added, i.e., 30 μm , at 3329 Hz, a further jump of the *CLC Oscillation* component to a lower frequency location in Fig. 6.23f.
- (e) With respect to the run-up simulations, the waterfall top-views of the run-down simulations are shown in Fig. 6.25. Compared to the run-ups in Fig. 6.23, at the lower end of the considered speed range, it can be seen that the existence of Sub 3 can still be observed below 500 Hz, which leaves a longer coexistence range of Sub 2 and Sub 3 than in the run-ups. In addition, the disappearing speed of Sub 2 in the run-ups is higher than that when it appears in the run-downs unless the unbalance offset is above 20 μm , specifically, 25 μm and 30 μm . At the higher end of the speed range, attributed to the hysteresis effect, the *CLC Oscillation* lasts longer than in the run-ups. Interestingly, in Fig. 6.25e and f, the sudden jumps of the subsynchronous component from Sub 3 to a higher frequency at the onset of *CLC Oscillation* shown in Fig. 6.23e and f cannot be observed in the run-downs. By contrast, with descending rotor speed from the top, one observes a turning point of the *CLC Oscillation* component first, corresponding to the slight increase of the mean value of bearing eccentricities at FRB 1 as well as FRB 2 in Fig. 6.26. Thereafter, steady decreases of the mean values of both inner eccentricities, particularly the one at FRB 1, can clearly be observed, although their amplitudes follow a quickly ascending trend. Regarding to both bearing outer eccentricities, the top positions of the mean values of them are retained and the amplitudes generally become smaller, especially the one at FRB 1, until the occurrence of Sub 3.

6.3.3 In phase unbalance: $\delta_c = \delta_t = 0$

Considering the variable in-phase unbalance offsets, the results of run-ups as well as run-downs are shown in Figs. 6.27-6.30. In contrast with the out-of-phase unbalanced case, the main difference is the jump from Sub 3 to *CLC Oscillation* cannot be observed in the in-phase unbalanced simulations and distinct jumps of the subsynchronous component appear. The characteristics of the obtained results are summarised as below.

- (a) When the added unbalance offset is as small as 5 μm , at the lower end of the considered speed range, the run-up result resembles the balanced run-up in Fig.

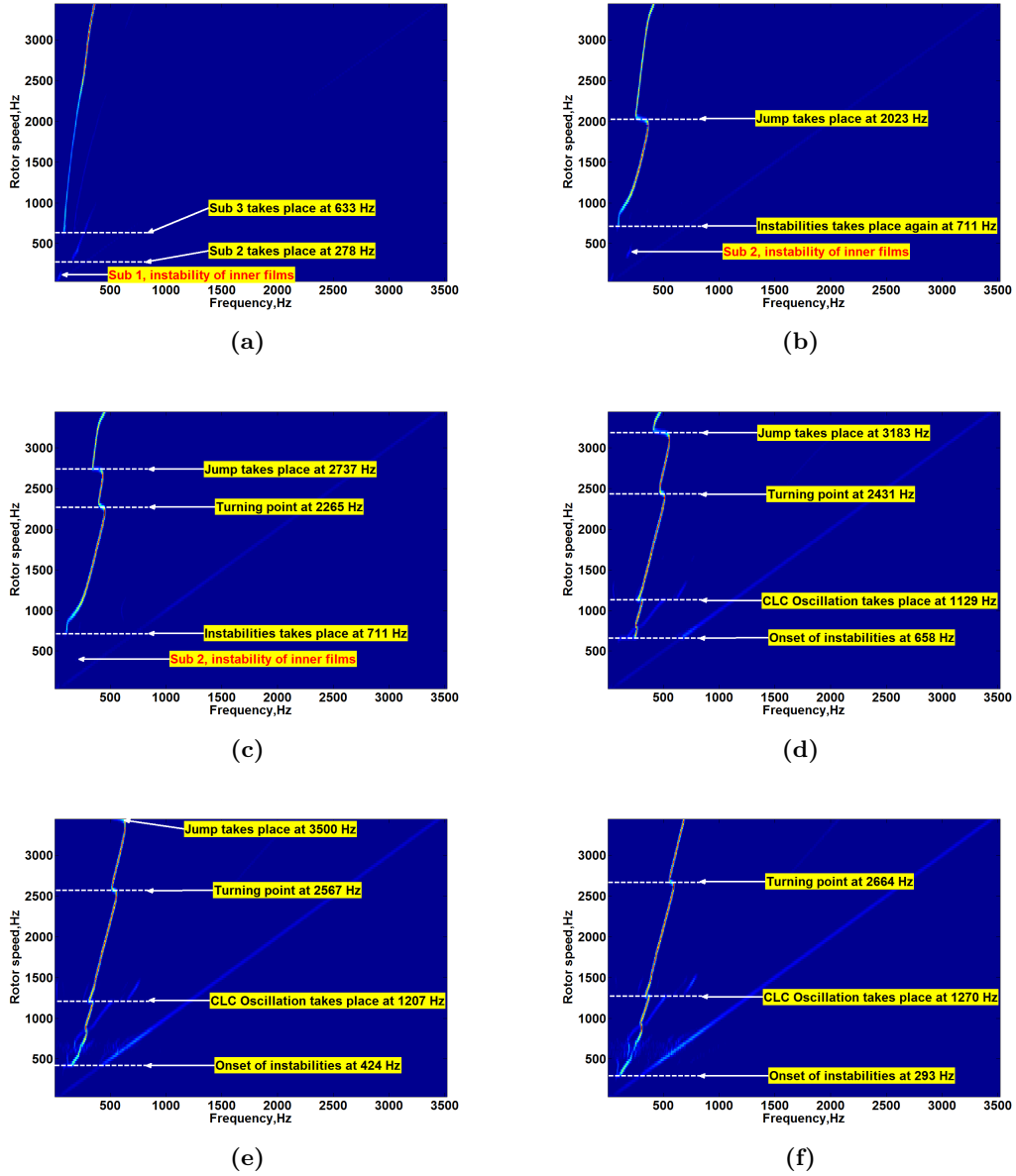


Fig. 6.27. Top-views of the waterfall plots of y_1/C_1 in run-up simulations when the in-phase unbalance is imposed ($\delta_c = 0$, $\delta_t = 0$) and $C_2 = 50 \mu\text{m}$: (a) $e = 5 \mu\text{m}$, (b) $e = 10 \mu\text{m}$, (c) $e = 15 \mu\text{m}$, (d) $e = 20 \mu\text{m}$, (e) $e = 25 \mu\text{m}$ and (f) $e = 30 \mu\text{m}$.

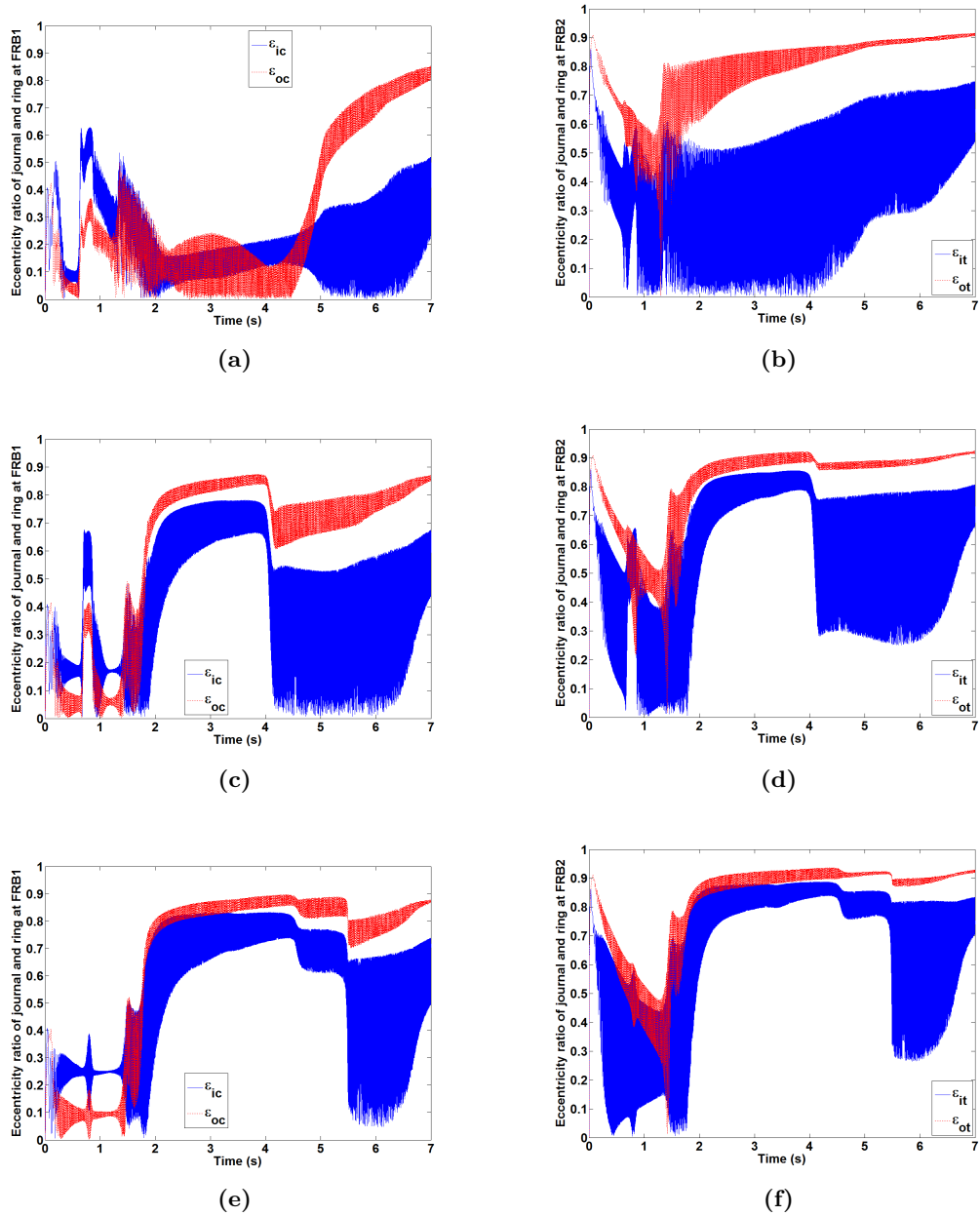


Fig. 6.28. FRB eccentricities in run-up simulations when $C_2 = 50 \mu\text{m}$ and in-phase unbalance is imposed: (a), (c), (e) and (g) bearing eccentricities at FRB 1 when $e = 5 \mu\text{m}$, $e = 10 \mu\text{m}$, $e = 15 \mu\text{m}$ and $e = 20 \mu\text{m}$, respectively, (b), (d), (f) and (h) bearing eccentricities at FRB 2 when $e = 5 \mu\text{m}$, $e = 10 \mu\text{m}$, $e = 15 \mu\text{m}$ and $e = 20 \mu\text{m}$, respectively.

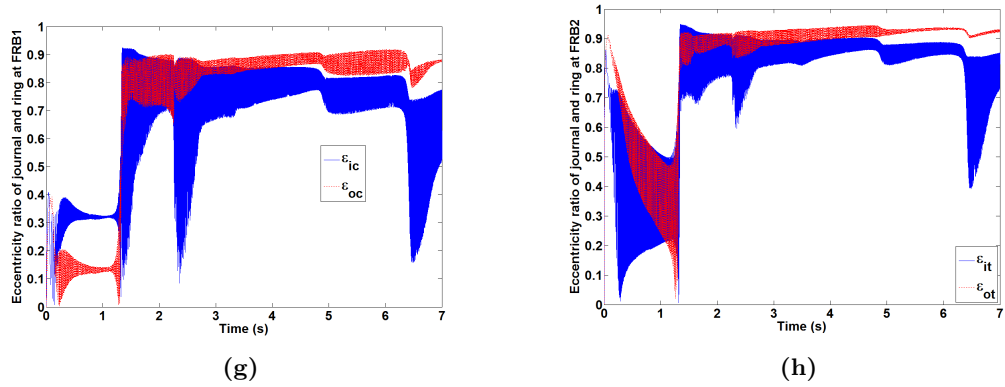


Fig. 6.28. (continued)

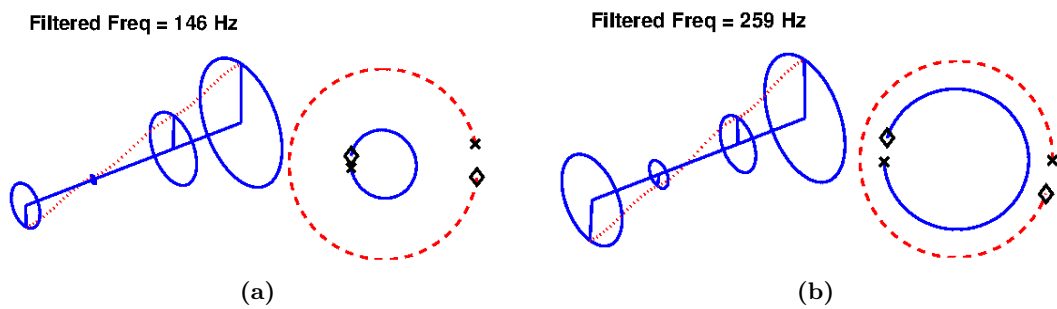


Fig. 6.29. Filtered mode shapes and orbits for subsynchronous components in run-up simulation when the outer clearances are 50 μm and 5 μm in-phase imbalance offset is imposed: (a) 1510 Hz and (b) 2508 Hz.

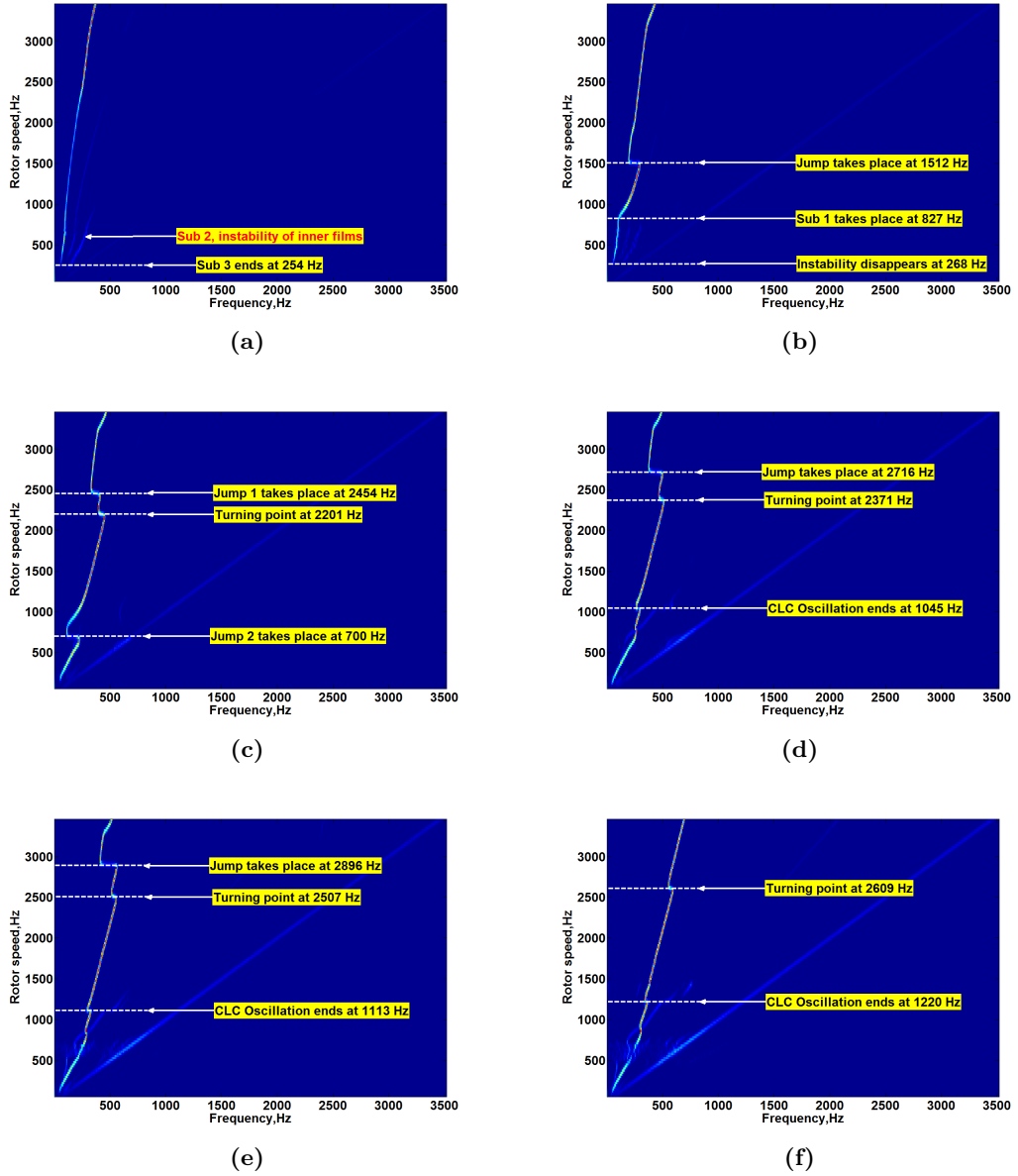


Fig. 6.30. Top-views of the waterfall plots of y_1/C_1 in run-down simulations when the in-phase unbalance is imposed ($\delta_c = 0$, $\delta_t = 0$) and $C_2 = 50 \mu\text{m}$: (a) $e = 5 \mu\text{m}$, (b) $e = 10 \mu\text{m}$, (c) $e = 15 \mu\text{m}$, (d) $e = 20 \mu\text{m}$, (e) $e = 25 \mu\text{m}$ and (f) $e = 30 \mu\text{m}$.

6.20, despite the slight differences in the onset speeds of Sub 2 and Sub 3. By contrast, at the higher end of the speed range, in Fig. 6.28a, what can be observed is the dramatic increase of the mean value of ϵ_{oc} , starting approximately from 4.5 s. Meanwhile, the climbing ϵ_{ic} can also be identified, although it is still clearly below 1. The filter mode shapes given in Fig. 6.29 show the appearance of ascending bearing eccentricities at FRB 1 will leave a change of the phase at Node 2 from out-of-phase with Node 1 to in-phase with Node 1.

- (b) With higher unbalance offsets, i.e., 10 μm and 15 μm , the existence of Sub 2 can also be identified, although the duration is much shorter than the case with 5 μm in-phase unbalance offset. Thereafter, the system undergoes purely unbalance induced vibrations. At 711 Hz, oil film instability takes place repeatedly, and one can see the considerable increases of the inner and outer eccentricities of both FRBs in Figs. 6.28c-f. At the moment, the *CLC Oscillation* is likely to be excited. Interestingly, a further frequency spectrum bifurcation or jump can be observed and a new subsynchronous component with lower frequency appears, e.g., at 2032 Hz in Fig. 6.27b. Correspondingly, sudden jumps of bearing eccentricities, especially the inner eccentricities, are shown in Fig. 6.28c and d. By contrast, prior to the occurrence of the above-mentioned frequency spectrum jump, the case with 15 μm unbalance offset shows a turning point first at 2265 Hz in Fig. 6.27c, accompanied by the slight decreases of the mean values of bearing eccentricities at both FRBs. The jump sets in at 2737 Hz afterwards.
- (c) With even bigger unbalance offsets, i.e., 20 μm , 25 μm and 30 μm , at the lower end of the speed range, Figs. 6.27d-f show Sub 2 completely disappears and the system is only subject to unbalance induced vibrations as the results in Fig. 6.7d as well as Figs. 6.16d-f. At the higher end of the speed range, with ascending offset values, the onset speed of the jump of the subsynchronous component will be significantly delayed and it cannot be observed in Fig. 6.16f. Additionally, as the unbalance offset value goes up, the speed with respect to the appearance of the turning point follows an ascending trend as well.
- (d) Correspondingly, the run-downs displayed in Fig. 6.30 indicate some distinct phenomena compared with the run-ups. When the unbalance offset is 5 μm , one can still see the existence of Sub 3 even though the rotor speed is lower than 500 Hz. In comparison with Fig. 6.27b, Fig. 6.30b shows the jump takes place earlier and the

following Sub 1 lasts much longer until 268 Hz after the end of *CLC Oscillation*. When the unbalance offset is as high as 15 μm , at the lower end of speed range, the appearance of Sub 1 derived from the inner and outer film instability of both FRBs is observed, compared to Fig. 6.27c. In addition, the onset speeds of the nonlinear jump and turning point become smaller than in the run-ups. With higher unbalance offsets, i.e., 20 μm , 25 μm and 30 μm , as shown in Figs. 6.30d-f, the pure unbalance vibration observed in the run-ups cannot be found, as the appearance of instability is able to extend to the very end of the run-downs.

6.4 Discussions of the Simulation Results

The above-mentioned simulation results reveal the complex effects placed by the variations of the imposed unbalance amount as well as distribution on the dynamic behaviours of the investigated TC rotor-FRB system. The main characteristics are discussed and summarised as below.

- (a) When the bearing outer clearance is 35 μm , the waterfall diagrams of the perfectly balanced run-up show the following jump sequence of the dominant subsynchronous component: Sub 1 (instability of the inner films) \rightarrow Sub 2 (instability of the inner films) and Sub 2 (instability of the inner films) \rightarrow Sub 1 (*CLC Oscillation*). The run-ups with out-of-phase unbalance offsets retain the main characteristics of the balanced run-up, provided that the imposed offset value is small enough, i.e., 5 μm and 10 μm . Higher out-of-phase unbalance offsets induce the occurrence of *CLC Oscillation* within the low-speed range. The run-downs deviate significantly from the corresponding out-of-phase unbalanced run-ups at the lower end of the considered speed range. In comparison with the balanced as well as the out-of-phase unbalanced simulations, even though the in-phase unbalance offset is as small as 5 μm , considerable differences have been observed in the depicted waterfall diagrams of the run-ups. The in-phase unbalanced run-downs exhibit a less sensitive state to the imposed unbalance when $e = 5 \mu\text{m}$. With higher unbalance offsets, the characteristics observed in the corresponding in-phase unbalanced run-ups reappears.
- (b) When the bearing outer clearance is 40 μm and the TC rotor is perfectly balanced, the dominant subsynchronous component jump sequence of the run-up is: Sub 1 (instability of the inner films) \rightarrow Sub 2 (instability of the inner films), Sub 2 (instability of the inner films) \rightarrow Sub 1 (coexistence of inner and outer film instability)

and subsequently Sub 1 (coexistence of inner and outer film instability) \rightarrow Sub 3 (instability of the outer film at FRB 2). Despite some differences in the onset speeds of nonlinear jumps, the out-of-phase unbalanced run-ups closely resemble the balanced run-up when the imposed offsets are 5 μm and 10 μm . Higher unbalance offset values, i.e., from 15 μm to 30 μm , bring out the onset of *CLC Oscillation* after the coexistence range of Sub 1 and Sub 2. The corresponding run-downs show the earlier appearance of *CLC Oscillation* than the run-up when $e = 10\mu\text{m}$. Another main difference is the *CLC Oscillation* as well as the Sub 1 and Sub 2 coexistence range are connected by Sub 3. The in-phase unbalanced run-ups indicate the occurrence of the nonlinear jump from Sub 3 to *CLC Oscillation* when the imposed unbalance offset is as small as 5 μm . Higher in-phase unbalance offsets give rise to the *CLC Oscillation* much earlier and Sub 3 cannot be observed any more. In the in-phase unbalanced run-downs, the simulation with 5 μm offset reveals, prior to the occurrence of Sub 3, the *CLC Oscillation* is followed by Sub 1 (coexistence of inner and outer film instability). The in-phase unbalanced run-downs with bigger offset values closely resemble the corresponding in-phase unbalanced run-ups.

- (c) When the bearing outer clearance is 50 μm and the TC rotor is in a perfectly balanced condition, the dominant subsynchronous component follows the following nonlinear jump frequency: Sub 1 (instability of the inner films) \rightarrow Sub 2 (instability of the inner films) and Sub 2 (instability of the inner films) \rightarrow Sub 3 (instability of the outer film at FRB 2). Under the slightly out-of-phase unbalanced condition, i.e., $e = 5\mu\text{m}$, the main characteristics of the balanced run-up are retained. Higher out-of-phase unbalance offsets bring out the occurrence of a further jump of the dominant subsynchronous component from Sub 3 to *CLC Oscillation*. With increasing unbalance offset value, the frequency location of the excited *CLC Oscillation* in the given waterfall plots follows an ascending trend and the onset speed of *CLC Oscillation* becomes smaller. The corresponding out-of-phase unbalanced run-downs exhibit a lower rotor speed when *CLC Oscillation* disappears, compared to the speed when it appears in the run-ups. In addition, the high unbalance offsets, i.e., 25 μm and 30 μm , introduce another *CLC Oscillation* component in the run-downs to reduce the mean values of both inner eccentricities steadily until Sub 3 occurs. The nonlinear jump from Sub 3 to *CLC Oscillation* cannot be observed in the in-phase unbalanced run-ups and run-downs. The considered smallest in-phase unbalance offset, i.e., 5 μm , can induce the onset of outer film instability at FRB 1, provided that the rotor

speed is high enough. With higher in-phase offsets, the *CLC Oscillation* is likely to be excited at a relatively low rotor speed, and a further jump of *CLC Oscillation* can be identified if the unbalance offset value is from 10 μm to 25 μm . Additionally, the onset speed of the further jump of *CLC Oscillation* increases with ascending unbalance offsets until it disappears when the highest offset, i.e. 30 μm , is imposed.

Chapter 7

Conclusions, Novel Contributions and Outlook

7.1 Summary of Results

In conclusion, the work of the author aims to investigate the nonlinear dynamic behaviour of a practical TC rotor-FRB system, which comply with the urgent need in the TC rotor-dynamic modelling. Deeper insights are obtained with the lately presented results. The conclusions of the main results are drawn as follows.

Turbocharger linear rotordynamics

Chapter 2 clearly presents and thoroughly discusses the linear rotordynamic characteristics of a realistic TC rotor-FRB system. Various linearized bearing models are introduced from the simplest constant stiffness spring to the more complex FRB linearization as two journal bearings in series. It is shown the utilisation of isotropic spring supports produce two rigid modes over the lower end of the frequency range, although the increase of spring stiffness leads to the considerable change of the mode shapes and the increase of the frequencies of the predicted modes. Anisotropic springs can produce mixed whirls owing to the anisotropic properties of the supports. The calculation with linearized journal bearings shows two unstable modes. They are mostly forward and rigid within the considered speed range. The linearization of FRBs without the ring mass exhibits similar results, although the damping properties of the predicted unstable modes will be affected by the increase of rotor speed. When the ring masses are included, additional unstable modes are brought about. In addition, it is shown that the FRB outer clearance can considerably affect the linear characteristics of the system. The synchronous calculation predicts a critical speed

at 2650 Hz, which produces the largest vibration amplitude over the considered speed range.

Stationary nonlinear simulation

Based upon the Capone's journal bearing model, a newly proposed FRB force model is developed and presented in Chapter 3. It has been validated through comparisons with the previous work. The perfectly balanced stationary simulations show that a synchronous component of 0.15 times of the rotor speed persist over the entire speed range. Another subsynchronous component of 0.25 times of the rotor speed can also be identified with much smaller amplitudes. When the 30 μm in-phase unbalance offset is induced at the two ends, it has been seen that the rotor response at relatively low speeds will be considerably affected. The subsynchronous vibrations appear later than in the perfectly balanced simulations. Moreover, the lower subsynchronous component is locked at approximately 0.20 times of the rotor speed, of which the frequency is higher than the component of 0.15 times of the rotor speed. Additionally, a higher mode with smaller amplitude is excited after 750 Hz. Furthermore, the linearly predicted critical speed cannot be identified in the nonlinear simulations, because of the high nonlinearity of the FRBs stiffens the rotor supports and considerably increase the natural frequencies of the higher modes.

Effects of engine excitation

The novel investigation taking into account the effects of engine induced vibrations is presented in Chapter 4. It is shown that, at relatively low speeds, the rotor response with engine vibrations deviates considerably from the case without engine vibrations. Complex rotor behaviour will be observed as the higher-order harmonic components of the engine rotating frequency are close to the low speeds of the TC rotor. However, the lower subsynchronous vibrations will also dominate the frequency spectrum at higher rotor speeds. In other words, the dominant effect of the subsynchronous vibrations can suppress the engine induced vibrations.

Nonlinear effects of bearing outer clearance

An investigation into the effects of FRB outer clearance on the TC rotordynamic performance has been carried out and presented in Chapter 5. It is shown the linear eigenvalue analysis can predict the occurrence of the nonlinear jump from Sub 1 to Sub 2. However, the nonlinear jumps at higher rotor speeds can hardly be linearly predicted, although

their appearances can possibly be linearly correlated with the predicted unstable modes. Both run-up and run-down simulations are carried out when the outer clearances of both bearings identically vary from 30 μm to 50 μm . The simulated rotor is assumed to be in a perfectly balanced condition to purely investigate the nonlinear properties of FRBs. The results, for the first time, systematically show the size of FRB outer clearance is critical to the response of the supported rotor. Accordingly, the turbocharger vibration level can be optimized and reduced through adjusting the bearing outer clearance to eliminate the undesired *CLC Oscillation*. Based upon the obtained simulation results, the considered bearing clearance range can be further divided into four groups as the rotor response exhibits similar characteristics within each group and presents qualitatively different phenomena providing that the clearance values are from different groups.

Nonlinear effects of unbalance

Based upon the results obtained from many run-up and run-down simulations, Chapter 6 systematically represents and discusses the latest findings on the effects produced by the unavoidable unbalance on the dynamics behaviours of the investigated TC rotor-FRB system. Three different FRB outer clearance values are examined in the performed simulations, and the variations of both the unbalance amount as well as distribution are included. In comparison with the perfectly unbalanced run-ups and run-downs, the results under the unbalanced condition show that the variable unbalance amount can alter the system response dramatically, which is indicated by the distinct sub-synchronous component patterns in the obtained waterfall diagrams. In the meantime, the variations of unbalance distribution, i.e., out-of-phase and in-phase unbalance offsets, can lead to significantly different phenomena as well. Additionally, the emergence of so-called *CLC Oscillation*, which can cause total failure of TC, can also be greatly influenced by the adoption of different unbalance amounts and distributions. Accordingly, the imbalance magnitude and distribution are critical parameters for the TC rotor-FRB system, and both of them need to be carefully considered during the dynamic analysis of the TC rotor-FRB system.

7.2 Novel Contributions

The obtained results show up the following novel contributions:

- (a) The linear stability analysis is thoroughly carried out in a gradually deepening manner. Predictions with linearized FRBs as two oil-films in series show that there are

mainly four unstable modes, which can be excited over the considered rotor speed range. Moreover, the variations of the FRB outer clearance can place a significant effect on the unstable Mode 1. With increasing bearing outer clearance, the unstable Mode 1 is suppressed, and the dominant range of the unstable Mode 2 appears. Furthermore, according to the stability map, unstable Mode 2 becomes weaker as the outer clearance becomes wider. By contrast, the onset speed of the unstable Mode 3 follows a descending trend, and it is more likely to be excited since its logarithmic decrement decreases as well.

- (b) A newly proposed calculation method extended from Capone's journal bearing model [2, 3, 18] for the desired nonlinear oil-film forces is detailed and validated through comparisons with previous work [11, 59]. The model is proved to be an efficient and reliable alternative to conduct the TC rotordynamic analysis. The preliminary studies considering unbalance reveal the onset of oil-film instability can be delayed under the assumed unbalanced condition.
- (c) The novel investigation concerning the engine excitation effect shows that the engine vibrations can considerably affect the rotor response over the lower end of the considered speed range. However, at higher rotor speeds, the engine induced vibrations become insignificant on the obtained waterfall diagrams, as a result of the suppression effect given by the dominant lower subsynchronous component.
- (d) It is seen that the variations of FRB outer clearance can dramatically influence the rotordynamic characteristics of the system. Nonlinearly simulated results show the appearances of distinct, intriguing phenomena within the considered range of FRB outer clearance, which can be further divided into four groups. Within the same group, the simulation results are qualitatively similar to each other but quite dissimilar from the results from different groups. Moreover, the unwelcome *Critical Limit Cycle Oscillation* can be avoided by increasing the outer clearance size. Additionally, in some cases, the run-down simulations reveal distinct nonlinear jump sequences as compared to the corresponding run-ups. Furthermore, it is seen that ring speed ratios can be considerably affected by the nonlinear jumps.
- (e) The amount and distribution of unbalance are proved to be the critical designing factors to improve the TC rotordynamic performance. The obtained new results clearly show the distinct phenomena brought about by the variations of the unbalance offset, which confirms that the unbalance level is a critical parameter for the

system response. In the meantime, the variations of unbalance distribution, i.e. out-of-phase and in-phase unbalance, can lead to entirely different simulation results as well, which proves the distribution of unbalance is not negligible during the dynamic analysis of the rotor-FRB system. Additionally, the occurrence of *Critical Limit Cycle Oscillation (CLC Oscillation)* can also be caused by the imposed unbalance amount and distribution.

7.3 Future Work

The following suggested work should be helpful for the further understanding of the complexity possessed by the TC rotor-FRB system.

- (a) Carry out the parameter studies considering the following additional bearing structural parameters: bearing inner clearance, bearing inner and outer length.
- (b) Study the thermal effects by considering the varying viscosity in the inner and outer oil-films.
- (c) Investigate the TC rotor-stator rub and the cracked rotor effects on the rotordynamic characteristics of the rotor-FRB system in TCs.
- (d) Study the effect of exhaust gas pulsation on the dynamic behaviours of the rotor-FRB system.
- (e) Examine the effect of radial aerodynamic forces on the rotordynamic performance of the TC rotor-FRB system.
- (f) Upgrade the bearing model using the finite bearing solutions to model the detailed FRB structure including the oil feeding holes to investigate the effect of oil feeding conditions on the TC rotordynamic characteristics.
- (g) Perform specific experiments to verify the simulation results.

References

- [1] Adams, M. (2009). *Rotating machinery vibration: from analysis to troubleshooting*, pages 158–163. CRC Press. [2.3](#), [2.4](#), [\(a\)](#), [3.3.2](#)
- [2] Adiletta, G., Guido, A., and Rossi, C. (1996). Chaotic motions of a rigid rotor in short journal bearings. *Nonlinear Dynamics*, 10(3):251–269. [1.2](#), [3](#), [3.1](#), [3.1](#), [3.1](#), [\(b\)](#)
- [3] Adiletta, G., Guido, A., and Rossi, C. (1997a). Nonlinear dynamics of a rigid unbalanced rotor in journal bearings. part i: Theoretical analysis. *Nonlinear Dynamics*, 14(1):57–87. [3.1](#), [\(b\)](#)
- [4] Adiletta, G., Guido, A., and Rossi, C. (1997b). Nonlinear dynamics of a rigid unbalanced rotor in journal bearings. part ii: Experimental analysis. *Nonlinear Dynamics*, 14(2):157–189. [1.2](#)
- [5] Aida, M., Umaoka, T., Mitsui, T., and Ushijima, Y. (1990). Development of a ball bearing turbocharger. *SAE Technical Paper 900125*. [1.3.9](#)
- [6] Alsaeed, A. (2005). Dynamic stability evaluation of an automotive turbocharger rotor-bearing system. Master’s thesis, Virginia Polytechnic Institute and State University. [1.3.6](#), [2](#)
- [7] Alsaeed, A. (2010). *A study of methods for improving the dynamic stability of high-speed turbochargers*. PhD thesis, Virginia Polytechnic Institute and State University. [1.3.6](#)
- [8] Amamou, A. and Chouchane, M. (2011). Non-linear stability analysis of floating ring bearings using hopf bifurcation theory. *Proceedings of the Institution of Mechanical Engineers, Part C: Journal of Mechanical Engineering Science*. [1.2](#), [1.3.5](#)
- [9] Ashtekar, A. and Sadeghi, F. (2011). Experimental and analytical investigation of high speed turbocharger ball bearings. *Journal of Engineering for Gas Turbines and Power*, 133(12):122501. [1.3.9](#)

-
- [10] Baines, N. (2005). *Fundamentals of Turbocharging*. Concepts NREC. 1.1
- [11] Bonello, P. (2009). Transient modal analysis of the non-linear dynamics of a turbocharger on floating ring bearings. *Proceedings of the Institution of Mechanical Engineers, Part J: Journal of Engineering Tribology*, 223(1):79–93. 1.3.6, 2.1, 3, 3.2, 3.3.1, 3.3.1, 3.3.2, 3.3.2, 3.4, (b)
- [12] Born, H. R. (1987). Analytical and experimental investigation of the stability of the rotor-bearing system of a new small turbocharger. In *32. ASME Gas Turbine Conference and Exhibition*, Anaheim, CA, USA. American Society of Mechanical Engineers. 1.3.6
- [13] Boyaci, A., Hetzler, H., Seemann, W., Proppe, C., and Wauer, J. (2009). Analytical bifurcation analysis of a rotor supported by floating ring bearings. *Nonlinear Dynamics*, 57(4):497–507. 1.3.5
- [14] Boyaci, A., Seemann, W., and Proppe, C. (2007). On the dynamics of a nonlinear rotor-floating ring bearing system. *PAMM*, 7(1). 1.3.5
- [15] Boyaci, A., Seemann, W., and Proppe, C. (2010). Stability analysis of rotors supported by floating ring bearings. In *The 8th IFToMM International Conference on Rotor Dynamics*, pages 286–295, Seoul, Korea. 1.2, 1.3.5, 1.3.6
- [16] Boyaci, A., Seemann, W., and Proppe, C. (2011). Bifurcation analysis of a turbocharger rotor supported by floating ring bearings. In *IUTAM Symposium on Emerging Trends in Rotor Dynamics*, pages 335–347. Springer. 1.2, 1.3.5, (c), (e), (a)
- [17] Cameron, A. and Mc Ettles, C. (1976). *Basic lubrication theory*, pages 95–97. E. Horwood. 2.1, 3.2
- [18] Capone, G. (1991). Analytical description of fluid-dynamic force field in cylindrical journal bearing. *L'Energia Elettrica*, 68:105–110 (in Italian). 1.3.6, 3, (b)
- [19] Chen, W. J. (2011). Rotordynamics and bearing design of turbochargers. *Mechanical Systems and Signal Processing*. 1.3.10
- [20] Cheong, Y. and Kim, K. (1994). An analysis of the circumferentially grooved floating ring journal bearing considering the variation of cavitation region. *JSME International Journal-Series C-Dynamics Control Robotics Design and Manufacturing*, 37(4):804–811. 1.3.3

-
- [21] Childs, D., Moes, H., and Van Leeuwen, H. (1977). Journal bearing impedance descriptions for rotordynamic applications. *Transactions of the ASME*, 99(2):198–210. [1.3.1](#), [1.3.6](#)
- [22] Clarke, D., Fall, C., Hayden, G., and Wilkinson, T. (1992). A steady-state model of a floating ring bearing, including thermal effects. *Journal of Tribology*, 114:141. [1.3.2](#)
- [23] de Castro, H. F., Cavalca, K. L., and Nordmann, R. (2008). Whirl and whip instabilities in rotor-bearing system considering a nonlinear force model. *Journal of Sound and Vibration*, 317(1-2):273–293. [1.2](#), [3.1](#)
- [24] De Choudhury, P. (2004). Rotordynamic stability case studies. *International Journal of Rotating Machinery*, 10(3):203–211. [1.3.10](#)
- [25] Dong, X. and Zhao, Z. (1990). Experimental and analytical research on floating-ring bearings for engine applications. *Journal of Tribology*, 112:119. [1.3.1](#)
- [26] Dowson, D., Ruddy, A., Sharp, R., and Taylor, C. (1985). An analysis of the circumferentially grooved journal bearing with consideration of lubricant film reformation. *Proceedings of the Institution of Mechanical Engineers, Part C: Journal of Mechanical Engineering Science*, 199(13):27–34. [1.3.3](#)
- [27] Friswell, M. (2010). *Dynamics of rotating machines*, pages 102–103. Cambridge University Press. [1.4](#), [2.1](#), [2.3](#), [2.4](#), (a)
- [28] Genta, G. (2005). *Dynamics of rotating systems*. Springer Verlag. [2.4](#)
- [29] Gjika, K. and LaRue, G. (2002). Dynamic behaviour of rotor-bearing systems involving two oil films in series - application to high-speed turbochargers. In *7th International Conference on Turbochargers and Turbocharging*, pages 91–100, London, UK. Institution of Mechanical Engineers. [1.3.6](#)
- [30] Gjika, K., San Andrés, L., and Larue, G. (2010). Nonlinear dynamic behavior of turbocharger rotor-bearing systems with hydrodynamic oil film and squeeze film damper in series: Prediction and experiment. *Journal of Computational and Nonlinear Dynamics*, 5(4):041006. [1.3.7](#)
- [31] Griffith, R., Slaughter, S., and Mavrosakis, P. (2007). Applying ball bearings to the series turbochargers for the caterpillar® heavy-duty on-highway truck engines. *SAE Technical Paper 2007-01-4235*. [1.3.9](#)

- [32] Gunter, E. and Chen, W. (2005). Dynamic analysis of a turbocharger in floating bushing bearings. In *ISCORMA-3 Conference, Cleveland Ohio, EEUU, September*. 1.3.6
- [33] Hamrock, B., Schmid, S., and Jacobson, B. (2004). *Fundamentals of fluid film lubrication*. CRC. 2.4
- [34] Hatakenaka, K., Tanaka, M., and Suzuki, K. (2002). A theoretical analysis of floating bush journal bearing with axial oil film rupture being considered. *Journal of Tribology*, 124(3):494–505. 1.3.3
- [35] Hemmi, M. and Inoue, T. (2002). Effects of characteristics of floating bush bearings on the stability of turbochargers. In *The 6th International Conference on Motion and Vibration Control*, pages 979–984, Saitama, Japan. 1.3.6, 2, 2.6.2
- [36] Hiereth, H. and Prenninger, P. (2007). *Charging the internal combustion engine*. Springer Verlag. 1.1, 1.1, 1.2
- [37] Holmes, R. (2002). Turbocharger vibration—a case study. In *Seventh International Conference on turbochargers and turbocharging*, pages 91–100, London, UK. Institution of Mechanical Engineers. 1.3.4
- [38] Holmes, R., Brennan, M. J., and Gottrand, I. (2004). Vibration of an automotive turbocharger—a case study. In *Eighth International Conference on Vibrations in Rotating Machinery*, pages 445–455, Swansea, UK. Institution of Mechanical Engineers. 1.2, 1.3.4, 3.4
- [39] Holt, C., Andres, L. S., Sahay, S., Tang, P., Rue, G. L., and Gjika, K. (2003a). Test response of a turbocharger supported on floating ring bearings: Part i — assessment of subsynchronous motions. In *ASME 2003 International Design Engineering Technical Conferences and Computers and Information in Engineering Conference (IDETC/CIE2003)*, number DETC2003/VIB-48418, Chicago, Illinois, USA. ASME. 1.3.6
- [40] Holt, C., Andres, L. S., Sahay, S., Tang, P., Rue, G. L., and Gjika, K. (2003b). Test response of a turbocharger supported on floating ring bearings: Part ii — comparisons to nonlinear rotordynamic predictions. In *ASME 2003 International Design Engineering Technical Conferences and Computers and Information in Engineering Conference (IDETC/CIE2003)*, number DETC2003/VIB-48419, Chicago, Illinois, USA. ASME. 1.3.6

-
- [41] Holt, C., Andres, L. S., Sahay, S., Tang, P., Rue, G. L., and Gjika, K. (2005). Test response and nonlinear analysis of a turbocharger supported on floating ring bearings. *Journal of Vibration and Acoustics*, 127(2):107–115. [1.3.6](#)
- [42] Howard, S. (1999). Rotordynamics and design methods of an oil-free turbocharger. *Tribology transactions*, 42(1):174–179. [1.3.10](#)
- [43] Inagaki, M., Kawamoto, A., Abekura, T., Suzuki, A., Rübél, J., and Starke, J. (2011). Coupling analysis of dynamics and oil film lubrication on rotor-floating bush bearing system. *Journal of System Design and Dynamics*, 5(3):461–473. [1.3.6](#), [3](#), [3.1](#)
- [44] Jing, J. P., Meng, G., Sun, Y., and Xia, S. B. (2004). On the non-linear dynamic behavior of a rotor-bearing system. *Journal of Sound and Vibration*, 274(3-5):1031–1044. [1.2](#)
- [45] Kamesh, P. (2011). *Oil-whirl instability in an automotive turbocharger*. PhD thesis, University of Southampton. [1.3.6](#)
- [46] Kamesh, P., Brennan, M. J., and Holmes, R. (2012). On the stabilising effect of gyroscopic moments in an automotive turbocharger. *Proceedings of the Institution of Mechanical Engineers, Part C: Journal of Mechanical Engineering Science*. [1.3.6](#)
- [47] Keller, R., Scharrer, J., and Pelletti, J. (1996). Alternative performance turbocharger bearing design. *SAE Technical Paper 962500*. [1.3.10](#)
- [48] Kelly, A. (2010). Rotordynamic characterization and comparison of turbocharger bearing systems. In *9th International Conference on Turbochargers and Turbocharging*, pages 325–334. [1.3.10](#)
- [49] Kettleborough, C. (1954). Frictional experiments on lightly-loaded fully floating journal bearings. *Australia Journal of Applied Science*, 5(3):211–220. [1.3.1](#), [1.3.2](#)
- [50] Kirk, R., Alsaeed, A., and Gunter, E. (2007). Stability analysis of a high-speed automotive turbocharger. *Tribology Transactions*, 50(3):427–434. [1.1](#), [1.2](#), [1.3.6](#), [2](#), [3.4](#)
- [51] Kirk, R., Alsaeed, A., Liptrap, J., Lindsey, C., Sutherland, D., Dillon, B., Saunders, E., Chappell, M., Nawshin, S., and Christian, E. (2008). Experimental test results for vibration of a high speed diesel engine turbocharger. *Tribology Transactions*, 51(4):422–427. [1.2](#), [1.3.6](#), [3.4](#)

- [52] Kirk, R. and Alsaeed, A. A. (2011). Induced unbalance as a method for improving the dynamic stability of high-speed turbochargers. *International Journal of Rotating Machinery*, 2011(Article ID 952869). [1.3.6](#), [2](#), [2.6.2](#)
- [53] Kirk, R., Kornhauser, A., Sterling, J., and Alsaeed, A. (2009). Turbocharger on-engine experimental vibration testing. *Journal of Vibration and Control*, 16(3):343–355. [1.2](#), [1.3.6](#), [3.4](#)
- [54] Kirk, R. G., Alsaeed, A., and Mondschein, B. (2011). Turbocharger vibration shows nonlinear jump. *Journal of Vibration and Control*. [1.3.6](#)
- [55] Knoll, G., Seemann, W., Proppe, C., Koch, R., Backhaus, K., and Boyaci, A. (2010). Run-up of turbocharger rotors in nonlinearly modelled floating bush bearings. *MTZ worldwide Edition: 2010-04*, pages 50–55. [1.3.6](#)
- [56] Kozhenkov, A. A. and Deitch, R. S. (2008). Three-dimensional finite element simulation of nonlinear dynamic rotor systems of a turbocharger. *Journal of Vibration and Acoustics*, 130(3):031003. [1.3.6](#)
- [57] Kuma, H., Inoue, T., Isogai, T., Shimizu, K., Iida, T., Inagaki, M., and Ohara, K. (2007). Development of reduction method for whirl noise on turbocharger. *SAE Technical Paper 2007-01-4018*. [1.3.6](#), [3](#), [5.2.2](#)
- [58] Li, C. (1982). Dynamics of rotor bearing systems supported by floating ring bearings. *Journal of Lubrication Technology-Transactions of the ASME*, 104:469–476. [1.3.6](#)
- [59] Li, C. H. and Rohde, S. M. (1981). On the steady state and dynamic performance characteristics of floating ring bearings. *Journal of Lubrication Technology-Transactions of the ASME*, 103:389–397. [1.3.1](#), [3](#), [3.3.1](#), [3.3.1](#), [\(b\)](#)
- [60] Maruyama, A. (2007). Prediction of automotive turbocharger nonlinear dynamic forced response with engine-induced housing excitations: comparisons to test data. Ms thesis, Texas A&M University. [\(document\)](#), [1.3](#), [1.3.7](#), [4](#), [4.1](#)
- [61] McLuckie, I. and Barrett, S. (2007). Plain and full floating bearing simulations with rigid shaft dynamics. In *ASME Conference Proceedings*, volume 1, pages 541–550. [1.3.6](#)
- [62] Miyashita, K., Kurasawa, M., Matsuoka, H., and Ikeya, N. (1987). Development of high efficiency ball-bearing turbocharger. *SAE Technical Paper 870354*. [1.3.9](#)

-
- [63] Mokhtar, M. (1981). Floating ring journal bearings: theory, design and optimization. *Tribology International*, 14(2):113–119. [1.3.1](#)
- [64] Mokhtar, M., El-Butch, A., and Ibrahim, I. (2005). Adoption of floating-ring bearing design in automotive applications. *SAE Technical Paper 2005-01-3783*. [1.3.10](#)
- [65] Muszynska, A. (1986). Whirl and whip–rotor/bearing stability problems. *Journal of Sound and vibration*, 110(3):443–462. [1.2](#)
- [66] Muszynska, A. (1988). Stability of whirl and whip in rotor/bearing systems. *Journal of Sound and Vibration*, 127(1):49–64. [1.2](#)
- [67] Nakagawa, E. and Aoki, H. (1973). Unbalance vibration of a rotor-bearing system supported by floating-ring journal bearings. *Bulletin of JSME*, 16(93):503–512. [1.3.1](#), [1.3.2](#)
- [68] Nikolajsen, J. (1973). The effect of variable viscosity on the stability of plain journal bearings and floating-ring journal bearings. *Journal of Lubrication Technology-Transactions of the ASME*, 95(4):447–456. [1.3.1](#)
- [69] Orcutt, F. and Ng, C. (1968). Steady-state and dynamic properties of the floating-ring journal bearing. *Journal of Lubrication Technology-Transactions of the ASME*, 90:243–253. [1.3.1](#), [1.3.2](#)
- [70] Pantelelis, N. G., Kanarachos, A. E., and Gotzias, N. (2000). Neural networks and simple models for the fault diagnosis of naval turbochargers. *Mathematics and Computers in Simulation*, 51(3-4):387–397. [1.3.8](#)
- [71] Pettinato, B. and DeChoudhury, P. (2003). Rotordynamic and bearing upgrade of a high-speed turbocharger. *Journal of Engineering for Gas Turbines and Power*, 125(1):95–101. [1.3.10](#)
- [72] Rivadeneira, J. (2006). Predictions versus measurements of turbocharger nonlinear dynamic response. Master’s thesis, Texas A&M University. [1.3.6](#), [3.1](#)
- [73] Rodríguez, H., Furman, A., and Panambur, S. (2003). Rotor dynamic improvement for a locomotive turbocharger. In *ASME 2003 Internal Combustion Engine and Rail Transportation Divisions Fall Technical Conference (ICERT2003)*, pages 93–98, Erie, Pennsylvania, USA. ASME. [1.3.10](#)

- [74] Rohde, S. and Ezzat, H. (1980). Analysis of dynamically loaded floating-ring bearings for automotive applications. *Journal of Lubrication Technology-Transactions of the ASME*, 102(3):271–277. [1.3.1](#), [3.2](#)
- [75] Rübél, J. (2009). *Vibrations in nonlinear rotordynamics: modelling, simulation, and analysis*. PhD thesis, Heidelberg University. [1.3.6](#), [3](#), [3.1](#)
- [76] Sahay, S. (1995). Turbocharger rotor-bearing design optimization. *SAE Technical Paper 952295*. [1.3.10](#)
- [77] Sahay, S. and LaRue, G. (1996). Turbocharger rotordynamic instability and control. In *Rotordynamic Instability Problems in High-Performance Turbomachinery*, pages 247–257. [1.3.10](#)
- [78] San Andrés, L. and Kerth, J. (2004). Thermal effects on the performance of floating ring bearings for turbochargers. *Proceedings of the Institution of Mechanical Engineers, Part J: Journal of Engineering Tribology*, 218(5):437–450. [1.2](#), [1.3.6](#)
- [79] San Andrés, L., Maruyama, A., Gjika, K., Xia, S., et al. (2010). Turbocharger nonlinear response with engine-induced excitations: predictions and test data. *Journal of Engineering for Gas Turbines and Power*, 132(3):032502. [1.3.7](#), [4](#), [4.1](#)
- [80] San Andrés, L., Rivadeneira, J., Chinta, M., Gjika, K., and LaRue, G. (2007a). Nonlinear rotordynamics of automotive turbochargers: Predictions and comparisons to test data. *Journal of Engineering for Gas Turbines and Power*, 129(2):488–493. [1.2](#), [1.3.7](#)
- [81] San Andrés, L., Rivadeneira, J., Gjika, K., Groves, C., and LaRue, G. (2007b). Rotordynamics of small turbochargers supported on floating ring bearings-highlights in bearing analysis and experimental validation. *Journal of Tribology*, 129(2):391–397. [1.3.6](#)
- [82] San Andrés, L., Rivadeneira, J., Gjika, K., Groves, C., and LaRue, G. (2007c). A virtual tool for prediction of turbocharger nonlinear dynamic response: validation against test data. *Journal of Engineering for Gas Turbines and Power*, 129(4):1035–1046. [1.2](#), [1.3.6](#)
- [83] San Andrés, L. and Vistamehr, A. (2010). Nonlinear rotordynamics of vehicle turbochargers: parameters affecting sub harmonic whirl frequencies and their jump. In *The*

-
- 8th IFToMM international Conference on Rotor Dynamics*, pages 1077–1086, Seoul, Korea. [1.3.7](#)
- [84] Schilder, F., Rübél, J., Starke, J., Osinga, H., Krauskopf, B., and Inagaki, M. (2008). Efficient computation of quasiperiodic oscillations in nonlinear systems with fast rotating parts. *Nonlinear Dynamics*, 51(4):529–539. [1.3.6](#)
- [85] Schweizer, B. (2009a). Oil whirl, oil whip and whirl/whip synchronization occurring in rotor systems with full-floating ring bearings. *Nonlinear Dynamics*, 57(4):509–532. [1.2](#), [1.2](#), [1.3.5](#), [1.3.6](#), [\(c\)](#), [\(a\)](#)
- [86] Schweizer, B. (2009b). Total instability of turbocharger rotors—physical explanation of the dynamic failure of rotors with full-floating ring bearings. *Journal of Sound and Vibration*, 328(1-2):156–190. [\(document\)](#), [1.4](#), [1.2](#), [1.3.5](#), [1.3.6](#), [2.1](#), [5](#), [\(c\)](#), [\(a\)](#), [\(a\)](#)
- [87] Schweizer, B. (2010). Dynamics and stability of turbocharger rotors. *Archive of Applied Mechanics*, 80(9):1017–1043. [1.2](#), [1.3.6](#), [2.1](#), [3.1](#), [3.4](#), [5](#)
- [88] Schweizer, B. and Sievert, M. (2009). Nonlinear oscillations of automotive turbocharger turbines. *Journal of Sound and Vibration*, 321(3-5):955–975. [1.2](#), [1.2](#), [1.3.6](#), [3.1](#)
- [89] Shaw, M. and Nussdorfer, T. (1947). An analysis of the full-floating journal bearing. *NACA Research Memorandum E 7A28a*. [1.3.1](#)
- [90] Shi, F. and Deng, D. (2011). An analysis for floating bearings in a turbocharger. *SAE Technical Paper 2011-01-0375*. [1.3.3](#)
- [91] Soh, K.-Y., Euo, D.-K., Bae, D.-H., and Kang, K.-T. (2003). Noise reduction in turbocharger system of diesel engines. In *The 32nd International Congress and Exposition on Noise Control Engineering*, pages 155–162, Seogwipo, Korea. [1.3.6](#)
- [92] Tanaka, M. (1996). A theoretical analysis of stability characteristics of high-speed floating bush bearings. In *IMEchE Conference Transactions*, volume 6, pages 133–142. [1.3.3](#), [1.3.4](#)
- [93] Tanaka, M. and Hori, Y. (1972). Stability characteristics of floating bush bearings. *Journal of Lubrication Technology-Transactions of the ASME*, 93(3):248–259. [1.3.1](#), [1.3.3](#), [1.3.4](#), [3.1](#)

- [94] Tatara, A. (1970). An experimental study of the stabilizing effect of floating-bush journal bearings. *Bulletin of JSME*, 13(61):858–863. [1.3.1](#), [1.3.3](#), [1.3.4](#), [1.3.6](#)
- [95] Tian, L., Wang, W. J., and Peng, Z. J. (2011). Dynamic behaviours of a full floating ring bearing supported turbocharger rotor with engine excitation. *Journal of Sound and Vibration*, 330(20):4851–4874. [1.3.6](#), [2](#), [2.1](#), [3.1](#)
- [96] Tomek, O., Šimek, J., and Svoboda, R. (2011). Theoretical and experimental analysis of the influence of oil film geometry on turbocharger rotor stability. In *SIRM 2011 - 9th International Conference on Vibrations in Rotating Machines*, Darmstadt, Germany. [1.3.10](#)
- [97] Tomm, U., Boyaci, A., Proppe, C., Seemann, W., Busch, M., Esmacil, L., and Schweizer, B. (2010). Rotor dynamic analysis of a passenger car turbocharger using run-up simulation and bifurcation theory. In *9th International Conference on Turbochargers and Turbocharging*, pages 335–347, London, UK. [1.3.6](#)
- [98] Trippett, R. and Li, D. (1984). High-speed floating-ring bearing test and analysis. *Tribology Transactions*, 27(1):73–81. [1.3.2](#), [1.3.3](#), [1.3.6](#)
- [99] Trippett, R. J. (1986). Measured and predicted friction in floating-ring bearings. *SAE Technical Paper 860075*. [1.3.1](#)
- [100] Vistamehr, A. (2009). Analysis of automotive turbocharger nonlinear vibrations including bifurcations. Master’s thesis, Texas A&M University. ([document](#)), [1.2](#), [1.2](#), [1.3.7](#), [3.1](#), [5.2.1](#), [5.2.2](#)
- [101] Wang, J., Cao, D., and Huang, W. (2010). A new fluid film force model of elliptical bearing: modelling and case studies. *Proceedings of the Institution of Mechanical Engineers, Part J: Journal of Engineering Tribology*, 224(J7):1–14. [3.1](#)
- [102] Ying, G., Meng, G., and Jing, J. (2009). Turbocharger rotor dynamics with foundation excitation. *Archive of Applied Mechanics*, 79(4):287–299. [1.3.6](#), [3.4](#), [4](#), [4.1](#), [4.1](#)
- [103] Zhang, H., Shi, Z., Gu, F., and Ball, A. (2011). Modelling of outer and inner film oil pressure for floating ring bearing clearance in turbochargers. In *Journal of Physics: Conference Series*, volume 305, page 012021. [1.3.3](#)

Appendix A

Research Publications

The following are published research papers generated as part of the work presented in the thesis. They are listed in the following order:

- (a) L. Tian, W.J. Wang, Z.J. Peng, Nonlinear effects of unbalance in the rotor-floating ring bearing systems of turbochargers, *Mechanical Systems and Signal Processing* (2012), <http://dx.doi.org/10.1016/j.ymssp.2012.07.017>
- (b) L. Tian, W.J. Wang, Z.J. Peng, Effects of bearing outer clearance on the dynamic behaviours of the full floating ring bearing supported turbocharger rotor, *Mechanical Systems and Signal Processing* 31 (2012) 155-175.
- (c) L. Tian, W.J. Wang, Z.J. Peng, Dynamic behaviours of a full floating ring bearing supported turbocharger rotor with engine excitation, *Journal of Sound and Vibration* 330 (20) (2011) 4851-4874.
- (d) Z. Peng, B. Liu, L. Tian and L. Lu, Analysis of Homogeneity Factor for Diesel PCCI Combustion Control, 2011 JSAE/SAE Powertrains, Fuels and Lubricants Conference (JSAE 20119266, SAE 2011-01-1832), Kyoto, Japan, 30 August – 2 September 2011. <http://papers.sae.org/2011-01-1832>